

AD/A-003 648

**FIELD TESTS OF A LASER RAMAN MEASURE-
MENT SYSTEM FOR AIRCRAFT ENGINE EXHAUST
EMISSIONS**

Donald A. Leonard

Avco Everett Research Laboratory, Incorporated

Prepared for:

Air Force Aero Propulsion Laboratory

October 1974

DISTRIBUTED BY:

NTIS

**National Technical Information Service
U. S. DEPARTMENT OF COMMERCE**

UNCLASSIFIED

Security Classification

DOCUMENT CONTROL DATA - R & D

AD/A-003648

(Security classification of title, body of abstract and indexing annotation not be entered when the overall report is classified)

1. ORIGINATING ACTIVITY (Corporate author) AVCO EVERETT RESEARCH LABORATORY, INC. 2385 REVERE BEACH PARKWAY EVERETT, MASSACHUSETTS 02149		2a. REPORT SECURITY CLASSIFICATION UNCLASSIFIED	
		2b. GROUP	
3. REPORT TITLE FIELD TESTS OF A LASER RAMAN MEASUREMENT SYSTEM FOR AIRCRAFT ENGINE EXHAUST EMISSIONS			
4. DESCRIPTIVE NOTES (Type of report and inclusive dates) Final Technical Report			
5. AUTHOR(S) (First name, middle initial, last name) Avco Everett Research Laboratory, Inc. Donald A. Leonard			
6. REPORT DATE October 1974	7a. TOTAL NO. OF PAGES 179	7b. NO. OF REFS 28	
8a. CONTRACT OR GRANT NO. F33615-71-C-1875	8b. ORIGINATOR'S REPORT NUMBER(S)		
8c. PROJECT NO. 3066	8d. OTHER REPORT NO(S) (Any other numbers that may be assigned this report) AFAPL-TR-74-100		
10. DISTRIBUTION STATEMENT Approved for public release; distribution unlimited.			
11. SUPPLEMENTARY NOTES		12. SPONSORING MILITARY ACTIVITY Air Force Aero Propulsion Laboratory Air Force Systems Command, USAF Wright Patterson Air Force Base, Ohio	
13. ABSTRACT Laser induced Raman and fluorescent measurements were made in the exhaust of a T53-L13A gas turbine engine with a new field portable instrument devised specifically for gas turbine exhaust emission measurements. The gas turbine exhaust was analyzed by conventional instruments for CO, CO ₂ , NO, NO _x , total hydrocarbons, smoke and temperature, and these data were used as a "calibration" standard for the evaluation of the laser Raman instrument. Results thus far indicate good correlations for CO ₂ , O ₂ , smoke, hydrocarbons and temperature. The instrument was not sensitive enough for NO detection but the data analysis indicates that 100 ppm may be detectable with instrument improvements. CO analysis was not attempted, but it is expected that CO could be detected with further research. NO ₂ (or NO _x) was not attempted because theoretical and experimental laboratory analysis indicated severe interference with CO ₂ . The most severe problem area was laser induced hydrocarbon fluorescence when the exhaust contained large total hydrocarbon concentrations. The overall conclusion was that the laser Raman method shows a good potential for aircraft gas turbine emission analysis.			

Reproduced by
NATIONAL TECHNICAL
INFORMATION SERVICE
US Department of Commerce
Springfield, VA. 22151

DD FORM 1473
1 NOV 66UNCLASSIFIED
Security Classification

UNCLASSIFIED

Security Classification

14	KEY WORDS	LINK A		LINK D		LINK C	
		ROLE	WT	ROLE	WT	ROLE	WT
	1. Analytical Raman Spectroscopy 2. Aircraft Emissions Monitoring 3. Combustion Emissions Monitoring 4. Pollution Monitoring 5. Pulsed Nitrogen Laser Applications						

UNCLASSIFIED

Security Classification

FOREWORD

This report was prepared by Avco Everett Research Laboratory, Inc., Everett, Massachusetts under USAF Contract F33615-71-C-1875. The work was administered under the direction of the Fuels Branch, Air Force Aero Propulsion Laboratory, Research and Technology Division, Air Force Systems Command, Wright-Patterson Air Force Base, Ohio. The monitors for the Air Force have been Captain Donald Champagne, Lt. William Blazowski, Lt. Gerald Bresowar and Dr. Melvyn Roquemore.

This report concentrates on work conducted from May 1972 to July 1974 and primarily concerns field test results and their analysis. The work under the subject contract conducted from July 1971 through May 1972 has been previously reported in Technical Report, Development of a Laser Raman Aircraft Turbine Engine Exhaust Emissions Measurement System, Avco Everett Research Laboratory Research Note 914, May 1972.

Mr. Donald A. Leonard was the Principal Investigator and Program Manager during the entire course of the contract, and he is the author of this technical report. Dr. Ramesh Sharma was responsible for the theoretical Raman scattering analysis; Mr. Robert Garris was responsible for the specialized laser and synchronized detection electronics; Mr. Bernard Caputo was responsible for the real-time computer control and display system; Mr. Henry Smith was the experimental assistant.

The cooperation and assistance of Mr. Phil Rubins and other personnel at the Stratford Division of Avco Lycoming for providing calibrated combustion sources is gratefully acknowledged.

The very thorough and enthusiastic assistance of Dr. Roquemore, especially in the programming and planning of the field testing, is gratefully acknowledged.

This technical report has been reviewed and is approved.

ABSTRACT

Laser induced Raman and fluorescent measurements were made in the exhaust of a T53-L13A gas turbine engine with a new field portable instrument devised specifically for gas turbine exhaust emission measurements. The gas turbine exhaust was analyzed by conventional instruments for CO, CO₂, NO, NO_x, total hydrocarbons, smoke and temperature, and these data were used as a "calibration" standard for the evaluation of the laser Raman instrument. Results thus far indicate good correlations for CO₂, O₂, smoke, hydrocarbons and temperature. The instrument was not sensitive enough for NO detection but the data analysis indicates that 100 ppm may be detectable with instrument improvements. CO analysis was not attempted, but it is expected that CO could be detected with further research. NO₂ (or NO_x) was not attempted because theoretical and experimental laboratory analysis indicated severe interference with CO₂. The most severe problem area was laser induced hydrocarbon fluorescence when the exhaust contained large total hydrocarbon concentrations. The overall conclusion was that the laser Raman method shows a good potential for aircraft gas turbine emission analysis.

TABLE OF CONTENTS

SECTION		PAGE
	Foreword	iii
	Abstract	v
	List of Illustrations	ix
I	INTRODUCTION	1
II	EXPERIMENTAL APPARATUS	3
	1. Laser	5
	2. Transmitter and Receiver Optics	5
	3. Double Spectrometer	7
	4. Photon Detection Electronics	7
	5. Real-Time Computer Control	13
	6. System Control Area	14
III	EXPERIMENTAL FIELD TESTS AND DATA ANALYSIS	17
	1. Combustion Sources	17
	2. Conventional Gas Analysis Equipment	20
	3. Procedures	30
	4. Experimental Results	31
	5. Comparison and Discussion of Results	55
IV	CONCLUSIONS	63
V	RECOMMENDATIONS	65
	References	69

TABLE OF CONTENTS (Cont'd)

APPENDICES		PAGE
I	LABORATORY FLUORESCENCE MEASUREMENTS	71
	References	76
II	SIGNAL-TO-NOISE CALCULATIONS	85
III	DEVELOPMENT OF A LASER RAMAN AIRCRAFT TURBINE ENGINE EXHAUST EMISSIONS MEASUREMENT SYSTEM	
IV	REMOTE PROBING OF A VOLUME AT FINITE CONJUGATES	

LIST OF ILLUSTRATIONS

FIGURE		PAGE
1	Functional Block Diagram of Laser Raman System	4
2	Schematic of Transmitter and Receiver Optical System Details	6
3	Photograph of Optical Transmitter and Receiver System Mounted in Portable Van	8
4	Receiver Efficiency as a Function of Wavelength	9
5	Gate Generator Mounted in NIM-BIN Rack	11
6	Delay Line Cables used with Gate Generator	12
7	Schematic of Portable Van	15
8	Photograph of System Control Area	16
9	Exhaust Gas Simulator with Laser Raman Van in Position for Measurements	18
10	Piston Engine	19
11	Photograph of T-53 Engine on Test Stand with Laser Raman Van in Position for Measurements	21
12	Photograph of T-53 Engine on Test Stand with Laser Raman Van in Position for Measurements	22
13	Photograph of T-53 Engine on Test Stand with Laser Raman Van in Position for Measurements	23
14	Schematic of On-Line Gas Sampling System	24
15	Correlation of T-53 Fuel-Air Ratio with Gas Analysis Fuel-Air Ratio for T-53 Engine	27
16	Schematic of the Lycoming Stained Filter Paper Smoke Analyzer	28

LIST OF ILLUSTRATIONS (Cont'd)

FIGURE		PAGE
17	Dual Exhaust Averaging Gas Sampling Probe (Gas and Smoke) for T-53 Engine	29
18	Ambient Air Nitrogen Vibrational Raman Line at 2330 cm^{-1}	32
19	Spectral Scan at 1876 cm^{-1} Showing System Noise Level	33
20	Atmospheric Water Vapor Vibrational Raman Line at 3652 cm^{-1}	34
21	Ambient Air Nitrogen Vibrational Raman Line at 2330 cm^{-1} with $\Delta J = \pm 2$ Rotational Sidebands	35
22	Nitrogen Vibrational Raman Line at 2330 cm^{-1} with Broad Band Hydrocarbon Fluorescence in Combustor Exhaust	36
23	Scan of Hydrocarbon Fluorescence Spectrum	38
24	Normalized Fluorescence Spectrum - Simulated Exhaust Gas Generator	39
25	Normalized Fluorescence Spectrum - Piston Engine	40
26	Normalized Fluorescence Spectrum - T-53 Gas Turbine Engine	41
27	Fluorescence Normalized to Nitrogen Raman as Function of Total Hydrocarbons	42
28	Corrected Fluorescence Normalized to Nitrogen Raman as Function of Total Hydrocarbons	44
29	Typical Data Showing Fluorescence Decay Time Measurements	45
30	Fluorescence Decay Time vs Wavelength	46
31	Typical Spectral Data of O_2 in Hot Exhaust Gases	47
32	O_2/N_2 Mole Ratio for T-53 Engine Raman Measurement vs Calculated Value	49
33	Volume % CO_2 as Measured from Raman Scattering vs Shaft Horse Power (SHP), %	50

LIST OF ILLUSTRATIONS (Cont'd)

FIGURE		PAGE
34	Raman/Fluorescence Data Obtained on the T-53 Exhaust in the Spectral Region of NO	52
35	Raman Counts from NO as a Function of P*t* with Fluorescence Interference Threshold	54
36	Geometry of N ₂ Density Method Temperature Profile	56
37	Temperature Profiles of T-53 Engine Exhaust using Raman Density Method	57
38	Comparison of Standard (AIA) Smoke Number to Normalized Laser Raman/Mie Measurement (Normalized at 60% Power)	61

APPENDIX I

1	Fluorescence Spectra of a Synthetic Lubricant at Various Excitation Wavelengths	78
2	Fluorescence Spectrum of Synthetic Lubricant Excited at 300 nm.	79
3	Excitation Spectrum of Synthetic Lubricant for Emission at 385 nm.	80
4	Excitation Spectrum of Synthetic Lubricant for Emission at 350 nm.	81
5	Comparison of Laser and Fluorimeter Fluorescence Spectra.	82
6	Variation of Projected Ratio of Raman Signal to Fluorescence Interference Due to Synthetic Lubricant.	83

SECTION I

INTRODUCTION

This report describes the experimental apparatus that was constructed and the test results that were obtained as a result of the work performed under Air Force Contract F33615-71-C-1875, Development of a Laser Raman Mode Aircraft Turbine Engine Exhaust Emissions Measurement System during the period July 1971 to July 1974.

The goal of Contract F33615-71-C-1875 was to demonstrate the performance of an experimental prototype of a measurement system based on laser Raman spectroscopy which would result in instrumentation which could be used by the Air Force to improve both the air quality of the environment and the performance of turbine engines. The work was motivated by a desire to develop an optical means of performing gas analysis of combustion products of aircraft turbine engines in the field which does not require the placement of a physical probe in the exhaust volume and which could be fully automated.

The optical method selected for investigation is the classical Raman scattering technique. (1) This type of optical interaction is well understood, both theoretically and experimentally, and can produce extremely accurate and absolute measurements of the mole fraction concentration of the molecular species in a gas mixture. Perhaps the best known field application of the Raman method has been its use by meteorologists to remotely determine with a ground based system the water vapor profiles as a function of altitude in the atmosphere. (2, 3)

No attempt was made during this investigation to study or compare the various other optical methods that are available for use in addition to the classical Raman technique. Certainly there are both scattering and absorption techniques using finely tuned lasers and resonant interactions that are currently being researched and developed and which may be as useful or more useful than the classical Raman process.

The basic physical principles involved in the Raman spectroscopy of high temperature (i. e., 900-1200°K) combustion gases were investigated, both theoretically and experimentally during the first year of this effort, and those results are contained in an interim Technical Report, Research Note 914. (4)

Because the physical basis and the engineering design of any measurement system are usually very closely coupled, the interrelationship between the physics and the required engineering was continually set forth in Research Note 914. Also presented in Research Note 914 was an engineering description of the Avco laser Raman gas analysis system for aircraft turbine engine

exhaust emissions analysis, as then conceived, including the laser, the transmitter/receiver optics, and the detection electronics. The laser transmitter was a pulsed nitrogen laser operating at 3371 \AA at a one-half watt average power level with 100 kilowatt pulses at 500 pulses per second. The receiver consisted of a fully computer controlled double 1-meter spectrometer with combined photon counting and synchronous detection.

Section II of this report presents a review of the experimental apparatus as it was finally constructed. While the basic concepts remained essentially the same as were discussed in Research Note 914, the physical embodiment of the experimental apparatus underwent significant changes as the final engineering design evolved.

Section III describes the tests which were conducted with the experimental apparatus as well as an analysis of the test results. The aircraft combustor utilized in this work was an Avco Lycoming T-53 Gas Turbine Combustor, the emissions from which had previously been thoroughly investigated by conventional methods.⁽⁵⁾ In addition the emissions from a small piston engine and a simulated exhaust gas generator were also utilized for purposes of instrument development and calibration. The aircraft combustor sources were operated under the direction of Mr. Phil Rubins, of the Avco Lycoming Division.

Raman data were obtained which could be used to accurately measure the mole fractions of the major species in the flow, i.e., N_2 , O_2 , and CO_2 over the entire range of engine operation conditions from idle to full power. These Raman measurements were compared with the expected values of the specie concentrations as calculated from the measured fuel/air ratio of the various operating conditions.

A problem area that was discovered during the investigation was the presence of a relatively high level of laser induced fluorescence which acted as a noise source and which prevented the detection via the Raman method of low level species such as NO for the laser power level and integration times used. The intensity of the fluorescence could be correlated, however, with the concentration of unburned hydrocarbons as independently measured by conventional means using a gas sampling probe technique.

Measurements as a function of engine power were also made of the radial profiles of the exhaust temperature, using the Raman N_2 - density method. Measurements of the direct laser scattering showed a correlation with the standard SAE number measurement of particulate emissions as a function of engine power.

The classical laser Raman technique has been shown experimentally to be a viable optical method for the analysis of aircraft engine exhausts under both laboratory and field conditions. Extrapolations using existing field data show that with modest upgrading and with appropriate use of fluorescence circumvention techniques the existing Raman measurement system can be useful as a measurement tool down to the 100 ppm specie concentration level, at high power conditions where the total hydrocarbon levels are in the 10's of ppm. At low power conditions with higher hydrocarbon levels, or if specie concentrations much lower than 100 ppm are to be measured, then the system must be significantly modified if successful Raman measurements are to be performed.

SECTION II

EXPERIMENTAL APPARATUS

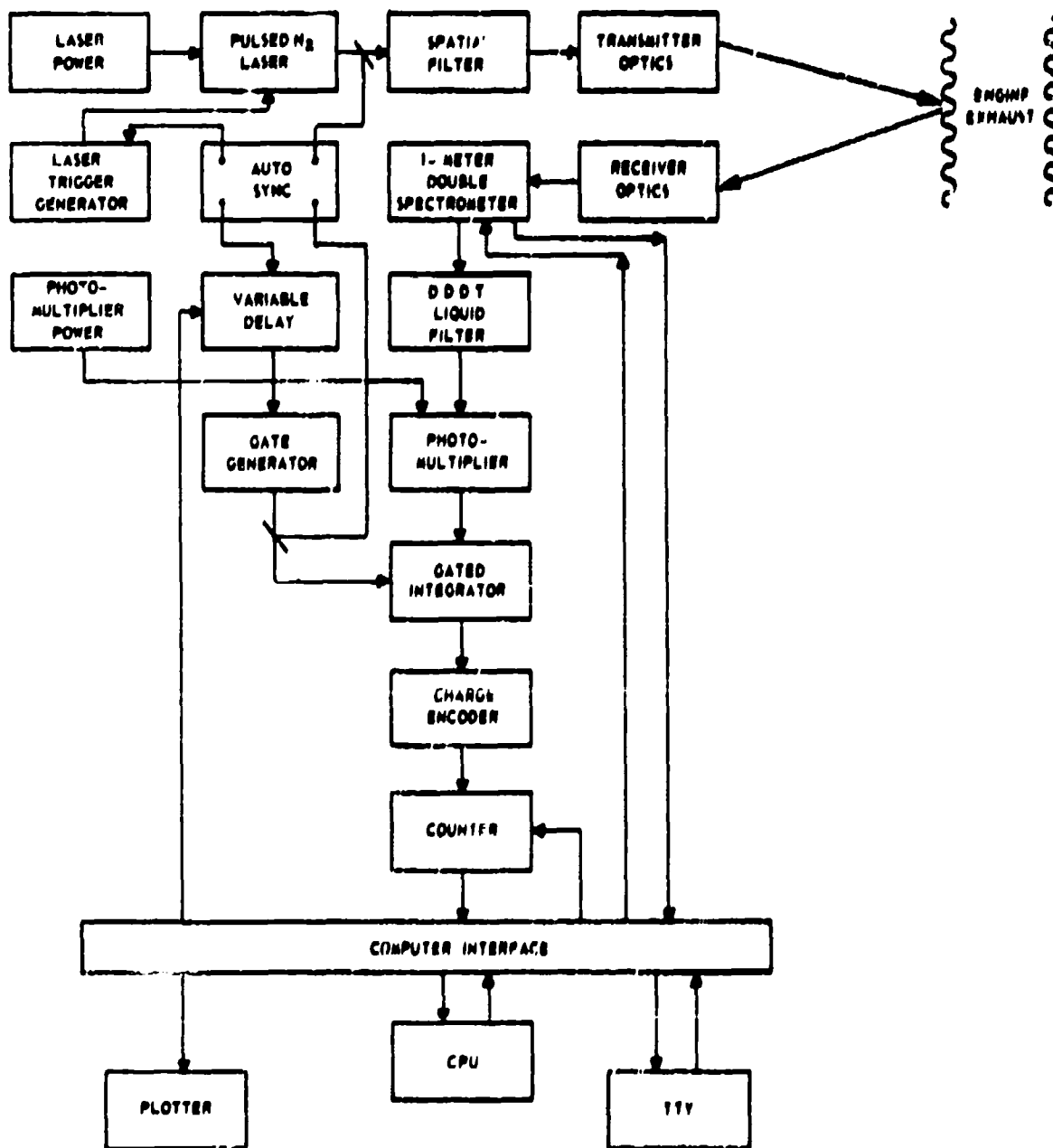
As noted in the Introduction to this report, the conceptual design of the experimental laser Raman apparatus that was utilized in this investigation has been previously described in detail in a previous Technical Report.⁽⁴⁾ The interrelationship between the basic physics and the engineering of the apparatus was stressed in that report. In this Section the experimental apparatus in its final form as used in the test program will be described.

The functional block diagram which describes the laser Raman system is shown in Figure 1. The overall functioning of the entire system will first be described and then the details of the key elements of the system will be discussed. Special emphasis will be placed on those features of the apparatus that are critical to the aircraft turbine engine exhaust measurements and their correct interpretation.

As shown in the block diagram of Figure 1, the output from the 3371 Å pulsed nitrogen laser is spatially filtered and is then focused onto the engine exhaust by the transmitter optics. The receiver optics collects the Raman scattering produced in the sample volume of the exhaust and focuses it onto the slit of a 1-meter focal length double spectrometer. After exiting from the spectrometer and passing through a liquid filter which blocks the direct nonwavelength shifted laser line, the Raman photons are detected by a photomultiplier.

Synchronous time gating is accomplished subsequent to the photomultiplier in a gated integrator which is synchronized to the laser trigger generator. The quantity of charge produced by the gated integrator is converted by a charge encoder into a pulse train proportional to the quantity of charge. The number of pulses thus produced are stored in a counter during each sampling time period.

The real-time computer system utilized a Data General Nova programmable digital processor for system control and data reduction and display. As shown in the block diagram of Figure 1 the computer interface connects the computer central processing unit (CPU) with the various system elements. The Raman and background counts stored in the counter are read into the computer upon command followed by a zero reset signal to the counter. Signals are sent to the spectrometer to produce spectral scans as desired. An encoder on the spectrometer grating shaft sends signals back to the computer interface to ensure failsafe redundant operation. A signal can be sent via the computer interface to the variable delay unit to scan the detection time gate relative to the time of the laser pulse. The computer interface also connects the real-time plotter and the teletype (TTY) to the CPU.



83775

Figure 1 Functional Block Diagram of Laser Raman System

1. LASER

The laser transmitter was an Avco Model C5000 pulsed nitrogen laser operating at a wavelength of 3371 \AA at a one-half watt average power level with 100 kilowatt peak power pulses at a pulse repetition rate of 500 pulses per second. The laser pulse width at half-maximum was 10 nanoseconds.

The pulsed feature enables synchronous detection which greatly reduces ambient light background noise and dark current photomultiplier tube noise. A typical example might be a 20 nanosecond detection gate which is opened every 2 milliseconds, i. e., corresponding to a 500 pulses per second laser pulse repetition rate. Using such a synchronous gating technique the noise is effectively reduced by a factor of $2 \times 10^{-3} / 2 \times 10^{-8} = 10^5$.

The ultraviolet wavelength was chosen because the $(1/\lambda)^4$ dependence of the Raman scattering cross-section favors the shortest possible wavelength in the laser transmitter. Also unfavorable fluorescence interference was known to be present from NO_2 at wavelengths longer than 3975 \AA .

2. TRANSMITTER AND RECEIVER OPTICS

To ensure observation of only the aircraft engine exhaust gases and not the intervening ambient air, the fields-of-view of the transmitter and receiver optics were arranged to overlap only within the exhaust volume. This is especially important since nitrogen was used as the calibration standard and the detection of higher density nitrogen in the ambient air would have severely distorted the average nitrogen calibration signal observed.

The primary function of the transmitter and receiver optics is therefore to transmit the laser beam to the desired volume of the exhaust gases to be analyzed and then provide for efficient collection of the Raman scattered photons from that same measurement volume. In addition, it is equally important that scattering caused by the laser beam from gas located outside the desired measurement volume be just as efficiently rejected.

In other words the laser beam and the field-of-view of the collector should have a sharply peaked overlap in the measurement volume of interest. The details of this optical engineering design trade-off have been previously reported by Munroe. (6)

The general schematic arrangement of the transmitter and receiver optics is shown in Figure 2. Basically the laser spatial filter slits are imaged by the transmitter onto the exhaust volume which is to be analyzed, and which is then re-imaged by the collector mirror onto the entrance slit of the double spectrometer.

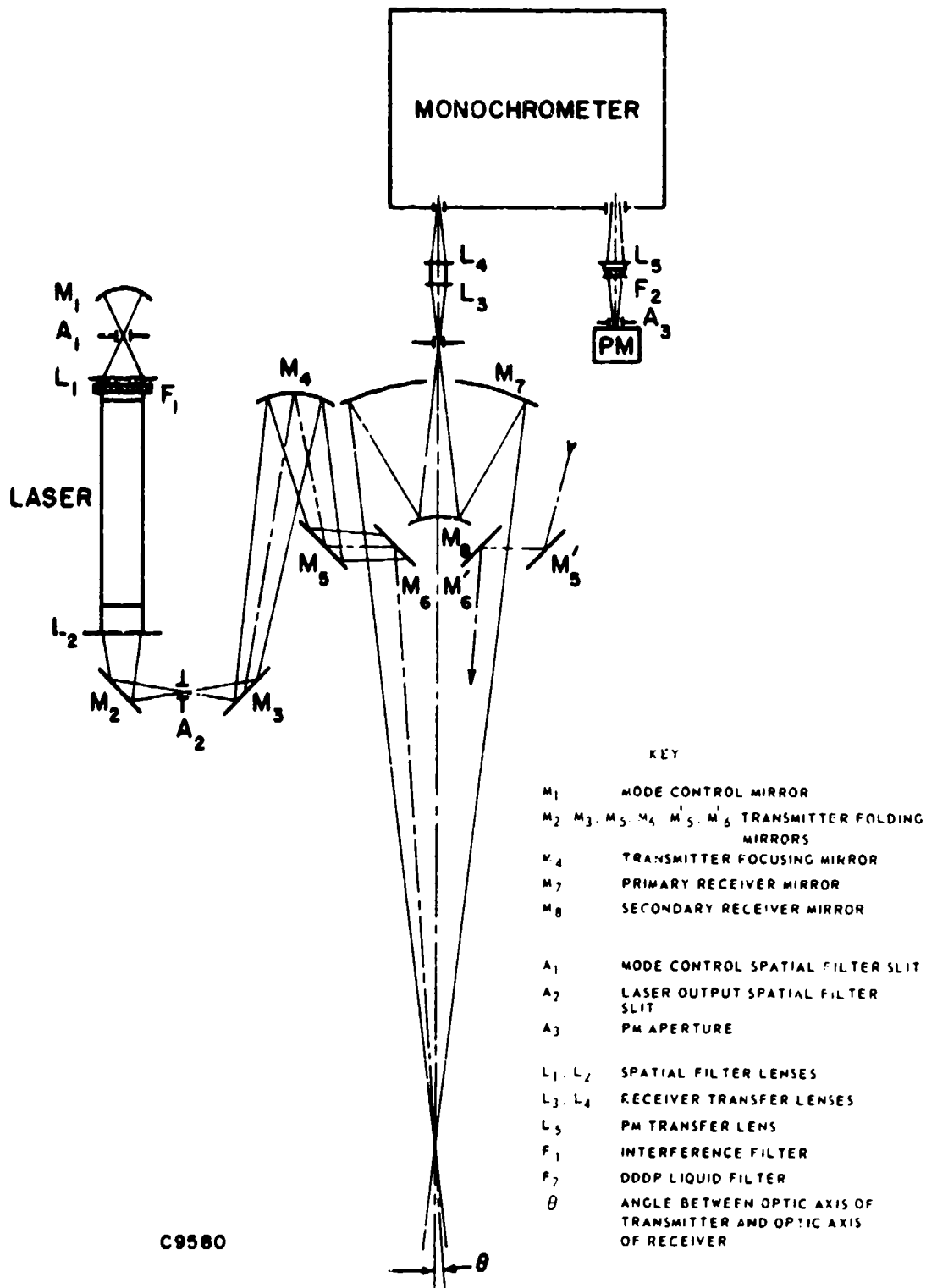


Figure 2 Schematic of Transmitter and Receiver Optical System Details

The aspect ratio of the laser spatial filters is matched to the rectangular entrance slit of the spectrometer. This technique of using coherent amplification in the laser itself to produce a beam of optimal specification improves the overall conversion efficiency of available laser energy to detected Raman signal.

The collection optical system was of the Cassegrain type with a 40-cm diameter primary mirror. The primary mirror was placed approximately 14 feet from the focal volume in the exhaust, approximately 7 feet of this distance being within the portable van and 7 feet being between the van and the engine exhaust. This arrangement provides an $f/7$ collection system which is matched to the $f/7$ aperture of the spectrometer. Although the obscuration of the secondary mirror prevents the central portion of the gratings from being used, the spectral resolution was still more than adequate to resolve the vibrational spectrum. The distance between M_6 and M_7 can be changed with a screw adjustment thus providing focusing capability to the system.

To ensure the integrity of the optical system, the entire transmitter and receiver optical system was mounted on a single large aluminum pallet. The pallet was constructed of 2 sheets of 3/4-inch thick aluminum 10-feet long, 6-feet wide, which were screwed to the top and bottom of a cross braced I-beam frame structure. This pallet was designed using a standard structural dynamic analysis, assuming that it was exposed to a full 130 dB sound pressure level in the frequency range of 100 to 3000 cycles per second. Attenuation is of course provided by the portable van enclosure which shields the optical system from direct exposure to the full acoustic level of the engine exhausts.

Figure 3 is a photograph which shows the optical transmitter and receiver system mounted on the rigid aluminum pallet and as installed within the mobile van. The rectangular box-like structure, with the pressure gauge mounted on the end plate, is the pulsed nitrogen laser. The operator is shown adjusting the wavelength setting of the double spectrometer. The round barrel-like structure behind and slightly to the left of center of the spectrometer is the Cassegrain collection optics. The pallet is isolated from the floor of the van by means of shock mounts.

3. DOUBLE SPECTROMETER

The scanning spectrometer that was utilized was a SPEX Model 1702, a double spectrometer with two gratings used in series in a mode such that the dispersion adds. The spectrometer was equipped with gratings blazed at a nominal 1.0 micron blaze angle. In order to increase the dispersion and, therefore, the slit width and throughput for a fixed wavelength the gratings were used in the 3rd order. Figure 4 shows the overall receiver efficiency as a function of wavelength as determined by means of a NBS Standard Lamp calibration procedure.

4. PHOTON DETECTION ELECTRONICS

Perhaps the most important part of any pulsed laser Raman spectrometer is the electronics associated with the time gating and integrating

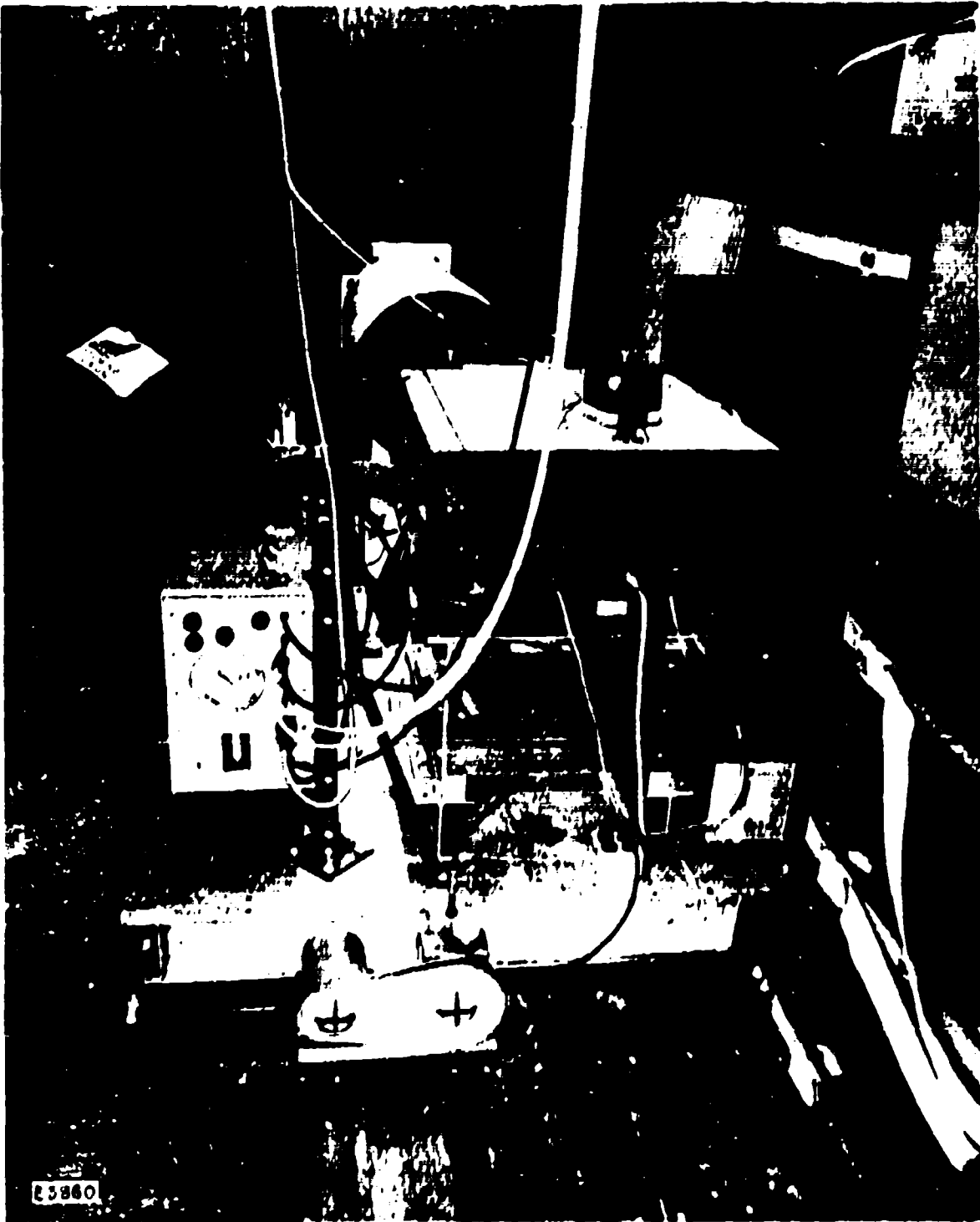


Figure 2 Photograph of Optical Transmitter and Receiver System Mounted in Portable Unit

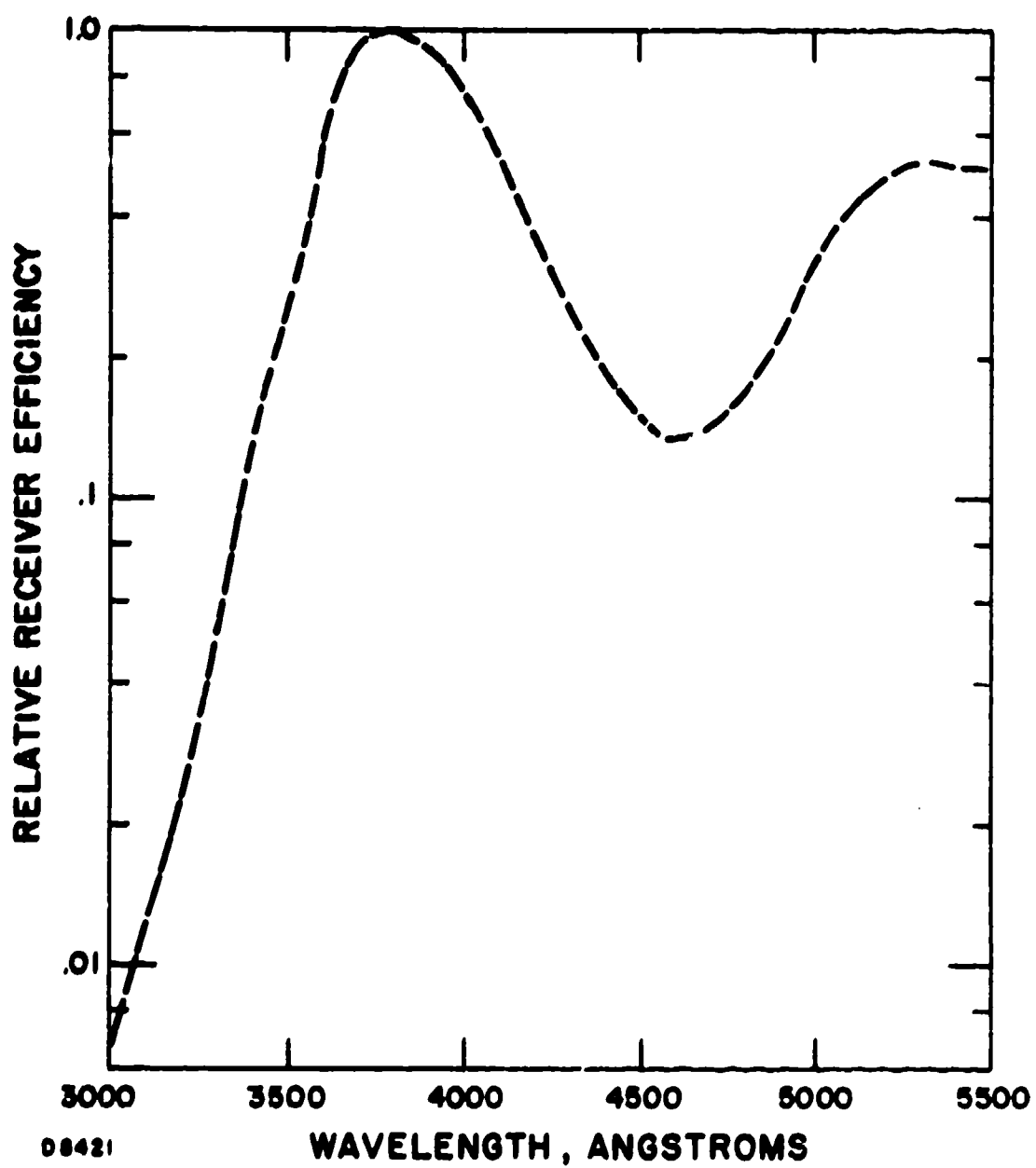


Figure 4 Receiver Efficiency as a Function of Wavelength

functions. As shown in the block diagram of Figure 1 after the backscattered photons are appropriately selected by the double spectrometer, they are detected by an RCA 8850 photomultiplier. The signal from the photomultiplier is then processed by a gated integrator, which integrates only that charge which is produced by the photomultiplier during a given preselected time gate period. The photomultiplier itself is not gated.

The gated integrator that was used was an EG&G LG102 Linear Gate and Stretcher the output of which was enclosed by an EG&G EA100N Amplitude Encoder. The gate generator that produced the time gates was custom built at AERL and Figure 5 shows the gate generator unit rack mounted in a standard NIM-BIN, together with the gated integrator and encoder modules.

The gate width is produced by using the gate start signal as the gate stop signal after suitable delay by means of transit in a delay line. Gates as short as 3 nanoseconds can be produced by means of external quick disconnect delay line cables which enables rapid change of gate width under field conditions. Figure 6 shows a set of the delay line cables which in combination with the gate generator can produce gate widths of between 3 and 30 nanoseconds. In Figure 5 such a delay cable is shown connected at the lower left of the gate generator NIM module.

The location in time of the time gate can be varied over a total range of approximately 100 nanoseconds. This can be accomplished either manually by use of the 10-turn potentiometer on the front panel of the gate generator NIM module or automatically by appropriate computer program control.

Although on a pulse-to-pulse basis, the appearance of the laser pulse relative to the input signal to the thyratron is repeatable with much less than one nanosecond time jitter, long term (hours and days) aging of the hydrogen thyratron requires, however, that the time gate be directly synchronized to the laser pulse itself.

An "auto-sync" unit was therefore incorporated into the gate generator NIM module. The purpose of the "auto-sync" unit is to ensure that the timing of the gate which controls the gated integrator is maintained in precise relative synchronism with the timing of the laser optical pulse. The two inputs to the "auto-sync" unit are the gate from the gate generator and an electrical pulse produced by a photodiode which detects a portion of the laser optical pulse.

The synchronism between these two pulses is monitored and maintained by appropriate automatic adjustment in the timing of the two outputs from the "auto-sync" unit, i. e., the input to the laser trigger and the input to the gate generator. The "auto-sync" unit thus maintains relative synchronism to a fraction of a nanosecond, independent both of the absolute location in time of the gate and of drift in the triggering of the laser or other critical components.

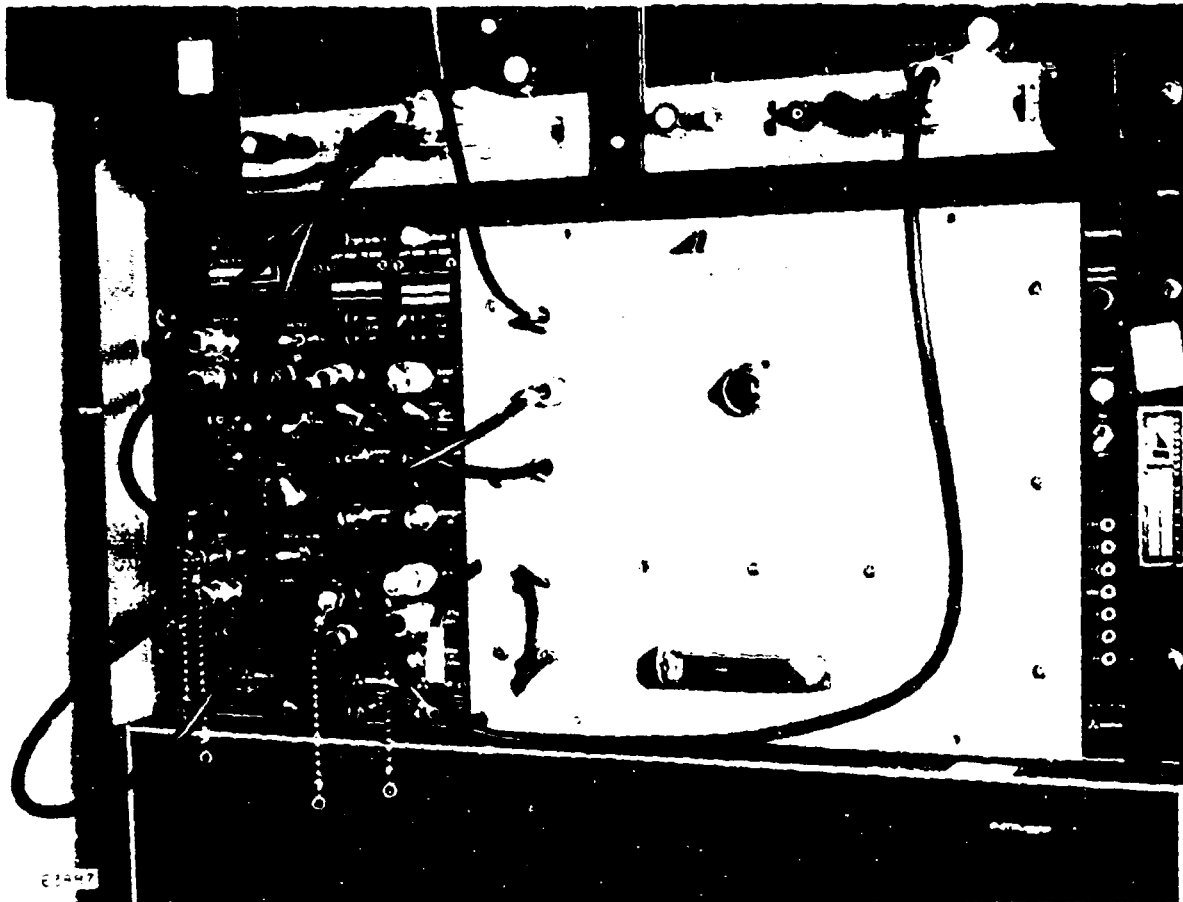


Figure 5 Gate Generator Mounted in NIM-BIN Rack

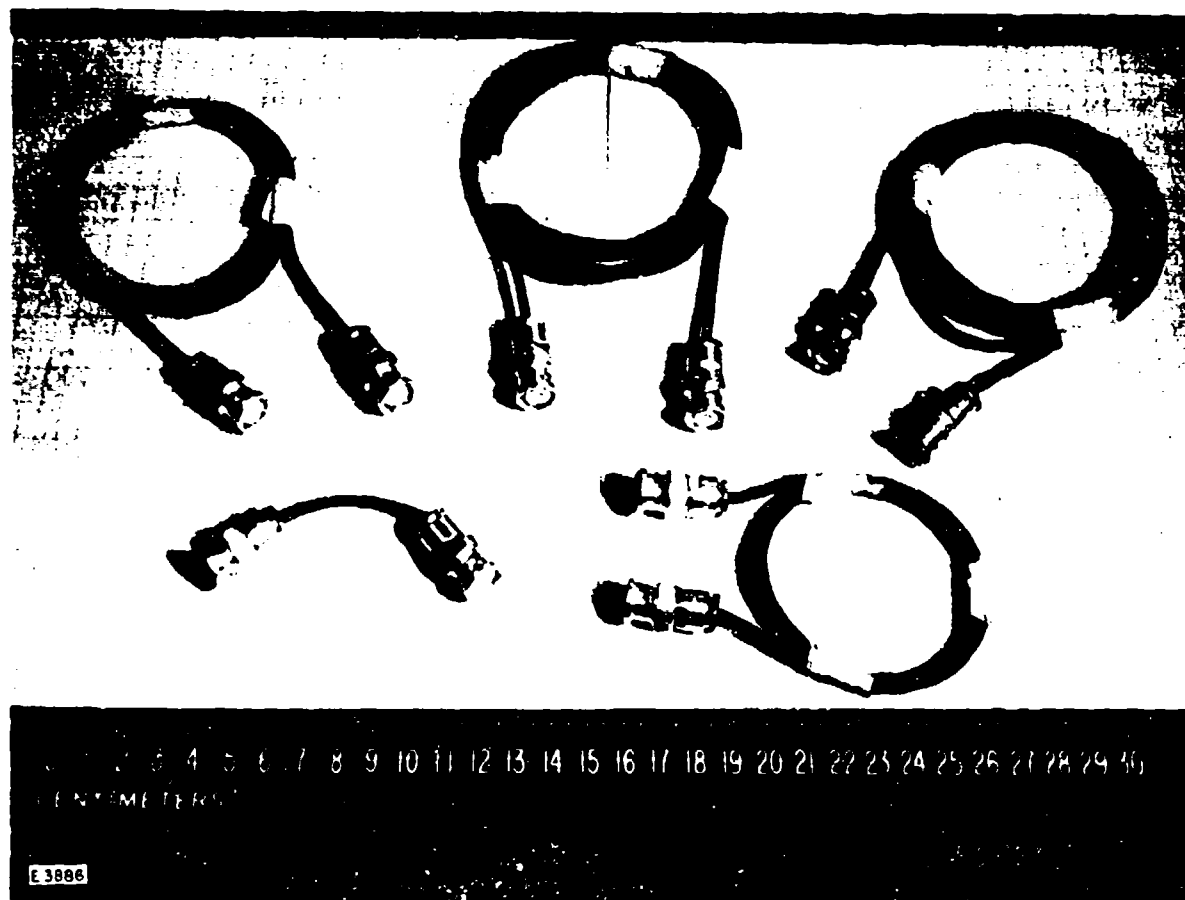


Figure 6 Delay Line Cables used with Gate Generator

5. REAL-TIME COMPUTER CONTROL

Real-time system control and data recording, processing and display were accomplished by means of a Data General Nova programmable digital processor. As shown in the block diagram of Figure 1 the computer CPU interfaces with the system in the following ways.

a. Data Recording

The Amplitude Encoder produces a 20 megahertz pulse train, with the number of pulses in the train being proportional to the charge from the photomultiplier. One photoelectron nominally produces 100 pulses. The number of pulses in the train is counted by a counter. The computer reads the counter between each laser pulse and resets the counter to zero prior to the next laser pulse.

b. Spectrometer Control

The SPEX double spectrometer is scanned in wavelength by the computer in a closed loop mode. Pulses are transmitted to drive the spectrometer stepping motor. The position of the gratings is determined by means of pulses obtained from a shaft encoder mounted on the grating shaft drive.

c. Time Gate Scan

The position of the detection time gate, relative to the laser pulse, can be adjusted by the computer over a range of 100 nanoseconds with a precision of 0.1 nanosecond.

d. Plotter

The system has a capability to produce real-time plots of the signal obtained either as a function of wavelength as the spectrometer is scanned or as a function of time as the time gate position is scanned. An "open loop" capability also exists whereby the signal obtained is plotted periodically and the time gate position and the spectrometer wavelength position may be manually adjusted. To provide sufficient dynamic range a 5 cycle semi-log ordinate is typically used.

e. TTY

A standard teletype is used both to provide program instructions in order to initialize the system and also to provide a hard copy of the details of system operation and data obtained.

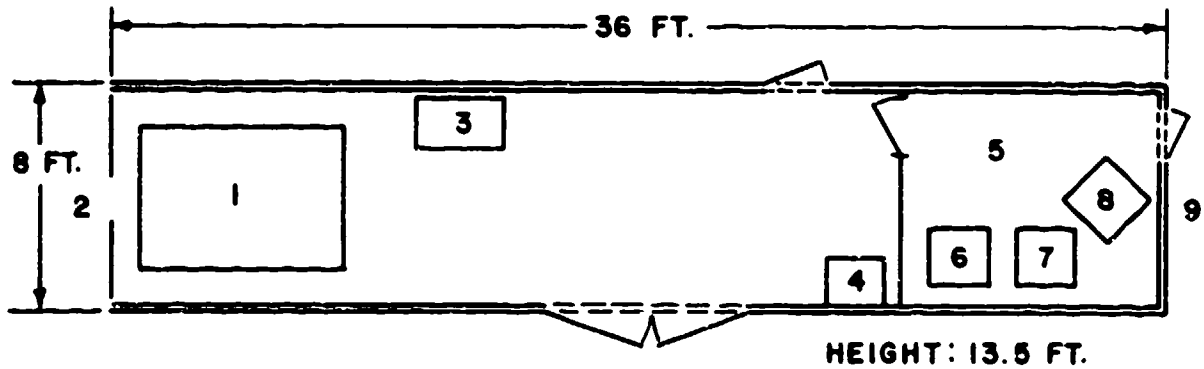
The specific details of the various program modes which are available are described in the operating manual of the system. A special feature of the data processing provides for actual signal quantum counting at the low light levels and for charge encoding at the higher light levels to allow for many photoelectrons being produced in one laser pulse gate time.

Other features of the data processing include automatic wavelength calibration of the spectrometer using the N_2 Raman line position, automatic programmable wavelength scanning and detection time gate scanning, ambient light background subtraction on a pulse-to-pulse basis, laser induced "fluorescence" subtraction using both the wavelength and time domains, and both temperature measurement and temperature corrections applied to the spectra to obtain correct specie concentration as a function of temperature.

6. SYSTEM CONTROL AREA

The laser Raman spectrometer system for aircraft engine exhaust analysis was designed for operation by an operator at a station remote from the laser transceiver module. As configured in a portable van for field tests the system control area occupies the front portion of the van and the laser transceiver the rear portion as shown in Figure 7, which is a schematic of the portable van. Figure 8 is a photograph of the system control area. The laser transceiver as installed within the van was previously shown in the photograph of Figure 3.

LASER RAMAN GAS ANALYZER VAN



LEGEND

- | | |
|----------------|-------------------------|
| 1 TRANSCEIVER | 5 CONTROL ROOM |
| 2 BEAM EXIT | 6 POWER CONSOLE |
| 3 LASER COOLER | 7 COUNTER/COMPUTER |
| 4 TRANSFORMERS | 8 PRINTER/KEYBOARD |
| | 9 POWER LINE CONNECTION |

08901

Figure 7 Schematic of Portable Van

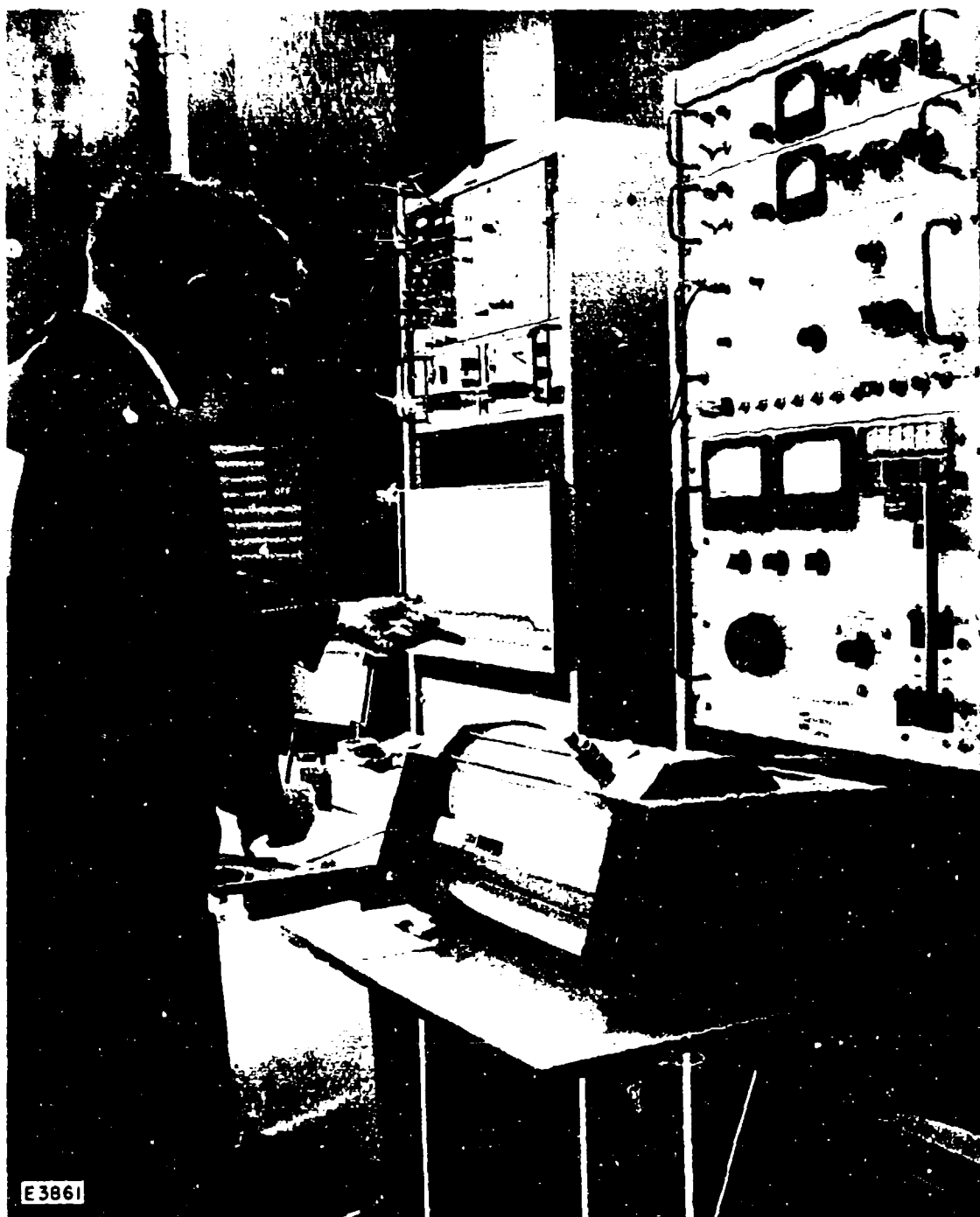


Figure 3 Photograph of System Control Area

SECTION III

EXPERIMENTAL FIELD TESTS AND DATA ANALYSIS

The utility of any new analytical instrumentation must first be exhaustively proven by experimental field tests before it can be accepted for routine use. The experimental field tests of the laser Raman gas analysis system utilized an Avco Lycoming T-53 gas turbine engine, the emissions from which had previously been thoroughly investigated by conventional methods.⁽⁵⁾ In addition, the emissions from a small piston engine and a simulated exhaust gas generator were also utilized for purposes of instrument development and calibration.

1. COMBUSTION SOURCES

a. Exhaust Gas Simulator

An exhaust stream simulation generator was assembled, consisting of a can combustor and mixing chambers, for the purpose of generating gases similar to aircraft engine exhaust emissions. This equipment, with the portable laser Raman van in position for measurements, is shown in the photograph of Figure 9. The exhaust simulator operated with JP-4 at flow rates between 100 lbs/hour and 200 lbs/hour corresponding to temperatures between 700°F and 1350°F. Using preheated air the maximum exhaust temperature could be increased to 1550°F in the simulator.

b. Piston Engine

A small 3 horsepower, one cylinder, four cycle Briggs and Stratton piston engine was obtained and used as a combustion source. The engine is shown in the photograph of Figure 10 as positioned on a platform behind the portable laser Raman van. This equipment was used as an inexpensive and convenient method for making initial tests with the laser Raman system.

c. Lycoming T53-L-13A Gas Turbine Engine

The T-53 engine was selected for use as the primary combustion test source for comparison purposes between the laser Raman system and conventional gas analysis instrumentation. This engine has been extensively tested by Avco Lycoming for the Eustis Directorate, U. S. Army Air Mobility Research and Development Laboratory under Contract DAAJ02-72-C-0102 as a part of evaluation of emission properties of gas turbine engines used by the U. S. Army. The composition of the exhaust of this engine, as a function of operating conditions, is therefore considered to be both well understood and reproducible. Probe measurements were therefore not made simultaneously with the laser tests.

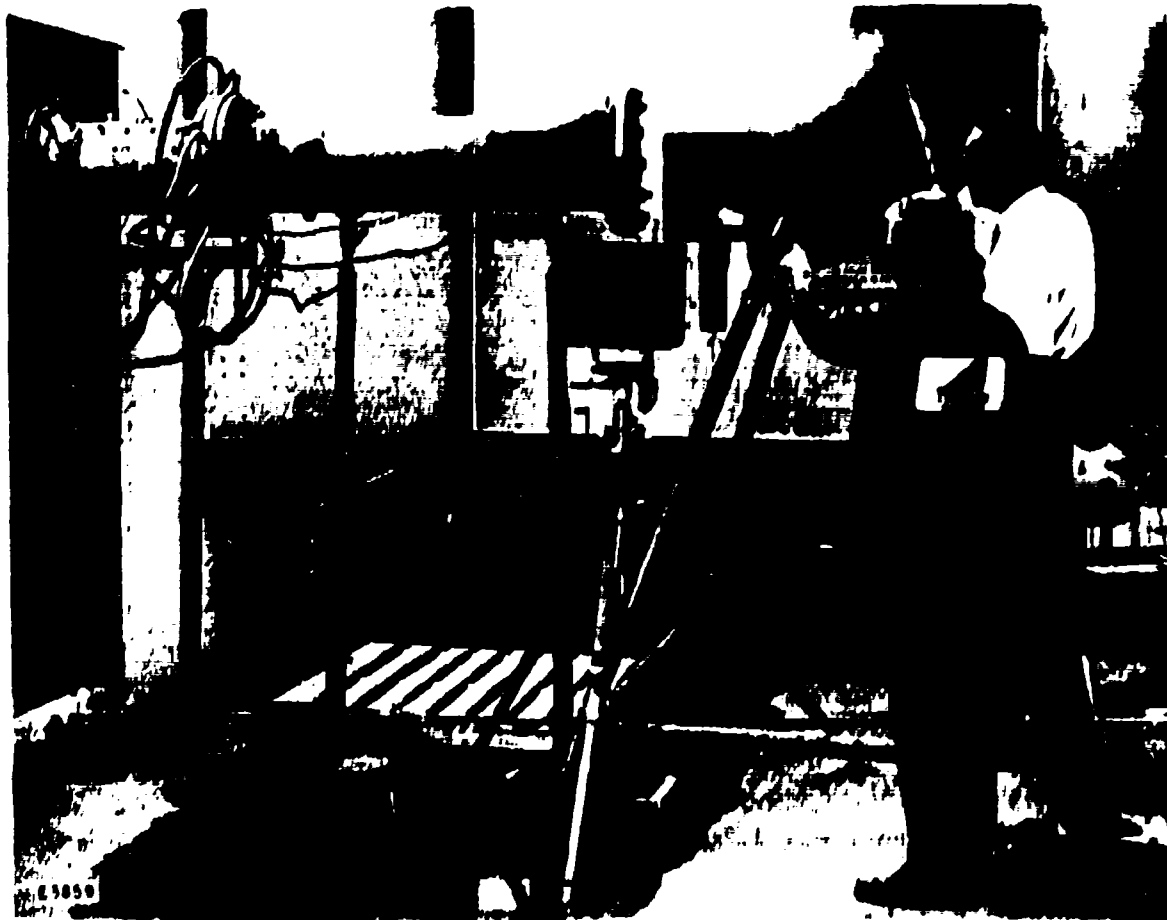


Figure 9 Exhaust Gas Simulator with Laser Beam Van in Position for Measurements

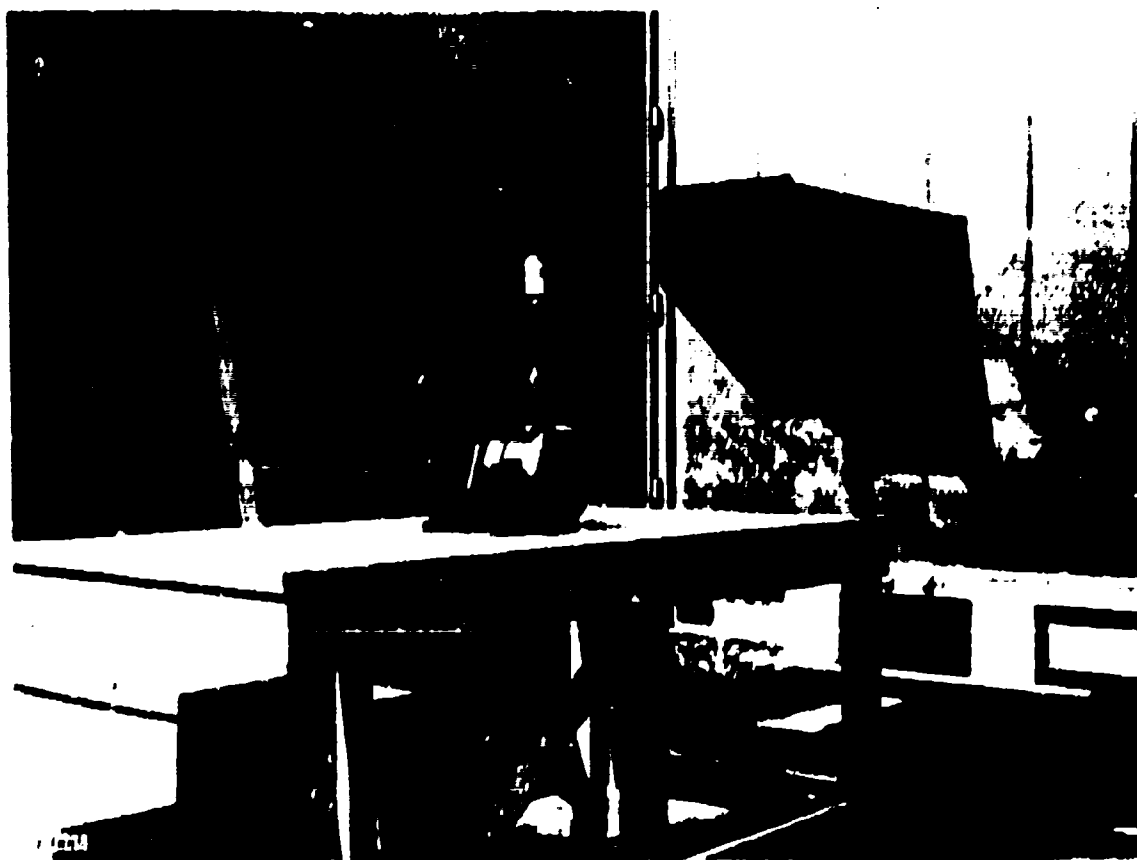


Figure 10 — Piston Engine

To conduct exhaust gas analysis tests with the laser Raman analyzer on the T53-L-13A engine, an outdoor adjustable test stand was used in close proximity to the laser gas analysis equipment. The engine on its test stand with the laser Raman van in position for measurements is shown in the photographs of Figures 11, 12 and 13. Control of the engine was maintained from a nearby control room. The engine power was absorbed by a water brake, and the full range of engine power could be obtained. A nearby cooling tower was used to cool and recirculate the water. Engine operating measurement instrumentation was included so that the important engine parameters were on record. The items of particular interest in this case were fuel flow, inlet airflow, ambient conditions, shaft horsepower, exhaust gas temperature, and compressor turbine speed.

For the water brake, a strain-gaged torque element mounted between the water brake and the engine inlet housing was used to measure output shaft torque in both instances. Engine airflow was measured with a calibrated inlet bellmouth. Other measurements included compressor speed, power turbine speed, fuel and oil flows, hydraulic and pneumatic pressures, and temperatures.

The test stand was controllable in the vertical direction, so that vertical traverses of the exhaust could be made by raising and lowering the engine. The test stand could also be rotated for precise alignment with the laser beam.

2. CONVENTIONAL GAS ANALYSIS EQUIPMENT

The gas analysis equipment used as a comparative standard for the laser Raman consisted of detectors similar to those specified by the SAE. They consisted of infrared detectors for CO, CO₂, and NO, a flame ionization detector for total hydrocarbons, and a polarographic detector for NO and NO_x as shown in the schematic of Figure 14. Thus, NO was measured by two different detectors. A list of the instruments used and their ranges is given in Table I. An error analysis of the estimated precision of the instruments is shown in Table II in order to promote realism in comparing the conventional and laser analysis methods. Most manufacturers specify 1% "accuracy" of instrument measurement, which is interpreted to really mean "repeatability". Another indication of more realistic accuracy is shown in Figure 15 where fuel-air ratio determined from gas analysis is compared to fuel-air ratio from engine fuel and air measurements.

In addition, a smoke analyzer was used to determine the AIA smoke number. The Lycoming smoke analyzer was designed to conform to SAE-ARP 1179.⁽⁷⁾ A schematic is shown in Figure 16. The analyzer consists of a pumping system which pulls a sample through heated lines, meters the flow, and passes the gas through a standardized filter paper. The sample is heated to prevent water condensation. The reflectance of the smoke deposit on the filter paper is measured with a McBeth model RD-400 reflection densitometer. ARP 1179 procedures are followed to determine the AIA smoke number. The gas sampling probe used is shown in Figure 17.

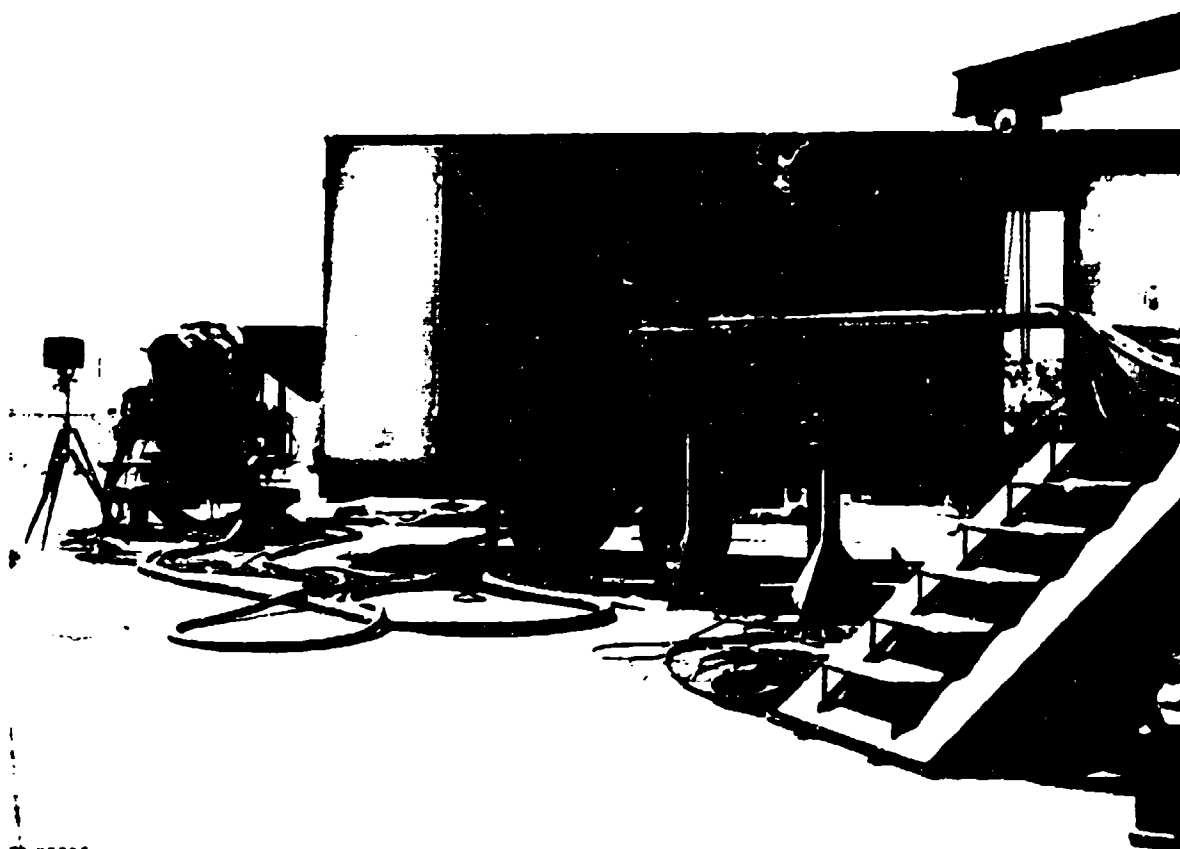


Figure 11 Photograph of T-53 Engine on Test Stand with Laser Raman
Van in Position for Measurements

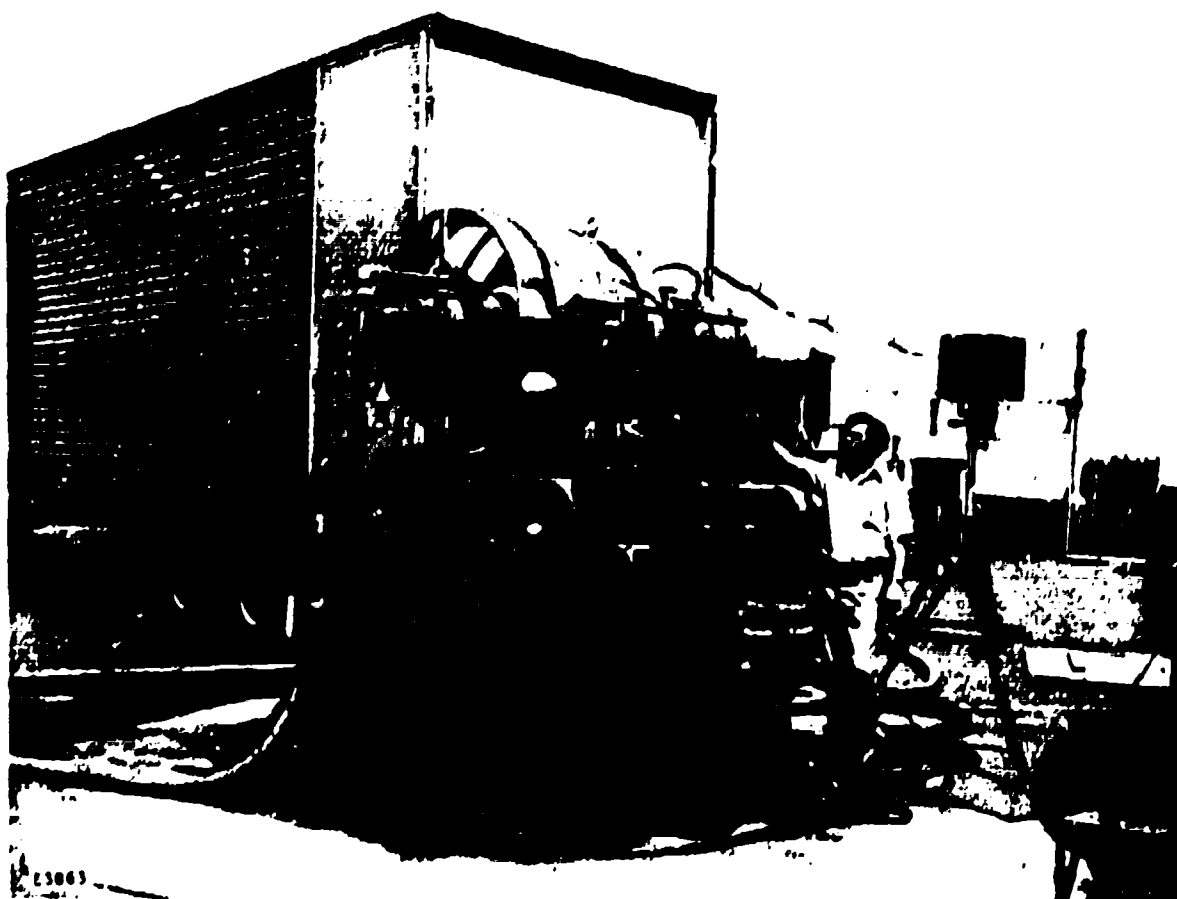


Figure 12 Photograph of T-53 Engine on Test Stand with Laser Raman
Van in Position for Measurements

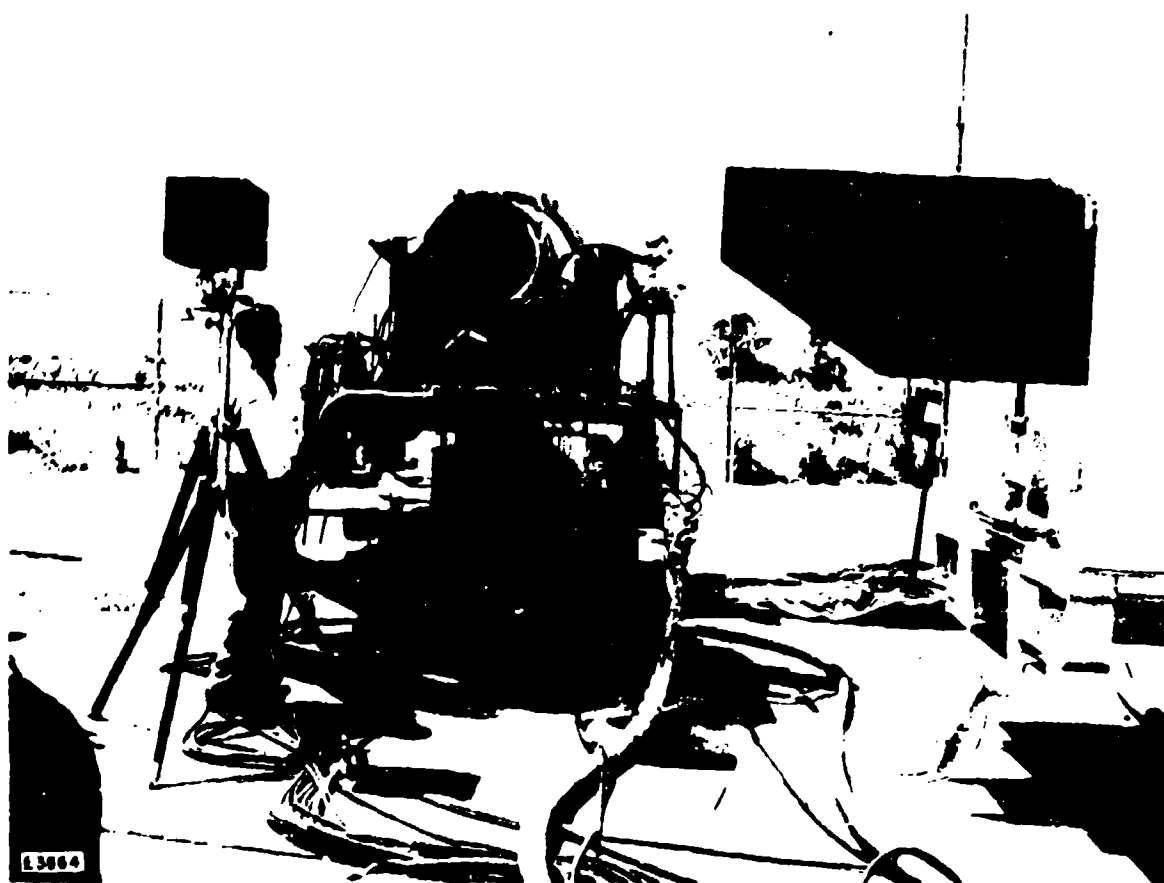
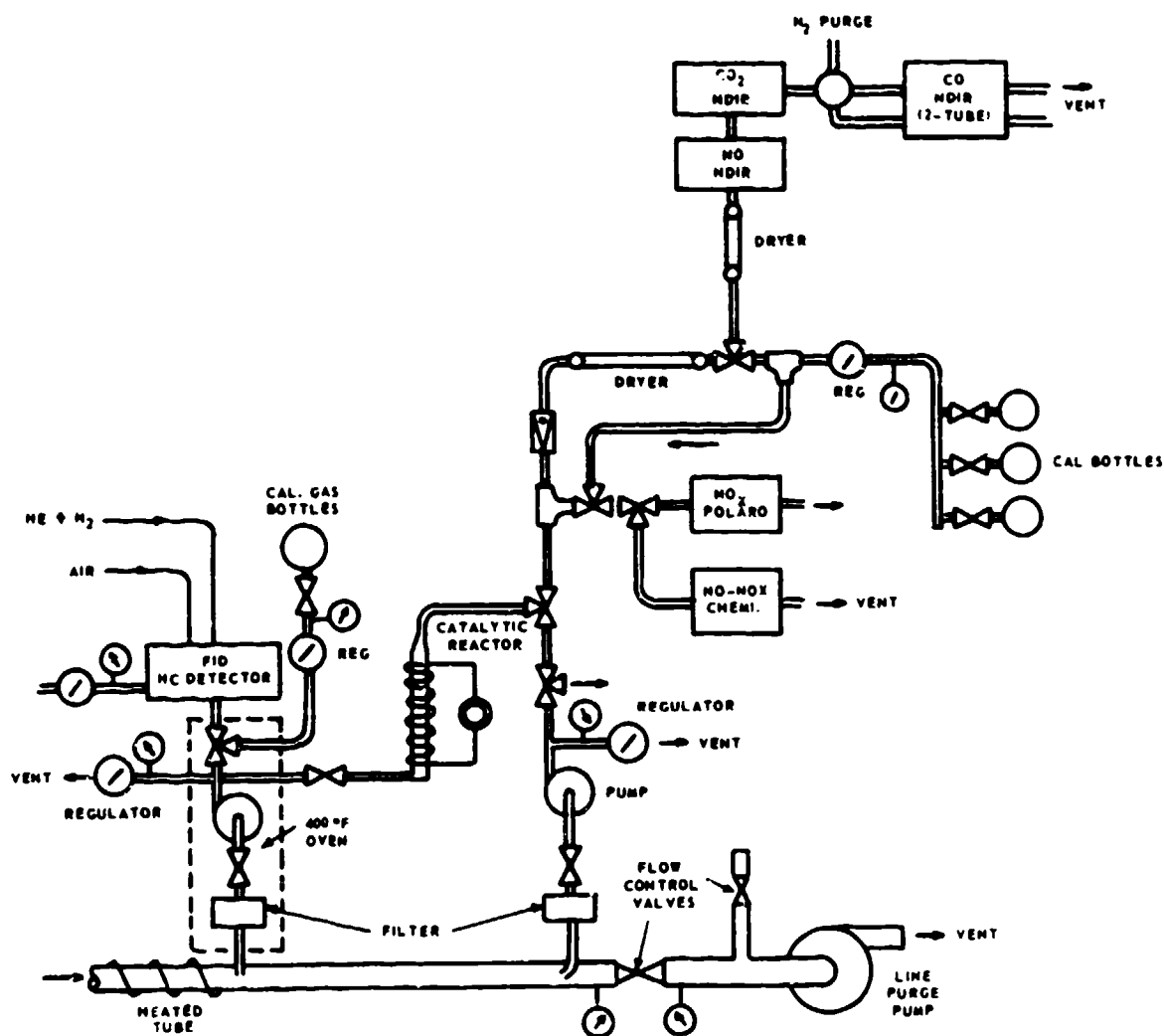


Figure 13 Photograph of T-53 Engine on Test Stand with Laser Raman
Van in Position for Measurements



E4182

Figure 14 Schematic of On-Line Gas Sampling System

TABLE I. GAS ANALYSIS DETECTOR COMPONENTS				
Gas	Model	Ranges	Full Scale Accuracy*	Response Time*
Nitric Oxide (NO)	MSA-200S Infrared detector	0-300 ppm 0-1500 ppm	±1%	90% in 5 sec
Carbon Monoxide	MSA-200 Dual tube infrared detector	Tube No. 1 0-200 ppm	±1%	90% in 5 sec
		0-800		
		0-3200		
Carbon Dioxide	MSA-300 Infrared detector	Tube No. 2 0-5%	±1%	90% in 5 sec
		0-8%		
		0-40%		
Oxygen	Beckman 715 Polarographic detector	0-5%	±1% (at constant temperature)	90% in 20 sec
		0-25		
Hydrocarbons	Varian 1400 Flame ionization detector	0-100 ppm to approx. 0-20,000 ppm	±2% in low range ±1% in high range	Approximately 90% in 10 sec
Nitrogen Oxides (NO _x)	EnviroMetrics NS-200	0-50 ppm to 0-10,000 ppm	±2%	90% in 5 to 10 sec 5 to 10 sec
*Per manufacturer's specifications				

TABLE II		
OPTIMUM AND PROBABLE GAS SAMPLE ANALYSIS PRECISION		
	Manufacturers Specification	More Probable Accuracy
<u>Full Scale</u>		
Instrument Accuracy	$\pm 1\%$	$\pm 3\%$
Calibration Bottle Accuracy	$\pm 1\%*$	$\pm 2\%$
Total Full Scale Accuracy	$\pm 2\%$	$\pm 5\%$
<u>At 30% of Full Scale</u>		
Instrument Accuracy	$\pm 3\%$	$\pm 10\%$
Calibration Bottle	$\pm 0.3\%**$	$\pm 1.4***$
Total for 30% of Full Scale	$\pm 3.3\%$	$\pm 11.4\%$
<p>It is assumed here that no error is present from poor calibration curves.</p> <p>*Calibration Bottles are obtainable guaranteed for 1% accuracy.</p> <p>**Assumes calibration gas for full scale deflection.</p> <p>***Assumes calibration gas for 1/2 of full scale, much more likely than when full scale calibration gas is obtainable.</p>		

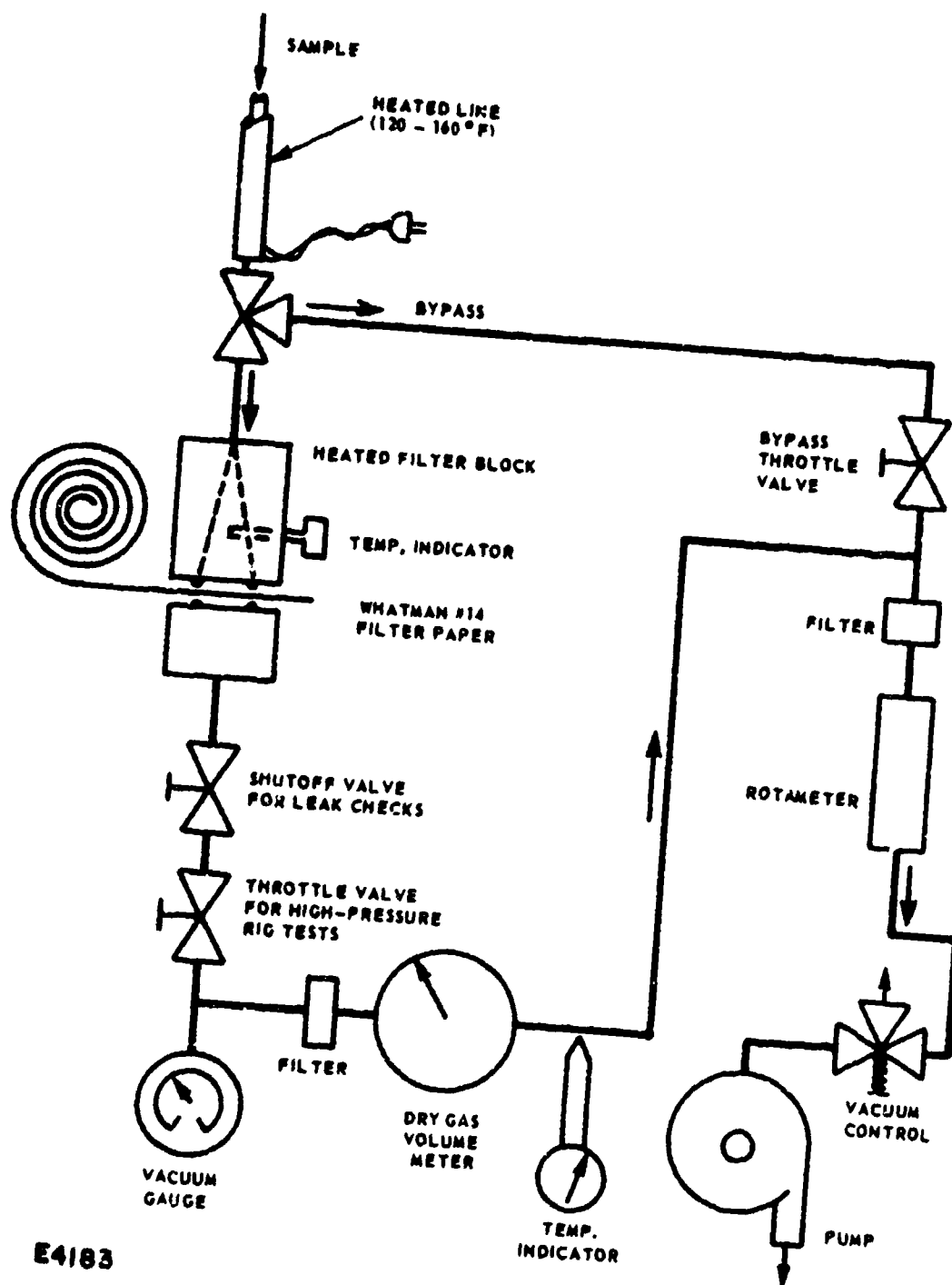


Figure 16 Schematic of the Lycoming Stained Filter Paper Smoke Analyzer

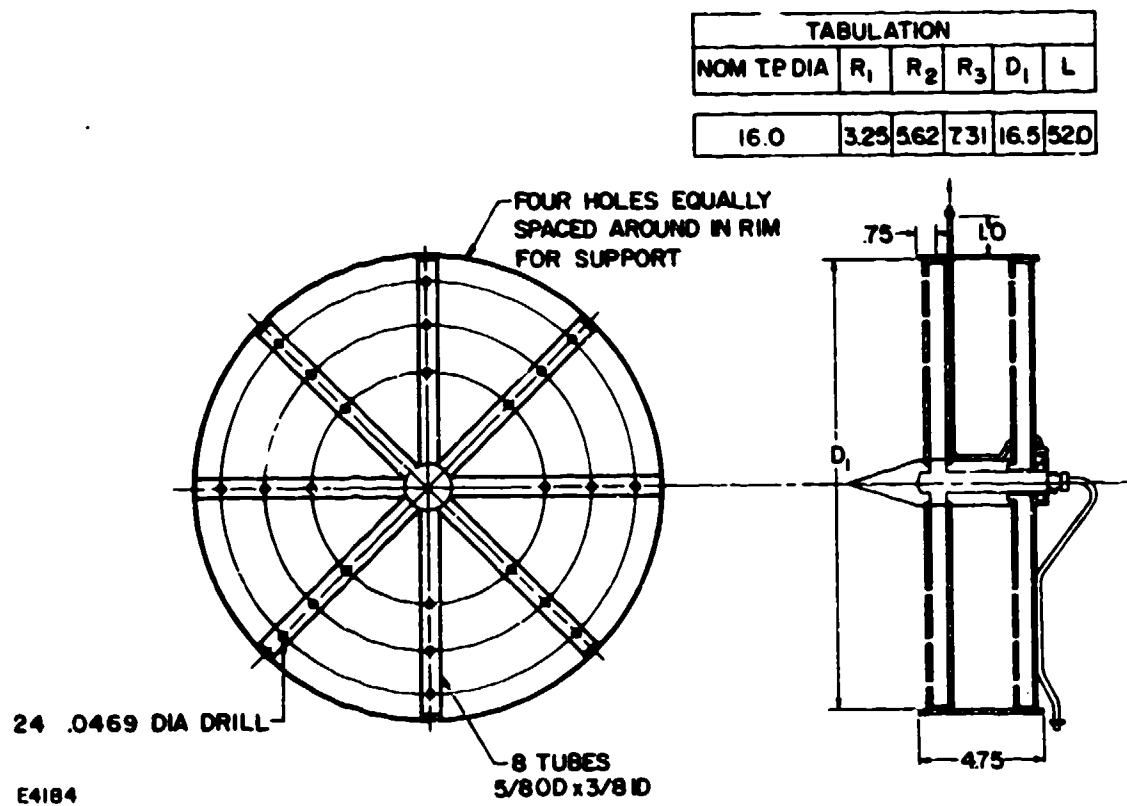


Figure 17 Dual Exhaust Averaging Gas Sampling Probe (Gas and Smoke)
for T-53 Engine

3. PROCEDURES

a. Exhaust Gas Generator Procedures

The exhaust gas generator was operated at fuel-air ratios simulating a typical engine, and at a steady-state condition. Data were recorded for air flow, fuel flow, and exhaust gas analysis while laser Raman were recorded.

b. Piston Engine Procedures

The piston engine was operated under essentially a no-load condition at a relatively fast idle. Gasoline was used as the fuel.

c. T-53 Engine Testing Procedures

The engine was operated as it would be normally over a range of power conditions from idle to full power during both daytime and nighttime operation. Nighttime operation was preferred for some tests where maximum laser Raman sensitivity was required and extraneous light was minimum. All engine operating data were recorded, and laser Raman measurements completed with steady-state operation of the engine.

The engine exhaust gas analysis data had been recorded during previous testing. (5) The laser test series was run on the same engine and there had been no engine operation in the time interval between the two tests. The previous gas analysis test data was used as the basis for comparison.

d. Laser Raman Procedures

The laser Raman system could be activated for use within 6 minutes. the warm-up time required by the hydrogen thyratron used as the main switching element in the pulsed nitrogen laser. During the warm-up time, background light level and instrument noise measurements were made. Typically, this noise level was 1/10,000 of the laser Raman signals from atmospheric nitrogen.

Following warm-up a high resolution wavelength scan of the nitrogen Raman line in the ambient atmosphere was routinely made. The characteristic shape of this line confirmed that the entire system was functioning normally. The amplitude of the peak signal from the line gave a measure of current system sensitivity, i. e., the cumulative effects caused by dirty optics, laser degradation, etc., could be determined. This atmospheric nitrogen scan required about 5 minutes.

Typical data were usually obtained by recording the backscatter signal while the wavelength of the spectrometer was scanned. Especially in cases of significant fluorescent background levels this procedure enabled complete spectral signatures to be obtained, rather than merely single channel data. Thus both background levels and Raman signals were obtained.

The scanning and data recording system was entirely computer controlled. The operator entered into the teletype the mode of operation required and other specific data. The system then responded by acquiring the data, printing tables of data, and making real-time plots of spectra.

4. EXPERIMENTAL RESULTS:

a. Preliminary Tests

Initial tests were conducted in air at the AVCO Everett Laboratories to verify the predicted performance of the laser Raman field unit. Figures 18, 19, and 20 show spectra obtained in the spectral regions that correspond to vibrational transitions in N_2 , NO and H_2O at 2330 cm^{-1} , 1876 cm^{-1} and 3652 cm^{-1} that will produce Raman lines at 3658, 3600, and 3844 Å, respectively. As shown in these figures, a dynamic range of about four orders of magnitude (i. e., 10,000) is available between the signal from N_2 in Figure 18 and the noise level at the NO spectral position in ambient air as shown in Figure 19. Based on these results, it would appear that concentrations of NO at the 100 ppm level should thus be easily observed and that the system had met its design goal of 100 ppm resolution.

Water vapor detection is shown in Figure 20, where a signal/noise ratio of about 100 at a relative concentration of about 1% of the atmospheric nitrogen signal is observed.

The portable van containing the laser Raman gas analyzer was then moved to the AVCO Lycoming engineering test facility and laser Raman tests were conducted first with a Lycoming simulated exhaust stream generator and later with a T-53 gas turbine engine.

The Raman spectrum was first rechecked in air and the spectrum obtained is shown in Figure 21, which is a reproduction of the real-time computer plotted data. This spectrum shows the expected atmospheric nitrogen vibrational line, as seen in Figure 18. Rotational side-bands are noted at about 1% of the peak value and the ambient noise level is about 0.01% of the nitrogen peak. The spectrum in Figure 21 thus showed that the laser Raman gas analyzer system was still operating properly after 200 miles of highway transport.

b. Hydrocarbon Measurements

When the exhaust stream generator was operated under simulated "idle" conditions and produced over one thousand ppm of hydrocarbon emissions, spectra such as shown in Figure 22 were obtained. This figure shows a scan of the same spectral region as previously shown in Figure 21 which includes the nitrogen Raman line in air. What is most apparent in Figure 22, is that with the high concentration of hydrocarbon emissions present, a laser-induced continuum level is produced which is the same order of magnitude as the nitrogen Raman peak.

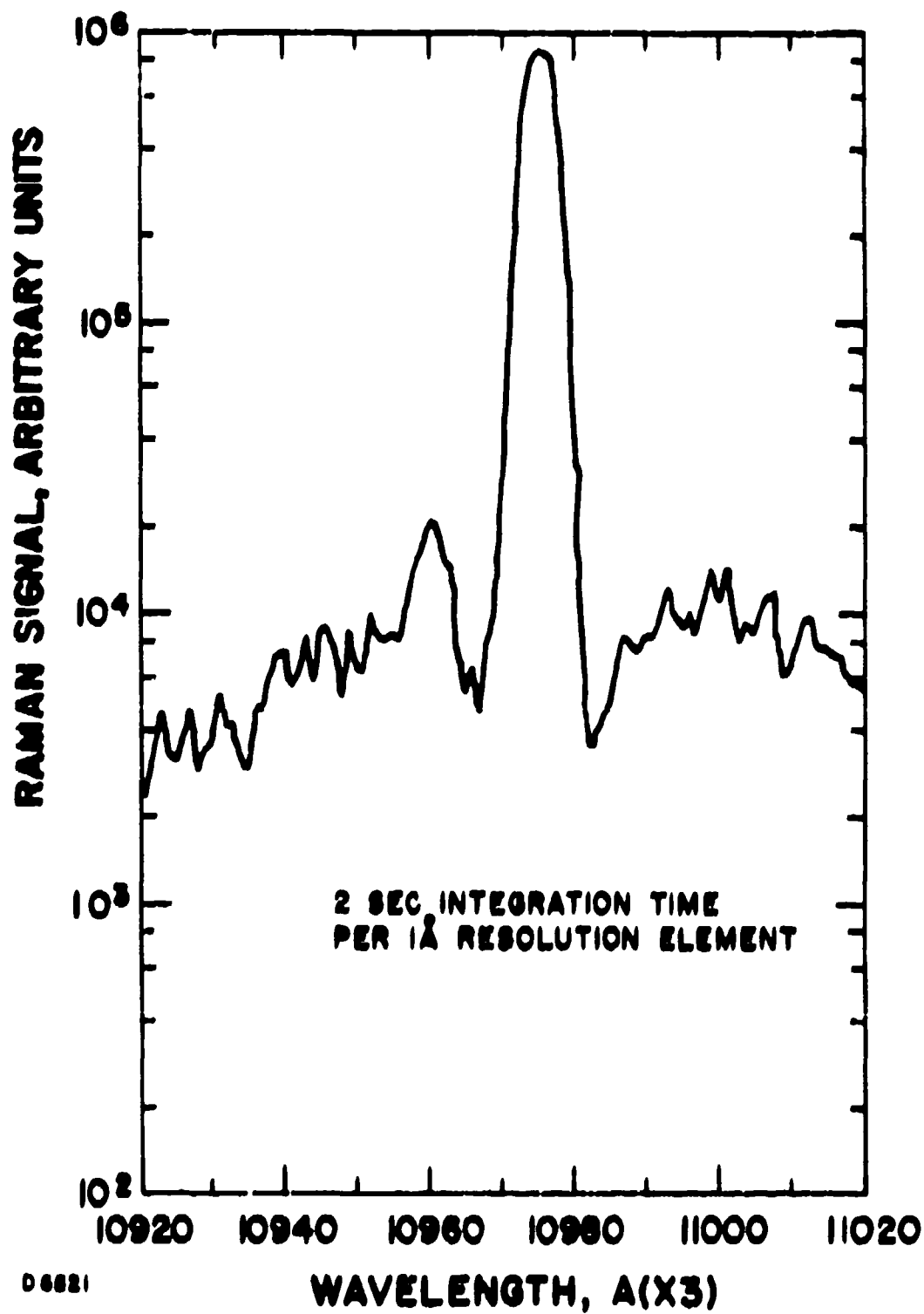


Figure 18 Ambient Air Nitrogen Vibrational Raman Line at 2330 cm^{-1}

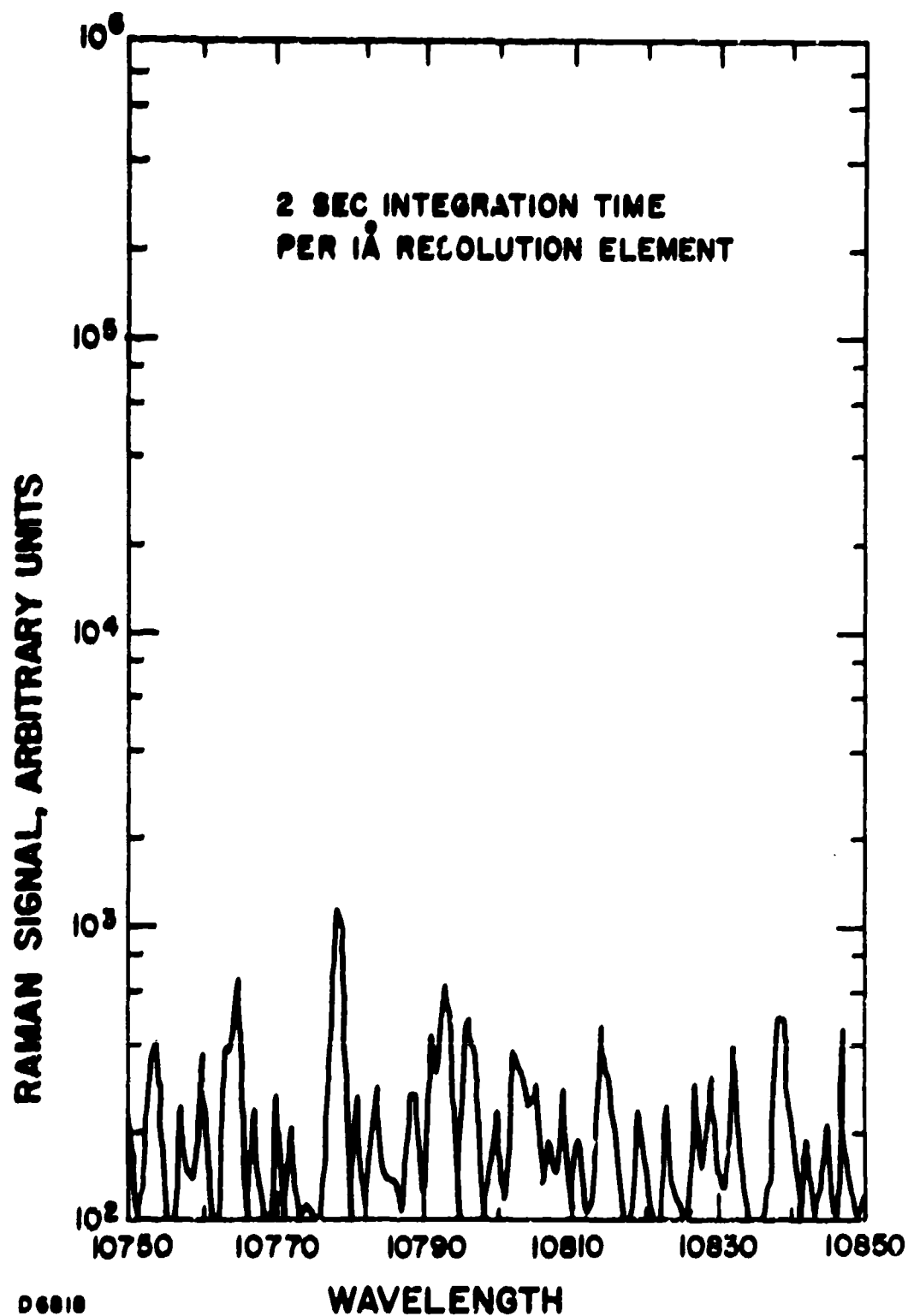


Figure 19 Spectral Scan at 1876 cm^{-1} Showing System Noise Level

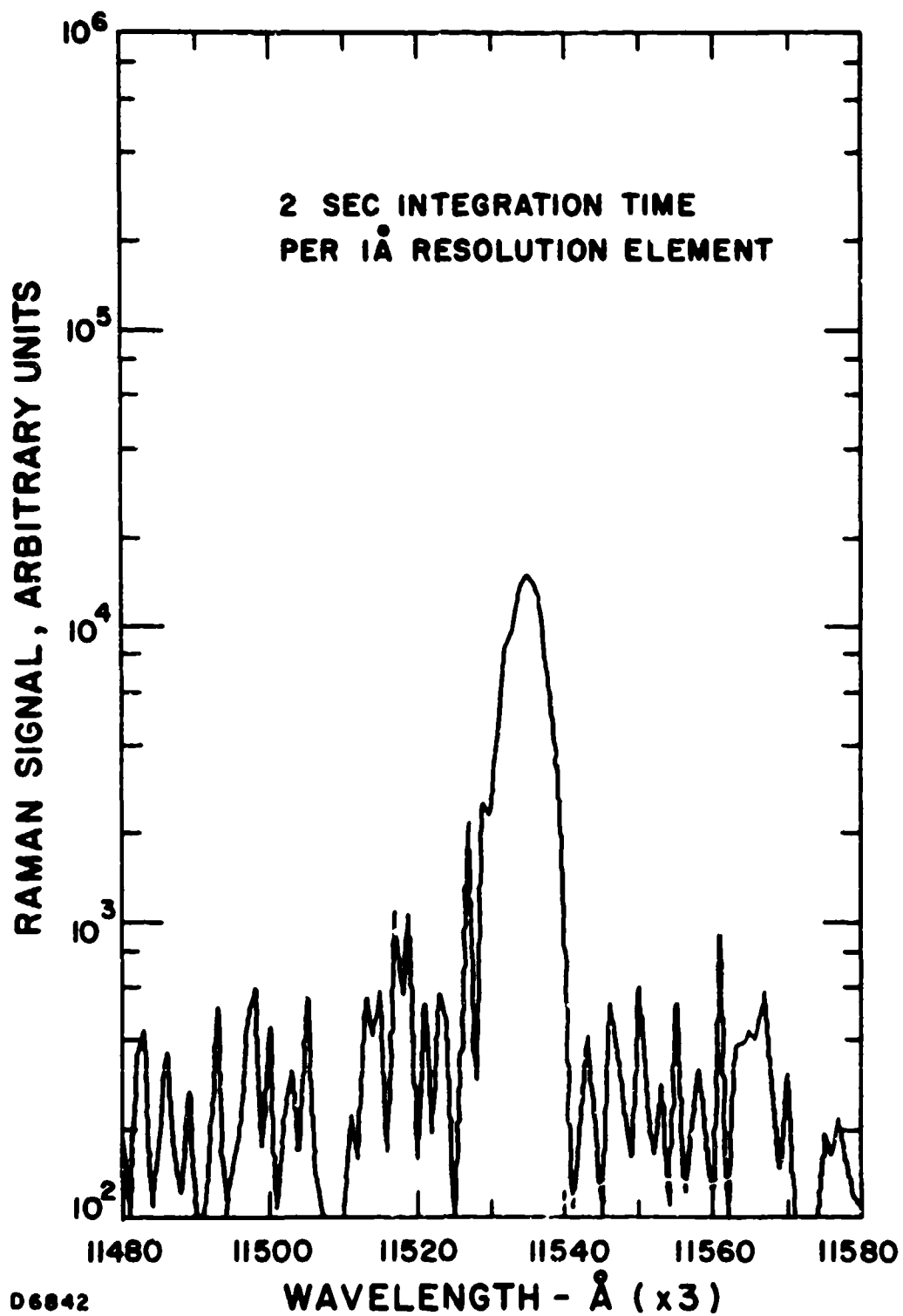


Figure 20 Atmospheric Water Vapor Vibrational Raman Line at 3652 cm^{-1}

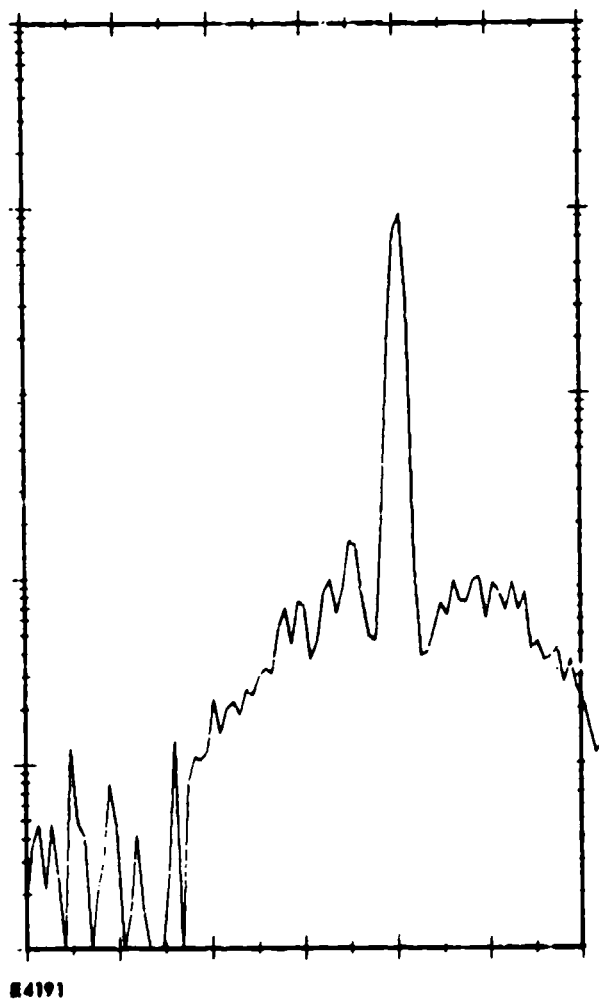


Figure 21 Ambient Air Nitrogen Vibrational Raman Line at 2330 cm^{-1}
with $\Delta J = \pm 2$ Rotational Sidebands

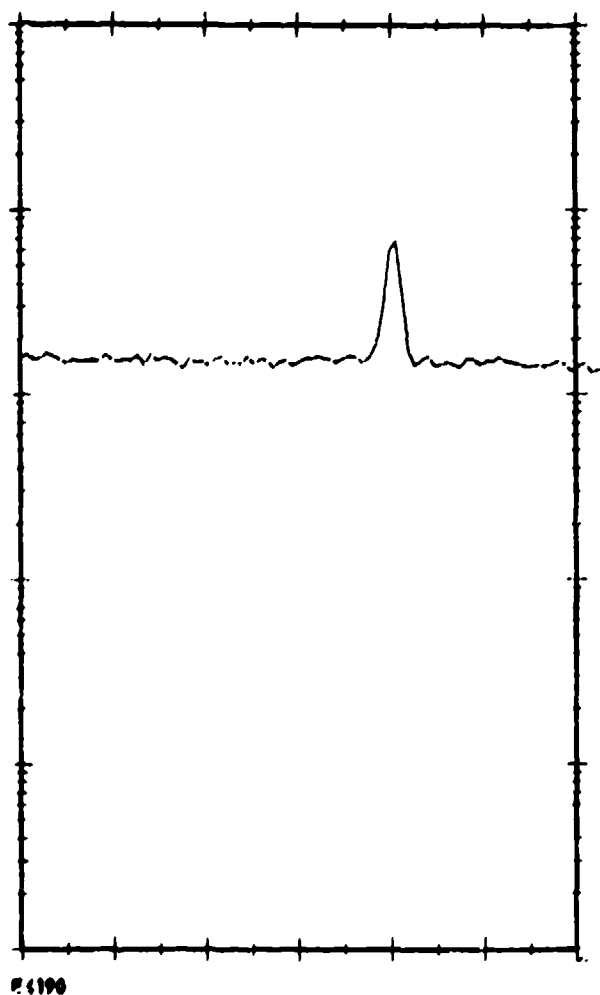


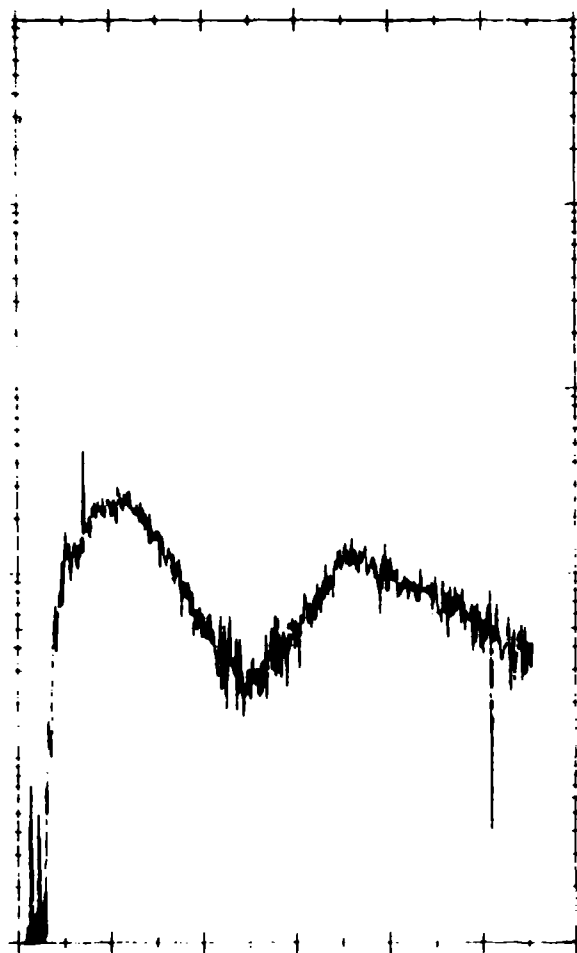
Figure 22 Nitrogen Vibrational Raman Line at 2330 cm^{-1} with Broad Band Hydrocarbon Fluorescence in Combustor Exhaust

A much broader spectral scan, from 3000 Å to 6000 Å, with the same exhaust condition, is shown in Figure 23. This figure shows that the continuum level is present from essentially the laser excitation wavelength at 3371 Å to beyond 5000 Å. Such a broad emission spectrum is typical of a mixture of unsaturated hydrocarbons which are excited by a 3371 Å source. The dip in the spectrum of Figure 23 at about 4500 Å is an artifact caused by the spectral response of the receiver - primarily due to the properties of the gratings used in the SPEX double spectrometer. The relative spectral response of the receiver, previously shown in Figure 4, clearly indicates a similar dip at 4500 Å. When the hydrocarbon fluorescence spectrum of Figure 23 is normalized with respect to the receiver response function in Figure 4, the actual hydrocarbon fluorescence is seen to be essentially flat in the 3500 Å to 5500 Å spectral region, as shown in Figure 24.

Similar measurements were made of the 3371 Å laser induced fluorescence properties of the exhaust of the Lycoming T-53 gas turbine engine and also the exhaust of the piston engine. The normalized fluorescence from these engines are shown in Figures 25 and 26. A good correlation can be made between the piston engine spectra and the T-53 spectra at idle conditions and with the fluorescence spectra of the T-53 engine oil as measured in the field and also in laboratory tests. (See Appendix I - Laboratory Fluorescence Measurements.) On the other hand, the spectra produced at the higher power settings with the T-53 is beginning to resemble the simulated combustor spectra where presumably no engine oil was present.

The T-53 unit utilized in the laser tests thus exhibits two distinct modes of operation. This is due to an oil pressure seal which produces small leakages of oil at the low power settings. Such leakage is common in gas turbine engines and is known to vary from engine to engine and with the stage of wear for a given engine. Since the laser tests immediately followed the Eustis tests with the same T-53 unit, the hydrocarbon levels were assumed to be comparable for both tests.

The magnitude of the laser-induced fluorescence signal from hydrocarbons was compared with the total hydrocarbon concentration as measured by a flame ionization detector. For both the simulated exhaust stream generator and for the T-53 turbine engine, the fluorescence signal increases with increasing total hydrocarbons, as shown in Figure 27. In this figure the ratio S_F/S_R , the fluorescence signal divided by the N_2 Raman signal, is plotted vs the independently measured hydrocarbon concentration. A variation of over an order of magnitude is seen between the simulated exhaust generator and engine data. We propose that the data be normalized with respect to decay time and wavelength bandwidth as follows:



E4109

Figure 23 Scan of Hydrocarbon Fluorescence Spectrum

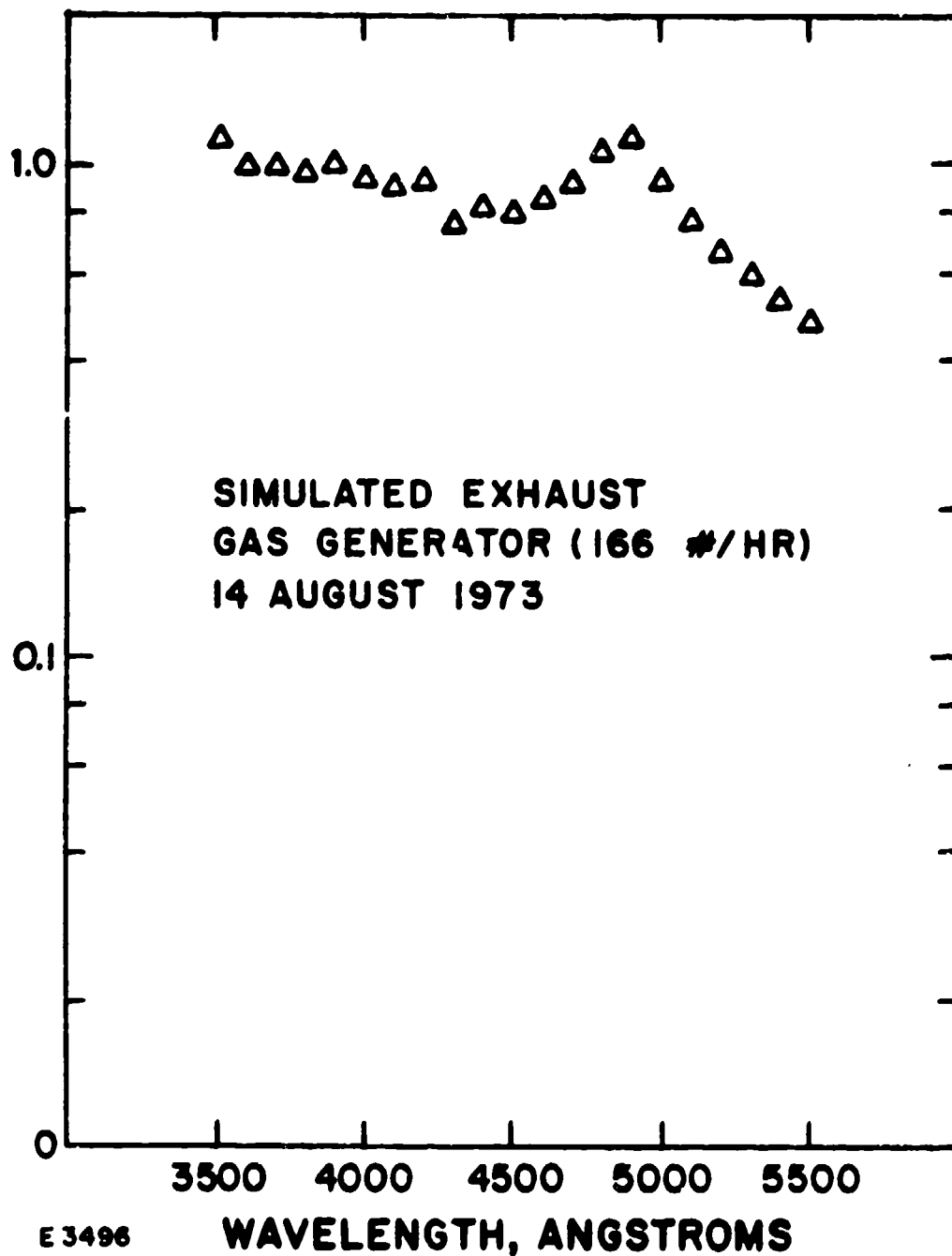


Figure 24 Normalized Fluorescence Spectrum - Simulated Exhaust Gas Generator

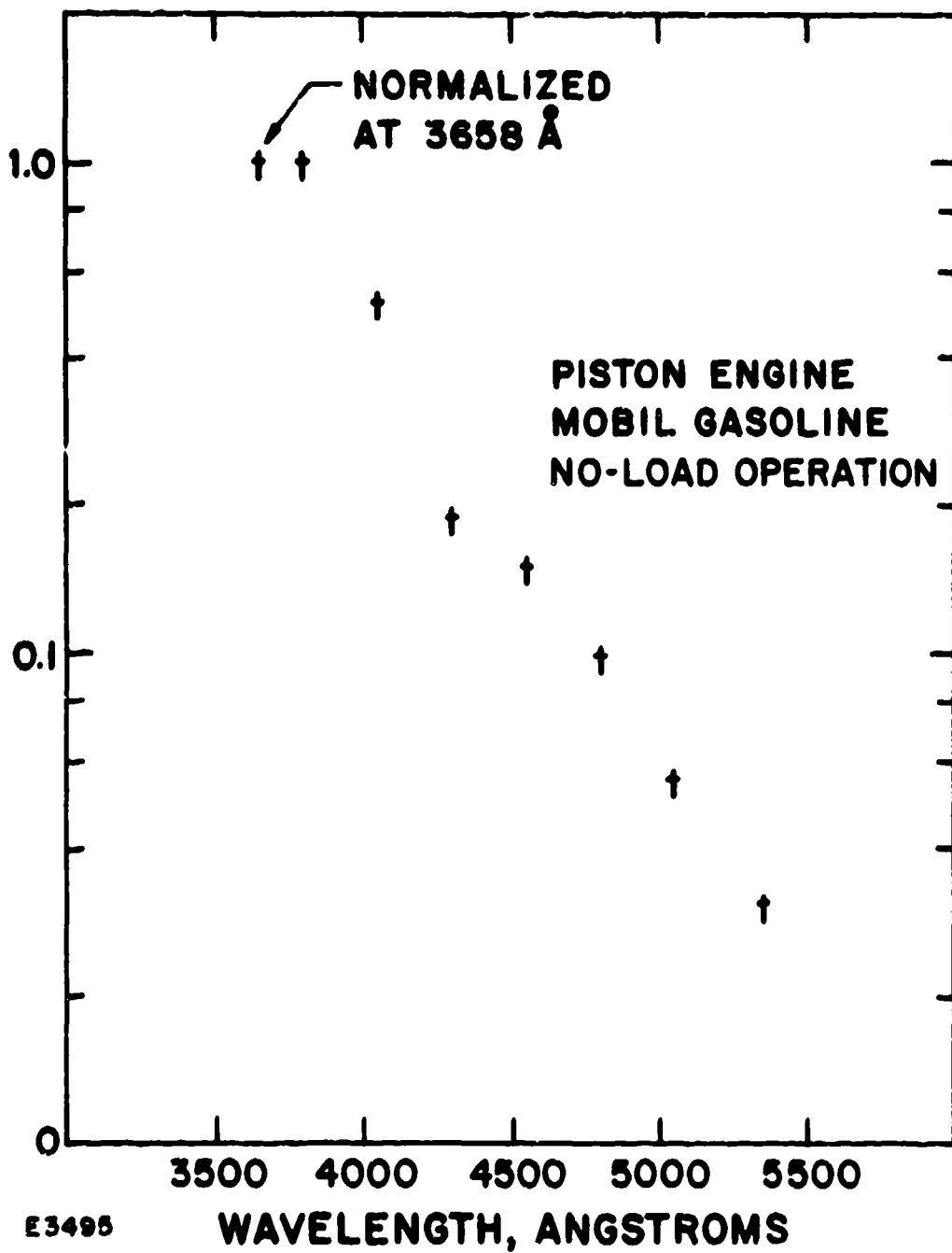


Figure 25 Normalized Fluorescence Spectrum - Piston Engine

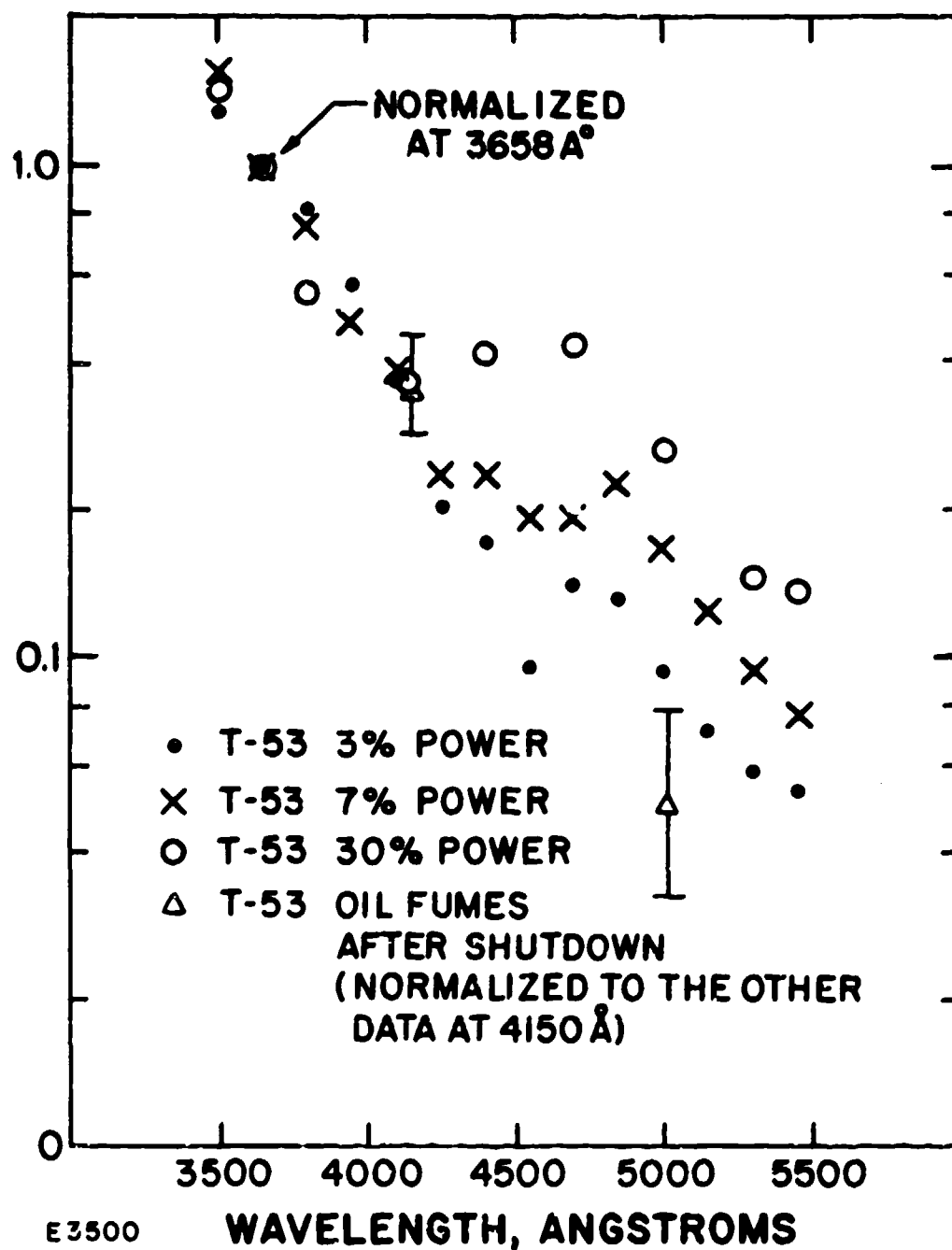


Figure 26 Normalized Fluorescence Spectrum - T-53 Gas Turbine Engine

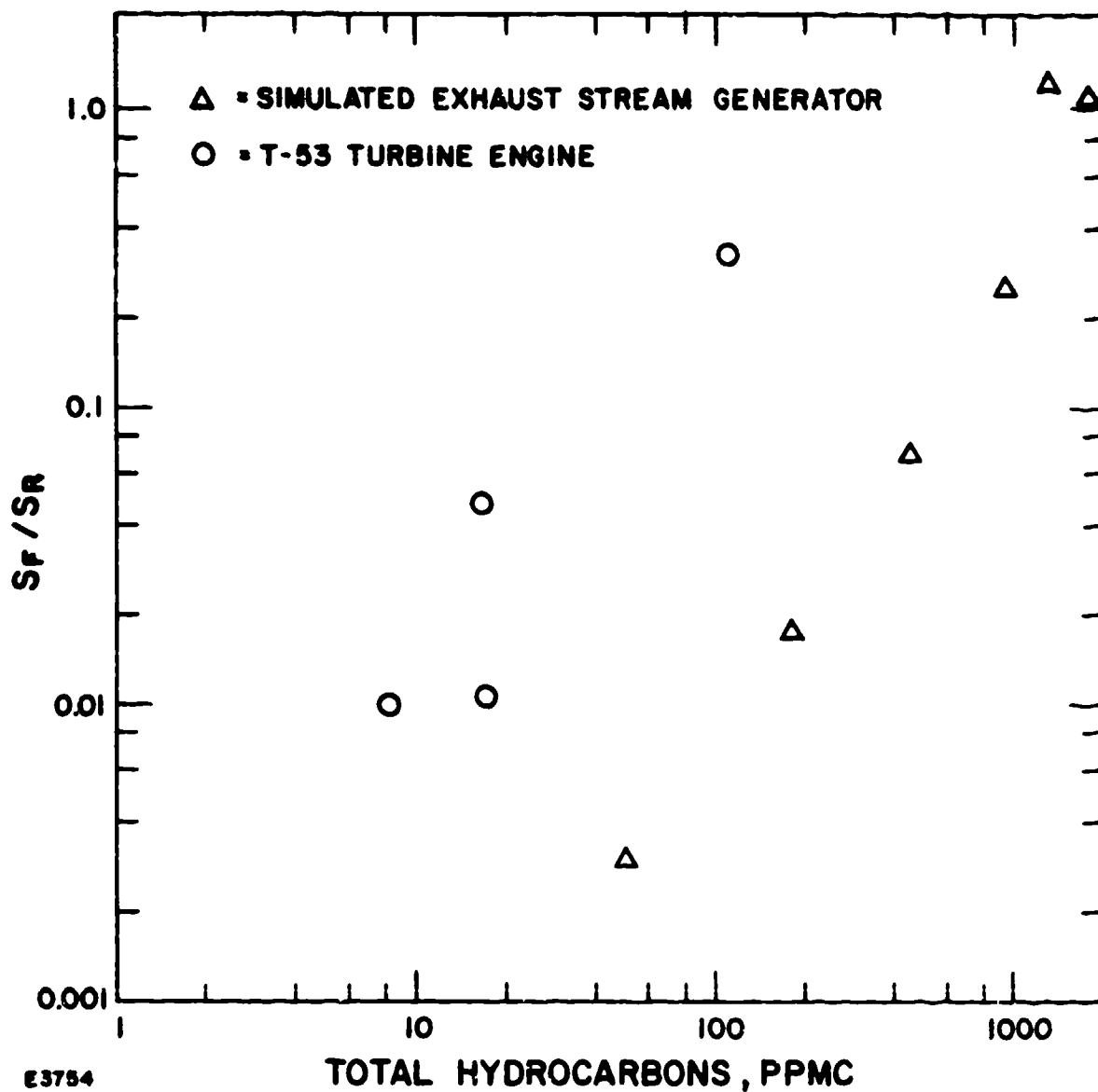


Figure 27 Fluorescence Normalized to Nitrogen Raman as Function of Total Hydrocarbons

$$S_F^* = S_F \left[\frac{t_M}{6 \text{ ns}} \right] \left[\frac{\Delta\lambda_F}{2000 \text{ \AA}} \right] \quad (7)$$

where 6 ns and 2000 Å are the values of t_M and $\Delta\lambda_F$ for the simulated exhaust stream generator. Using the values of 3 ns and 400 Å for the T-53 engine the data plot shown on Figure 28 is obtained. On this plot both sets of data fall within a factor of ± 2 of the hydrocarbon concentration, as shown by the shaded band.

It is planned in the future to conduct a careful double integration in both wavelength and time over the total fluorescence band to see if further improvements may be obtained in correlating laser induced fluorescence and total hydrocarbons.

The Raman spectrum is prompt, i. e., it follows the laser pulse shape, whereas the fluorescence spectrum exhibits a delay time which may be considerably longer than the laser pulse duration. This difference in time response offers an opportunity to discriminate and detect laser Raman signals in the presence of interfering laser induced fluorescence. Measurements were made of the lifetime of the fluorescence in the piston engine exhaust and in the T-53 exhaust. A 5 nanosecond wide detection gate was scanned in time in 2.5 nanosecond increments over a 100 nanosecond total range of time which included the coincidence condition, i. e., the time at which the Raman lines are observed. Typical of such time dependent data is the data obtained from the exhaust of a piston engine operating at idle conditions and which is shown in Figure 29. This data is taken at the wavelength of the nitrogen Raman line and shows a combined Raman and fluorescence time history. The fluorescence decay time is determined by the trailing edge of such data.

A plot of the measured fluorescence decay times as a function of wavelength is shown in Figure 30. The observed decay time increases with wavelength from about 4 nanoseconds at 3600 Å to about 10 or 12 nanoseconds at 5000 Å. The laser pulse decay time of 3 nanoseconds should be subtracted from the observed fluorescence decay times to obtain the true values.

c. Oxygen Measurements

Raman measurements were made of the O₂ concentrations in the T-53 engine exhaust. These measurements show excellent agreement when compared with the expected values of the concentration on the basis of the measured fuel/air ratio from the operating engine.

Typical data of the O₂ vibrational Raman line in the hot exhaust gases are shown in Figure 31. These data correspond to an engine power setting of 30%. The dip in the data trace at the right side shows the results of temporarily turning off the laser during the scan, indicating that the background level is entirely a laser induced signal. The value

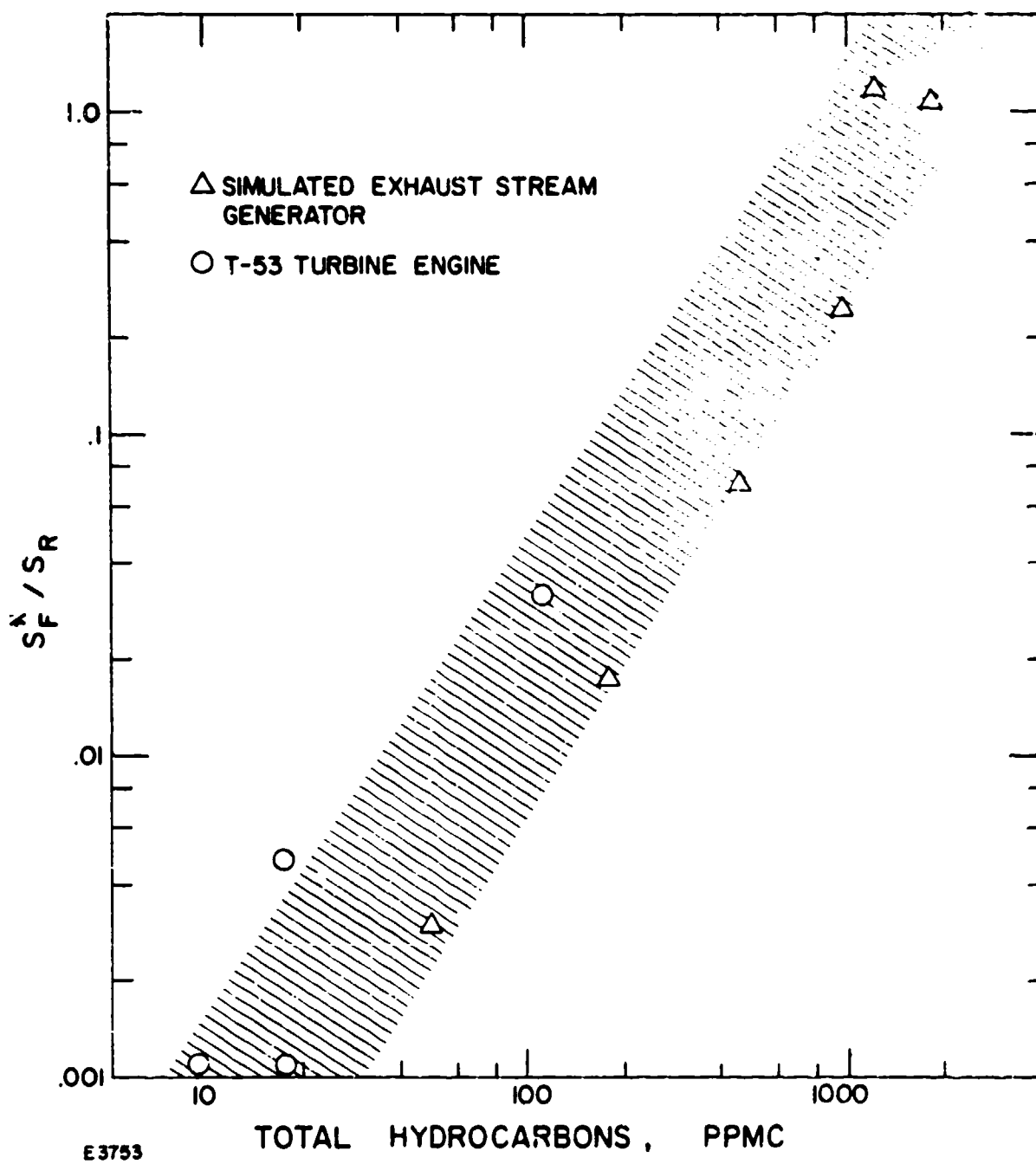
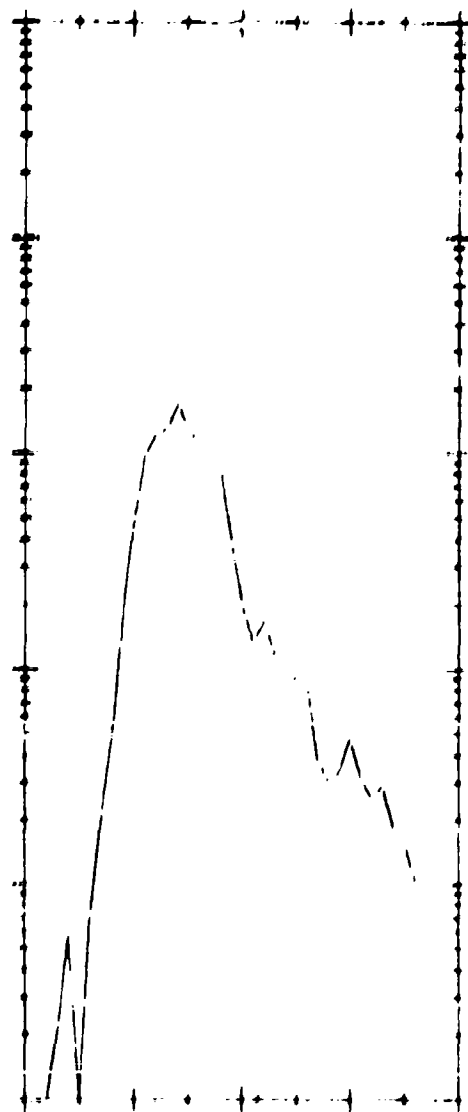


Figure 28 Corrected Fluorescence Normalized to Nitrogen Raman as Function of Total Hydrocarbons



84187

Figure 29 Typical Data Showing Fluorescence Decay Time Measurements

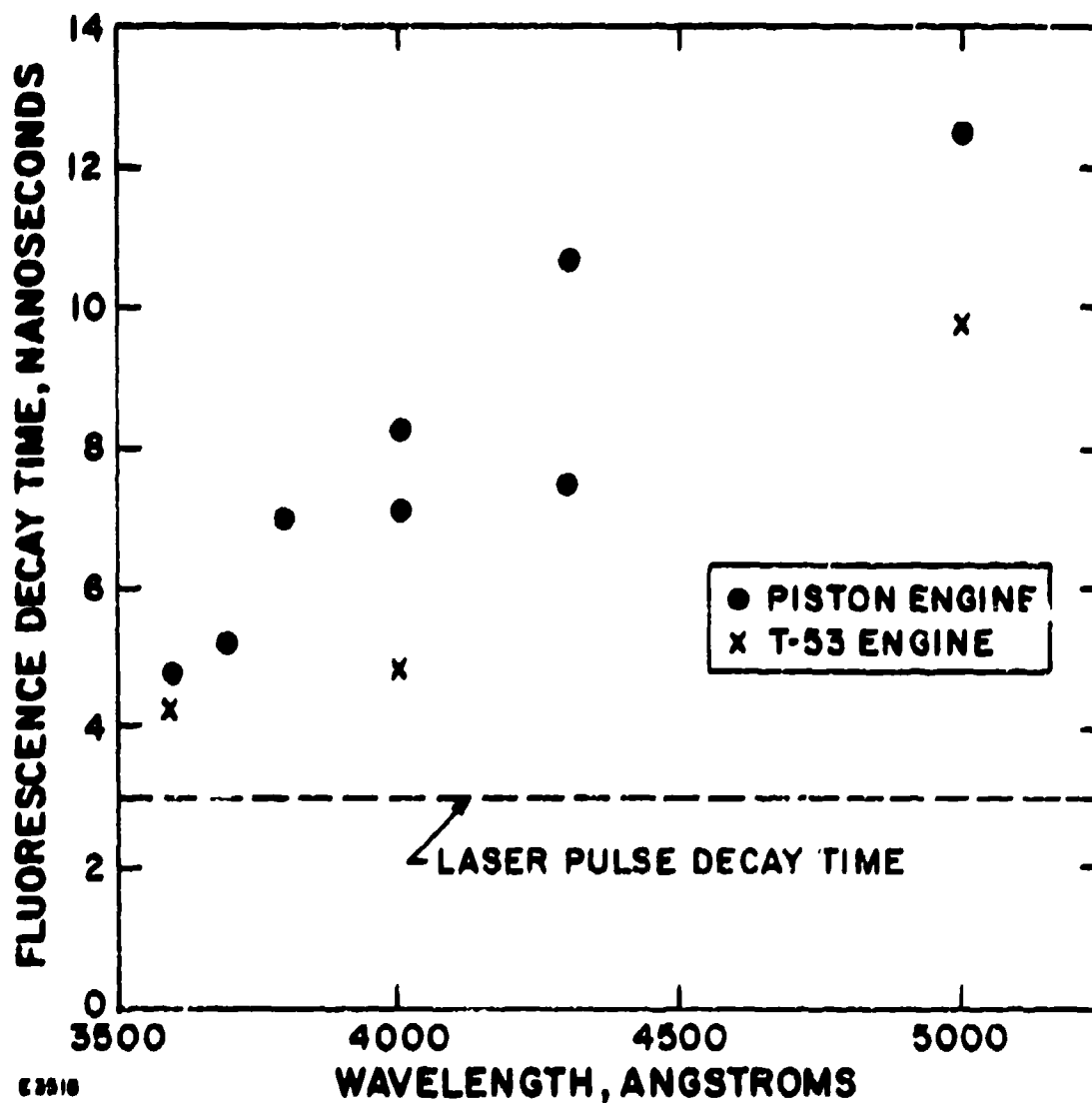


Figure 30 Fluorescence Decay Time vs Wavelength

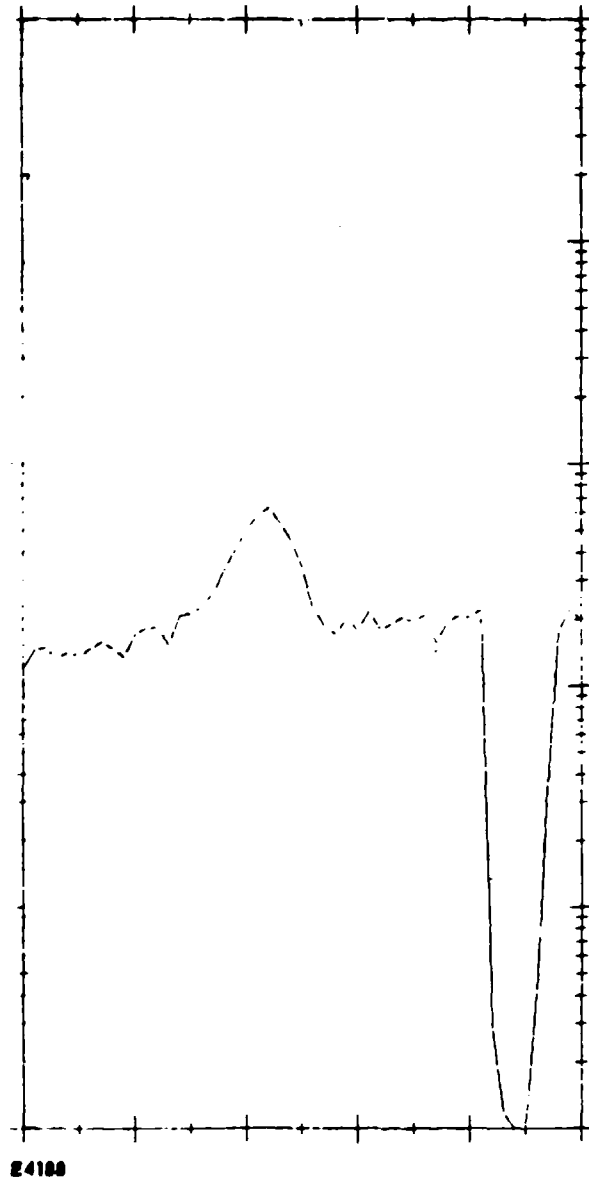


Figure 31 Typical Spectral Data of O_2 in Hot Exhaust Gases

of the O₂ signal is obtained by subtracting the average fluorescence level from the observed signal at the O₂ Raman line position. In a similar manner the N₂ Raman signal for the same engine condition is obtained after suitable corrections for the fluorescence level in that spectral region. The ratio of the corrected O₂ to N₂ Raman signals can then be used to obtain the O₂/N₂ mole ratio. The system was calibrated in the field for effective cross section and system transfer function by using the O₂/N₂ ratio obtained from ambient air and by assuming that air is 21% O₂ and 78% N₂ on a mole basis.

The results of the oxygen measurements are shown in Figure 32 where the O₂/N₂ mole ratio is calculated from the fuel/air ratio of the operating T-53 engine, using an approximate value of hydrogen/carbon mole ratio of 2.0. Perfect agreement would cause the data to fall in the line connecting zero with the point labeled "air". It can be seen that the data fall generally along that line to within the accuracy of the respective measurements. The error bars are mainly caused by the "shot noise" in the Raman signal at the high power conditions, and are affected by the fluctuations in the fluorescence signal at the low power conditions. A minor temperature correction caused by the difference in the vibrational Boltzmann factor between O₂ and N₂ should be applied to these data if higher precision is required.

d. Carbon Dioxide Measurements

Similar Raman measurements were made of the CO₂ concentration in the T53 turbine engine exhaust and are shown in Figure 33. The Raman data were normalized to the gas analysis data at the 60% power point. Absolute CO₂ calibrations using the atmosphere were not conducted in the field because of the uncertainty in the CO₂ concentration of the air in the Bridgeport, Connecticut industrial area.

e. Water Vapor Measurements

Water vapor Raman data were also obtained from the T53 engine exhaust under all operating conditions. Uncertainty in the water vapor Raman cross section as a function of temperature has precluded the use of the water vapor Raman data to obtain water vapor quantitative concentrations. This measurement will become useful when Raman cross-section data are available. Raman measurements of the ambient water vapor were obtained which agreed with the nearby Bridgeport Airport Weather Bureau within $\pm 20\%$.

The water vapor Raman data that was obtained from the exhaust of the T-53 engine is shown in the following tabulation:

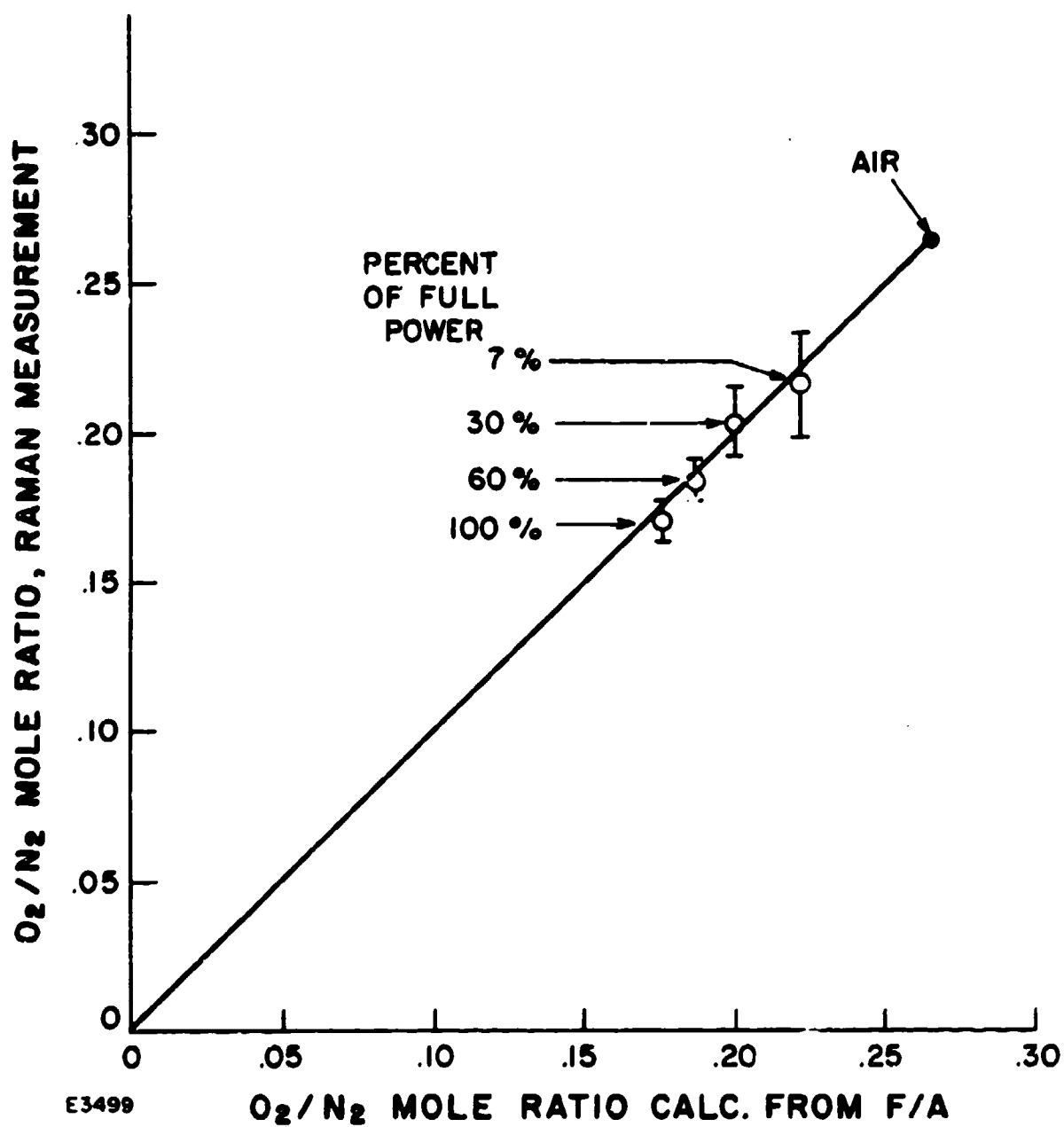


Figure 32 O₂/N₂ Mole Ratio for T-53 Engine Raman Measurement vs Calculated Value

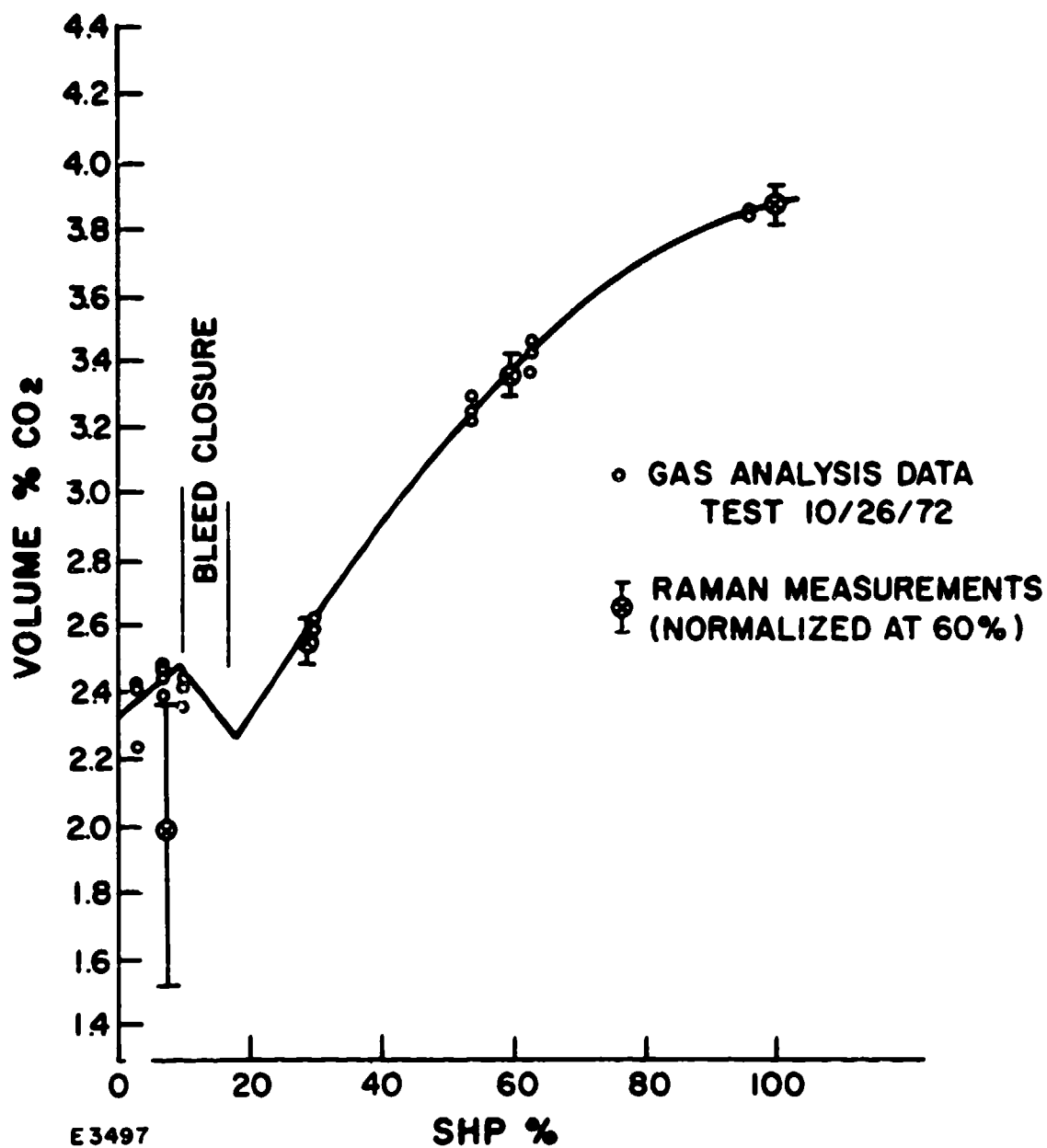


Figure 33 Volume % CO₂ as Measured from Raman Scattering vs Shaft Horse Power (SHP), %

Power Setting	H ₂ O/N ₂ Mole Ratio		
	Raman Measurement	Calculated From F/A	Apparent Cross-Section Decrease
(1)	(2)	(3)	(4)
7%	0.0274	0.0372	0.74
30%	0.0216	0.0416	0.52
100%	0.0226	0.0567	0.40

The Raman Measurement values in (2) are the ratios of the peak value of the water Raman signals in the 3652 cm⁻¹ band to the peak value of the nitrogen Raman signals at 2330 cm⁻¹. The system was calibrated using the ambient air values. The calculated values used the same F/A data as was used in the above O₂ and CO₂ comparisons and included a slight correction for the ambient air water vapor.

The Apparent Cross-Section Decrease in (4) is obtained by taking ratio of column (2) to column (3). It should be noted that the water Raman band was observed to broaden with increasing temperature so that the decrease in apparent water vapor cross-section when based on peak value alone is reasonable.

f. Nitric Oxide (NO) Measurements

An attempt was made to detect nitric oxide (NO) in the T53 exhaust using the 1876 cm⁻¹ vibrational Raman transition. The T53 engine typically produces 100 ppm of NO when operating at full power. Because the fluorescence level in the T53 at full power was about 100 times greater than the expected signal from NO, the required integration times for detection were longer than the test time available. The data obtained and shown in Figure 34 do illustrate the problem, however. This figure shows a spectral scan through the wavelength region of the NO Raman line. The average value of the fluorescence level is approximately 56 counts for each measurement time period of 90 seconds. During the same time period the expected NO Raman signal of 100 ppm will be 0.7 counts. Since this is well within the standard deviation of the fluorescence level (6.9 counts) the NO was not detected by the measurement. As shown on the figure a level of 2000 ppm of NO would have been detectable, since that concentration would have satisfied the detection criteria that the mean of the NO + fluorescence signal and the mean of the fluorescence signal would be separated by two standard deviations.

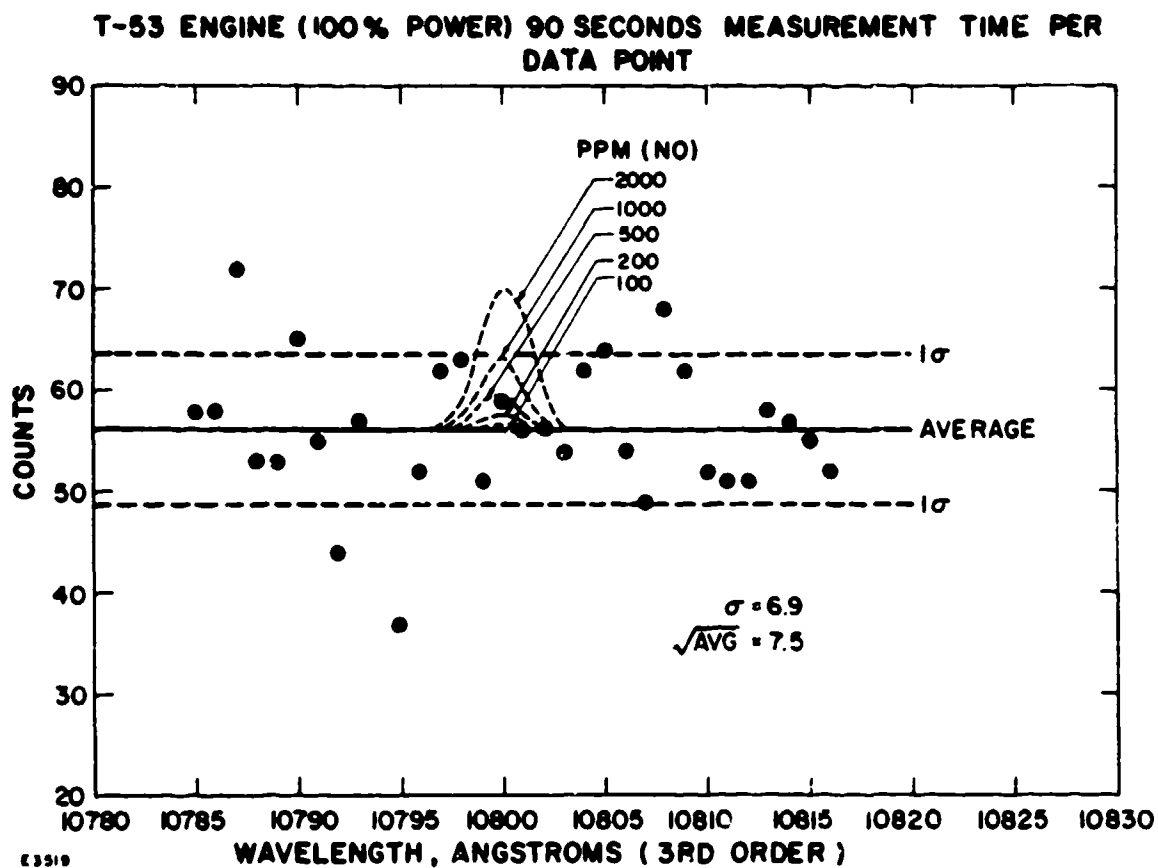


Figure 34 Raman/Fluorescence Data Obtained on the T-53 Exhaust in the Spectral Region of NO

The chart of Figure 35 shows the scaling of the above fluorescence subtraction-type measurement with NO concentration, laser power and integration time. The Raman signal from NO for various concentrations is plotted in this Figure as a function of P^*t^* , a normalized laser power times integration time product. P^*t^* is set equal to unity for the conditions of the 100% power, T-53 test which was described in Figure 34. In that test P was 3% of the design value, due to severe optical transmission losses, and t was 90 seconds. For this same test the NO concentration was expected to be 100 PPM and produce 0.7 counts per measurement as previously described. This operating point corresponds to the intersection of the 100 PPM NO line with the ordinate in Figure 35.

A detection criteria of 2 standard deviations was selected as the detection threshold. This means that a Raman signal will be considered to have been detected when its value equals or exceeds twice the square root of the fluorescence background level. The assumption that the square root of the fluorescence level can be set equal to the standard deviation of the measurement was verified in the 100% power, T-53 test data of Figure 34. In this test a fluorescence level of 56 counts in 90 seconds was observed, giving a Raman detection limit of $2\sqrt{56}$ or 15 counts. This value occurs on the ordinate of the chart of Figure 35 at the intersection point of the line labeled $2x\sqrt{\text{fluorescence}}$ and was the basis for the position of the line which defines the detection threshold limits on the chart.

The value of one-half for the slope of the detection threshold limit line may be derived from the last equation in Appendix II of this report. This equation, when rearranged, shows that in the case where laser induced noise such as fluorescence is the dominant noise source, i. e., $F \gg 1$, the Raman signal to noise is proportional to the square root of the laser power times integration time product to fluorescence level ratio, i. e., $S/N \sim \sqrt{PT/F}$. Since the Raman signal is proportional to PT, the fluorescence noise is thus shown to be proportional to \sqrt{PTF} . As the fluorescence level changes, the detection threshold limit line therefore moves up and down on the chart at a rate proportional to the square root of the fluorescence level.

The use of the chart of Figure 35 may be illustrated by the following example. A value of $P^*t^* = 100$ would be required to detect NO at 200 PPM. This could be accomplished by increasing P to the design value (i. e., cleaning the optics) and integrating for 4.5 minutes.

g. Temperature Measurements

The temperature of the T53 exhaust was measured by means of the N₂ Raman density method whereby the temperature is assumed to be inversely proportional to the density of nitrogen, with a constant static pressure. (8) If the dynamic pressure is a significant portion of the total pressure, i. e., in a high velocity flow, then a correction for this must be made to the data.

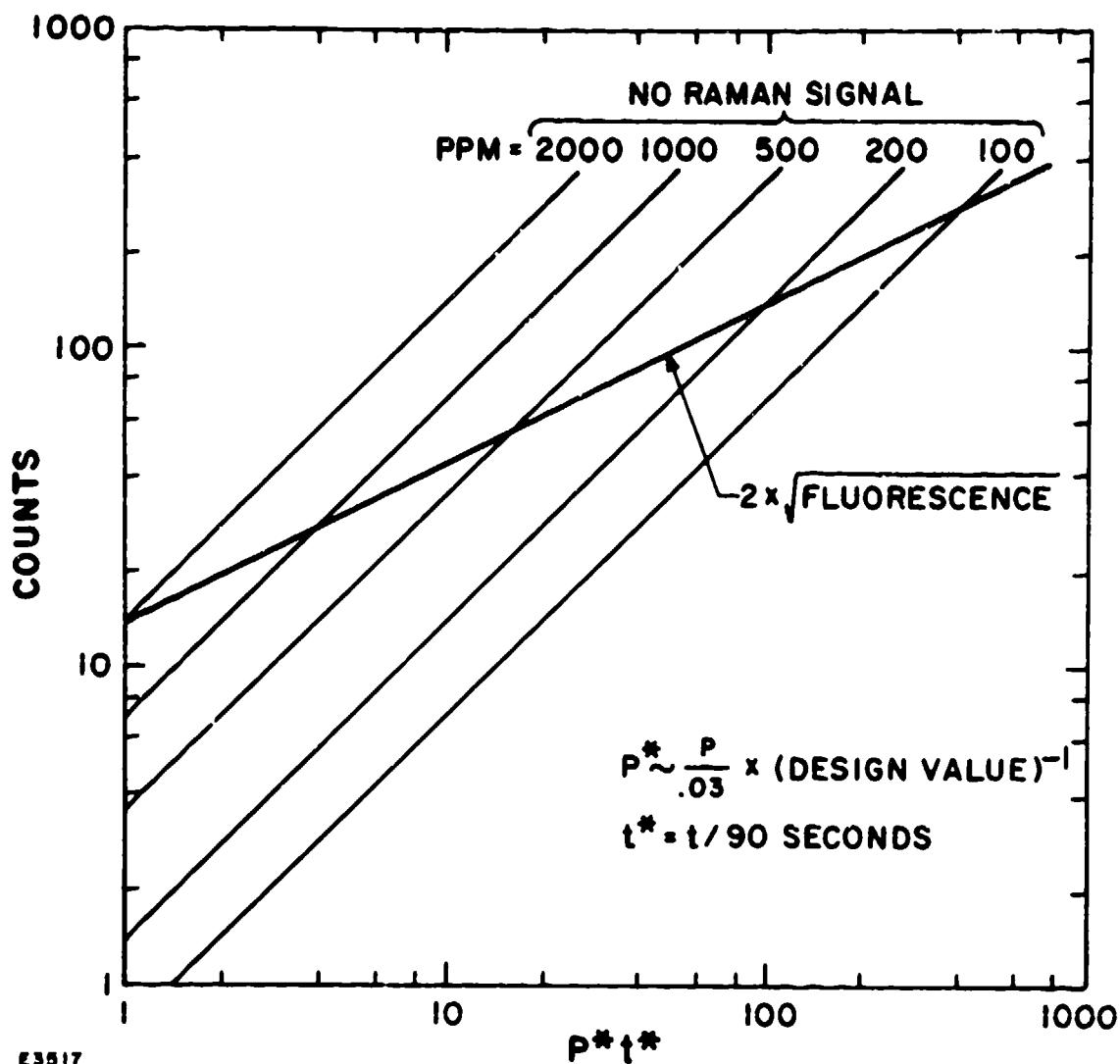


Figure 35 Raman Counts from NO as a Function of P^*t^* with Fluorescence Interference Threshold

The density of nitrogen was measured at 6 points in the exhaust stream of the T-53 for each of the 4 operating conditions. The geometry of the profile and the position of the measurements points in the exhaust stream is shown in Figure 36. The temperature and density of the ambient air was used as a scale factor to obtain the temperature profiles.

The temperature profiles obtained in this way are plotted in Figure 37 and appear quite reasonable. Thermocouple measurements in the exhaust stream gave an average of 725°K for the 7% power point and 890°K for the 100% power point, which is good agreement with the Raman data. Since it is not subject to thermocouple heat loss corrections, the laser Raman data is inherently a more reliable and accurate thermometer than a thermocouple. Further work is required however to definitely establish the precision of the laser Raman method as a hot gas temperature measurement technique.

Unsuccessful attempts were also made to utilize the Raman scattering from excited vibrational levels, the so-called "hot bands", in both CO₂ and N₂ for the purpose of making temperature measurements in the T-53 engine exhaust. The fluorescence interference prevented accurate temperature measurements to be made in this way. Further theoretical study is required to analyze the precision of "hot band" temperature measurements in the presence of laser induced fluorescence interference. Previous laboratory experiments as well as the basic theory of the use of "hot bands" for temperature measurement will be found in Appendix III of this report.

h. Smoke Analysis

During the course of testing, it was noted that the backscattering at the laser wavelength increased as the power increased. This was attributed to smoke particles. Since the molecular Rayleigh to Raman cross-section ratio is known to be approximately 1000, the Mie component can be determined by the following simple formula.

$$S(\text{MIE}) = S(\text{MIE} + \text{RAYLEIGH}) - 1000 S(\text{RAMAN})$$

where $S(\text{MIE} + \text{RAYLEIGH})$ is the value of the detected light scattered at (λ_0), $S(\text{RAMAN})$ is the value of the detected light scattered at (λ_R), and $S(\text{MIE})$ is the value of the Mie scattering from the smoke at λ_0 .

The method is self-calibrating by using the Raman signal as a normalizing factor. If the above equation is divided by $S(\text{RAMAN})$ the following normalized quantity is obtained from the ratio of the measured quantities.

$$\frac{S(\text{MIE})}{S(\text{RAMAN})} = \frac{S(\text{MIE} + \text{RAYLEIGH})}{S(\text{RAMAN})} - 1000$$

In the exhaust measurements the Mie scattering dominated the light scatter at the laser wavelength, so that the correction factor of 1000 could be neglected.

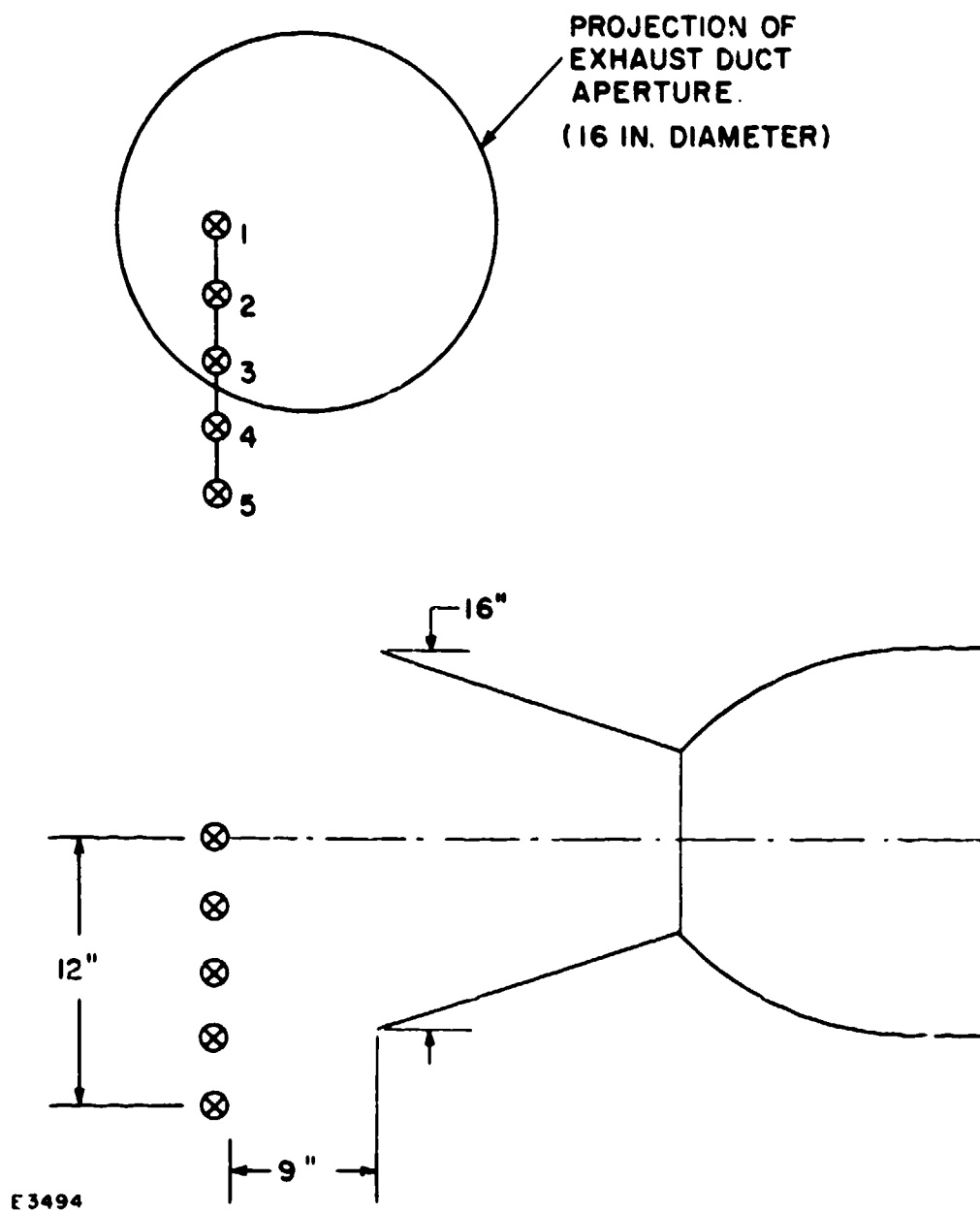


Figure 36 Geometry of N₂ Density Method Temperature Profile

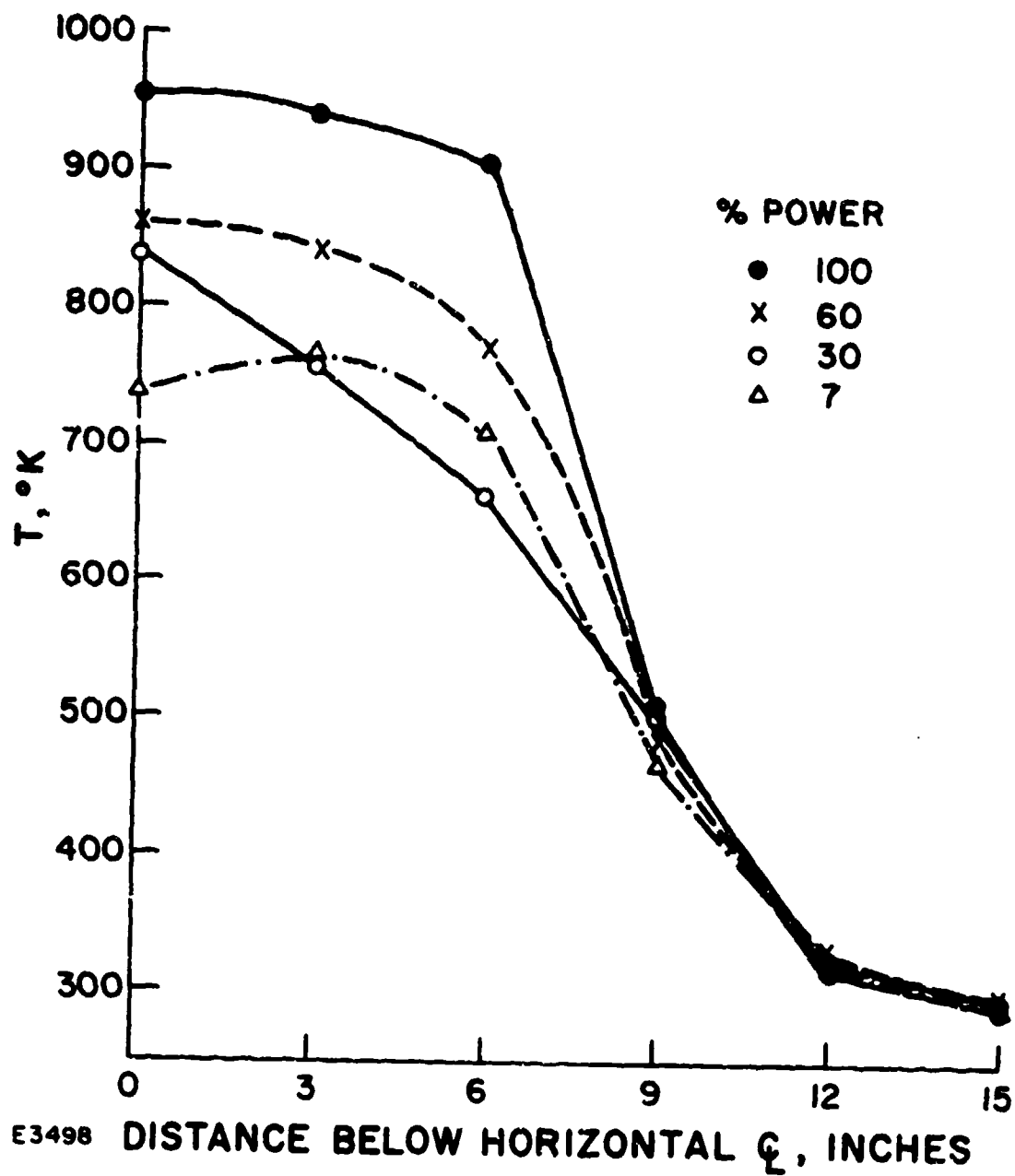


Figure 37 Temperature Profiles of T-53 Engine Exhaust using Raman Density Method

5. COMPARISON AND DISCUSSION OF RESULTS

The laser Raman data were compared with conventional exhaust gas analysis and evaluated as to present state effectiveness or future potential effectiveness. The various measurements are discussed separately, as follows:

a. Hydrocarbon Fluorescence Correlation

It was found that total hydrocarbons are easily detected by wide-band laser induced fluorescence. It was also found that this fluorescence is time dependent and decays over a period of time following the laser pulse. Therefore, if a calibration curve for hydrocarbon fluorescence is desired in the situation where a wide range of hydrocarbon concentrations are present, a correction factor for both the emission decay time and the spectral band width must be incorporated. An approximate normalizing factor equation has been proposed. This equation was demonstrated in correlating Raman signal to hydrocarbon concentration in Figure 28.

In the case where the hydrocarbon concentration range is limited, as in the exhaust of a gas turbine engine, this correction is expected to be small. To date, the data accumulated show a correlation between laser fluorescence and conventional HC response within a factor of ± 2 . It is expected that the correlation between the two measurements can be substantially improved by further research, including:

- (1) Refinement of the details of double integration over wavelength and decay time of the fluorescent signal.
- (2) Further comparison experiments to establish the validity of the method for a variety of combustion processes.

The calibration base for hydrocarbons is quite good, consisting of continual reference to the N_2 Raman in the exhaust gases.

b. Oxygen

Excellent agreement was obtained between laser Raman oxygen measurements (O_2/N_2 ratio) and the O_2/N_2 ratio calculated from fuel/air determination from exhaust gas analysis, as shown in Figure 25. The Raman measurements are within 1 to 3% of the conventional instrument determination, although the probable error band from "shot noise" and fluorescence is several percent in some cases. This O_2 measurement is of interest in determining the capabilities and sensitivities of the laser Raman. However, for oxygen concentrations to be useful in exhaust gas analysis, it must be measured to an unusually high degree of precision. For example, in progressing from equivalence ratios of 0 to 0.3, O_2 concentration varies from 21 to about 14%. Therefore, combustion efficiency of 0-100% must be measured by the 7% difference in O_2 consumption. If three significant figures are desired, i. e., 98.5%, this dictates

an O₂ detection of 1/1000 of the 7% oxygen difference. This sensitivity is considerably beyond the conventional O₂ analyzer. Theoretical calculations have shown that laser Raman accuracy can be increased to detect O₂ with this degree of precision. Further work is needed, however, to engineer such a precision Raman instrument for field use.

c. Carbon Dioxide

The response of the laser Raman instrument to CO₂ was calibrated at the beginning of the test program with a T53 engine by using the previous conventionally measured CO₂ concentration from this engine at the 60% power setting. Subsequent laser Raman measurements at the same and other power settings were found to agree just as well with the conventional instrumentation measurements, indicating negligible Raman calibration shift. These data are displayed in Figure 33 which shows the volume percent CO₂ as a function of the percent shaft horsepower of the engine.

d. Water Vapor

Water vapor measurements could also be used as an indication of fuel/air ratio, if we assume high combustion efficiency and allow for ambient water vapor.

Water could be detected at all operating conditions of the T53 engine. However, because of the uncertainty of the Raman cross section with temperature, the data could not be used quantitatively. Further work on laser Raman should include establishing the temperature-cross-section relationship, and thus permit another useful laser Raman measurement.

e. Nitric Oxide (NO)

As was stated, nitric oxide detection was masked by the hydrocarbon fluorescence, and considerably more sensitivity would be required to detect NO in the 100 ppm concentration range. Methods of increasing the sensitivity of the system were discussed, but even this could not equal the detection capability of present infrared or chemiluminescence NO detection instruments. A radical modification in the laser Raman method used would be required to equal the existing analytical methods. Fluorescence suppression techniques such as changing the laser excitation wavelength, using polarization, sensitive detection, or using much shorter laser pulse durations will be required to detect trace species, such as NO, at concentrations significantly less than 100 ppm.

f. Temperature

Accurate temperature profiles were obtained in the T-53 exhaust using laser Raman scattering from nitrogen via the density method. The spectral analysis of "hot bands" was found to be a less accurate method in the T-53 exhaust because of the high level of laser induced fluorescence. Although the feasibility has now been demonstrated, further work is required to quantify the precision of the laser Raman method for temperature measurements in aircraft engine exhaust streams.

The following laser Raman methods should be considered when a temperature measurement capability is being designed:

1) N₂ or Major Specie Density Method. This method, used in the T-53 tests, has the advantage that it used the scattering from the dominant species and is therefore less subject to fluorescence interference. The disadvantages are that profiles or before and after ambient calibrations are required for absolute temperature measurements, and the velocity, if high, must be known. The density method measures the translational temperature directly.

2) Anti-Stokes/Stokes Ratio Technique. This method has the advantage that it compares the intensity of anti-stokes scattering from an excited state of a molecule with the stokes scattering intensity from the ground state of the same molecule. Thus providing an in situ absolute calibration. This method is probably preferred when the temperature is very high so that the ground state population becomes significantly depleted, i. e., above 1500°K for nitrogen.

3) "Hot Band" Analysis. This method uses stokes scattering from ground states and excited states of the same molecule and has the same general advantages and disadvantages as method 2 above. The analysis of a band shape in the presence of broad band laser induced fluorescence interference may present special problems however.

g. Smoke

The detection of exhaust smoke was an unexpected bonus in the engine tests. The AIA smoke number is specified by procedures requiring flow measurement for the quantity of gas producing smoke particles, plus reflectance measurements from the deposited particles. However, it was found that by calibrating the laser Raman smoke detection response with only one AIA smoke number, the entire smoke measurement scale was determined, within the experimental error. The data are shown plotted on Figure 38, where the Mie data were normalized with AIA smoke number at the 60% power point.

The precision of these data appear to be essentially as good as the smoke determination by the SAE ARP 1179 method. This is consistent with previous statements by Champagne⁽⁹⁾ that particulate density is approximately proportional to smoke number for smoke numbers less than about 30.

h. Limitations and Problem Areas

The major problem area and the limiting source of system noise has been laser induced fluorescence. At idle conditions in the T-53 exhaust the fluorescence level was comparable to a Raman signal from N₂ at about one atmosphere of density. As the T-53 engine power level was raised the fluorescence level decreased until at 100% power it was two orders of magnitude less, but still masking 100 PPM Raman signals by

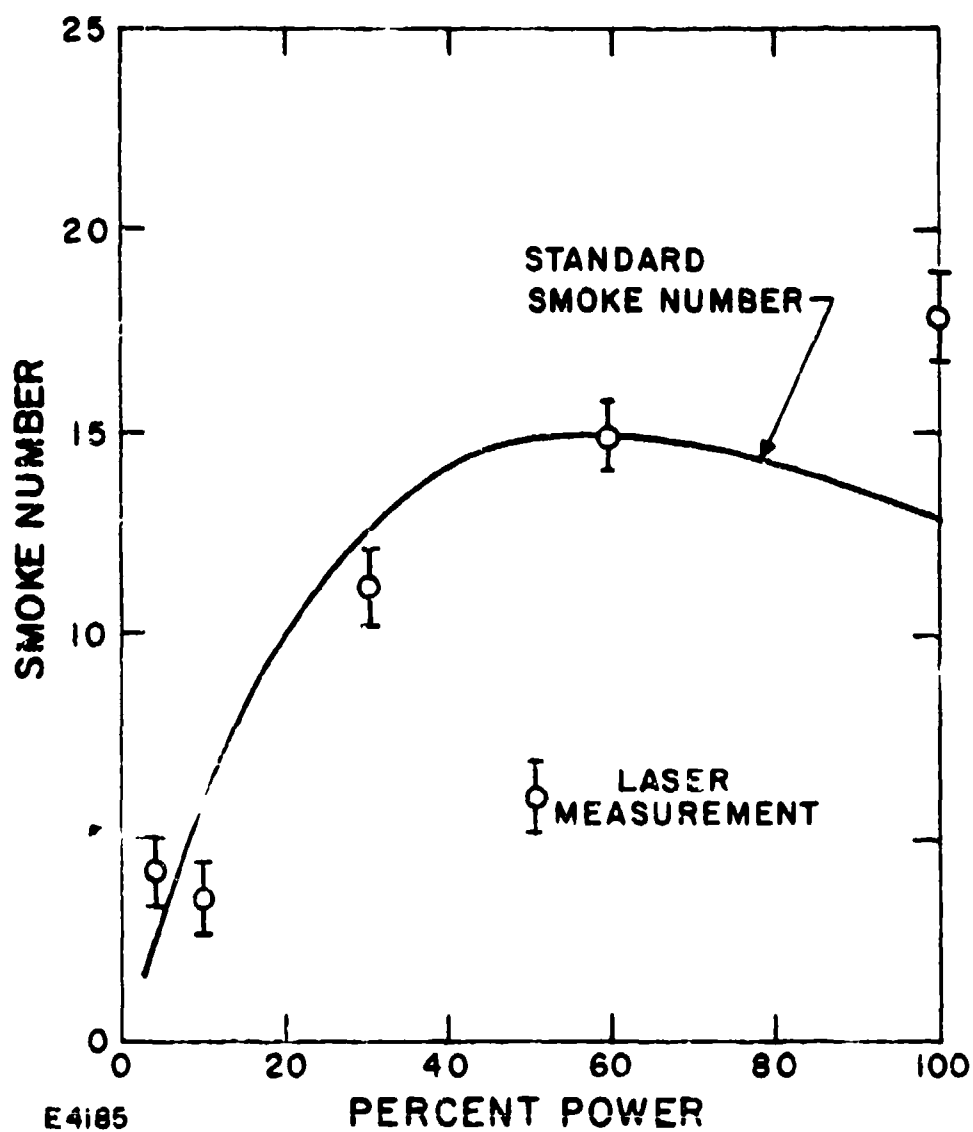


Figure 36 Comparison of Standard (ALA) Smoke Number to Normalized Laser Ramat./Mic Measurement (Normalized at 60% Power)

two orders of magnitude. Considerable effort was therefore spent during the course of this program on possible methods of fluorescence noise circumvention.

The circumvention technique that was actually employed and which has been discussed throughout this report is the "subtraction" technique. The average continuum fluorescence level, as measured on both sides of a raman line, is subtracted from the value of the data at the line position. This method was successfully employed to enable the measurement of O₂ and CO₂ concentrations under all operating conditions in the T-53 engine exhaust stream. An analysis of the use of the subtraction technique for the detection of NO at high power conditions was also presented in this report but was not yet implemented experimentally.

Other circumvention techniques such as the use of differential time gating in combination with the shortest possible pulse duration laser, the use of lasers with longer wavelengths than the 3371 Å pulsed nitrogen laser, and the use of polarization control are also considered possibilities that should be investigated in the future in addition to the subtraction technique.

A second major area of concern was the interference from ambient sunlight when outdoor operation was conducted during daylight hours. It was necessary, as shown in Figures 11, 12 and 13, to employ a dark background target and a sun shield on the portable van to bring the ambient noise level to within a factor of 10 of that of night operation. Further shielding of the direct scattering of sunlight from the exhaust gas itself is now needed if the system noise level is to be reduced to a value as low as that obtained during night operation.

SECTION IV

CONCLUSIONS

The classical laser Raman technique has demonstrated experimentally a prototype optical method which can be used to analyze several aircraft engine exhaust gas components under field testing conditions. Tests were made comparing the laser Raman with conventional gas analysis methods. The accomplishments of the laser Raman prototype equipment thus far has shown:

- (1) Excellent agreement of O_2 and CO_2 measurements with conventional exhaust gas measurements and correlations with engine fuel-air ratio.
- (2) Excellent agreement with smoke number measurements, with a calibration at one point only.
- (3) Good agreement of temperature profile measurements with thermocouple data.
- (4) Total hydrocarbons were detected and compared to flame ionization measurements to within a factor of ± 2 over a range of three decades of concentration.
- (5) Water vapor has been detected in exhausts under all conditions. Calibration requires fundamental water cross-section data as a function of temperature, which is not now available.
- (6) The limiting signal to noise (S/N) in the Raman field system which was built and tested was shown to be "shot noise", i. e., quantum fluctuations in the laser induced signals, rather than instrument noise such as photomultiplier, dark currents, or ambient light levels. This means that the instrument sensitivity is greater than instrument background noise.

The species present at lower concentrations, such as NO at 100 ppm, have not been detected in actual field measurements because of interference with the low level hydrocarbon fluorescence background. However, extrapolations from the data obtained indicate that a refurbished optical system operating at its nominal design throughout could detect NO at 100 ppm in less than 5 minutes integration time. Still further development would be required to detect NO concentrations of the order of 10 ppm or less. NO_2 detection is not considered feasible at this time because of a strong interference with CO_2 .

CO detection was not attempted. However theoretical and experimental laboratory studies have shown a CO measurement capability could be added to the laser Raman system with a more extended research effort.

The most severe problem area was laser induced hydrocarbon fluorescence interference when the test gas contained large total hydrocarbon concentrations. A circumvention technique was employed to somewhat improve the system capability whereby the average continuum fluorescence level, as measured on both sides of a Raman line, was subtracted from the value of the data at that line position.

The entire concept of a truck-mounted laser system for measuring aircraft engine exhaust gas components at a remote position (airport location) has been shown to be a practical one. The advantages of optical exhaust gas measurements versus probing systems has been demonstrated. It now remains to solve the remaining technical details to make laser Raman a competitive method for aircraft exhaust measurements.

SECTION V

RECOMMENDATIONS

The work described in this report has experimentally demonstrated the use of classical Raman scattering as a means of remote gas analysis of aircraft engine exhausts. The task is now to develop confidence in the use of the Raman method as a practical tool for general purpose combustion gas analysis. The following recommendations are intended to help expedite and broaden the utilization of the laser Raman method as a standard and dependable tool which can be put in the hands of combustion engineers and scientists for routine use. The recommendations in this section are a compilation of the insights that have accumulated during the course of the past work and which for various reasons it was not possible to incorporate into the existing system.

1. USING AND UPGRADING THE EXISTING SYSTEM

a. Anti-Stokes Gratings

The system was designed without taking into consideration the possibility of laser induced fluorescence interference throughout the visible spectrum, which indeed did occur. The anti-stokes spectrum should be examined for the possibility that significantly less fluorescence interference will be produced. Appropriate blocking filters for the existing third order gratings or new first order gratings should be selected and procured so that the anti-stokes Raman spectrum may be studied experimentally.

b. Excitation Wavelength Studies

The existing system utilizes a 3371 Å pulsed nitrogen laser source. This source was considered optimum in the absence of fluorescence interference considerations. A study should now be made of possible alternate lasers which could be employed in the existing system so that excitation wavelengths longer than 3371 Å can be experimentally investigated and compared in terms of laser induced fluorescence and overall signal-to-noise.

c. Software Modifications

The full potential of the NOVA digital processor that now exists in the laser Raman system has not yet been realized. Improvement in overall system capabilities can be immediately realized by modifications in the following software areas.

(1) Scan Speed Control

In the present system much time is wasted when the spectrometer is scanning without taking data between wavelength regions that are widely separated. The program should be modified to move the spectrometer at an optimum variety of speeds during a given data taking/scan cycle.

(2) Automatic Ambient Background Calibration

The existing software includes an ambient light background subtraction routine which involves sampling the ambient light level before and after each laser pulse. However, the calibration constant between the data gate and the background gate must now be manually determined. With a multiplicity of gate widths now possible, an automatic calibration of the ambient background calibration should be included in the program software options.

(3) Data Smoothing and Averaging

Additions to the software in the area of data smoothing and averaging should be studied. Real-time display of averaged data which has been processed by using the available proven techniques for noise circumvention will enable experimental scientists and engineers to make optimal use of their decision-making capabilities during the execution phase of experiments.

d. Elevation Scan Capability

It was shown during the past field tests of the laser Raman system of the desirability of producing profiles of the gas properties of an engine exhaust. This was accomplished during the field tests by raising and lowering the engine, keeping the laser Raman system fixed. If a variety of aircraft engines are to be studied in order to establish a valid data base with the Raman system, an elevation scan capability of the Raman system itself would enable exhaust profiles to be obtained with all engines, not just those engines capable of being raised and lowered.

2. RECOMMENDED MODIFICATIONS AND ADDITIONS

a. Laser Smoke Number Measurement

The experimental demonstration during the field tests that laser scattering could be used to determine smoke number was an unexpected bonus to the program. The addition of this measurement into the laser Raman measurement system should now be considered. A design recommendation for incorporating the laser smoke number measurement into the system should be developed.

b. RMS Point Measurements

The goals of the laser Raman measurement program have to date been directed toward measurement of average values of the gas properties such as composition and temperature. The fluctuations in these gas properties could be measured by adding a second laser to the system. By varying

the time delay between the firing of the second laser with respect to the first laser an RMS correlation function for each gas property could be obtained. A study should be undertaken to determine the validity of this assumption and to specify the way in which such an RMS point measurement capability might be implemented.

c. Laser Doppler Velocimeter (LDV)

It may also be desirable to be able to measure the velocity of a gas flow as well as its composition and temperature. The laser Raman system NOVA digital data processor has the capability to service such additional measurements. If velocity information is desired a study should be initiated to specify the ways in which such additional capability could be added to the system.

d. Data Handling and Recording Modifications

Early consideration should be given to the possible expansion of the data handling and recording capabilities of the computer system. As the total system nears fully operational levels, data will be produced in ever increasing amounts. At present, the system employs two basic data output devices:

1. Hard Copy Teletype Writer (TTY)
2. Drum Plotter.

The TTY is an electro-mechanical device of vintage design with a severely limiting throughput rate of 10 characters/sec. It can easily be envisioned that more sophisticated applications of the system will generate substantially greater volumes of data at much higher rates. If the data is to be preserved, high speed recording mediums such as industry compatible magnetic tape or tape cassettes will become necessary. A cost/benefits study should be generated to determine whether additional recording peripherals should be added to the computer or if data from the system should be linked to the burner data collection system.

The recently used Cal Comp plotter is a "borrowed" device which has been deleted from the system and returned to its owner. It is possible to replace the plotter with one of like specifications or consider the addition of a CRT graphics display with hard copy attachment. The CRT is inherently magnitudes faster at data plotting and much more flexible.

Higher data rates and quantities and/or substantial software modification may create a need for additional core memory to be added to the system. At the present time the CPU hosts 8K words of memory. As the CPU was purchased with future expansion in mind, additional memory may be added in 8K increments at modest cost to occupy currently vacant electronic card slots.

Depending upon the future role to be played with the total system, significant software modification can most economically be implemented through the addition of a high speed input device. Many manhours are lost in the assembly and debugging of programs due to the 10 cps read/write paper tape method currently employed.

REFERENCES

1. Raman, C. V. and Krishnan, K. S., "A New Type of Secondary Radiation," *Nature* 121, 501 (1928).
2. Melfi, S., Lawrence, J. and McCormick, M., "Observation of Raman Scattering by Water Vapor in the Atmosphere," *Applied Physics Letters* 15, 295 (1969).
3. Strauch, R. G., Derr, V. E. and Capp, R. E., "Atmospheric Water Vapor Measurement by Raman Lidar," *Remote Sensing of Environment* 2, 101 (1972).
4. Leonard, D. A., "Development of a Laser Raman Aircraft Turbine Engine Exhaust Emissions Measurement System - Technical Report," Avco Everett Research Laboratory, Research Note 914, May 1972. (This reference is included in this report as Appendix III.)
5. Rubins, P. M. and Doyle, B. W., USAAMRDL Technical Report 73-47, "T53 and T55 Gas Turbine Combustor and Engine Exhaust Emission Measurements," U. S. Army Air Mobility Research and Development Laboratory, Fort Eustis, Virginia.
6. Monroe, J. L., "Remote Probing of a Volume at Finite Conjugates," *Optical Engineering* 13, 79 (1974). (This reference is included in this report as Appendix IV.)
7. "Aircraft Gas Turbine Exhaust Smoke Measurement," SAE Aerospace Recommended Practice, Report ARP 1179, 4 May 1970.
8. Strauch, R. G., Derr, V. E. and Capp R. E., "Atmospheric Temperature Measurement Using Raman Backscatter," *Applied Optics* 10, 2665 (1971).
9. Champagne, D. L., "Standard Measurement of Aircraft Gas Turbine Engine Exhaust Smoke," ASME Publication 71-GT-88.

APPENDIX I
LABORATORY FLUORESCENCE MEASUREMENTS

Preceding page blank

Monsanto

MONSANTO RESEARCH CORPORATION

Dayton Laboratory
1515 Nicholas Road
Dayton, Ohio 45407
Phone: (513) 268-3411
TWX 810-459-1681

19 August 1974

AVCO Everett Research Laboratory
Attn: Mr. D. A. Leonard
2385 Revere Beach Parkway
Everett, Massachusetts 02149

Dear Don:

Enclosed are the results of our fluorescence work of the synthetic lubricant, Mobil Jet Oil II. This work may be included as an appendix to your final report if you see fit. Some of the methods of data treatment are in accordance with suggestions made by Dr. Mel Roquemore of AFAPL in his memos of 25 February and 14 April 1974.

If any questions arise, please feel free to call.

Very truly yours,

F. N. Hodgson, Jr.
F. N. Hodgson

FNH:jsw

Enclosure

cc: Dr. R. D. Butler - AFAPL
Dr. W. M. Roquemore - AFAPL

Preceding page blank

-73-

Specimens of Mobil Jet Oil-II, M-3987-S14M3 were subjected to fluorescence spectral characterization using an Aminco-Bowman Spectrophotofluorimeter. This instrument, which is used to measure the fluorescence of liquids, can be used to record two different types of spectra. Emission spectra can be recorded by exciting fluorescence with a specific wavelength of irradiating light while plotting the intensity of the emitted light versus its wavelength. Alternatively, excitation spectra can be obtained by measuring fluorescence emission at a fixed wavelength while varying the wavelength of the exciting radiation. Both types of spectra were recorded for the subject synthetic lubricant.

Emission spectra are shown in Figure 1 for a 100 ppmV solution of the oil in hexane. A variety of excitation wavelengths were employed ranging from 220 to 450 nanometers (nm). In all cases except one, the same spectral distribution was observed. The peak obtained at approximately 385 nm is quite intense at excitation wavelengths of 337.1 and 350 nm. It will be noted that excitation at 300 nm resulted in a slightly different spectral curve. Along with the peak at 385 nm, a second peak appears at 345-350 nm. This becomes more apparent in a fluorescence spectrum obtained at a higher multiplier sensitivity, Figure 2.

Excitation spectra were recorded for emission at 350 and 385 nm, the wavelengths of the fluorescence peaks. The excitation spectrum for fluorescence at 385 nm, Figure 3, shows that the greatest intensity is obtained with an excitation wavelength of 340 nm. Note that the intensity of fluorescence produced by exciting at 337.1 is approximately the same. The excitation spectrum for fluorescence at 350 nm, Figure 4, shows maximum intensity at 300 nm. The fluorescence peaks at 350 and 385 nm appear to be due to two different fluorescing species.

The use of the fluorimeter in this study is based on the assumption that fluorescence observed for liquid specimens is similar to fluorescence for the same species in the vapor state, when excited by radiation of the same wavelength. The fluorescence literature has shown (ref. 1,2) this assumption to have validity. The foregoing spectral data clearly indicate that if the synthetic lubricant is present in the engine exhaust, it can fluoresce when excited at 337.1 Å. A comparison is shown in Figure 5 of the fluorescence obtained from the lubricant using the fluorimeter, and of the laser excited fluorescence¹ from the exhaust of the T-53 engine operating with the oil under a no-load condition.

¹Data by D. A. Leonard, AVCO Everett Research Laboratory.

In both cases, excitation is at 3371 Å and data have been normalized at 3658 Å. Fluorometric data have been corrected for variations in instrument response. The similarity between these spectral plots suggests that at least a portion of the Laser excited fluorescence is due to the synthetic lubricant.

It is desirable to obtain quantitative information on how the fluorescence interference would shift at wavelengths above and below the 3371 Å excitation wavelength. For this purpose the fluorescence data can be used to calculate (ref. 3) ratios of the relative magnitude of fluorescence measured at 2330 wave numbers from 3371 Å to that at 2330 wave numbers from other excitation wavelengths. The value 2330 cm^{-1} corresponds to the Raman shift for diatomic nitrogen. A plot of these ratios versus excitation wavelengths gives the relative magnitude of the fluorescence interference which might be expected with the N_2 Raman line. All data, of course, must be corrected for instrument response.

Since the Raman signal is wavelength dependent and varies with the fourth power of the wavelength (λ), this variation should be taken into account when analyzing the fluorescence data. Thus if the fluorescent intensity excited at λ_{ex} and measured at λ is represented by $n_F^{\lambda_{\text{ex}}}(\lambda)$, the variation of the fluorescence interference with the Raman signal may be expressed (ref. 4) by a plot of

$$\frac{n_F^{337.1}(365.8) \cdot (365.8)^4}{n_F^{\lambda_{\text{ex}}}(\lambda) \cdot \lambda^4}$$

versus excitation wavelengths, λ_{ex} .

To calculate a series of these ratios, fluorescence measurements were made for the specimen at a number of different excitation wavelengths from 300 to 450 nm. Essentially no fluorescence was observed at λ_{ex} above 400. Data are presented in Table I. A semilog plot of these data points, shown in Figure 6, reflects the variation of the ratio of the Raman signal to fluorescence interference. This experimental projection of the fluorescence interference to be expected indicates that a much more favorable Raman to fluorescence ratio can be obtained at excitation wavelengths above 375 nm.

References

1. Proc. R. Soc. Lond. A. 333, 385-402 (1973).
2. Anal. Chem. 43, 1976-1981 (1971).
3. Memo for record, 4 Apr 1974, by Dr. W. M. Roquemore.
4. Memo to F. N. Hodgson, 12 Apr 1974, by Dr. W. M. Roquemore.

Table I

ESTIMATION OF FLUORESCENCE INTERFERENCE WITH RAMAN SIGNAL

λ_{ex}	λ	$n_{\text{F}}^{\lambda_{\text{ex}}(\lambda)}$ (corrected)	$\frac{n_{\text{F}}^{337.1 \text{ nm}(365.8)} \cdot (365.8)^4}{n_{\text{F}}^{\lambda_{\text{ex}}(\lambda)} \cdot \lambda^4}$
300	322.5	47.4	22.1
315	340.0	65.6	12.8
325	351.0	121.9	6.1
337.1	365.8	636.4	1
340	369.3	783.3	0.77
350	381.1	742.8	0.72
365	398.9	224.1	1.99
385	422.9	8.48	41.9
400	441.0	5.20	58.2

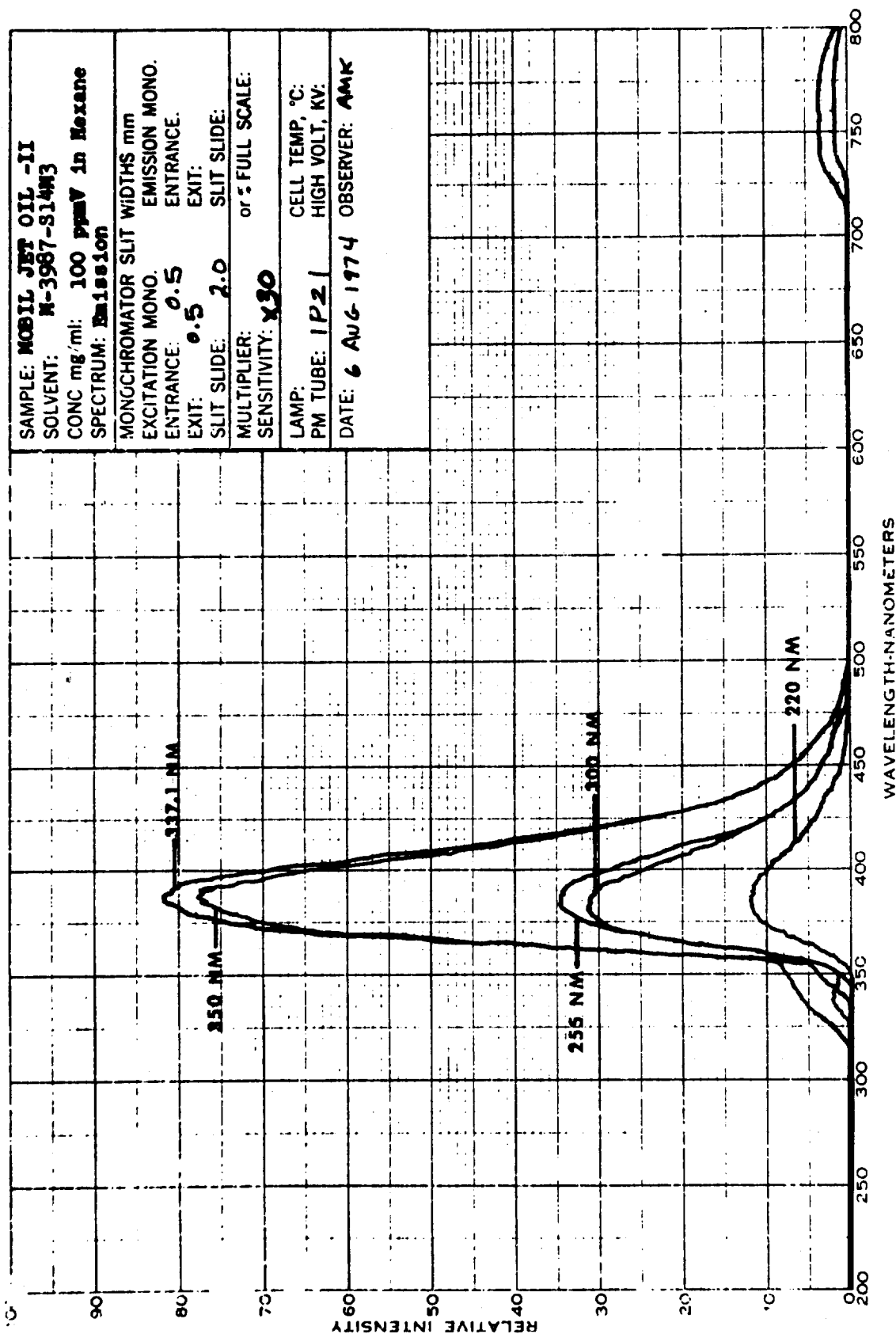


Figure 1. Fluorescence Spectra of a Synthetic Lubricant at Various Excitation Wavelengths.

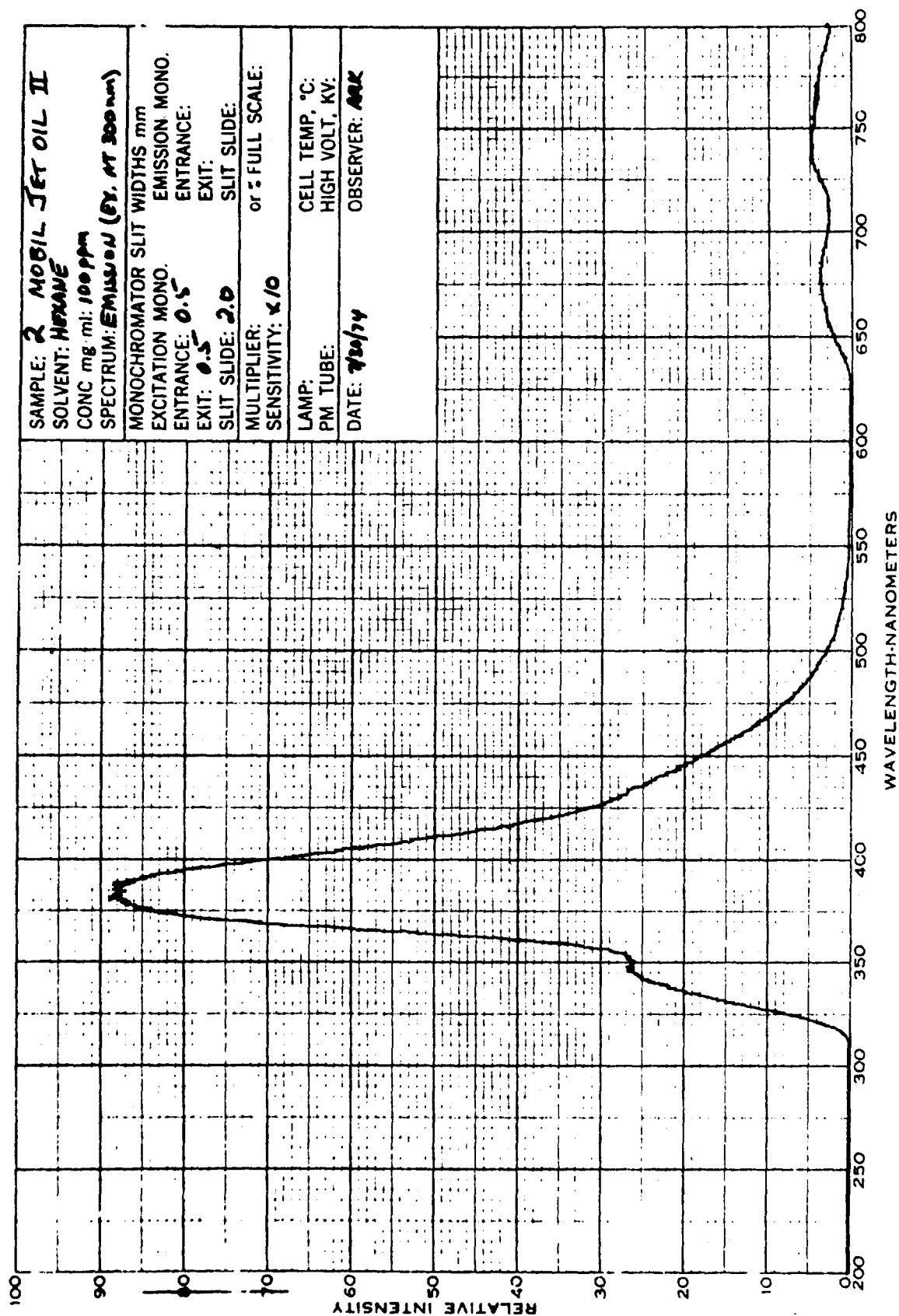


Figure 2. Fluorescence Spectrum of Synthetic Lubricant Excited at 300 nm.

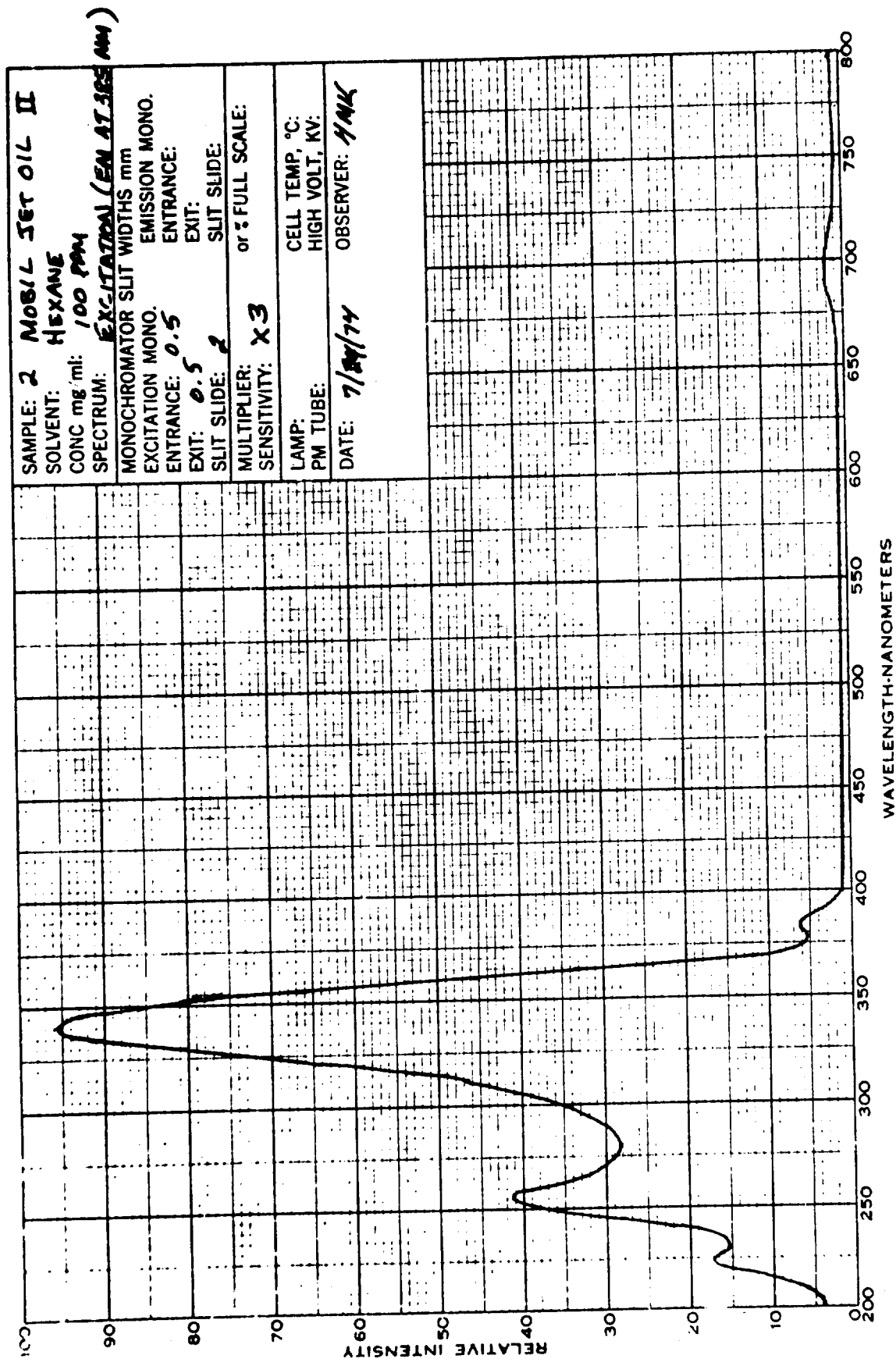


Figure 3. Excitation Spectrum of Synthetic Lubricant for Emission at 385 nm.

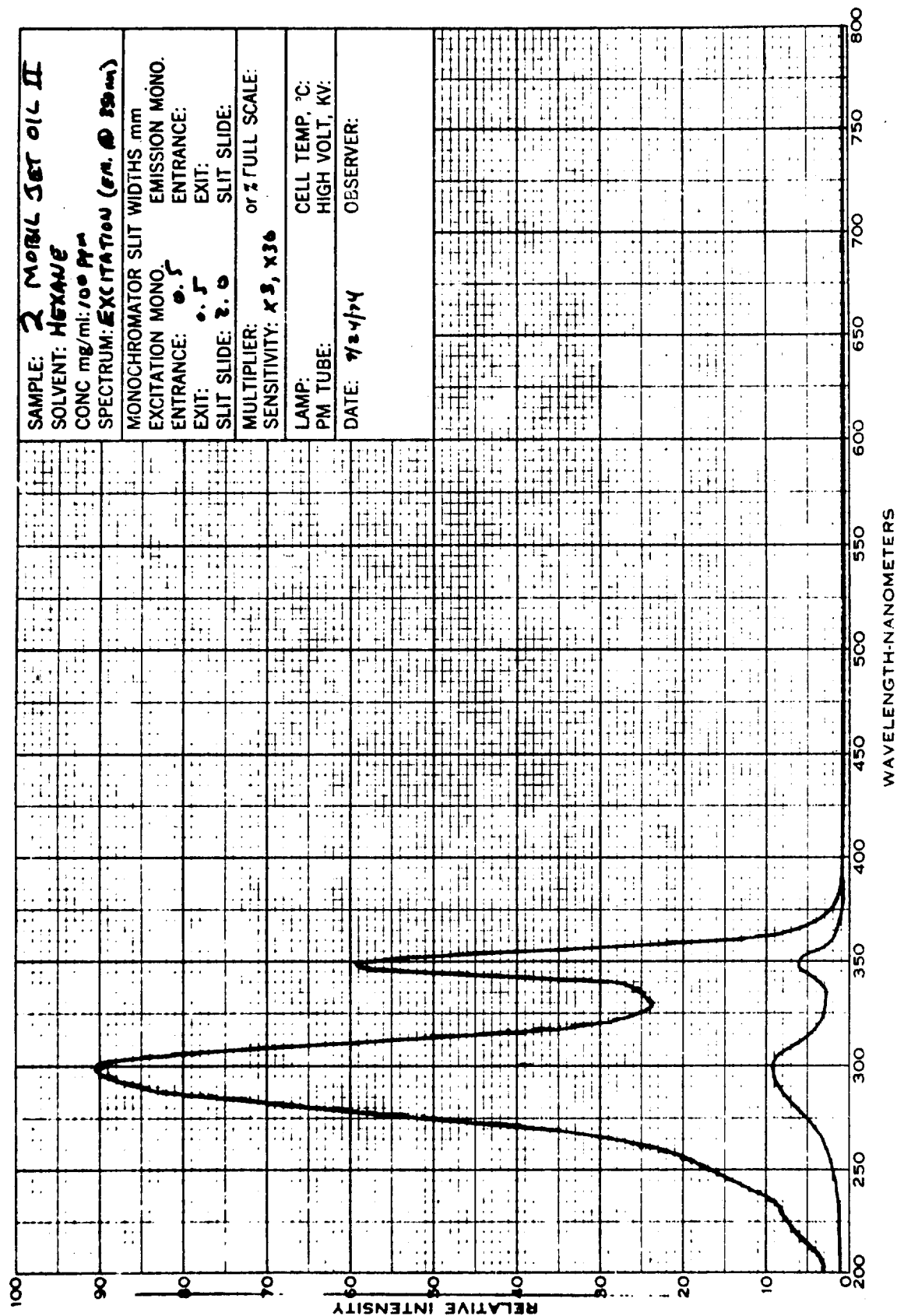
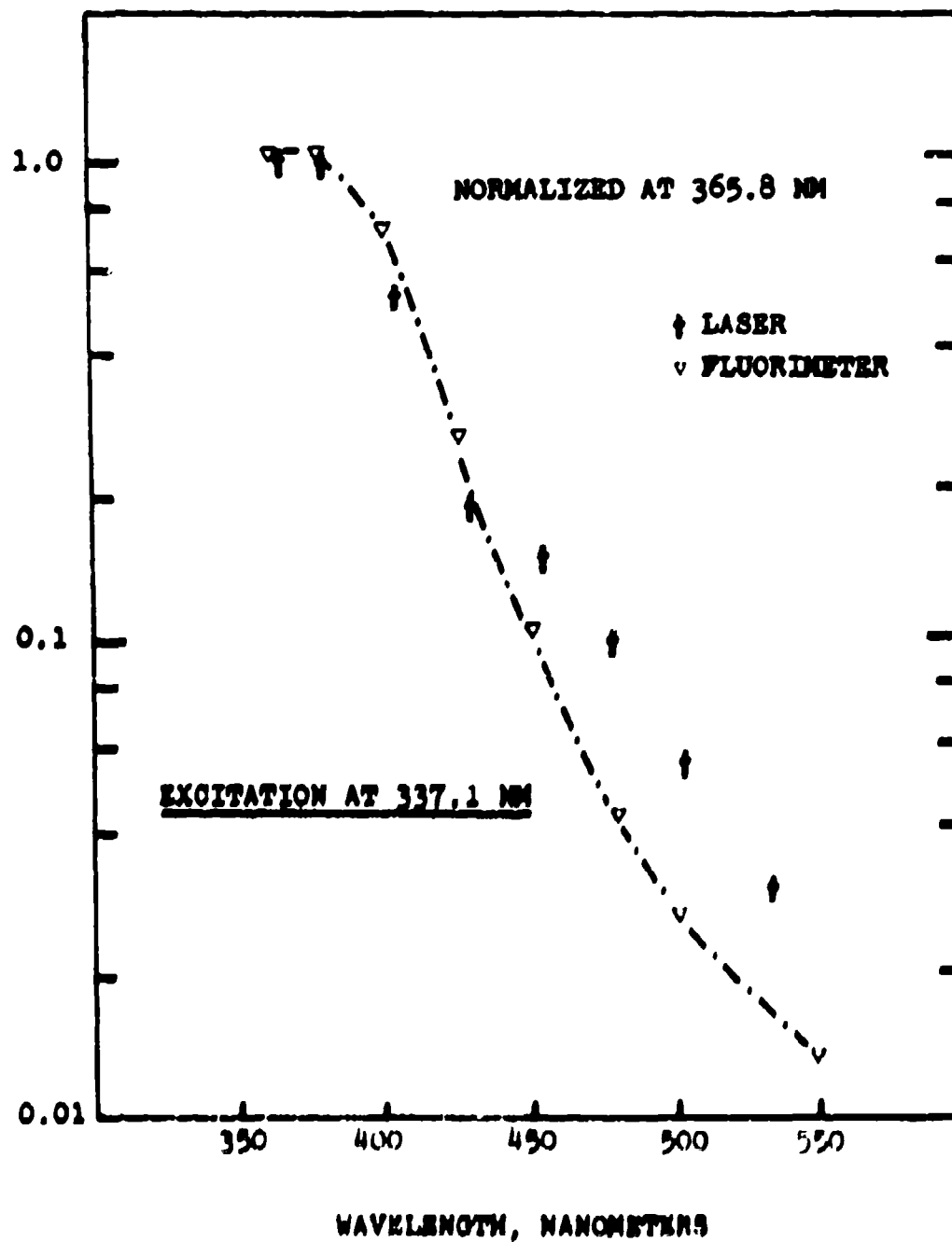


Figure 4. Excitation Spectrum of Synthetic Lubricant for Emission at 350 nm.



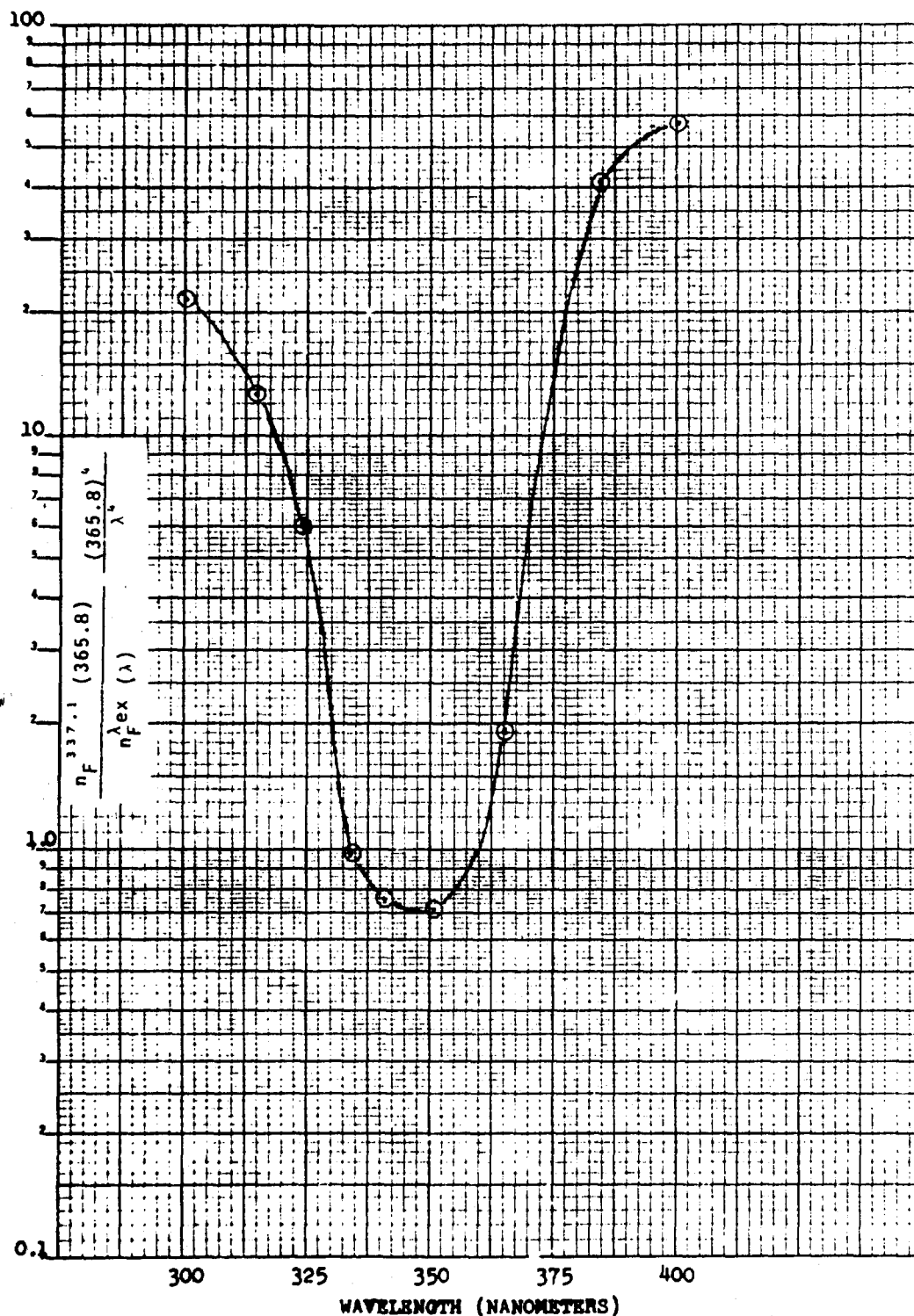


Figure 6. Variation of Projected Ratio of Raman Signal to Fluorescence Interference Due to Synthetic Lubricant.

APPENDIX II

SIGNAL-TO-NOISE CALCULATIONS

This appendix summarizes calculations which show the scaling of the signal-to-noise for laser induced noise such as fluorescence. The limiting noise is assumed in the calculation to be the "shot noise" in the laser induced signal itself. This was confirmed during the experimental test program.

Consider two detection gates, a signal gate and a background gate, each of width τ . The signal detection is synchronized to be coincident with the laser pulse which is also of width τ . The background detection is opened in between the signal gates at a time when the laser pulse is not present.

Let $B\tau/h\nu$ = counts appearing in each background gate and let $B\tau/h\nu + \eta E/h\nu$ = counts appearing in each signal gate where E is the transmitted laser energy per pulse, η is the overall transmitter/receiver efficiency and B is the background noise.

If we integrate for n pulses then the signal $S = n$ (signal gate - background gate) = $n\eta E/h\nu$. The sum of the fluctuations in the two gates is the noise $N = [n(\text{signal gate} + \text{background gate})]^{1/2}$.

Therefore the signal-to-noise ratio S/N is:

$$S/N = \frac{n\eta E/h\nu}{\sqrt{n\left(\frac{\eta E}{h\nu} + \frac{2B\tau}{h\nu}\right)}}$$

or

$$(S/N)^2 = \frac{n\eta E}{h\nu} \frac{1}{1 + \frac{2B\tau}{n\eta}}$$

If the time to make a single measurement is written as $T = n/R$ where R is the laser pulse repetition rate then the above expressions can be rewritten in terms of T and the various laser powers as follows:

$$\left(\frac{S}{N}\right)^2 = \frac{\eta}{h\nu} T P_{AVE} \left[\frac{1}{1 + \frac{2 P_{NEP}}{P_{PK}}} \right]$$

∴ for a given S/N the time to generate a data point is

$$T = \frac{h\nu}{\eta} \left(\frac{S}{N}\right)^2 \frac{1}{P_{AVE}} \left[1 + \frac{2 P_{NEP}}{P_{PK}} \right]$$

where P_{AVE} = average laser power = ER

P_{PK} = peak laser power = E/τ

P_{NEP} = background noise equivalent power = B/η .

In general the following three conditions apply:

I. $P_{PK} \ll P_{NEP}$ i.e., background noise limited

$$\begin{aligned} T &= \frac{2h\nu P_{NEP}}{\eta} \left(\frac{S}{N}\right)^2 \frac{1}{P_{PK} P_{AVE}} \\ &= \frac{2h\nu P_{NEP}}{\eta} \left(\frac{S}{N}\right)^2 \frac{1}{P_{RMS}^2} \end{aligned}$$

(Note: The laser used in the field experiments described in this report has an RMS power of $(0.5 \times 10^5)^{1/2} = 220$ watts based on an average power of 0.5 watts and a peak power of 10^5 watts.)

II. $P_{PK} \gg P_{NEP}$ i.e., shot noise limited

$$T = \frac{h\nu}{\eta} \left(\frac{S}{N}\right)^2 \frac{1}{P_{AVE}}$$

III. $P_{PK} < \frac{h\nu}{\eta\tau} \left(\frac{S}{N}\right)^2$ not noise limited

$$T = \frac{1}{R}$$

Laser Induced Background (i. e., Fluorescence)

Assumptions:

1. Fluorescence is broad in wavelength compared to the Raman spectrum.
2. Ambient background is "white".

Introduce a wavelength shifted gate coincident in time with the laser pulse. Define F equal to fluorescence to Raman ratio.

$B_T/h\nu + F\eta E/h\nu =$ counts appearing in each wavelength shifted background gate.

$B_T/h\nu + F\eta E/h\nu + \eta E/h\nu =$ counts appearing in each signal gate.

Integrating for n pulses:

$$S = n (\text{signal gate} - \text{background gate}) = n\eta E/h\nu$$

$$N = [n (\text{signal gate} + \text{background gate})]^{1/2}$$

$$S/N = \frac{n\eta E/h\nu}{\sqrt{n \left[\frac{(2F + 1) \eta E}{h\nu} + \frac{2B_T}{h\nu} \right]}}$$

$$\left(\frac{S}{N}\right)^2 = \left(\frac{n\eta E}{h\nu}\right)^2 \frac{1}{(2F + 1) + \frac{2B_T}{h\nu}}$$

$$T = \frac{h\nu}{\eta} \left(\frac{S}{N}\right)^2 \frac{1}{P_{AVE}} \left[2F + 1 + \frac{2 P_{NEP}}{P_{PK}} \right]$$

In the limit of $P_{PK} \gg P_{NEP}$ (shot noise limit)

$$T = \frac{h\nu}{\eta} \left(\frac{S}{N}\right)^2 \frac{1}{P_{AVE}} (2F + 1)$$

This equation was used to generate the scaling relations for NO detection shown in the chart of Figure 35.

APPENDIX III

DEVELOPMENT OF A LASER RAMAN AIRCRAFT
TURBINE ENGINE EXHAUST EMISSIONS
MEASUREMENT SYSTEM

TECHNICAL REPORT
(Final - Conceptual Design Finalization)

Contract F33615-71-C-1875

RESEARCH NOTE 914

DEVELOPMENT OF A LASER RAMAN AIRCRAFT TURBINE
ENGINE EXHAUST EMISSIONS MEASUREMENT SYSTEM

TECHNICAL REPORT

(Final - Conceptual Design Finalization)

by

Donald A. Leonard

prepared by

AVCO EVERETT RESEARCH LABORATORY
a division of
AVCO CORPORATION
Everett, Massachusetts

May 1972

Contract F33615-71-C-1875

prepared for

AIR FORCE AERO PROPULSION LABORATORY
AIR FORCE SYSTEMS COMMAND
UNITED STATES AIR FORCE
Wright-Patterson Air Force Base, Ohio

FOREWORD

The Avco Everett Research Laboratory, a Division of Avco Corporation has prepared this Conceptual Design Technical Report on Contract F33615-71-C-1875. This report contains no classified information.

The program is being sponsored by the Air Force Aero Propulsion Laboratory, Wright-Patterson Air Force Base, as part of the Air Force effort to comply with the President's Executive Orders 11507 and 11514 calling for an improvement in environmental quality. The Program Monitors for the Air Force have been Captain Donald Champagne and Lt. William Blazowski.

The author of this report was Mr. Donald A. Leonard, who is the Program Manager for Avco for this program.

ABSTRACT

The work described in this report represents the first six months of a research and development effort, the goal of which is to demonstrate an experimental prototype of a measurement system based on laser Raman spectroscopy. The conceptual design is based upon earlier work as well as continuing research results obtained from this six months of Air Force sponsored work.

The physical property of turbine exhausts that most significantly influences Raman spectroscopic analysis is the relatively low pollutant concentrations in combination with elevated temperatures such that significant upper level excitations occur with subsequent broadening and overlapping of the Raman spectra. This report describes the necessary basic Raman spectroscopy as it relates to turbine exhaust analysis, including cross-sections, temperature dependence and possible interferences.

Experiments were performed at elevated temperatures in a propane exhaust to actually measure Raman spectra and make comparisons with theoretical calculations. Good agreement was obtained between the theory and the experiments. Comparison data, both theoretical and experimental, is presented for CO_2 and N_2 at 300°K and 1000°K .

The report also describes the engineering considerations leading to the conceptual design including laser, monochrometer, transmitter and receiver optics, the electronics and calibration methods, and environmental problem areas, especially the high acoustic levels to be encountered.

TABLE OF CONTENTS

	<u>Page</u>
Foreword	i
Abstract	iii
List of Illustrations	vii
List of Tables	ix
I. INTRODUCTION AND SUMMARY	1
II. RAMAN SPECTROSCOPY OF COMBUSTION GASES	3
1. BASIC THEORY	3
2. CROSS SECTIONS	5
3. THEORETICAL CALCULATION OF SPECTRA	11
4. EXPERIMENTAL MEASUREMENTS OF SPECTRA	23
5. TEMPERATURE SENSITIVITY	32
6. INTERFERENCE EFFECTS	36
III. ENGINEERING CONSIDERATIONS	45
1. TRADEOFF DISCUSSION LEADING TO CONCEPTUAL DESIGN	45
2. CONCEPTUAL SYSTEM DESIGN DETAILS	50
REFERENCES	69

LIST OF ILLUSTRATIONS

<u>Figure</u>		<u>Page</u>
1	Potential Energy Diagram for Diatomic Molecule Undergoing Vibrational Raman Scattering	4
2	Structure of the Vibrational Raman Band for N_2 at $T = 300^\circ K$ Using a 3371 \AA Laser as a Source	6
3	Typical Raman Spectrum from Room Temperature Combustion Gases Using a 3371 \AA Laser Source	7
4	Computed Raman Intensity for Nitrogen as a Function of Wavelength at a Temperature of $300^\circ K$ as would be observed by a Detector having a Resolution of 1 \AA	14
5	Computed Raman Intensity for Nitrogen as a Function of Wavelength at a Temperature of $600^\circ K$ as would be observed by a Detector having a Resolution of 1 \AA	15
6	Computed Raman Intensity for Nitrogen as a Function of Wavelength at a Temperature of $800^\circ K$ as would be observed by a Detector having a Resolution of 1 \AA	16
7	Computed Raman Intensity for Nitrogen as a Function of Wavelength at a Temperature of $900^\circ K$ as would be observed by a Detector having a Resolution of 1 \AA	17
8	Computed Raman Intensity for Nitrogen as a Function of Wavelength at a Temperature of $1000^\circ K$ as would be observed by a Detector having a Resolution of 1 \AA	18
9	Computed Raman Intensity for Nitrogen as a Function of Wavelength at a Temperature of $1200^\circ K$ as would be observed by a Detector having a Resolution of 1 \AA	19
10	Computed Raman Intensity for Nitrogen as a Function of Wavelength at a Temperature of $1500^\circ K$ as would be observed by a Detector having a Resolution of 1 \AA	20
11	Computed Raman Intensity for Nitrogen as a Function of Wavelength at a Temperature of $2100^\circ K$ as would be observed by a Detector having a Resolution of 1 \AA	21
12	Computed Raman Intensity for Nitrogen as a Function of Wavelength at a Temperature of $3000^\circ K$ as would be observed by a Detector having a Resolution of 1 \AA	22

<u>Figure</u>		<u>Page</u>
13	Optical System used to Measure 90° Raman Scattering from Gas within a Closed Test Cell	24
14	Schematic of the Photon Counting Electronic Detection System	26
15	Experimental Raman Spectrum of Nitrogen at Room Temperature	27
16	Computed Raman Intensity for Nitrogen at $T=300^\circ$ (same as Figure 4) with Experimental Points taken from Figure 15	28
17	Experimental Raman Spectrum of Carbon Dioxide at Room Temperature	29
18	Experimental Raman Spectrum of Nitrogen at $\sim 1000^\circ\text{K}$ in a Propane/Air Burner Exhaust	30
19	Computed Raman Intensity for Nitrogen at $T=1000^\circ\text{K}$ (same as Figure 8) with Experimental Points taken from Figure 18	31
20	Experimental Raman Spectrum of Carbon Dioxide at $\sim 1000^\circ\text{K}$ in a Propane/Air Burner Exhaust	33
21	Computed Nitrogen Normalization Error as a Function of Temperature for a Detector with a Resolution of 1 \AA	34
22	Computed Carbon Dioxide Normalization Error as a Function of Temperature for a Detector with a Resolution of 1 \AA	35
23	The Computed Temperature Dependence of the Ratio of the Raman Scattering from the 010 Level of CO_2 to the Raman Scattering from the 000 Level of CO_2 .	37
24	The Fraction of Light Absorbed at 3371 \AA as a Function of NO_2 Concentration with Path Length in Meters as a Parameter	39
25	Computed Raman Intensity for Nitrogen at 1200°K (Same as Figure 9) and for Carbon Monoxide at 100 PPM Relative to Nitrogen. The use of polarized light to reduce the interference of N_2 with respect to CO is also shown.	40

<u>Figure</u>		<u>Page</u>
26	Experimental Raman Spectrum of Nitrogen at Room Temperature for both Unpolarized and Plane Polarized Laser Illumination	42
27	The Computed Ratio of Nitrogen Raman Scattering ($\Delta J=2$) at $\lambda = 3624 \text{ \AA}$ to Nitrogen Raman Scattering ($\Delta J=0$) at $\lambda = 3658 \text{ \AA}$	43
28	Schematic of Laser Raman Aircraft Engine Exhaust Emissions Measurement System	46
29	Function Block Diagram of System	52
30	Mode Controlled Pulsed Nitrogen Laser	55
31	Schematic of Transmitter and Receiver Optical System Details	56
32	Rectangular Laser Beam Image in Turbine Exhaust is Oriented to Sample the Maximum Number of Stream Lines and is Matched to Monochrometer Entrance Slit	57
33	Control and Display Front Panel	63
34	Acoustic Attenuation Characteristics of Equipment Shelters	65
35	Acoustic Levels Encountered from Typical Engine within and without Shelters	66

LIST OF TABLES

<u>Table</u>		
I	Raman Cross Section Data for Species of Interest	8
II	Relative Values of Cross-Sections	9
III	Conceptual System Parameters	53
IV	Transmitter/Receiver Characteristics	58

SECTION I

INTRODUCTION AND SUMMARY

This report describes the conceptual design of a Laser Raman Mode Aircraft Turbine Engine Exhaust Emissions Measurement System and is intended to satisfy the requirements of sequence number A008 of the Contract Data Requirements List of Contract F33615-71-C-1875 between the United States Air Force and the Avco Everett Research Laboratory (AERL).

The goal of Contract F33615-71-C-1875 is to demonstrate an experimental prototype of a measurement system based on laser Raman spectroscopy which will result in instrumentation which can be used for the Air Force to improve both the air quality of the environment and the performance of turbine engines.

The objective of the conceptual design presented herein is to show and describe all the relevant aspects of the AERL Laser Raman Turbine Exhaust Measurement System in sufficient detail so that an objective assessment can be made of the AERL design approach, as well as the general degree of usefulness and fitness for intended purpose of the Laser Raman Turbine Measurement Concept.

This conceptual design report divides naturally into two major areas of specialization: (1) The basic physical principles involved in the Raman spectroscopy of high temperature (i. e., 900 - 1200°K) combustion gases and (2) the engineering, design, construction and testing of a Raman spectrometer for turbine exhaust field use. However, the physical basis and the engineering design of any measurement system are usually very closely coupled, and therefore the interrelationship between the physics and engineering will be continually set forth throughout the discussion of the conceptual design.

Section II discusses the Raman spectroscopy of combustion gases in the specie concentration ranges and temperatures of interest with special attention paid to the questions of cross-sections, temperature dependence, specificity and interference. Both theoretical calculations and supporting experiments are included in this Section.

Section III is an engineering description of the AERL Laser Raman Spectrometer System for Turbine Exhaust Analysis as now currently conceived, including laser, transmitter/receiver optics, and detection electronics.

SECTION II

RAMAN SPECTROSCOPY OF COMBUSTION GASES

The physical property of turbine exhausts that most significantly influences Raman spectroscopic analysis is the relatively low pollutant concentrations in combination with elevated temperatures such that significant upper level excitations occur with subsequent broadening and overlapping of the Raman spectra. This section describes the necessary basic Raman spectroscopy as it relates to turbine exhaust analysis, including cross-sections, temperature dependence and possible interferences.

1. BASIC THEORY

The photon energies observed in Raman scattering correspond to the photon energy of the incident light shifted by an energy corresponding to some difference in allowed energy levels of the scattering molecule. The molecular energy shift can be either positive or negative, i.e., energy can be either subtracted from ("Stokes process") or added to ("anti-Stokes process") the incident photon.

A simplified potential energy diagram for a typical diatomic molecule undergoing a vibrational Stokes Raman scattering process is shown in Figure 1. In the general case, photons of energy $h\nu$ are incident on the molecule, which is originally in rotational level J_m of vibrational level V_k . Photons of energy $h\nu_{\text{RAMAN}}$ are scattered, and the molecule is left in the higher vibrational energy state V_e with rotational quantum number J_n . The difference in energy between the incident and scattered photons is exactly equal to the energy added to the molecule, i.e.,

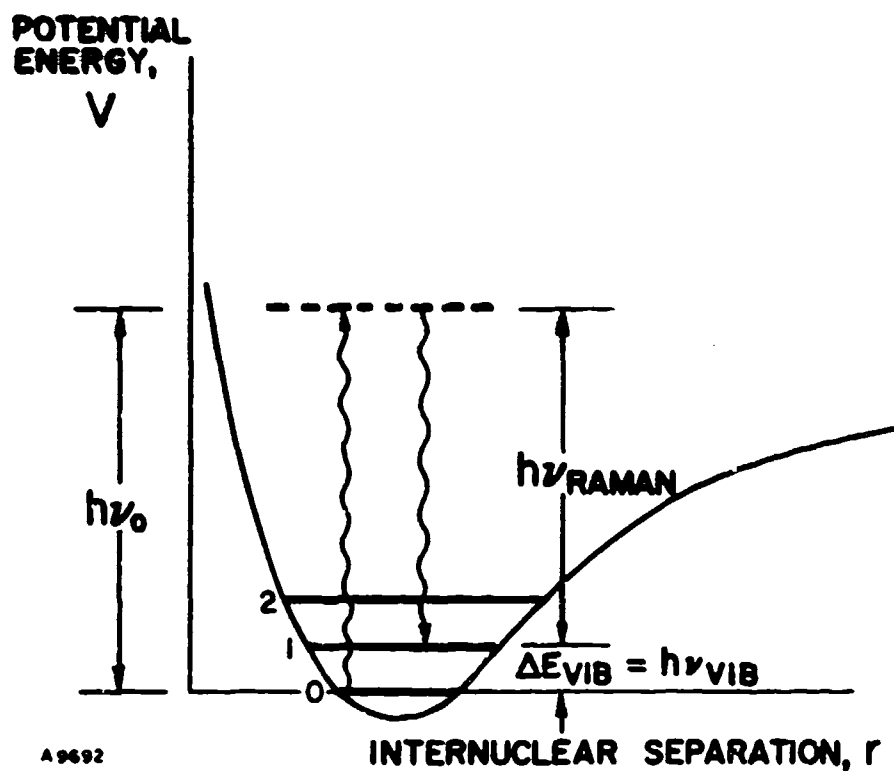
$$h\nu_o - h\nu_{\text{Raman}} = E(V_k, J_m) - E(V_e, J_n).$$

The rules governing which transitions among the levels in a molecule are allowed during Raman scattering are called "selection rules." The selection rules for a diatomic molecule are:

$$\Delta V = 0, \pm 1$$

$$\Delta J = 0, \pm 2$$

The same rules generally apply separately to each vibrational mode in polyatomic molecules, although special circumstances may act to modify the rules, e.g., "Fermi resonance" effects such as in CO_2 .



$$h\nu_{RAMAN} = h\nu_0 - \Delta E_{VIB}$$

Figure 1 Potential Energy Diagram for Diatomic Molecule Undergoing Vibrational Raman Scattering

At low temperatures all the lines having $\Delta J = 0$ lie very close to each other in energy and are not resolved except with very high resolution spectroscopy. The $\Delta J = +2$ transitions, however, are well separated in energy and appear as side bands on either side of the intense $\Delta J = 0$ line. Figure 2 is a schematic representation of the vibrational Raman scattering for molecular nitrogen at a temperature of 300°K excited with a 3371 Å pulsed nitrogen laser, showing the intense $\Delta J = 0$ line with much weaker side bands for the $\Delta J = -2$ and $\Delta J = +2$ transitions.

This figure was drawn for a temperature of 300°K with the assumption that the basic scattering cross-section for a $\Delta J = +2$ transition is 0.19 times as strong as a $\Delta J = 0$ transition, as indicated by a theoretical calculation by Sharma.⁽¹⁾ The exact magnitude of this cross-section is important for possible interference of the $\Delta J = -2$ branch of N_2 with the main $\Delta J = 0$ band of CO. An experiment to measure this cross-section is described in a following section of this report.

2. CROSS SECTIONS

The molecular species of importance for laser Raman turbine exhaust analysis are listed in Table I. The basic vibrational energy spacing, the wavelength at which the vibrational Raman scattering appears (assuming a 3371 Å pulsed nitrogen laser source) and the vibrational Raman scattering cross-section (i.e., the value for $\Delta J = 0$ at low temperatures) for each species currently being used by AERL in this program are also shown in this Table. The relative cross-section values listed in Table I can be compared with those recently presented by Lapp et al (GE)⁽²⁾ and Schwiesow (NOAA)⁽³⁾. This comparison is shown in Table II, where it is seen that the values are generally in agreement to a factor of two or better. The absolute values listed in Table I are all based on the value for nitrogen and are an order of magnitude smaller than those previously used by AERL in the baseline design for this program (see AERL Research Note 862).⁽⁴⁾ These current absolute values are now in close agreement with those of other workers (see Lapp et al,⁽²⁾ Fouche and Chang⁽⁵⁾ and Murphy).⁽⁶⁾ This decrease in the absolute value of the cross-sections reflects itself in the engineering of the device as a requirement for faster optics, $\sim f/4$ rather than $\sim f/7$, and more realistic numbers for optical and photo-electric efficiencies which had previously been conservatively rated (50%) due to previous disagreement between theoretically calculated and experimentally observed signals.

The absolute Raman signal strengths can be calculated for a given laser Raman transceiver system using the above cross-sections and such a calculation is performed in Section III of this report. In addition to absolute Raman signal strengths, the interference and possible overlap among the Raman scattering from the various molecular constituents of typical combustion products can also be estimated. Figure 3 shows schematically the Raman spectrum produced by combustion gases at 300°K (see next section of report for high temperature discussion), including the $\Delta J = \pm 2$ rotational lines shown as unresolved

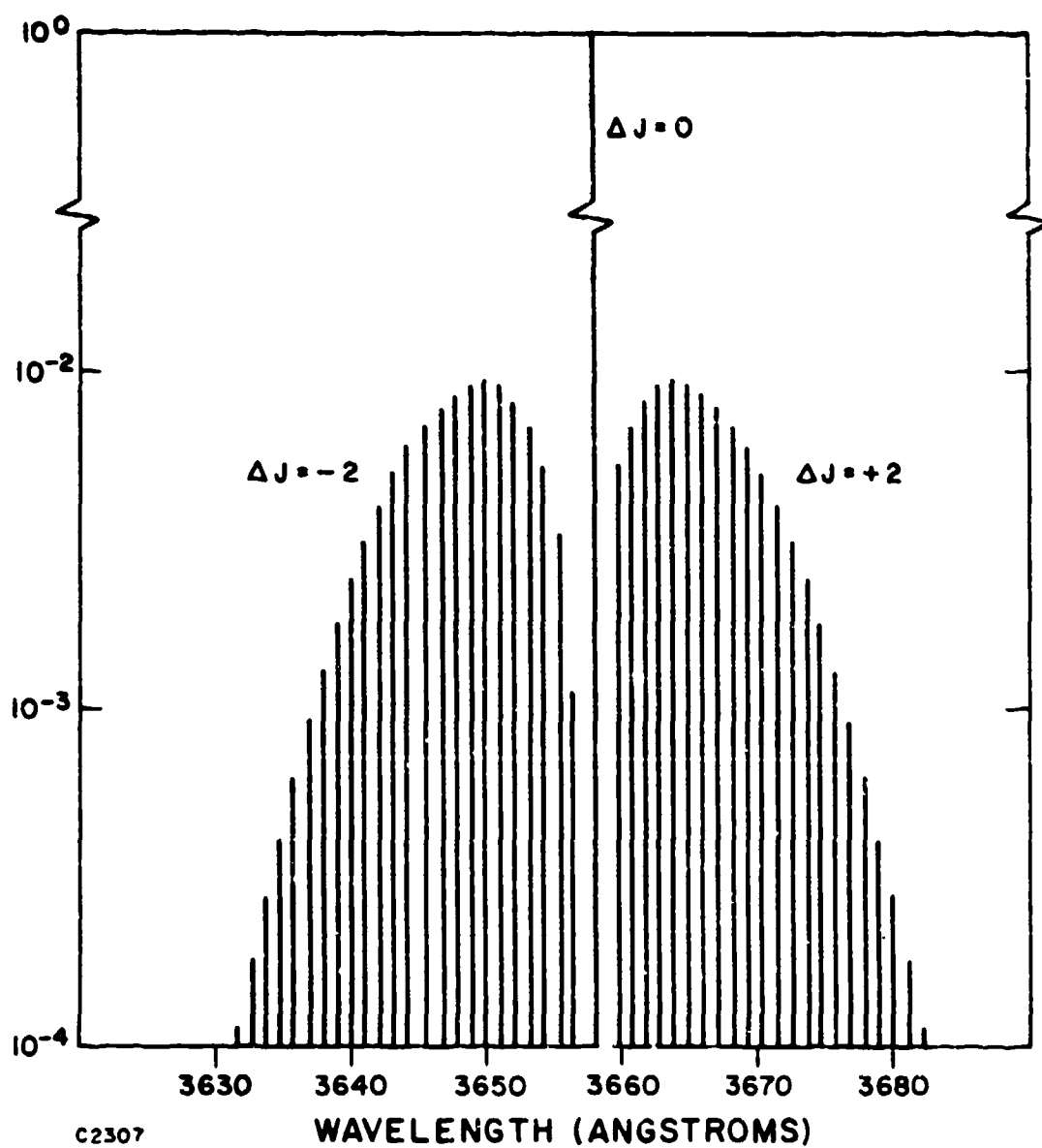


Figure 2 Structure of the Vibrational Raman Band for N_2 at $T=300^\circ K$
Using a 3371 Å Laser as a Source

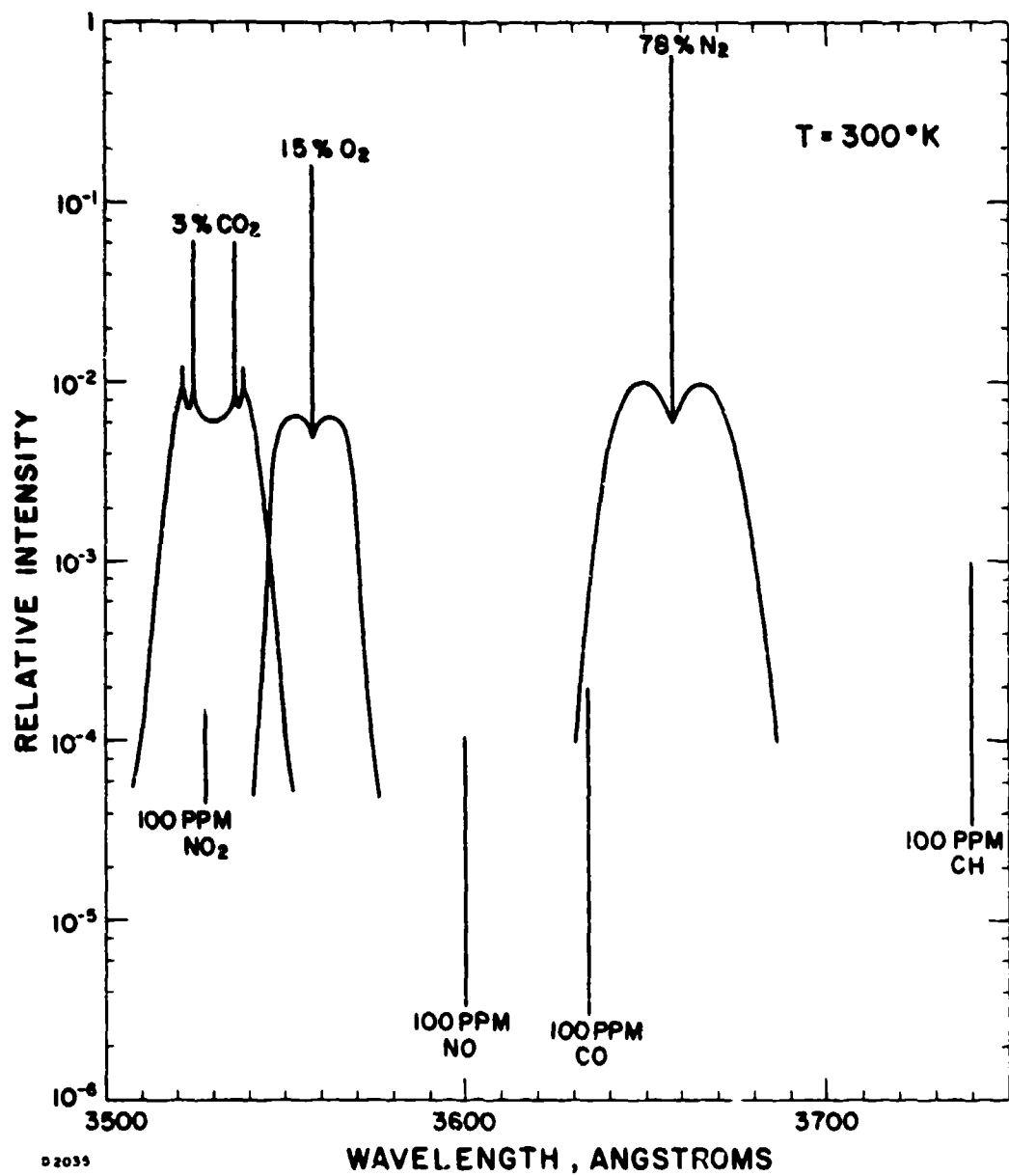


Figure 3 Typical Raman Spectrum from Room Temperature Combustion Gases Using a 3371 Å Laser Source

TABLE I

RAMAN CROSS SECTION DATA FOR SPECIES OF INTEREST

<u>Molecule</u>	<u>Vibrational Energy Spacing</u>	<u>Wavelength of Raman Scattering With 3371 Å Laser Source</u>	$\frac{\sigma_{\text{RAMAN}}}{\sigma_{\text{RAMAN}}(\text{N}_2)}$	<u>Absolute Cross-section</u>
SO ₂	1151 cm ⁻¹	3507 Å	2.4 (A)	4.8 x 10 ⁻³⁰ cm ² /ster
CO ₂	1286	3524	2.2 (B)	4.4 x 10 ⁻³⁰
	1388	3537	2.2	4.4 x 10 ⁻³⁰
O ₂	1556	3558	1.5 (C)	3.0 x 10 ⁻³⁰
NO ₂	1621	3566	not available *	
H ₂ CO	1744	3582	not available *	
NO	1876	3599	0.5 (D)	1.0 x 10 ⁻³⁰
CO	2143	3634	2.0 (E)	4.0 x 10 ⁻³⁰
N ₂	2330	3658	1.00	2.0 x 10 ⁻³⁰
CH	2920 (average)	3740	10 (F)	2.0 x 10 ⁻²⁹
H ₂ O	3652	3844	4.2 (G)	8.4 x 10 ⁻³⁰

(A), (D) Leonard, D.A., J. Appl. Physics 41, 4238 (1970).

(B) Derr, V., Wave Propagation Laboratory, NOAA, Boulder, Colorado,
Private Communication

(C) Widhopf and Ledermann, Polytechnic Institute of Brooklyn, Report No. 69-46.

(E), (F) Leonard, D. A., Unpublished results at AERL.

(G) Cooney, John, Drexel Institute of Technology,
Private Communication.

* The cross-sections if not yet available when needed will be measured by AERL as part of the program.

TABLE II

RELATIVE VALUES OF CROSS-SECTIONS *

<u>Gas</u>	<u>AERL</u>	<u>Lapp et al (GE) Palo-Alto (11/9/71)</u>	<u>Schwiesow (NOAA) Boulder Palo-Alto (11/9/71)</u>
N ₂	1.0	1.0	
O ₂	1.5	1.2	
NO	.50	.46	.36
CO	2.0	.96	
SO ₂	2.4	5.5	5.2
CO ₂	2.2	1.2	
CH ₄	10	8.2	
H ₂ O	4.2		3.0

* Normalized to N₂.

sidebands. The $\Delta J = 0$ components have been normalized to a signal of unit strength for N_2 in accordance with their concentration and scattering cross-section.

The $\Delta J = +2$ components for N_2 are shown in Figure 3 as previously described. The amplitude of the $\Delta J = +2$ components for the Raman lines of the other species are also shown approximately two orders of magnitude weaker than the corresponding $\Delta J = 0$ component. (See Figure 15 for experimental check.) The width of the various $\Delta J = +2$ components is, however, scaled proportional to the $1/2$ power of the rotational constant (B_e in Herzberg's notation)⁽⁷⁾ for each species.

The justification for this scaling can be seen by differentiating the expression for N_J , the number of molecules per rotational level.

$$N_J = \frac{1}{Q} (2J+1) e^{\frac{-BJ(J+1) 1.44}{T}}$$

$$\frac{dN_J}{dJ} = \frac{1}{Q} 2e^{\frac{-BJ(J+1) 1.44}{T}} - \frac{1.44B}{T} (2J+1)^2 e^{\frac{-BJ(J+1) 1.44}{T}}$$

and setting the derivative equal to zero and solving for J_{Max} as a function of B

$$J_{Max} = \frac{1}{2} \left(\frac{1.44T}{B} - 1 \right)$$

$$\lambda_0 - \lambda_{J_{Max}} = \Delta E \lambda_0^2 = B (4J+6) \lambda_0^2$$

$$\lambda_0 - \lambda_{J_{Max}} = BT$$

The widths of the $\Delta J = +2$ sidebands were scaled according to $B_e = 2.01, 1.44, .39, 9.5 \text{ cm}^{-1}$ for N_2, O_2, CO_2 and H_2O , respectively. (7)

3. THEORETICAL CALCULATIONS OF SPECTRA

As the temperature of the turbine exhaust gas under consideration is increased, the Raman spectra becomes more complex, the rotational $\Delta J = +2$ bands broaden, more $\Delta J = 0$ lines appear, and all $\Delta J = 0$ lines broaden into bands with slightly shifted peak values. These effects must be correctly taken into account if Raman scattering is to be used for quantitative analysis at elevated temperatures.

The physical basis for these effects is twofold: Firstly, as the temperature increases the populations of the various excited levels increase exponentially with temperature according to the appropriate Boltzman factor and degeneracy for the level in question. Secondly, because of the anharmonicity of molecular vibrational potentials and the vibration-rotation interaction the energy levels of the excited states are not uniformly spaced, as would be those of an isolated harmonic oscillator and rigid rotor.

Mathematically, the energy of a diatomic molecule in vibrational state (V) and rotational state (J) can be written in the following way (following the notation of Herzberg):⁽⁷⁾

$$E(V, J) = w_e \left(V + \frac{1}{2}\right) - w_e x_e \left(V + \frac{1}{2}\right)^2 + w_e y_e \left(V + \frac{1}{2}\right)^3 + \dots \text{(VIB.)}$$

$$+ B_e J(J+1) - D_e J^2(J+1)^2 \dots \text{(ROT.)}$$

$$- a_e \left(V + \frac{1}{2}\right) J(J+1) - \beta_e \left(V + \frac{1}{2}\right) J^2(J+1)^2 \text{(VIB-ROT.)}$$

As indicated, this represents the energy of level (V, J) as composed of three components, the vibrational energy written as an expansion in powers of $(V + 1/2)$, the rotational energy written as an expansion in powers of $J(J+1)$, and the vibration-rotation interaction energy written as an expansion in powers of $J(J+1)$ with $(V + 1/2)$ as a coefficient. For purposes of turbine exhaust analysis at the temperature range of interest (i.e., 900 - 1200°K) calculations have shown the terms with coefficients w_e , $w_e x_e$, B_e and a_e to be significant. Keeping only these significant terms, the energy absorbed by a diatomic molecule for $\Delta V = 1$ and $\Delta J = 0$ is

$$\begin{aligned}
E(V+1, J) - E(V, J) &= w_e \left(V + \frac{3}{2}\right) - w_e \left(V + \frac{1}{2}\right) \\
&- w_e x_e \left(V + \frac{3}{2}\right)^2 + w_e x_e \left(V + \frac{1}{2}\right)^2 + B_e J(J+1) \\
&- B_e J(J+1) - a_e \left(V + \frac{3}{2}\right) J(J+1) + a_e \left(V + \frac{1}{2}\right) J(J+1)
\end{aligned}$$

$$E(V+1, J) - E(V, J) = w_e - 2(V+1) w_e x_e - a_e J(J+1)$$

The two negative terms in this expression produce a smaller energy separation between the laser line and the Raman lines thus producing a shift toward shorter wavelengths (a spectral "blue shift") of the Raman spectrum. These negative terms become increasingly important as the temperature is raised and levels corresponding to higher values of V and J become increasingly populated.

Again keeping only the significant terms, the energy change for $\Delta V = 1$ and $\Delta J = \pm 2$ is:

$$\begin{aligned}
E(V+1, J \pm 2) - E(V, J) &= w_e \left(V + \frac{3}{2}\right) - w_e \left(V + \frac{1}{2}\right) \\
&- w_e x_e \left(V + \frac{3}{2}\right)^2 + w_e x_e \left(V + \frac{1}{2}\right)^2 \pm \left\{ \frac{B_e (J+2)(J+3)}{B_e (J-2)(J-1)} \right\} \\
&- B_e J(J+1)
\end{aligned}$$

$$E(V+1, J \pm 2) - E(V, J) = w_e - 2(V+1) w_e x_e \pm 4 B_e \left(J + \frac{1}{2} \pm 1\right)$$

The above expressions together with the selection rules determine the spectral positions of the various possible vibrational Raman transitions. The strengths of the transitions are given by the following expressions:

$$\underline{\Delta J = 0}$$

$$S(V, J) \sim \sigma(V+1) N(V, J)$$

$$\underline{\Delta J = \pm 2}$$

$$S(V, J) \sim 0.19 \sigma(V+1) N(V, J)$$

where σ is the vibrational Raman cross-section listed in Table I.

The factor 0.19 was calculated by Sharma for N_2 as previously discussed. Experiments, conducted at AERL, and described later in this report, have measured this factor to be 0.10 for N_2 .

Calculations were carried out using an IBM 370/145 computer which clearly illustrate the aforementioned temperature effects. Nitrogen is used in the following discussion as the illustrative example. Detailed knowledge of the nitrogen spectrum is especially important because of its use in the laser Raman turbine exhaust measurement system as a natural in-site calibration gas and also because of the serious overlap of the nitrogen spectrum with carbon monoxide.

The results of the calculations are illustrated in Figures 4-12, which are computer plotted representations of the Raman scattering from molecular nitrogen as a function of wavelength. The plots in these figures cover a temperature range from $300^\circ K$ to $3000^\circ K$. A detector (monochromator) bandpass of $\Delta\lambda = 1 \text{ \AA}$ was used. The wavelength scale is drawn to correspond to a 3371 \AA pulsed nitrogen laser used as the excitation source, with the peak of the band occurring at approximately 3658 \AA . The ratio of the strength of $\Delta J = \pm 2$ to $\Delta J = 0$ transitions was 0.1 in these calculations.

The main features of the computed molecular nitrogen spectra are seen to be as follows. At the lowest temperatures in Figure 4 and Figure 5 the spectra are seen to consist essentially of a central maximum which contains the $V = 0$, $\Delta J = 0$ transitions, and two broad bands on either side which contain the $V = 0$, $\Delta J = \pm 2$ transitions. As the temperature increases higher lying rotational states are becoming increasingly populated and the $\Delta J = \pm 2$ side bands are seen to broaden with the maximum of the side band decreasing slightly and moving away from the central $\Delta J = 0$ peak.

At a temperature of $600^\circ K$ in Figure 5, a secondary central maximum is beginning to appear. This corresponds to Raman Stokes transitions from the $V = 1$ level (i.e., the first excited vibrational level).

As the temperature is further increased to $1000^\circ K$, as shown in Figure 8, a third central maximum appears which corresponds to Raman Stokes transitions from the $V = 2$ vibrational level. The wavelength separation between these central maxima is caused by the first anharmonic term in the expansion of the vibrational energy component of the level energy of a diatomic molecule, i.e., the term $w_e x_e (V + 1/2)^2$ which results in a "blue shift" contribution of $2(V + 1)w_e x_e$ to the Raman spectrum.

Also at about $1000^\circ K$ the effect of the $a_e J(J+1)$ energy term (i.e., the interaction of rotation with vibration) in producing a further "blue-shift" is also becoming apparent. The effect is to produce a distortion in the $\Delta J = 0$ maxima, shifting the peaks to slightly shorter

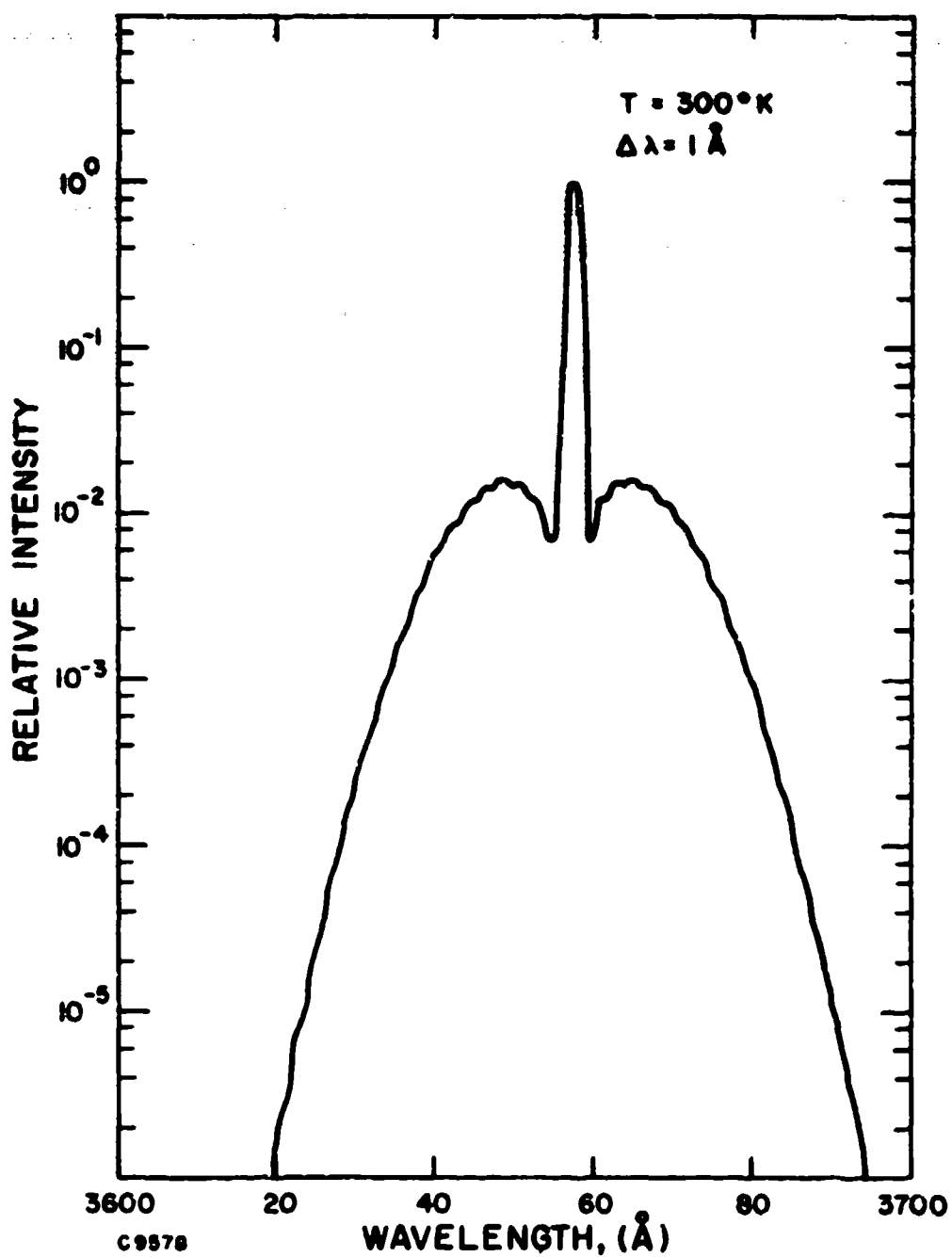


Figure 4 Computed Raman Intensity for Nitrogen as a Function of Wavelength at a Temperature of $300^\circ K$ as would be observed by a Detector having a Resolution of 1 \AA

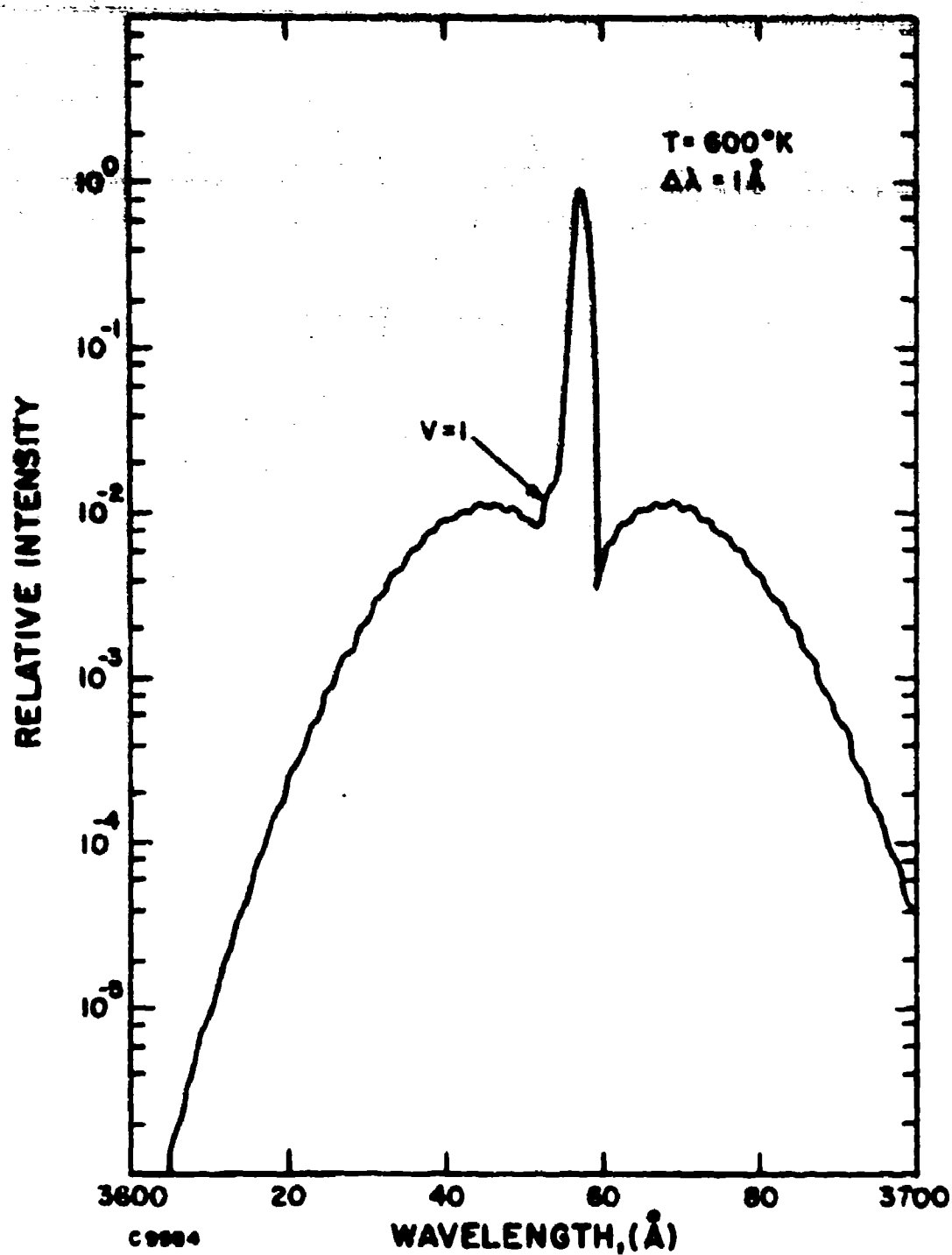


Figure 5 Computed Raman Intensity for Nitrogen as a Function of Wavelength at a Temperature of 600°K as would be observed by a Detector having a Resolution of 1 Å

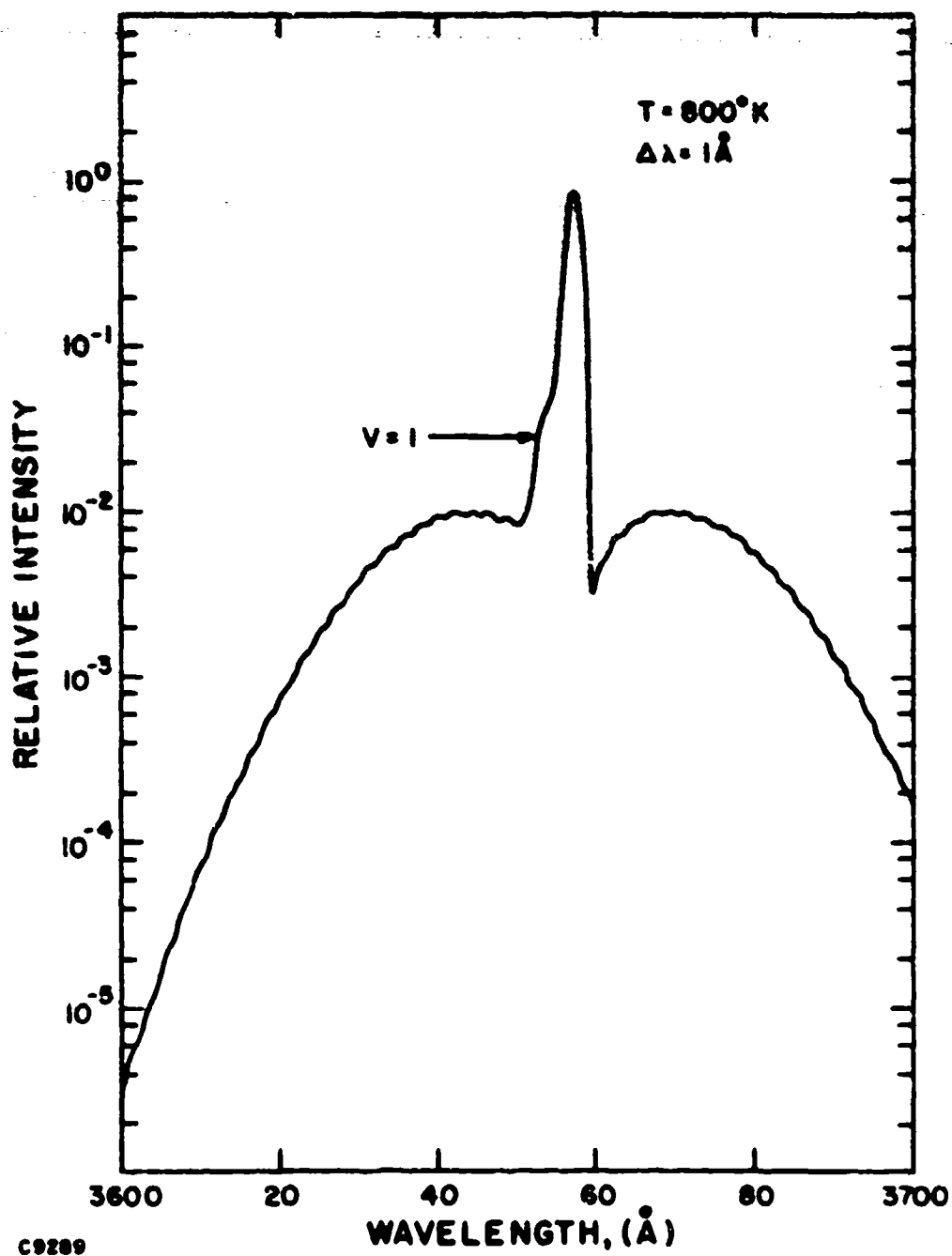


Figure 6 Computed Raman Intensity for Nitrogen as a Function of Wavelength at a Temperature of 800°K as would be observed by a Detector having a Resolution of 1 Å

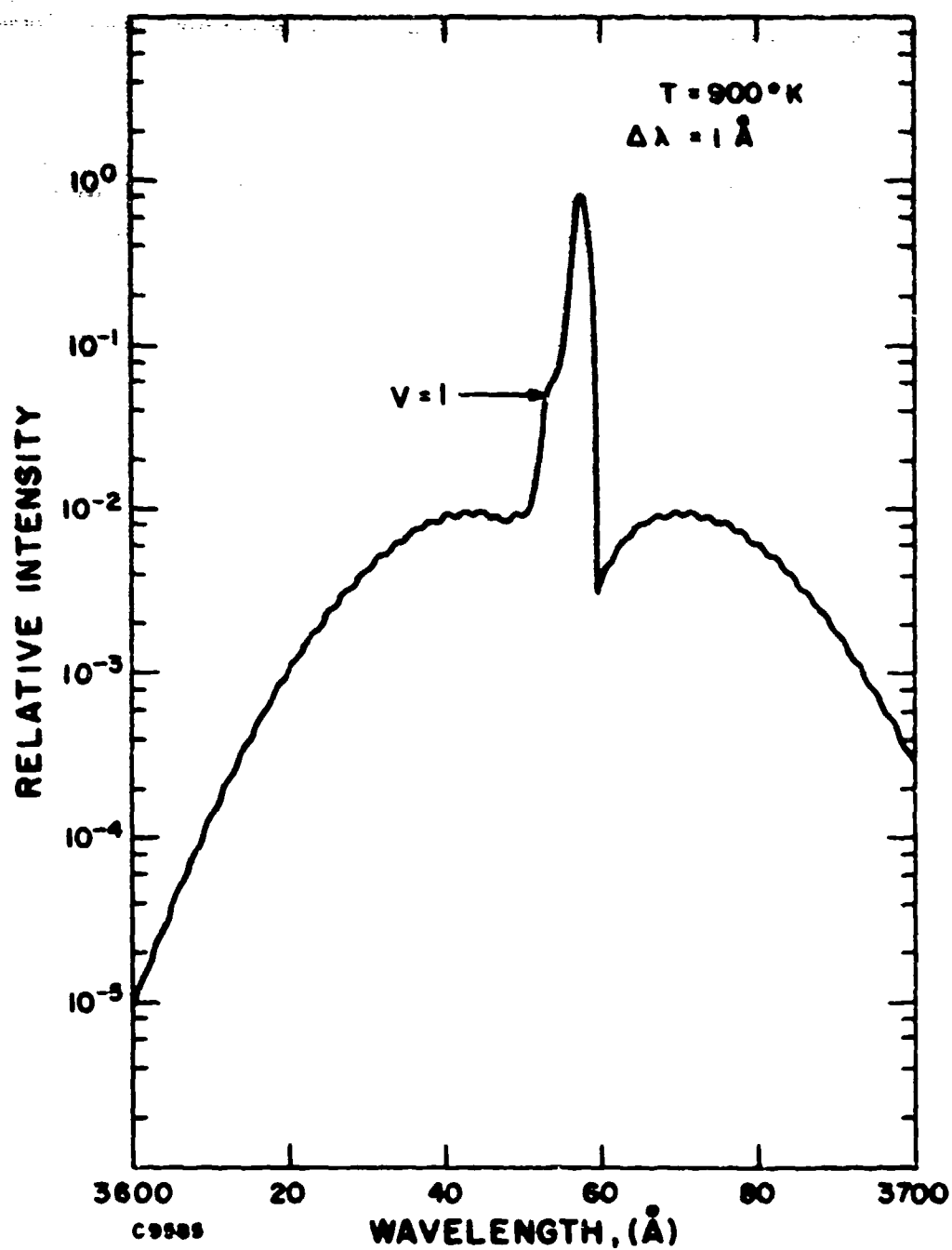


Figure 7 Computed Raman Intensity for Nitrogen as a Function of Wavelength at a Temperature of 900°K as would be observed by a Detector having a Resolution of 1 \AA

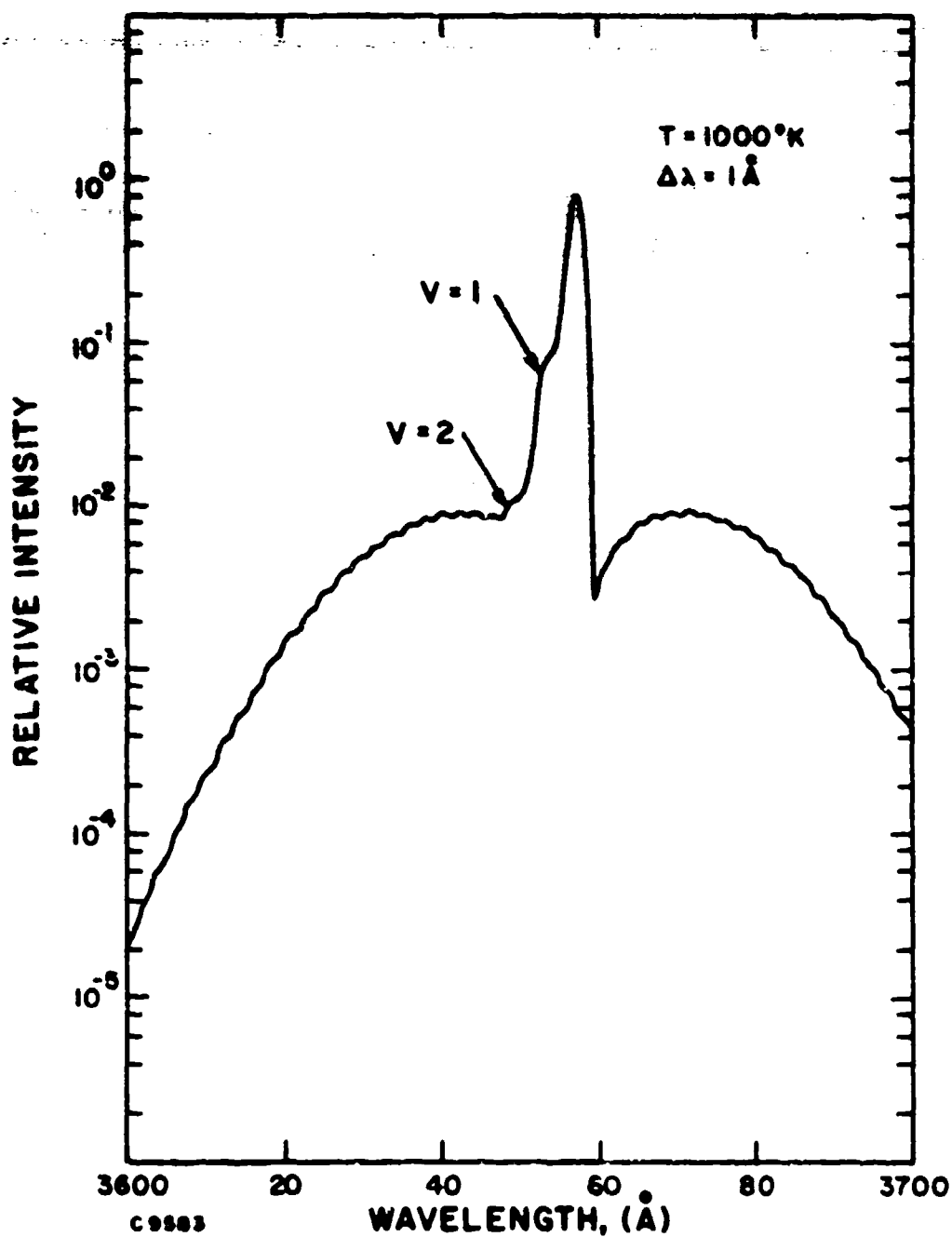


Figure 8 Computed Raman Intensity for Nitrogen as a Function of Wavelength at a Temperature of 1000°K as would be observed by a Detector having a Resolution of 1 \AA

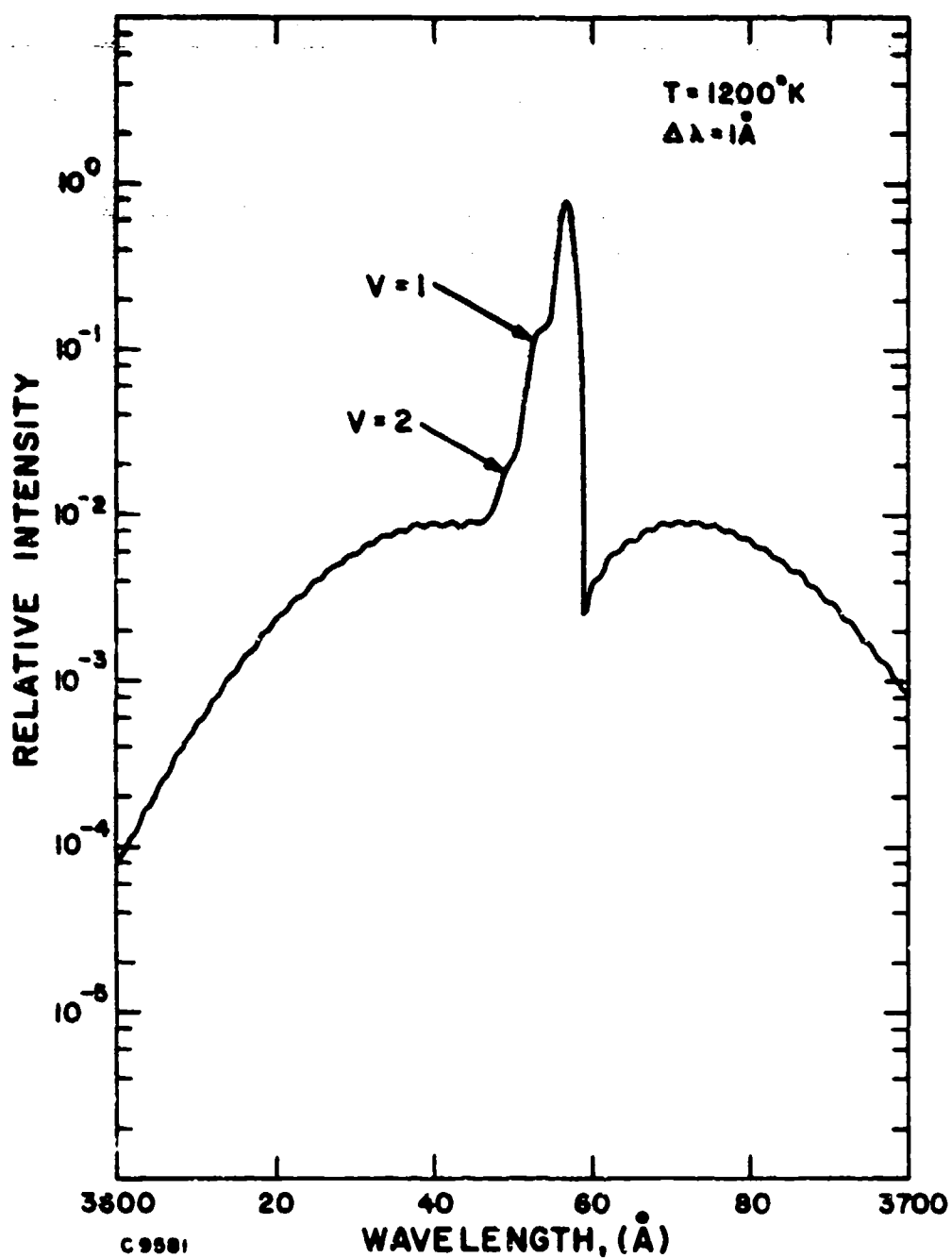


Figure 9 Computed Raman Intensity for Nitrogen as a Function of Wavelength at a Temperature of 1200°K as would be observed by a Detector having a Resolution of 1\AA

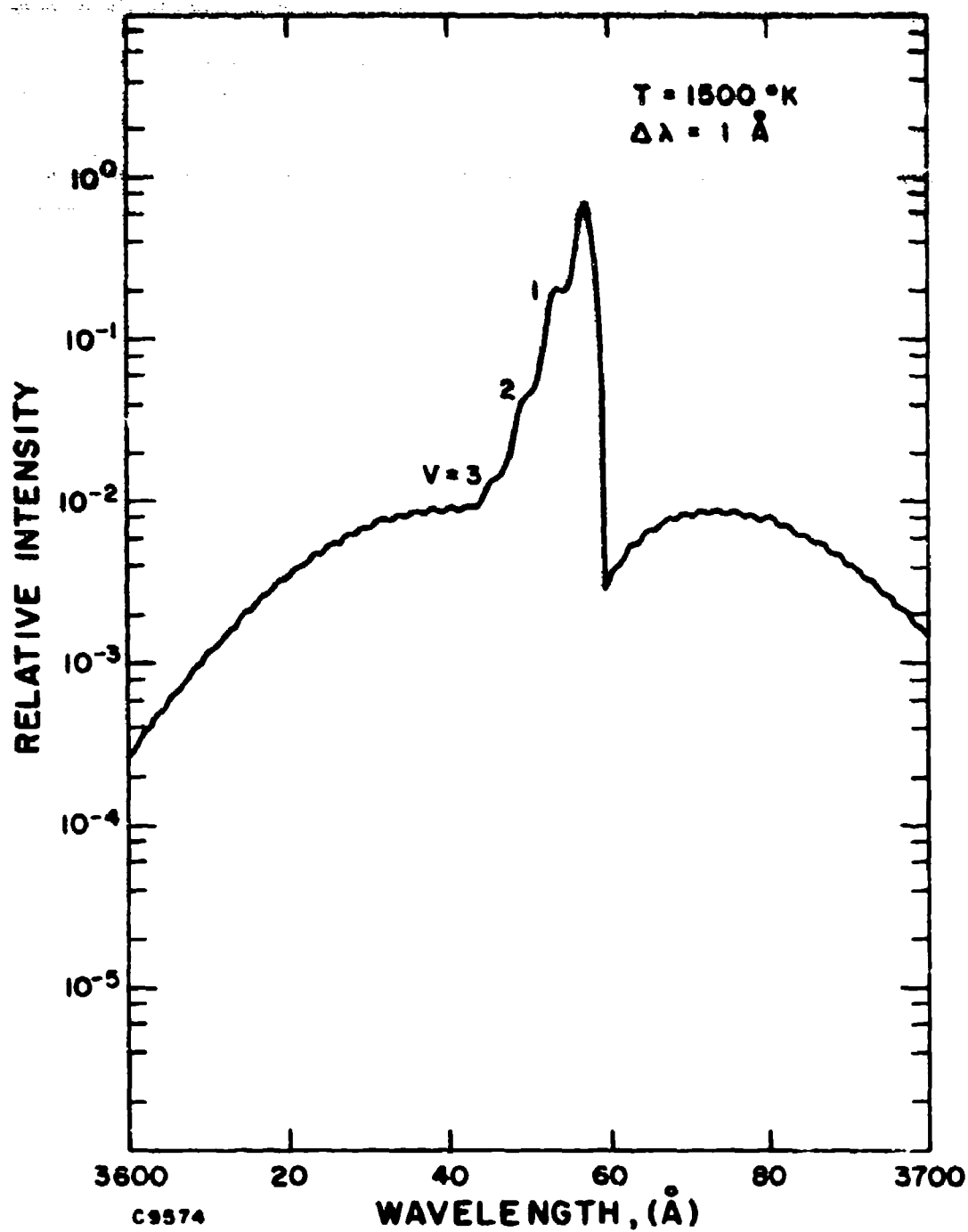


Figure 10 Computed Raman Intensity for Nitrogen as a Function of Wavelength at a Temperature of 1500°K as would be observed by a Detector having a Resolution of 1 \AA

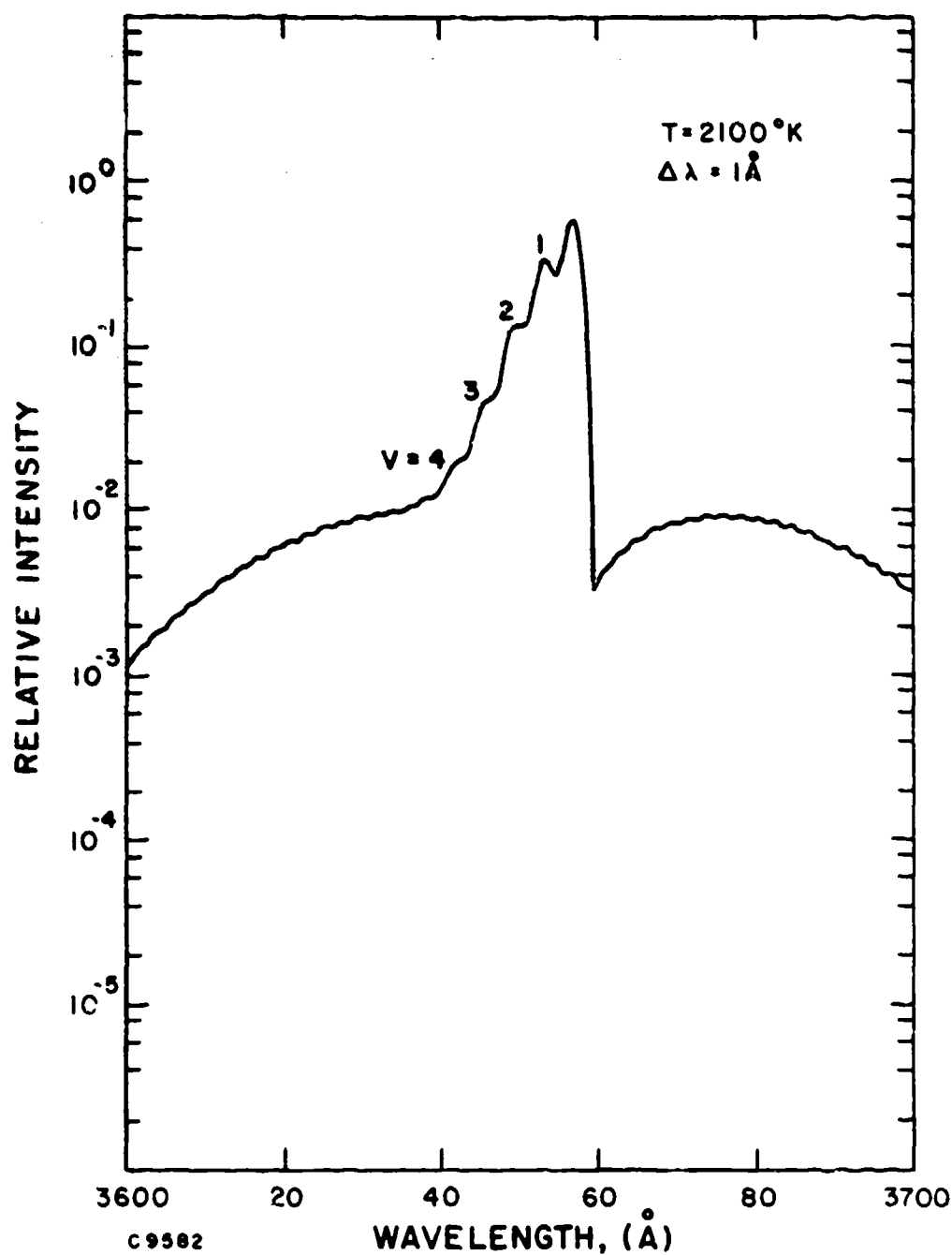


Figure 11 Computed Raman Intensity for Nitrogen as a Function of Wavelength at a Temperature of 2100°K as would be observed by a Detector having a Resolution of 1\AA

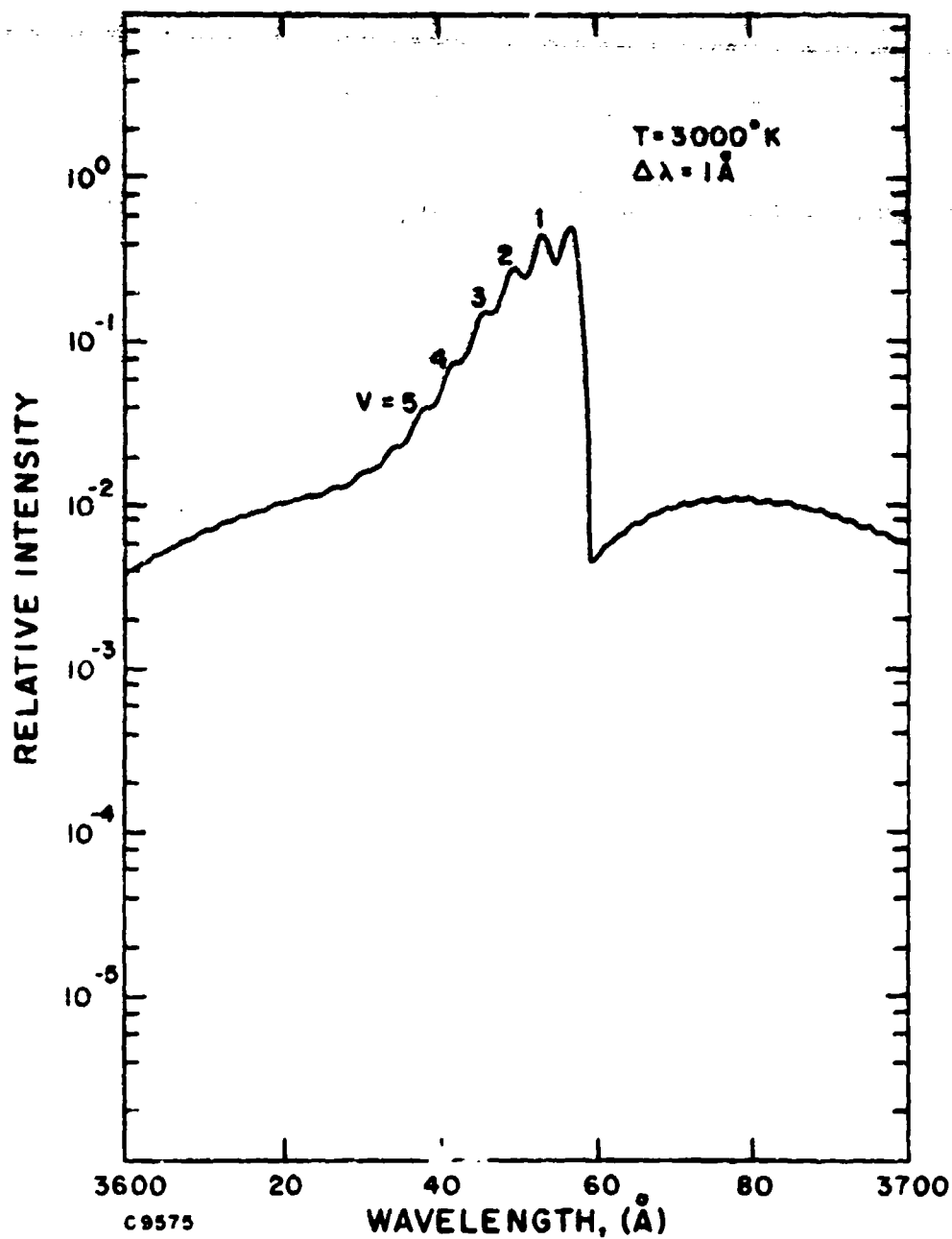


Figure 12 Computed Raman Intensity for Nitrogen as a Function of Wavelength at a Temperature of 3000°K as would be observed by a Detector having a Resolution of 1\AA

wavelengths and putting more integrated energy on the short wavelength side of the peak with a correspondingly steeper wavelength "cliff" on the long wavelength side of the peak.

As the temperature is further increased, the $\Delta J = + 2$ side bands broaden still further, more $\Delta J = 0$ maxima appear from higher vibrational levels and the effect of the $\alpha_e J(J+1)$ term in distorting and shifting the $\Delta J = 0$ maxima becomes more and more pronounced.

4. EXPERIMENTAL MEASUREMENTS OF SPECTRA

The Raman scattering cross-sections for the species of interest for turbine exhaust analysis have now been experimentally measured by several independent workers and the relative values are now known to a high degree of precision with a high confidence level. The absolute magnitude of Raman cross-sections is also now generally agreed upon to within a factor of two. However, what has been always measured and reported in the past for vibrational Raman scattering is the room temperature value ($T \sim 300^\circ\text{K}$) for the line which is the sum of the $\Delta J = 0$ transitions.

Several parameters of importance for the turbine exhaust analysis were not known to have been previously measured. Also the Raman spectra of the species of interest at high temperatures (i.e., $900\text{--}1200^\circ\text{K}$) while presumably calculable, were not known to have been previously recorded. The experiments were thus performed to both measure previously undetermined fundamental cross-sections and also to verify the theoretical predictions of the form of the Raman spectrum at elevated temperatures.

The experimental apparatus used is shown in Figure 13. An Avco Model C5000 3371 Å pulsed nitrogen laser emitting 100 kilowatt peak power pulses of 10 nanosecond duration at 500 pulses per second was used as the Raman light source. The laser beam was passed through an interference filter designed to pass the 3371 Å laser line but attenuate by more than three orders of magnitude the spontaneous emission occurring in the laser discharge channel at the same wavelengths as the Raman lines. The laser beam was then further spatially filtered and focused onto the test region.

The focal region in the test cell was imaged onto the entrance slit of a SPEX Model 1702 scannable spectrometer which was equipped with a Bausch & Lomb grating blazed at 3000 Å and guaranteed by the manufacturer to produce less than .01% stray light scattering. The exit slit of the spectrometer was focused onto an aperture placed in front of an RCA 8850 photomultiplier. A liquid filter consisting of a water solution of 2, 7-dimethyl-3, 6-diazacyclohepta-1, 6-diene perchlorate (DDDP) was placed adjacent to the lens. This filter has the property of essentially complete volume isotropic bulk absorption of the 3371 Å laser line and almost complete transparency in the Raman spectral region for wavelengths longer than 3500 Å. The use of a blocking

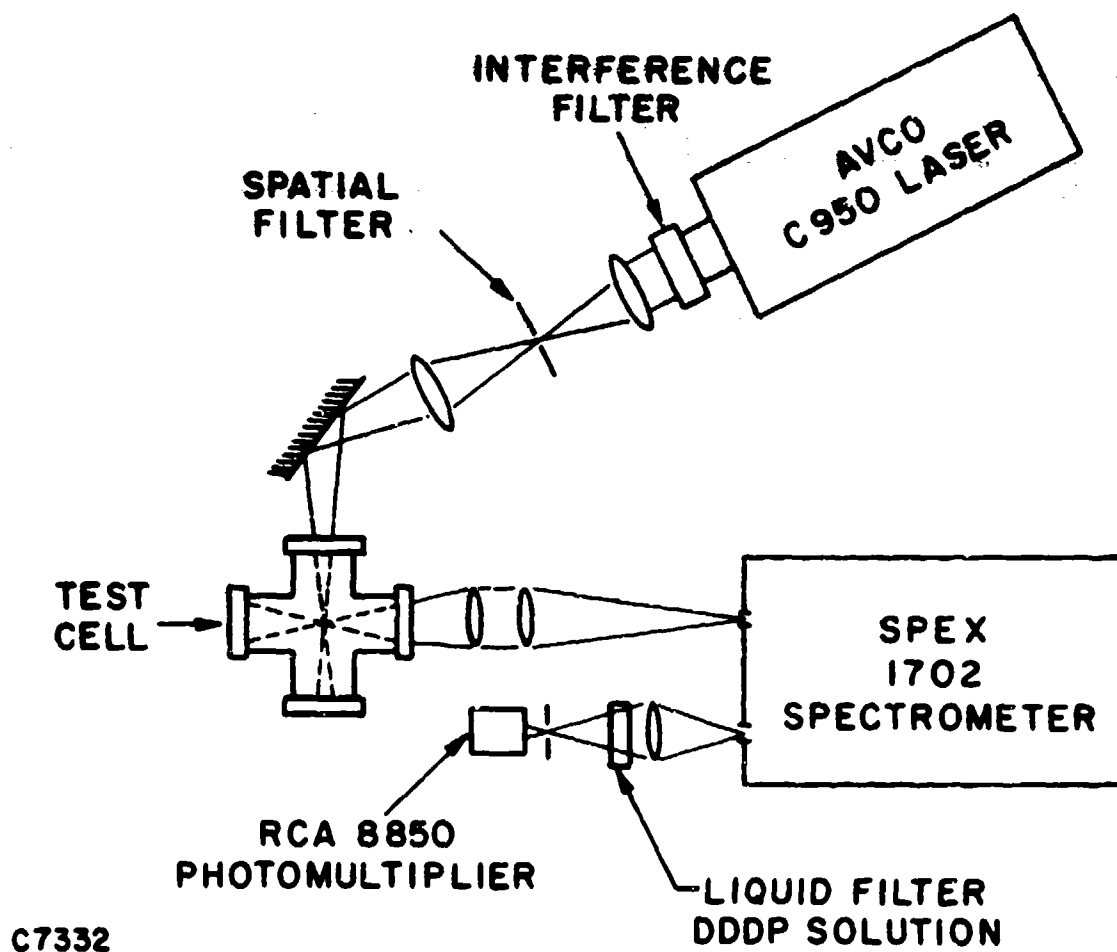


Figure 13 Optical System used to Measure 90° Raman Scattering from Gas within a Closed Test Cell

filter for the laser line simplified the spectrometer requirements and eliminated the need for a double spectrometer.

A schematic of the photon counting detection electronics is shown in Figure 14. The photoelectron pulses from the photomultiplier are passed into one input of an "AND" gate coincidence circuit. A 20 ns gate pulse is automatically synchronized with the laser and is passed into the other input of the coincidence circuit. If a photoelectron pulse occurs within the duration of the 20 ns gate pulse, the coincidence circuit is activated and produces a pulse which is counted by a counter. This circuit was originally designed for low light level work with Raman scattering from trace concentrations of gas pollutants where the condition 0 or 1 photoelectron is an adequate description of the signal being detected.

Room temperature experiments were conducted in room air to measure for nitrogen the ratio of the strength of the $\Delta J = 0$ transitions to the strength of the $\Delta J = +2$ transitions. The spectrum which was obtained for the nitrogen band centered on 3658 Å is shown in Figure 15, and has the general form predicted by theory. The position of the peak of the carbon monoxide (CO) Raman band is also indicated.

The detailed comparison between theory and experiment is shown in Figure 16, which combines the experimental data of Figure 15 with the corresponding theoretical calculation of Figure 4. The best overall agreement, as shown, occurs using 0.1 as the ratio of the strengths of $\Delta J = +2$ and $\Delta J = 0$ transitions. The remaining significant differences between theory and experiment will be investigated.

A further example of a room temperature Raman spectrum is shown in Figure 17, which is the spectrum of the CO₂ doublet at 1285 and 1388 wave numbers. Of special interest is the appearance of secondary peaks at 1265 and 1409 wave numbers which correspond to transitions from the lowest excited vibrational level of CO₂, the 010 level. This level is appreciably populated even at room temperature. Measurement of the ratio of the secondary to the primary peak is a sensitive means of temperature measurement throughout the temperature range of interest for turbine exhausts as will be shown later in this report.

Raman spectra at elevated temperatures were obtained from the exhaust of a propane/air burner. Figure 18 shows the measured spectrum of the nitrogen Raman band at 3658 Å at a temperature of 1000°K as measured with a thermocouple in the burner exhaust. The predicted features of the "blue shift" are clearly visible in this experimental spectrum. This verifies data presented by Lapp.⁽²⁾

The detailed comparison between theory and experiment is shown in Figure 19 which combines the experimental data of Figure 18 with the corresponding theoretical calculation of Figure 8. The agreement is seen to be generally good again verifying the overall calculational method and especially the ratio of 0.1 as an upper limit to the strength

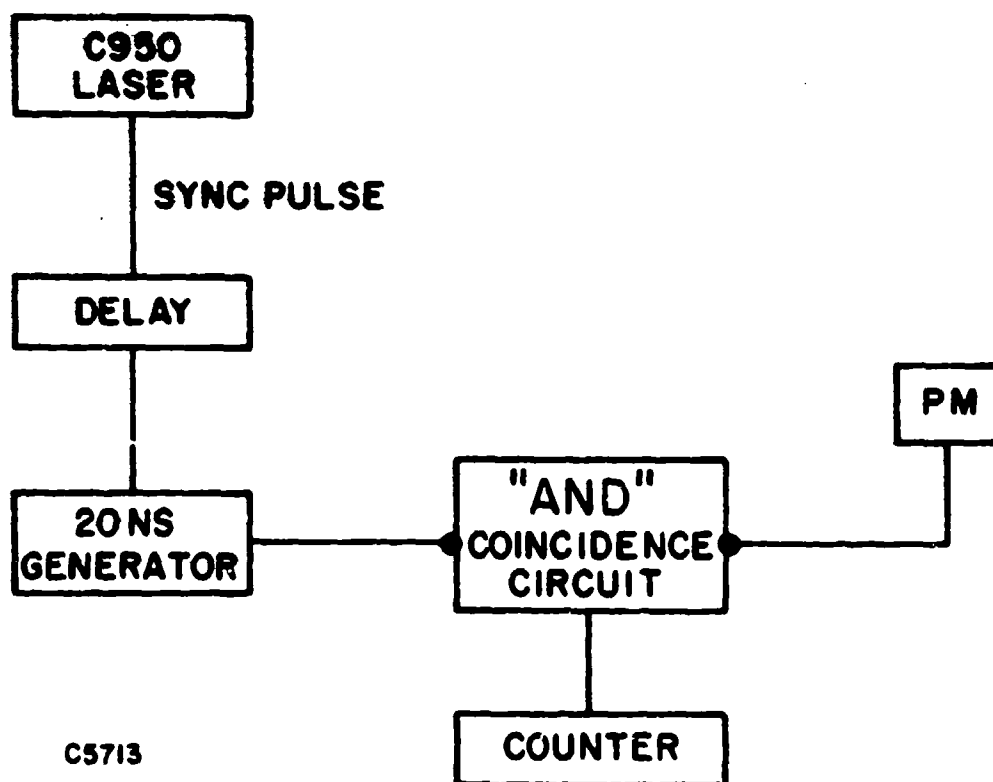


Figure 14 Schematic of the Photon Counting Electronic Detection System

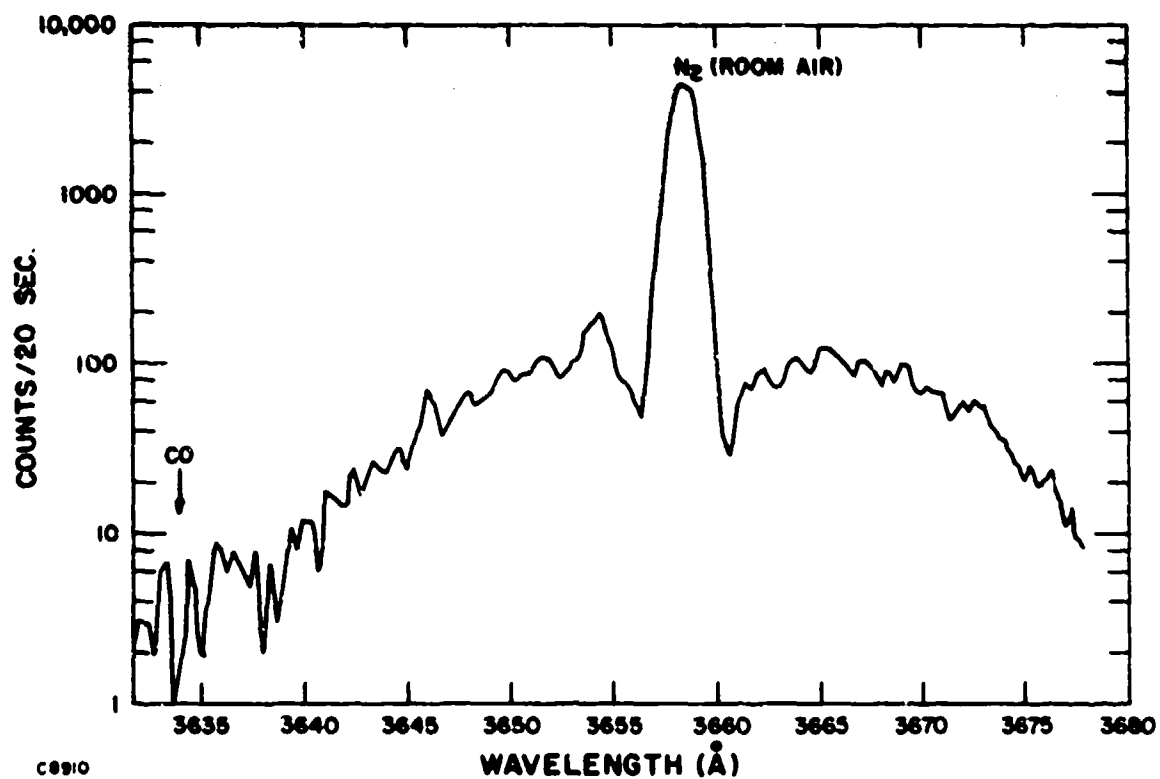


Figure 15 Experimental Raman Spectrum of Nitrogen at Room Temperature

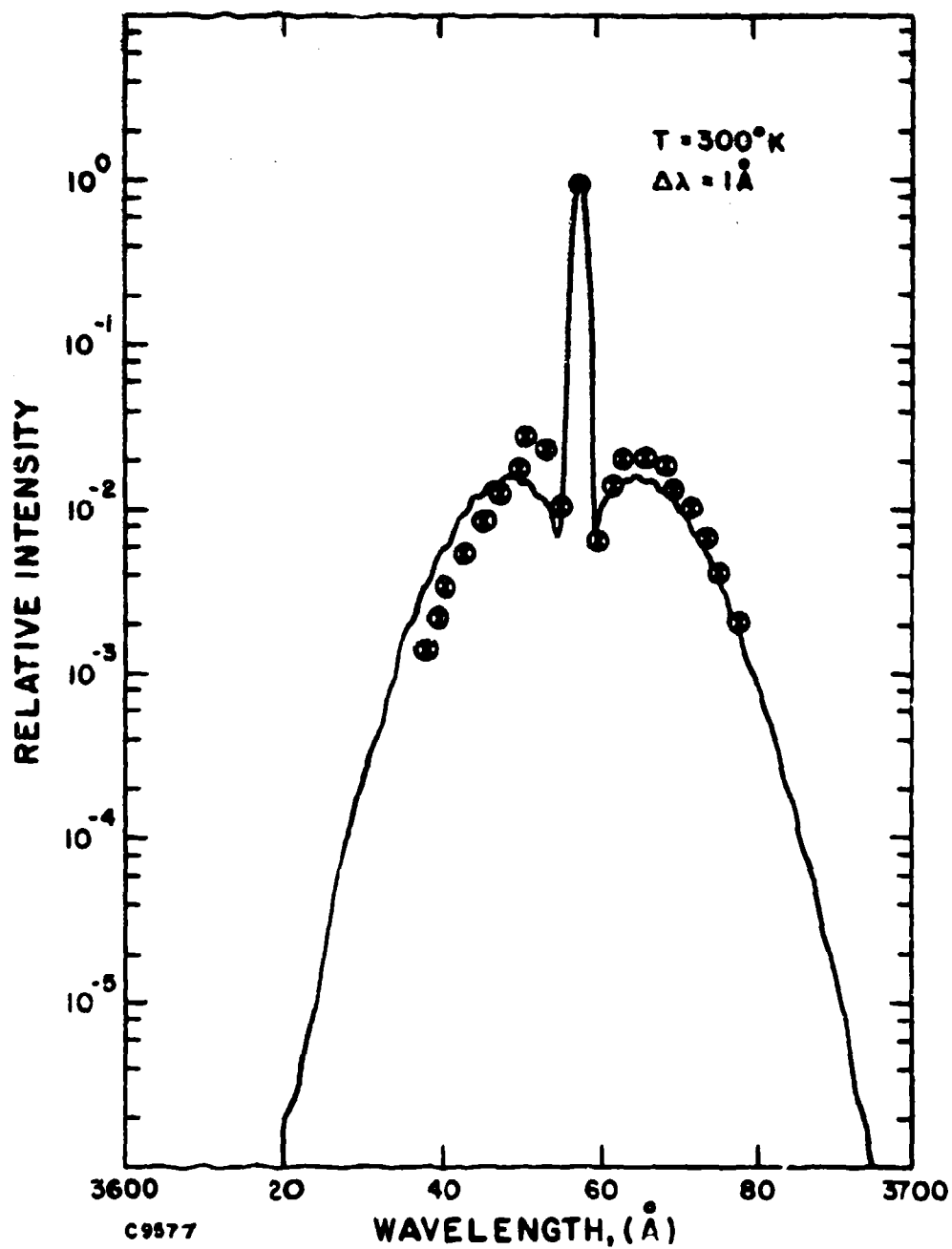


Figure 16 Computed Raman Intensity for Nitrogen at $T=300^{\circ}$ (same as Figure 4) with Experimental Points taken from Figure 15

CO₂ RAMAN SPECTRUM

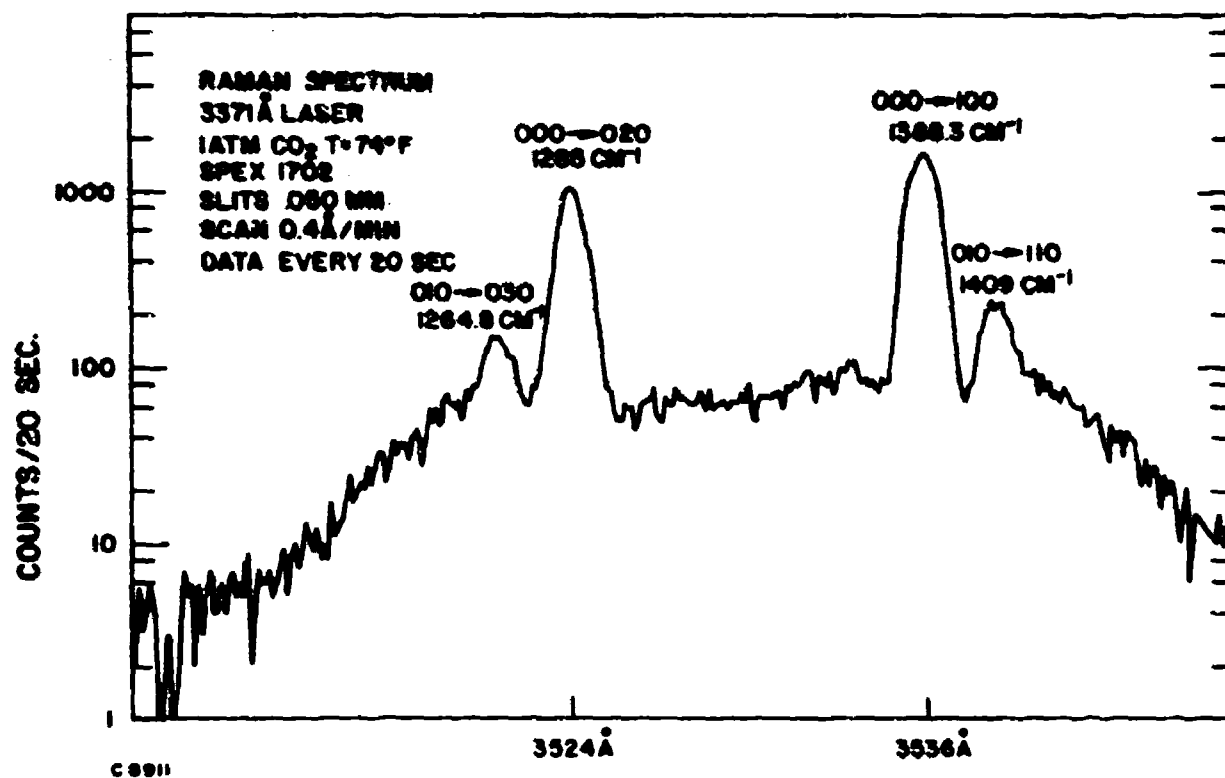


Figure 17 Experimental Raman Spectrum of Carbon Dioxide at Room Temperature

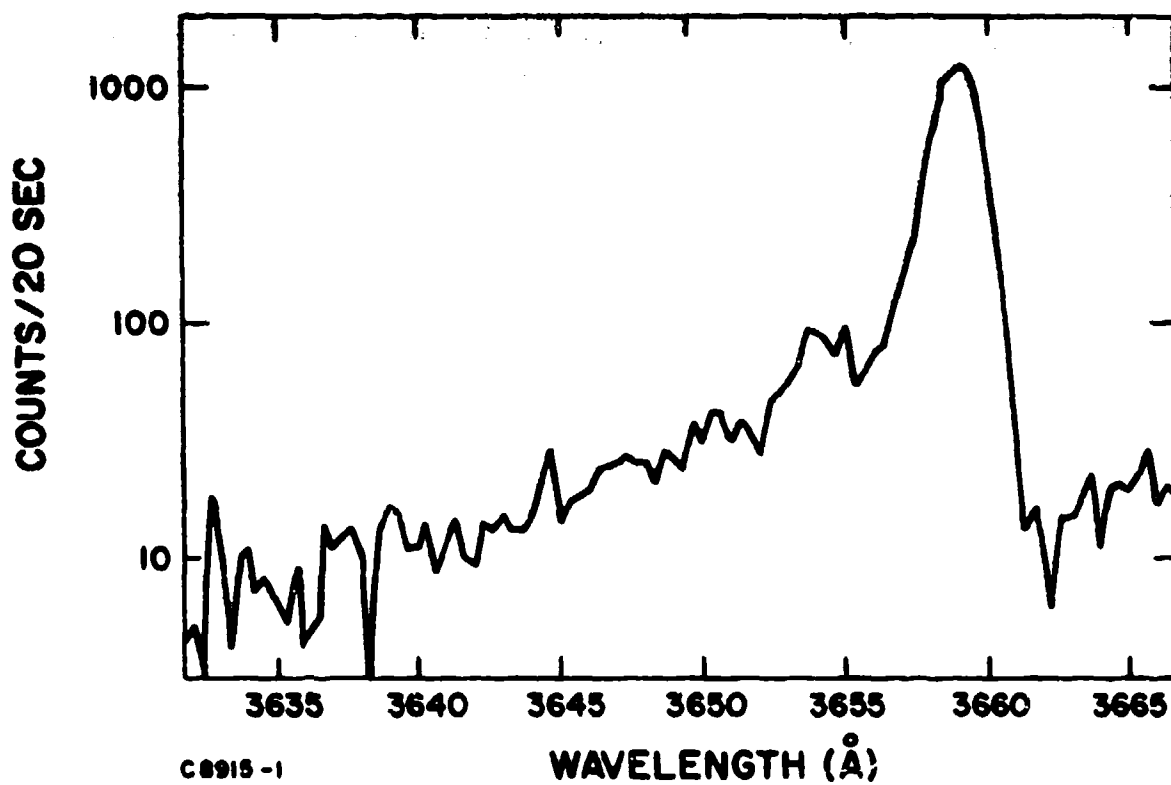


Figure 18 Experimental Raman Spectrum of Nitrogen at $\sim 1000^{\circ}\text{K}$ in a Propane/Air Burner Exhaust

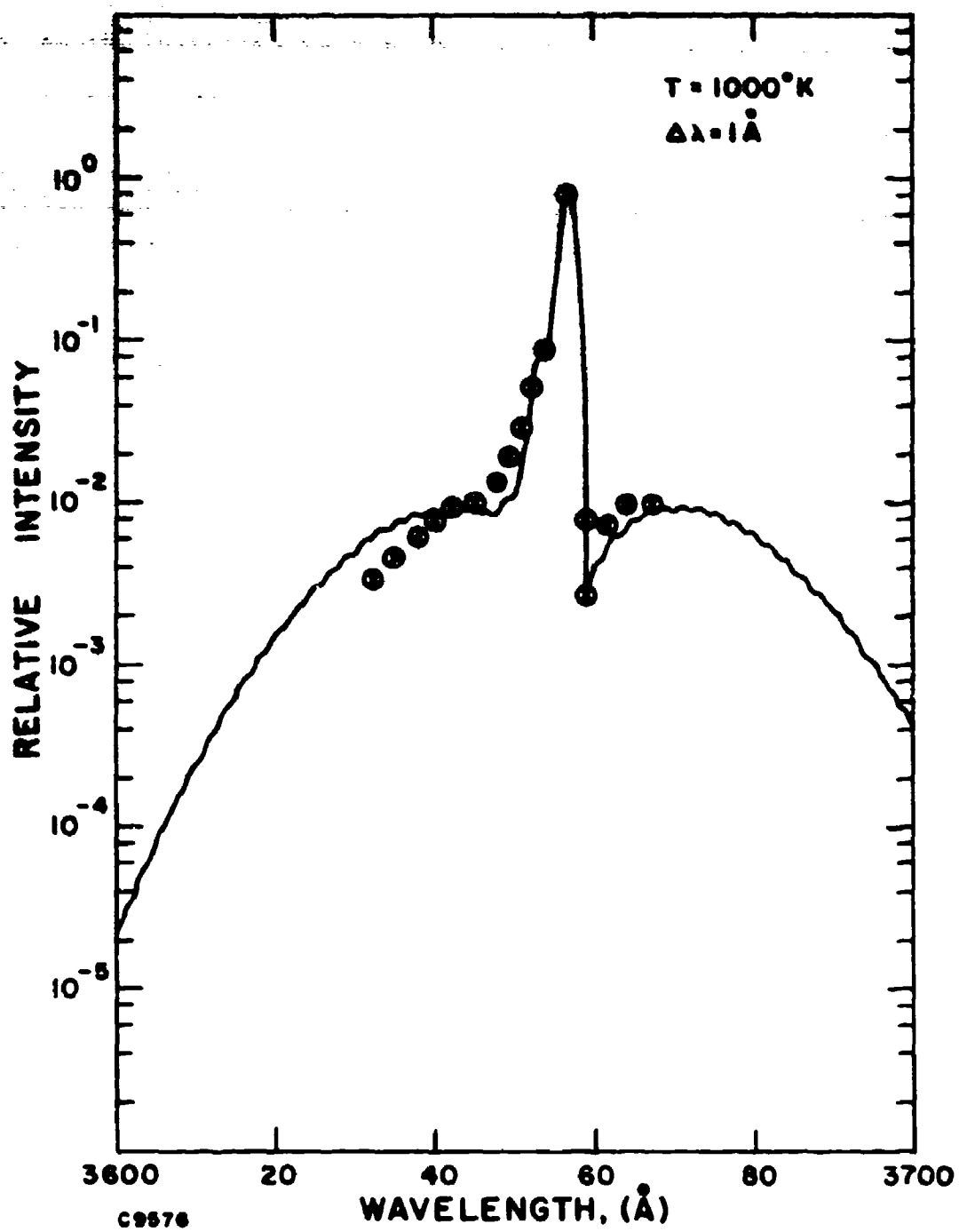


Figure 19 Computed Raman Intensity for Nitrogen at $T=1000^{\circ}\text{K}$ (same as Figure 8) with Experimental Points taken from Figure 18

of $\Delta J = +2$ relative to $\Delta J = 0$. Improvements in the theory are now in progress to attempt to improve the agreement.

The spectrum of CO_2 at 1000°K in the propane burner exhaust is shown in Figure 20. The 010 peaks, which appeared as much weaker secondary peaks in the room temperature CO_2 spectrum of Figure 17, have now increased so that the 010 peaks are nearly equal to the 000 main peaks. Also, other transitions appear to be appearing at wavenumbers shorter than 1265 cm^{-1} and longer than 1409 cm^{-1} . The reasons for the anomalous "red shift" band adjacent to the 1409 cm^{-1} transition are related to the "Fermi resonance" phenomena in CO_2 .

5. TEMPERATURE SENSITIVITY

The effects of increasing temperature become important to the laser Raman turbine exhaust analysis system in many ways. Foremost is the effect on the ratio of the peak Raman signal intensity of a particular species to the actual concentration of that species. The tacit assumption in previous work has usually been that the Raman signal is proportional to species concentration. However, over the temperature range of interest this proportionality constant is somewhat temperature dependent.

The case of nitrogen is especially important since the nitrogen signal is intended to serve as the reference signal against which the signal from the other species will be normalized. Figure 21 shows the calculated (for $\Delta\lambda = 1\text{ \AA}$) ratio of the peak N_2 signal to the total N_2 concentration as a function of temperature, both for the effect of the thermal excitation of upper states and for the effect of the $\Delta J = 0$ "blue-shift" broadening. The combined effect is shown as the product of the two above effects. The temperature sensitivity averaged over the 900°K to 1200°K range of interest is 4.4% per 100°K . This means that if the temperature is uncertain to 100°K , the nitrogen normalization is uncertain to 4.4%. An instrumental bandpass larger than 1 \AA would minimize this effect.

To some extent the same effects apply to the other species and will to some extent cancel out. However, for species with vastly different properties, the residual net effect can be significant. Figure 22 shows the estimated ratio of the peak (000) CO_2 signal to the total CO_2 concentration as a function of temperature. The many low lying levels become significantly populated with increasing temperature causing the rapid decrease in the solid curve labeled $\text{N}(000)\text{CO}_2$.

The dashed curve labeled $\text{N}(000)\text{CO}_2/\text{N}(\text{N}_2\text{ V}=0)$ indicated the partial recovery toward unit normalization when the $\text{N}(000)\text{CO}_2$ curve is divided by the curve labeled (3) in Figure 21. The temperature sensitivity averaged over the 900°K to 1200°K range of interest is 12% per 100°K as shown. This means that if the temperature is uncertain to 100°K the CO_2 normalization is uncertain to 12%, based on the estimate of Figure 22.

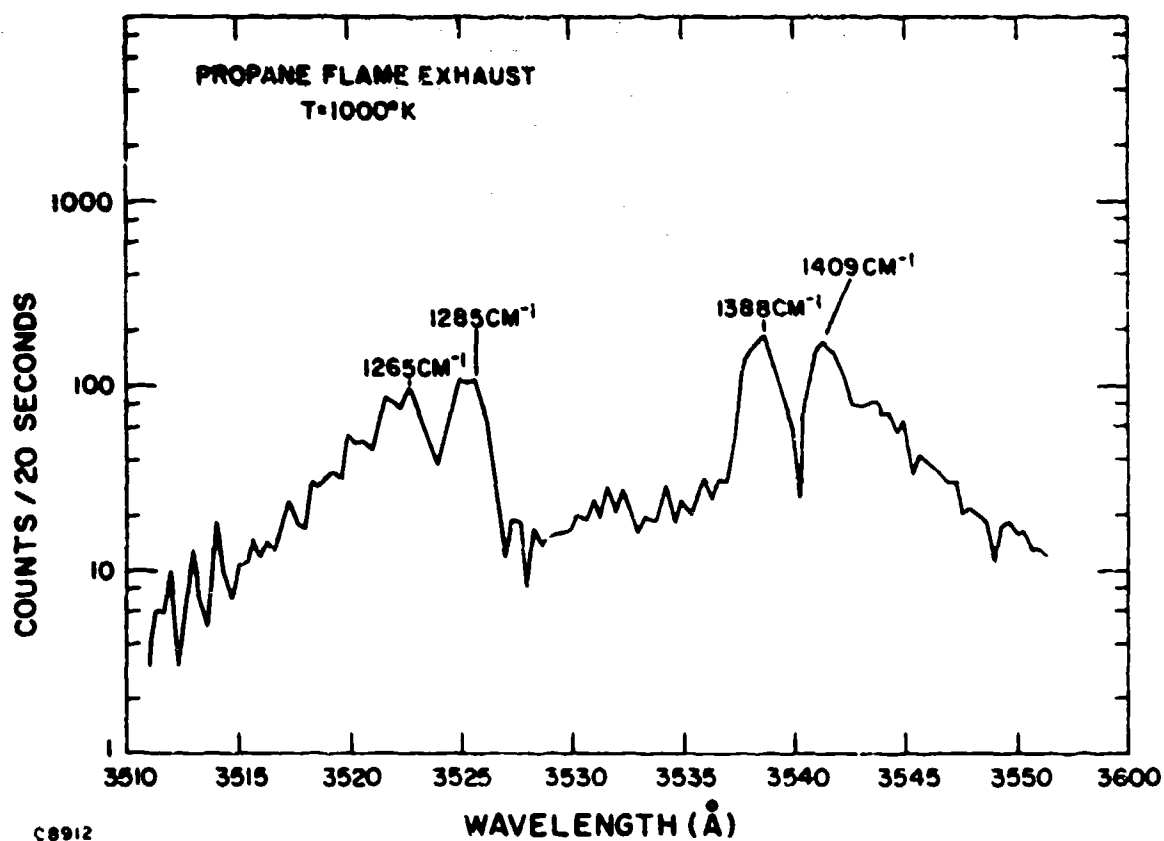


Figure 20 Experimental Raman Spectrum of Carbon Dioxide at ~1000°K in a Propane/Air Burner Exhaust

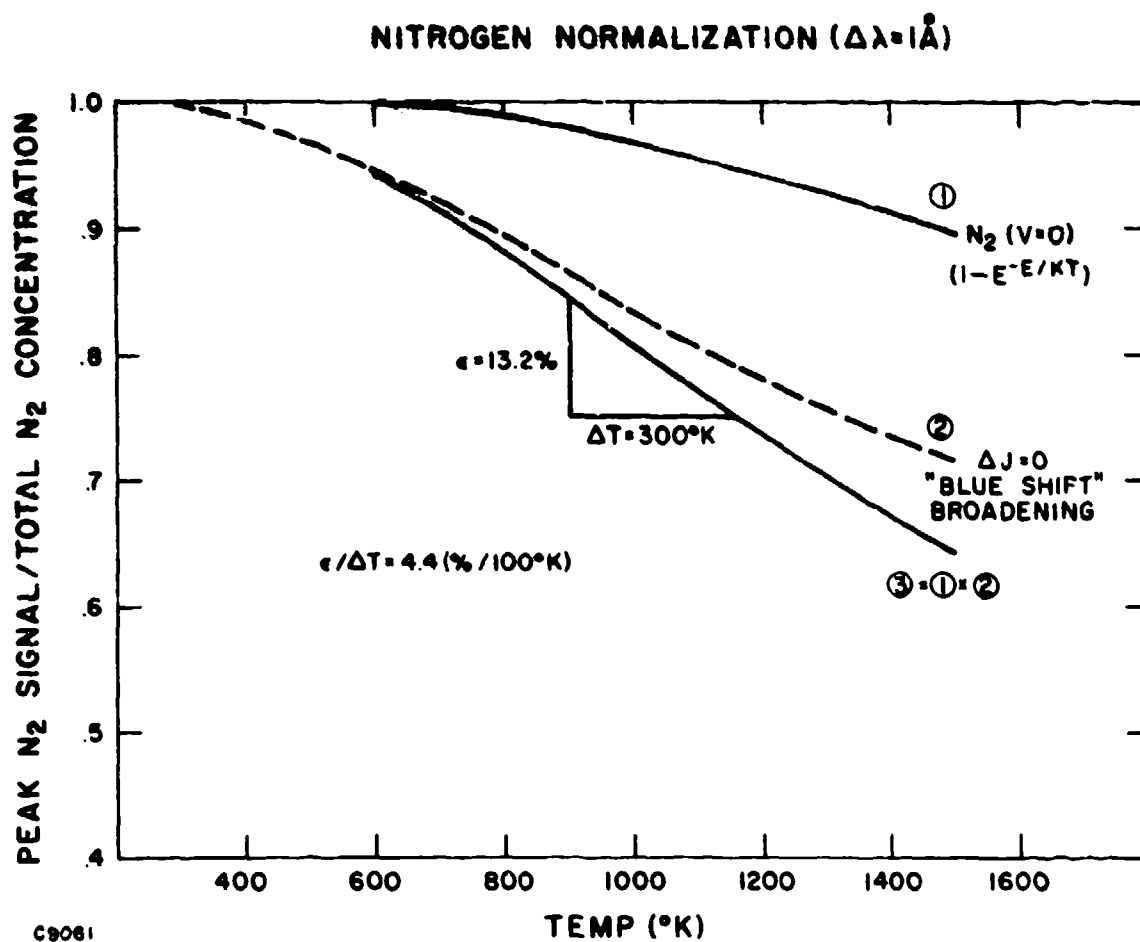


Figure 21 Computed Nitrogen Normalization Error as a Function of Temperature for a Detector with a Resolution of 1 Å

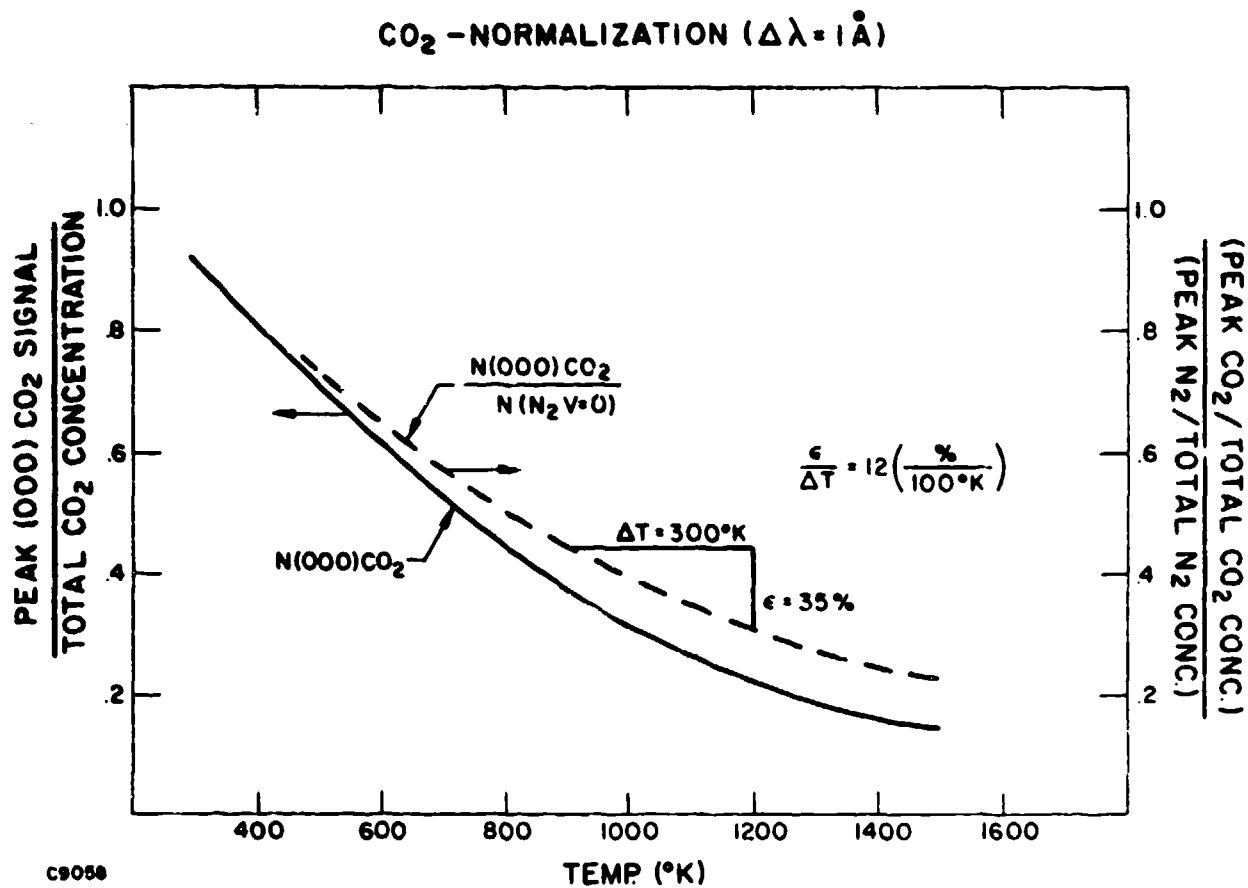


Figure 22 Computed Carbon Dioxide Normalization Error as a Function of Temperature for a Detector with a Resolution of 1 Å

From the above, it is apparent that an independent method of temperature measurement is a desirable adjunct to a laser Raman turbine exhaust measurement system. The use of the CO₂ Raman spectrum seems to be a reasonable means to satisfy this requirement. In particular the measurement of the ratio of the (000) CO₂ peak to the (010) CO₂ peak seems especially well suited for a temperature determination.

The ratio of the population of the (010) level to the (000) level in CO₂ is given by the expression $N(010)/N(000) = 2e^{-[E(010)-E(000)]/kT}$ where the factor 2 represents the double degeneracy of the 010 level. Figure 23 shows a curve representing the above ratio as a function of temperature. The calculated temperature sensitivity is such that a 1% experimental determination of the ratio will yield a temperature measurement with an 11 K uncertainty.

Also shown in Figure 23 are two experimental points representing a room temperature determination which agrees exactly with the theoretical curve and a higher temperature data point obtained from the propane/air burner exhaust CO₂ spectra. The disagreement of the high temperature data point with respect to theory is probably caused by a combination of noise and the positioning error of the thermocouple used to measure the temperature vs. the position of the laser focal point in the propane burner exhaust. More careful experiments to verify this theoretical curve and/or to calibrate the functional relationship of $N(010)/N(000)$ vs temperature should be conducted.

6. INTERFERENCE EFFECTS

The fact that the Raman method can separately detect and measure all the relevant molecular species would be of mere academic interest if there were serious interference of one species with another or with other molecules and substances in the turbine exhaust or from some other source. This section discusses particular cases of possible interference and how such interferences, if a problem, can be suitably handled. The near-impossibility of an absolute proof of noninterference in the use of a new measurement system in a new circumstance is close to axiomatic. Thus, interference will always remain a finite element of risk until a laser Raman turbine exhaust measurement system is proof-tested under actual field conditions.

The following possible interferences were considered:

a. NO₂ Absorption and Fluorescence

(NO₂) and nitric oxide (NO) are both present in the exhausts of gas turbine engines. The relative amount of each is variable, depending on the time history of the gas and uniformity of combustion. The amount of NO₂ is usually considered to be less than 10% of the total oxides of nitrogen. The total concentration of oxides of nitrogen is usually the order of a few hundred PPM.

CO₂ USED AS THERMOMETER

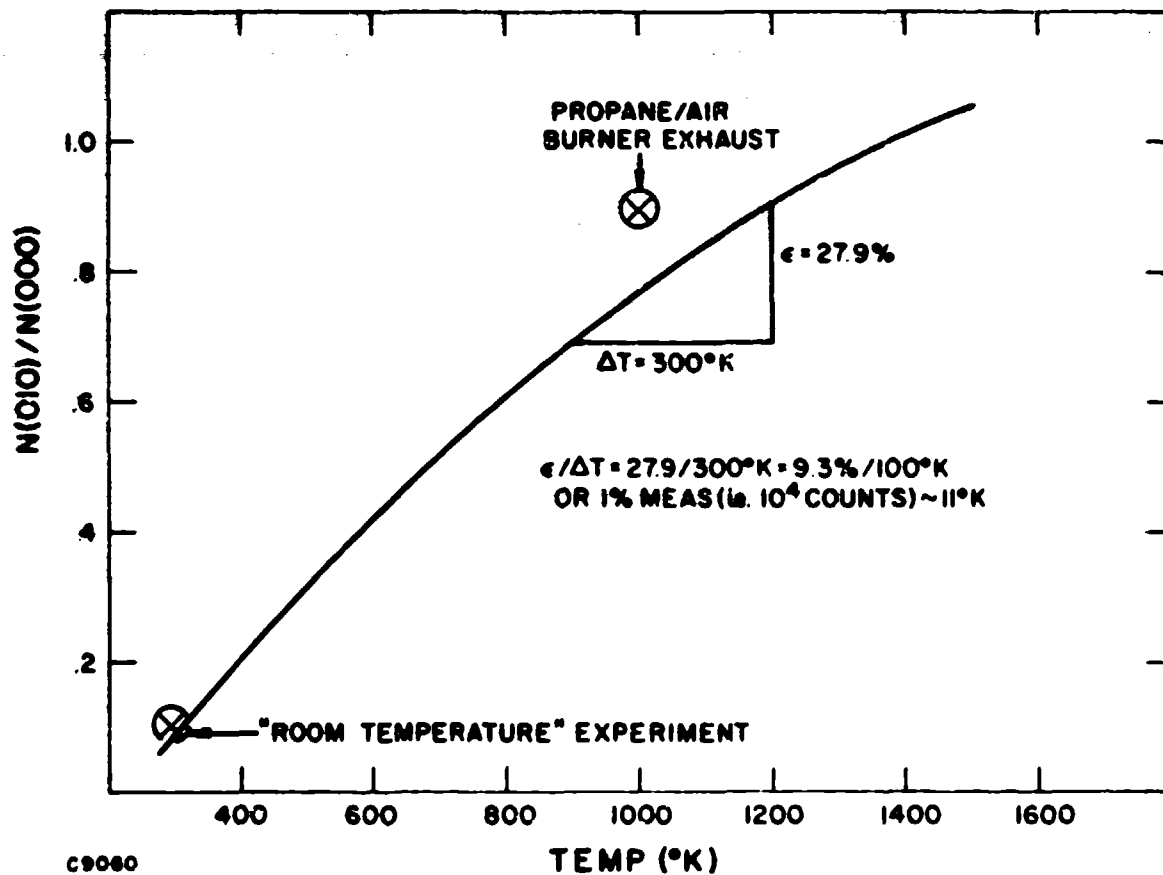


Figure 23 The Computed Temperature Dependence of the Ratio of the Raman Scattering from the 010 Level of CO₂ to the Raman Scattering from the 000 Level of CO₂. Two Experimental Points are shown.

Although the NO_2 Raman line at 1621 cm^{-1} can be used for detection and measurement, NO_2 can also be an interference for Raman analysis of exhaust gases for two reasons: (1) The absorption coefficient of NO_2 is large enough so that at large values of the product of concentration and path length the attenuation can be great. An analogous problem with SO_2 was encountered in the design of remote Raman laser devices for power plant plume analysis. (8) The solar blind lasers (i.e., $\lambda < 3100 \text{ \AA}$) were not practical for power plant plumes because of the very strong absorption of SO_2 in this spectral region, and the fact that power plant plumes typically contain SO_2 in the concentration range of 1000-2000 PPM. Figure 24 shows the fraction of the incident absorbed as a function of NO_2 concentration and path length. (9) The expected operating region for turbine exhausts is shown cross-hatched and absorption is not expected to be a problem, i.e., $\sim 10^{-3}$. (2) The second possible cause of interference by NO_2 is the excitation of fluorescence. The brown color of NO_2 seen by the eye when NO_2 is excited by visible light is well known. When using lasers of wavelength greater than the 3975 \AA photodissociation limit the fluorescence spectrum of NO_2 can be a serious interference to the Raman spectrum as discussed by Lapp. (2) A detailed study of the NO_2 fluorescence excited by visible lasers has recently been published. (10)

However, for lasers of wavelength shorter than 3975 \AA , which includes, of course, the 3371 \AA pulsed nitrogen laser, the NO_2 is photodissociated by the incident laser photons and no appreciable fluorescence is produced, due to the highly favorable ratio of the dissociation time ($\sim 10^{-11} \text{ sec}$) to the fluorescence radiative lifetime ($\sim 50 \times 10^{-6} \text{ sec}$). This result has been confirmed by experiments at AERL with the 3371 \AA pulsed nitrogen laser.

b. Sunlight Background

A second cause of possible interference is the scattering of photons of solar origin by particles in the exhaust during daylight operation. A calculation was carried out using solar flux data at sea level. (11) The solar scattering in a 1 \AA band was found to be equal to the Raman scattering from a species at the 100 PPM concentration level using a 100 kW, 3371 \AA , 10 nanosecond laser if 10% of the solar flux was attenuated by scattering in the exhaust. Typical exhausts attenuate the order of 1% and therefore the solar background by scattering is sufficiently close to the expected low level Raman scattering that the exhaust should probably be shaded from direct solar illumination.

c. N_2 Sideband Interference with CO

The third interference effect which was considered was the overlap of the $\Delta J = -2$ transitions of the N_2 Raman band with the main $\Delta J = 0$ peak of the carbon monoxide Raman band at 3634 \AA . Figure 25 is a plot which shows at a temperature of 1200°K a calculation of the N_2 Raman band at 3658 \AA and the CO Raman band at 3634 \AA at a concentration of CO at 100 PPM relative to the nitrogen.

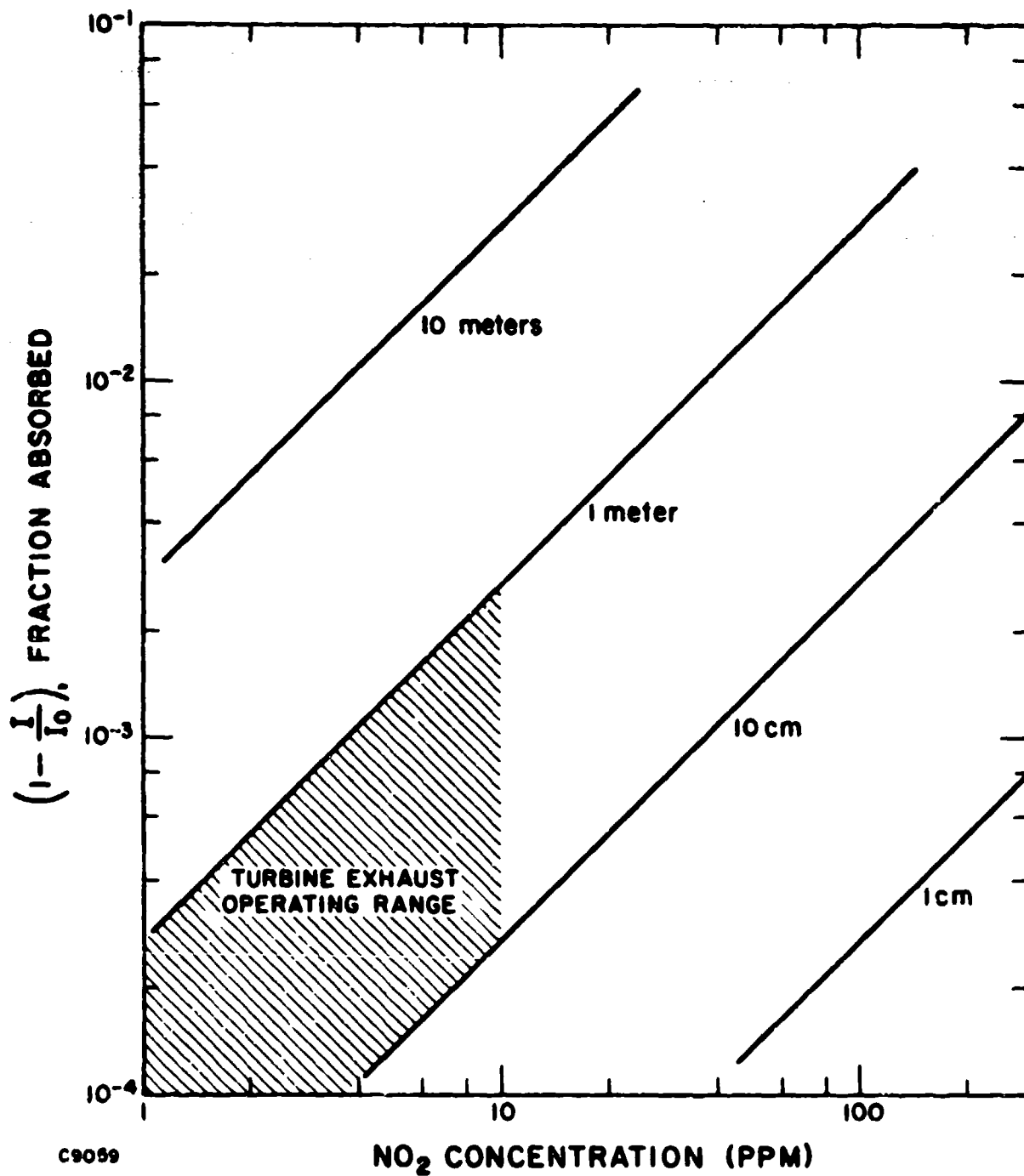


Figure 24 The Fraction of Light Absorbed at 3371 Å as a Function of NO_2 Concentration with Path Length in Meters as a Parameter

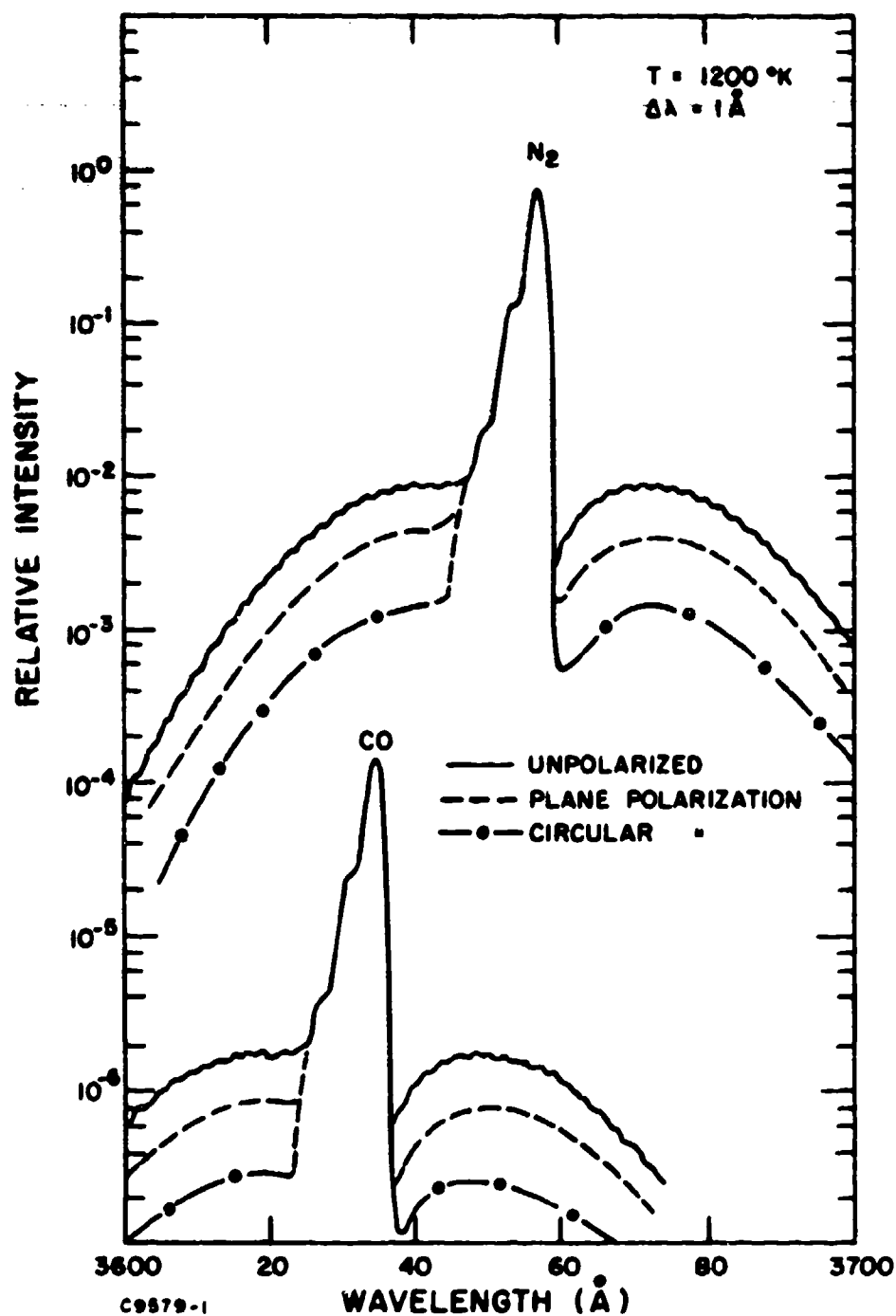


Figure 25 Computed Raman Intensity for Nitrogen at 1200°K (Same as Figure 9) and for Carbon Monoxide at 100 PPM Relative to Nitrogen. The use of polarized light to reduce the interference of N₂ with respect to CO is also shown.

As shown in Figure 25 the effect of the interference is reduced by the use of polarized light. A factor of two reduction has been both calculated⁽¹²⁾ and measured for plane polarization and a factor of six has been calculated⁽¹²⁾ for circular polarization. With circular polarization the ratio of the contribution of the CO Raman scattering at 3634 Å to the sum of the CO and N₂ Raman scattering at 3634 Å is about 10% for a 100 PPM mixture of CO in N₂.

Experiments have been performed with a plane polarized laser beam and a plane polarized detector which show the expected factor of two reduction in the $\Delta J = +2$ transitions relative to the $\Delta J = 0$ transitions. Figure 26 is experimental data for the N₂ Raman band which was obtained with the apparatus previously described in Figures 13 and 14. The solid line represents the Raman signal for an unpolarized laser and an unpolarized detector. The solid points are data obtained with both the laser and the detector plane polarized and the signal normalized to the peak of the unpolarized data. The predicted factor of two reduction in signal in the $\Delta J = +2$ wings was obtained. A similar experiment is planned using circular polarization.

In practice the ratio of the scattering at 3634 Å to the scattering at 3658 Å would be measured and compared with that expected for pure N₂ at the temperature of operation. The excess scatter at 3634 Å would be attributed to CO.

The sensitivity of the method is shown in Figure 27, which is a plot of the ratio of the Raman scattering at 3634 Å to the Raman scattering at 3658 Å for pure nitrogen as a function of temperature. Over the expected range of turbine exhaust operation, i. e., 900°K to 1200°K, the uncertainty in the ratio is 9% per 100°K or about 1% per 11°K temperature uncertainty - an attainable value using the (010)/(000) CO₂ Raman ratio method as previously discussed. Since the Raman intensity in the $\Delta J = -2$ side band of N₂ (with circular polarization) corresponds to about an apparent level of 1000 PPM of CO, a 1% measurement of the side band intensity would enable detection and measurement of 10 PPM CO. This is difficult, requiring an S/N of 100 at low signal levels, but can in principle be done.

The limiting inaccuracy would appear to be the stability and the constancy of the exhaust stream gas conditions during the integration period of the measurement, especially if single channel sequential detection is used. This difficulty could be minimized with multichannel detection and real time data acquisition and normalization for each laser pulse.

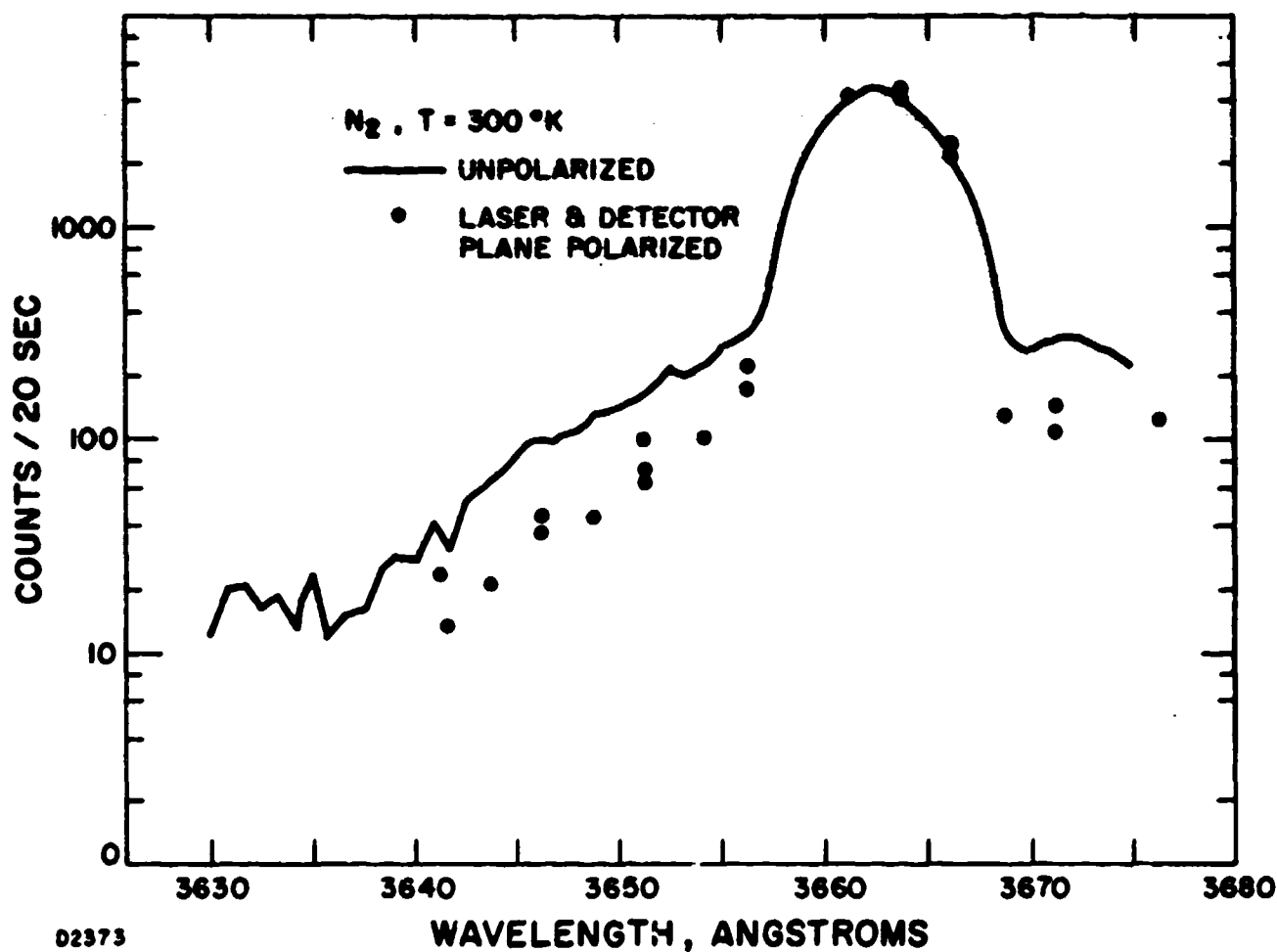


Figure 26 Experimental Raman Spectrum of Nitrogen at Room Temperature for both Unpolarized and Plane Polarized Laser Illumination

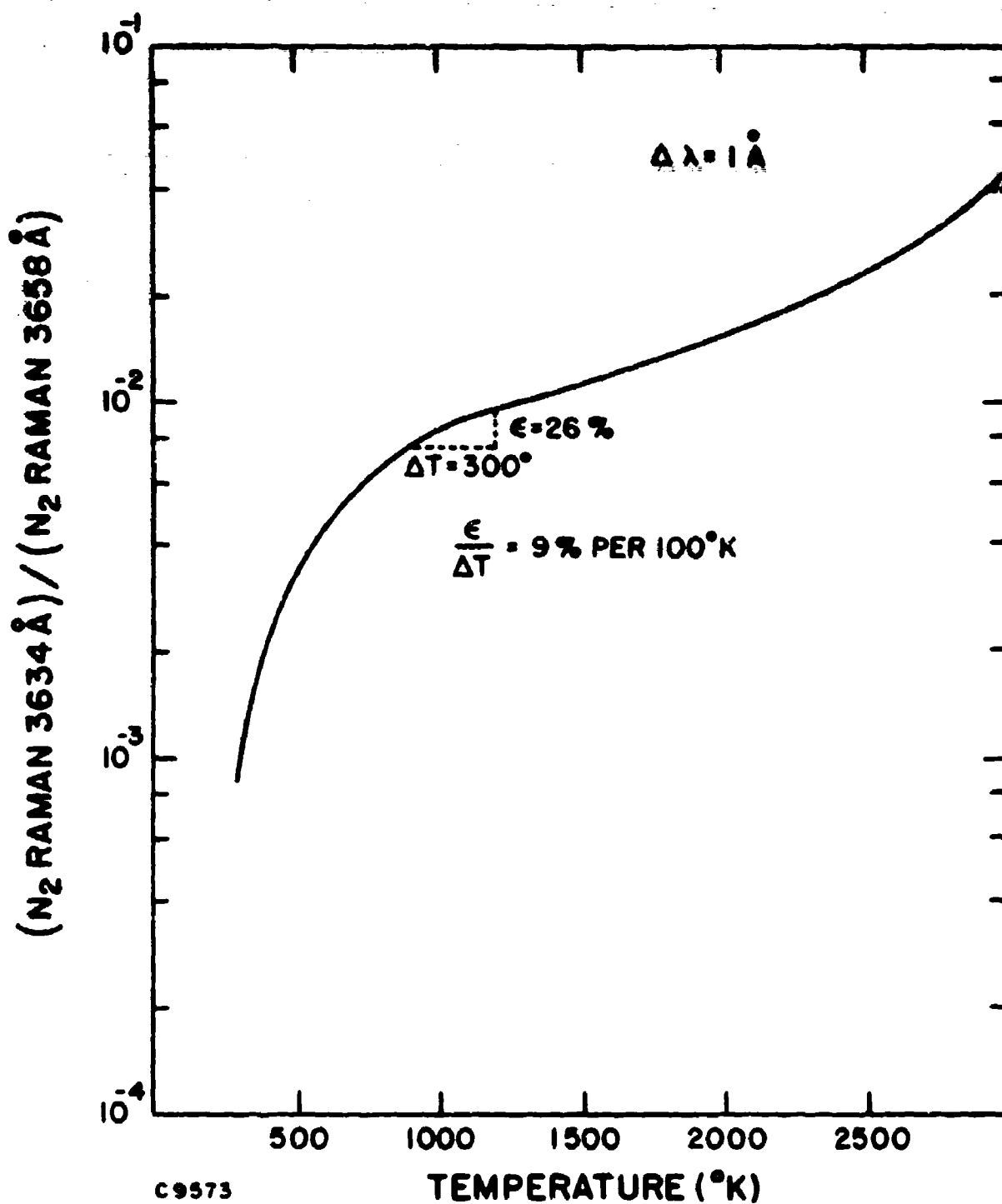


Figure 27 The Computed Ratio of Nitrogen Raman Scattering ($\Delta J=2$) at $\lambda = 3624 \text{ \AA}$ to Nitrogen Raman Scattering ($\Delta J=0$) at $\lambda = 3658 \text{ \AA}$

SECTION III

ENGINEERING CONSIDERATIONS

1. TRADE-OFF DISCUSSION LEADING TO CONCEPTUAL DESIGN

In considering the use of a laser Raman system for gas turbine engine emissions analysis, many different operating situations may be encountered. These could range all the way from the analysis of the exhaust of a small engine on a fixed test stand to the remote tracking and analysis of the emissions of a large C5A during routine taxi, take-off and landing procedures at an operational airfield. The system therefore should be single ended with the laser transmitter and the Raman receiver contained on the same rigid, steerable and mobile platform. A retroreflector or focusing element was also considered for placement directly behind the exhaust for increased signal collection but was ruled out of our conceptual design on the grounds of (1) severe vibration/alignment problems in the severe acoustic environments and (2) negates possibility of single-ended remote tracking capability as a system growth possibility.

As seen in Figure 28, the conceptual system is built as two transportable units, each capable of being separately transported without disassembly.

The systems package contains laser, transmitter and receiver optics, monochrometer and detection systems and supporting equipment such as cooling, pumping and power conditioning. The operator enclosure package contains the control and display panel and an enclosure for the operator and is capable of being positioned remotely from the systems package and turbine exhaust region for operator safety and comfort. A dark background plate of anodized aluminum, placed in the field of view of the receiver, behind the exhaust reduces daylight background interference to negligible levels.

a. Laser

The choice of laser very quickly narrows down to a pulsed ultra-violet laser of relatively low energy pulse and relatively high pulse repetition rate. The pulsed feature enables synchronous detection which greatly reduces ambient light background and dark current tube noise. Typical example might be a 20 nanosecond detection gate which is opened every 2 milliseconds (i.e., 500 pps laser pulse repetition rate). This technique effectively reduces noise by the factor $2 \times 10^{-3} / 2 \times 10^{-8} = 10^5$ and has been successfully utilized in Raman systems engineered by AERL. Pulsing the laser enables range resolution by gating techniques.

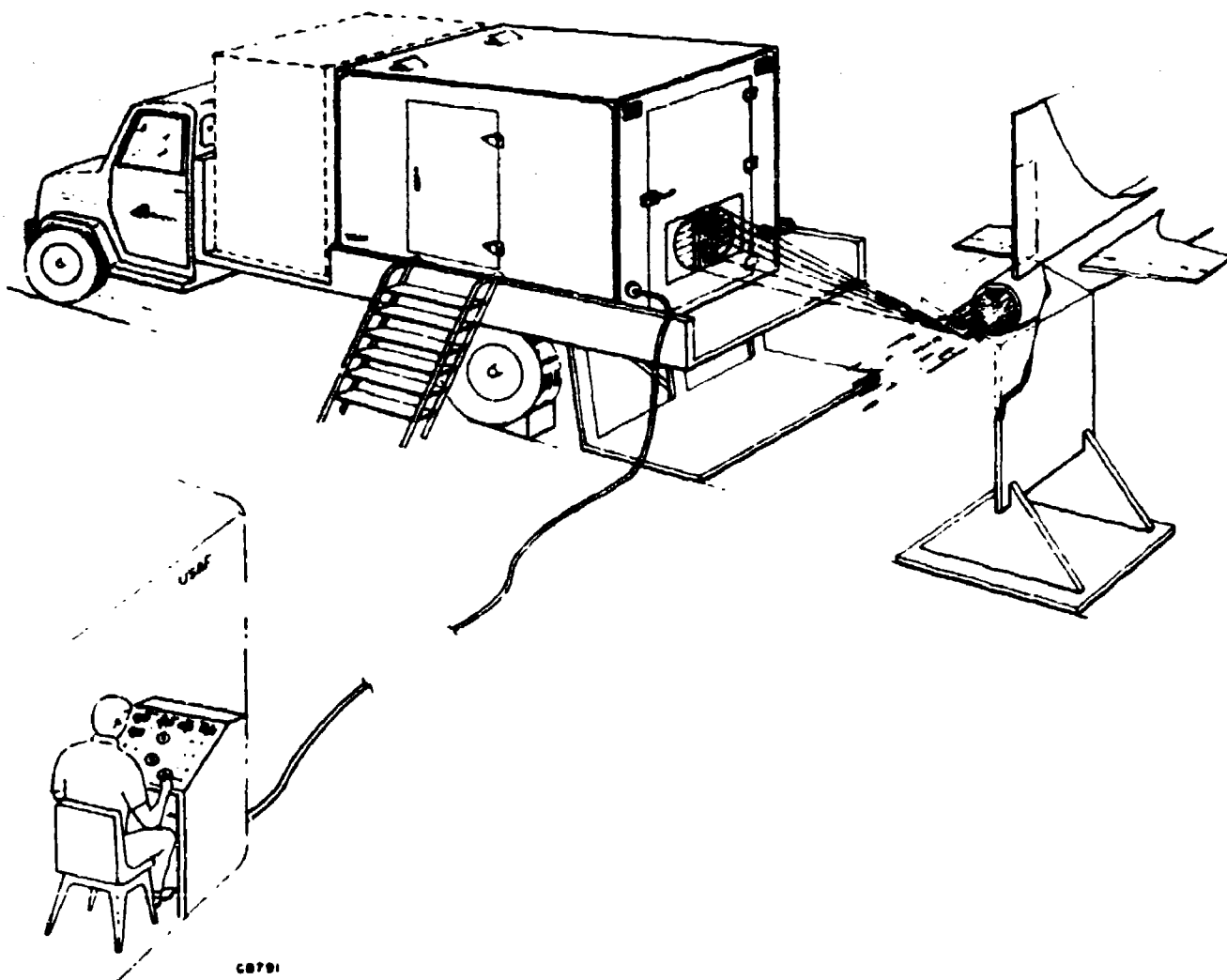


Figure 28 Schematic of Laser Raman Aircraft Engine Exhaust Emissions Measurement System

Also, with a pulsed laser noise can be suppressed by gating which may occur from multiple scattering in the receiver optical system or from background objects in the field of view.

The choice of laser wavelength depends on a variety of factors, among which are: (1) the availability of high power lasers in each wavelength region, (2) the $(1/\lambda)^4$ dependence of the Raman scattering cross-section favors the shortest possible wavelength (except for occasional enhancements by resonance Raman effects), (3) photoelectric efficiencies are highest below 5000 Å, (4) solar background falls off rapidly below 3000 Å (solar blind region), (5) unfavorable absorptions may occur which indicate wavelength regions for certain situations must be avoided, e.g., atmospheric absorption below 2500 Å and SO₂ absorption in stack gases between 2500 Å and 3200 Å, (6) unfavorable fluorescences may occur in certain wavelength regions such as the very strong fluorescence from NO₂ at wavelengths longer than 3975 Å, and (7) eye safety problems are less serious below 3400 Å where the vitreous fluid is much less transparent with subsequently greatly reduced hazard to the retina.

Consideration of all these factors leads to the choice of the 3371 Å ultraviolet pulsed nitrogen laser which operates on the O, O transition of the second positive band system of the nitrogen molecule. The high pulse repetition rate and low energy per pulse of this laser also favors eye safety.

AERL is thoroughly familiar with this laser having pioneered the research and development relating to the gaseous electronics of the discharge which produces the inversion, the high voltage engineering required to produce a practical device and the utilization of the laser in many applications including, of course, Raman spectroscopy. It is intended that the program will use the best state-of-the-art pulsed N₂ laser available.

b. Monochrometer

The monochrometer in a laser Raman spectroscopic system usually has as its primary function the suppression of the direct non-frequency shifted laser light which is strongly scattered by particulate matter or other solid objects in the field of view of the receiver optics. This will be especially important in the Raman analysis of turbine exhausts which contain significant quantities of particulate matter. AERL's approach which we have used in our previous Raman spectroscopy of combustion emissions is to insert an isotropic bulk volume absorption filter in an appropriate position in the receiver optical train.

With the 3371 Å laser as a source our choice of such filter has been a water solution of 2, 7-dimethyl-3, 6-diazacyclohepta-1, 6-diene perchlorate (DDDP) which has the property of essentially complete absorption at 3371 Å but with nearly complete transparency in the vibrational Raman region at wavelengths of 3500 Å and longer. Being a tuned

molecular system it is far superior in this regard than the best available interference filters both in transmission characteristics and in angle requirements.

By the use of DDDP filter to suppress the laser line, the function of the monochromometer is now reduced to that of distinguishing and scanning among the various Raman lines. The strengths of the Raman lines will vary over 4 or 5 orders of magnitude due to the corresponding large variation in concentration (e.g., N_2 at 80% vs NO at 100 ppm). The monochromometer must therefore have a stray light rejection ratio of better than 10^{-4} or 10^{-5} . Our conceptual design choice is the commercially available SPEX Model 1702 single monochromometer which has stray light rejection properties which are adequate for the requirements of the proposed program. This spectrometer is equipped with a stepping motor which can be digitally programmed to provide automatic sequential scans of the Raman spectrum being continuously monitored.

Very high linear dispersion in the monochromometer eases the through-put matching requirement. Our experience however with highly dispersive systems such as high order eschelle crossed prism spectrometers has been that the stray light rejection properties (necessary for low PPM Raman analytical studies) within each order is generally much poorer than can be obtained with well engineered standard monochromometers such as the SPEX 1702. Matching is accomplished in our baseline design by imaging optics in the transmitter to produce a small rectangular illuminated region in the exhaust flow which can be efficiently imaged onto and matched to the 1702 monochromometer slit. The rectangular illuminated region in the flow will be orientated to include the maximum number of streamlines for the best possible spatial average over the exhaust exit plane.

A polychromometer with a multiplicity of fixed slits or a raster-type display with a crossed-prism and high order eschelle grating may well be best for an ultimate operational system. However, for preliminary investigations of the basic feasibility with an experimental prototype our engineering experience has shown that it is best to first start out with a single channel instrument and later upgrade with multi-channels if system reliability and cost are not overly compromised.

c. Transmitter and Receiver Optics

To ensure observation of the turbine exhaust gases only and not the intervening ambient air, the fields of view of the transmitter and receiver optics should be arranged to overlap only within the turbine exhaust. This is especially important since nitrogen will be used as the calibration standard and the detection of higher density ambient nitrogen would severely distort the average nitrogen calibration signal observed.

The required off-axis arrangement can be accomplished by mounting a transmitter folding mirror within the collection aperture of

the primary collector and in the obscuration zone of the secondary mirror of a Cassegrain type system. Care should be taken to completely shield and isolate the transmitter optics from the collection optics except for the Raman interaction region within the turbine exhaust sample volume.

The transmitter optics should include a spatial filter section which will transmit with high efficiency ($>90\%$) the collimated laser beam but severely attenuate the spontaneous emission also being produced in the laser discharge tube. Much of this spontaneous emission can lie in the region of Raman interest. In particular for the 3371 Å pulsed nitrogen laser a strong emission line occurs at 3577 Å corresponding to the O, 1 transition of the same second positive band of molecular nitrogen. This line at 3577 Å, for example, if allowed to transmit strongly could be scattered from the particulates in the sample region with an intensity sufficient to interfere with the nearby line at 3582 Å corresponding to the 1744 cm^{-1} vibration of the C = O carbonyl group in formaldehyde.

The transmitter optics also includes a beam expander element which focuses the transmitted laser beam into a small beam of rectangular cross-sectional area in the turbine exhaust. The cross-sectional area of the laser beam has the same aspect ratio as the monochromator slit and is appropriately oriented. The entire optical system should be appropriately and adequately baffled and no element in the optical train of either the transmitter or receiver should be at or near a focal point in order to avoid fluorescence at a point which will be efficiently imaged onto the detector.

d. Electronics and Calibration

The most efficient photoelectric detection scheme at low light levels is actual quantum counting. However, the system will be built to handle a large dynamic range since sequential wavelength scans (each scan time a few seconds), being short compared to the drift time (many minutes) of turbine engine performance, of all components over a single photomultiplier channel will be provided. To allow for many photoelectrons being produced in one laser pulse gate time (which are not resolvable due to the finite resolution of photomultipliers), a charge to pulse train converter will process the photomultiplier output. The pulse trains thus produced will be sent to a counter for storage for the total sampling time. This method of photoelectron pulse counting and storage has been found by AERL to be ideally suited for pulsed laser Raman spectroscopy and has been proven entirely satisfactory in both our laboratory and field experience.

Calibration of the entire system will be accomplished by measuring the Raman scattering signal from molecular nitrogen. The signals received from the Raman scattering from the various molecular species being analyzed will be continuously ratioed to the signal received from the molecular nitrogen. This normalization of Raman scattering to

molecular nitrogen is a well known technique routinely used by AERL in its remote Raman spectroscopy. The technique was recommended in 1969 by the Standards Committee of the Group on Laser Atmospheric Probing, National Center for Atmospheric Research (NCAR), Boulder, Colorado. In the laser Raman turbine emissions analysis program the procedure of normalization to nitrogen will serve primarily to eliminate absolute instrument and laser calibrations as well as to continuously compensate for long term optical and electronic drift and degradation and changing atmospheric and exhaust transmission effects. The drift in calibration due to temperature effects can be compensated by an independent measurement of exhaust temperature using the Raman scattering from the 010 level of CO_2 .

2. CONCEPTUAL SYSTEM DESIGN DETAILS

The number of Raman photoelectrons collected per second by an optical detector in a pulsed laser backscattering system can be expressed by the following equation:

$$N_{\text{PE}} = N_{\text{LASER}} N_{\text{SCAT}} \sigma_{\text{RAMAN}} \Delta R \Omega \epsilon_{\text{pe}} \epsilon_{\text{op}} T_{\lambda_1} T_{\lambda_2} \quad (1)$$

where N_{PE} = number of Raman photoelectrons detected

N_{LASER} = number of laser photons per second

N_{SCAT} = density of molecular scatterers of a given species

σ_{RAMAN} = Raman scattering cross-section per particle steradian

ΔR = range resolution

Ω = detection solid angle

ϵ_{pe} = photocathode photoelectric efficiency

ϵ_{op} = optical system efficiency

$T_{\lambda_1} T_{\lambda_2}$ = two-way transmission, T_{λ_1} at laser wavelength
 T_{λ_2} at Raman wavelength

It can be seen from Eq. (1) that, if the transmitter and receiver system parameters, N_{LASER} , σ_{RAMAN} , ΔR , the detection solid angle and the detection efficiencies are known, the only two quantities remaining are the density of scattering molecules N_{SCAT} and the two-way transmission factor $T_{\lambda_1} T_{\lambda_2}$ to the range of interest. Thus a measure

of the Raman scattering from a single range cell can be used to directly determine the product of the density of the scatters of a given species and the two-way transmission to the region of interest. If the nitrogen is monitored, since its relative concentration is known and changes only slightly even in a turbine exhaust, this gives directly the product $T_{\lambda_1} T_{\lambda_2}$ for the N_2 Raman scattering. The assumption will then be made that T_{λ_2} varies in the same way for the other Raman lines.

A calculation was carried out using the above range equation with system parameters which assume state-of-the-art well engineered components. The parameters assumed are listed in Table III with a brief rationale for the particular choice. All the system components and their interaction will be discussed in detail below in connection with the functional block diagram of Figure 29.

The results of inserting the conceptual system design parameters of Table III into Eq. (1) is a calculated Raman photoelectron detection rate of 56 photoelectrons per second for the assumed NO concentration of 100 PPM. This would mean that a total of 112 Raman photoelectrons are collected in the two second minimum integration time and that 1680 are collected in 30 seconds, the maximum allowable integration time, corresponding to a measurement standard deviation based on the photo-statistics alone, of $\pm 9.4\%$ or ± 9.4 ppm in the 2-second case and $\pm 2.4\%$ or ± 2.4 ppm in the 30-second case.

From another point of view, a 99.74% level of confidence (or ± 2.8 standard deviations) that the measurement of NO is within ± 10 ppm is reached when 784 photoelectrons have been obtained, which takes 7 seconds. NO is the worst case since all the other species of interest are known to have larger cross-sections. However, subtraction of interference effects, such as $CO-N_2$ will require longer measurement times.

The functional block diagram describing the conceptual system is shown in Figure 29. The 3371 Å pulsed nitrogen ultraviolet laser beam, after being spatially filtered is focused onto the turbine exhaust by the transmitter optics. The receiver optics collects the Raman scattering produced in the sample volume of the exhaust and focuses it onto the slit of a scanable monochromator which is programmed to continuously and repetitively scan in a sequential manner, by means of a stepping motor, the Raman lines of interest. After passing through a liquid filter which blocks the direct nonwavelength shifted laser line, the Raman photons are detected by a standard nongated photomultiplier. Gating is accomplished subsequent to the photomultiplier in a gated integrator which is synchronized to the laser trigger generator. The quantity of charge produced by the gated integrator is converted into a pulse train proportional to the quantity of charge. The number of pulses thus produced are stored in a counter during the sampling time period. The total count recorded for each species during each specie sample time is stored and processed by a logic network which divides each specie

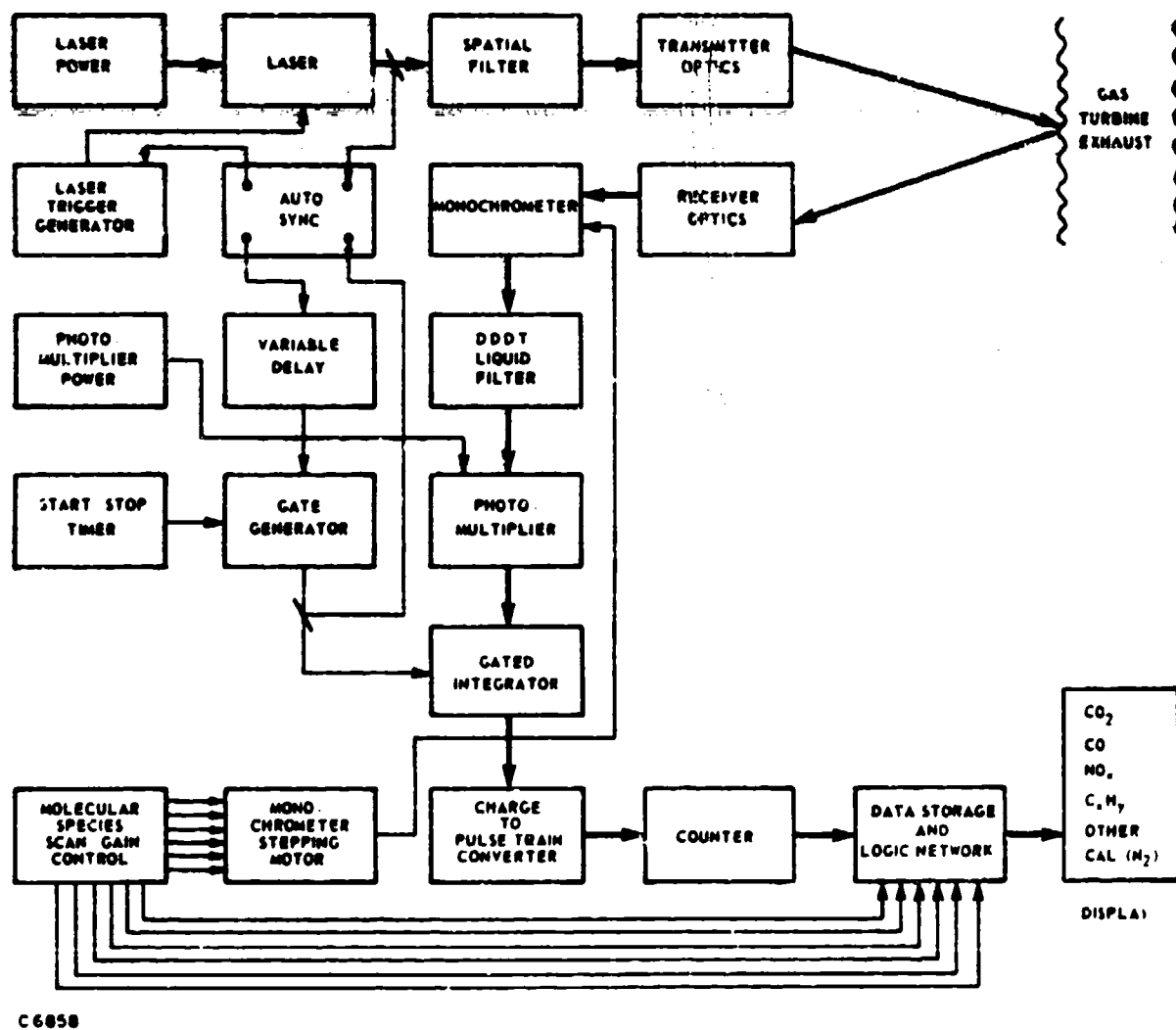


Figure 29 Function Block Diagram of System

TABLE III

CONCEPTUAL SYSTEM PARAMETERS

<u>System Parameter</u>	<u>Value Assumed</u>	<u>Rationale</u>
N_{LASER}	$1.7 \times 10^{18} \frac{\text{photons}}{\text{sec}}$	This value corresponds to 1.0 watt of average power in the ultraviolet. This average power is currently available from an Avco prototype commerical device. Higher power levels have been obtained from experimental devices.
N_{SCAT}	$8.2 \times 10^{14} \frac{\text{particles}}{\text{cm}^3}$	Corresponds to a temperature of 1500°F and a relative particle concentration of 100 ppm -- a mean range for turbine exhausts under consideration.
σ_{RAMAN}	$1 \times 10^{-30} \frac{\text{cm}^2}{\text{particle-steradian}}$	This is the value for NO which is given in Table 2-1. It is the lowest cross-section listed and therefore represents the worst case.
ΔR	10 cm	Corresponds to the minimum sample size, i. e., the 4-inch diameter exhaust duct.
Ω	4×10^{-2} steradian	This collection solid angle responds to a 2-foot diameter Cassegrain collection telescope with a 20% obscuration ratio placed 8 feet from the exhaust sample region.
ϵ_{pe}	0.30	Typical RCA 8850 photomultiplier photocathode sensitivity in the 3500 Å to 3900 Å region.
ϵ_{op}	0.30	Typical transmission of monochrometer plus transfer optics.
$T_{\lambda_1} T_{\lambda_2}$	1.0	This factor can vary from near unity to near zero, depending upon the turbine combustion conditions.

count by the molecular nitrogen count and adjusts for temperature dependence before being displayed as a digital readout.

Specific details of the subsystems are described in Table III.

a. Laser

As described above, a 3371 Å pulsed nitrogen laser was selected as the best available laser source for this Raman spectrometer. A modified Master Oscillator Power Amplifier (MOPA) arrangement will be used for the pulsed nitrogen laser in order to produce a highly collimated beam with good spectral purity. Figure 30 shows the arrangement which will be used. The backward traveling wave in the laser power amplifier is filtered in the mode control unit. The filtered wave is then amplified as it traverses the laser power amplifier in the opposite direction. The MOPA in the conceptual design produces one watt of average power at the exit of the output spatial filter.

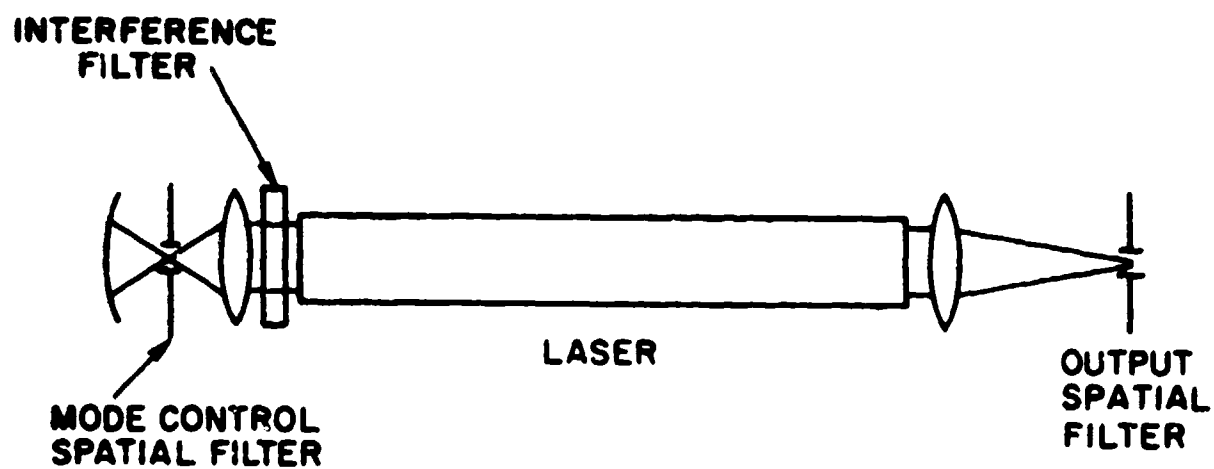
It is our considered opinion that a one watt average power pulsed N₂ laser, properly mode controlled will adequately satisfy all the requirements of the current program. Higher power pulsed N₂ lasers which appear feasible, but which are not available as fully developed hardware will provide the same basic system with increased capability when retrofitted into it.

b. Transmitter/Receiver Optics

The general schematic arrangement of the transmitter and receiver optics is shown in Figure 31. Basically the laser output spatial filter slit is imaged by the transmitter mirror onto the exhaust which is then re-imaged by the collector mirror onto the entrance slit of the monochromometer.

A typical monochromometer slit size might be .025 cm wide by 1.0 cm high, which for the SPEX 1702 considered in the conceptual design would provide a resolution of about 1 Å. As can be seen from Table IV with perfect matching in both transmitter and receiver (i.e., conservation of brightness or ΩA) the required laser output spatial filter slit size is .490 cm x .0123 cm. This will correspond to a degree of collimation in the laser amplifier of 16 milliradians x 0.4 milliradians which is many times diffraction limited and easily obtained. Also, the rectangular image of the output spatial filter is optimally matched to both (1) the rectangular monochromometer entrance slit requirement and (2) the sampling of many streamlines in the exhaust.

The details of the laser beam as it passes through the turbine exhaust is shown in Figure 32. The vertical image of the MOPA spatial filter slit is oriented in the exit plane of the turbine exhaust thus sampling many streamlines. In the conceptual design the area of the sampled volume normal to the flow would be .572 cm x 10 cm = 5.72 cm².



C9620

Figure 30 Mode Controlled Pulsed Nitrogen Laser

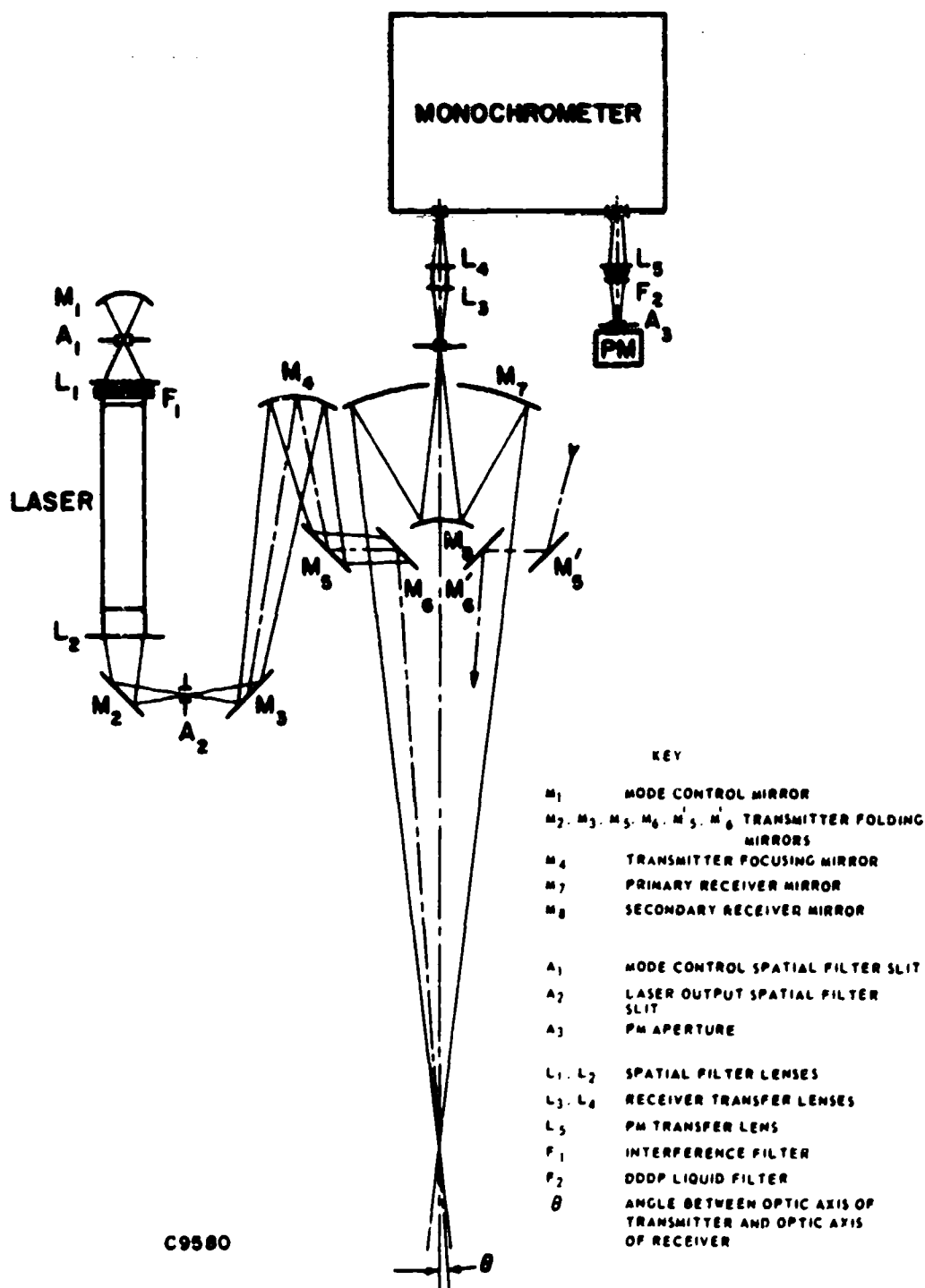


Figure 31 Schematic of Transmitter and Receiver Optical System Details

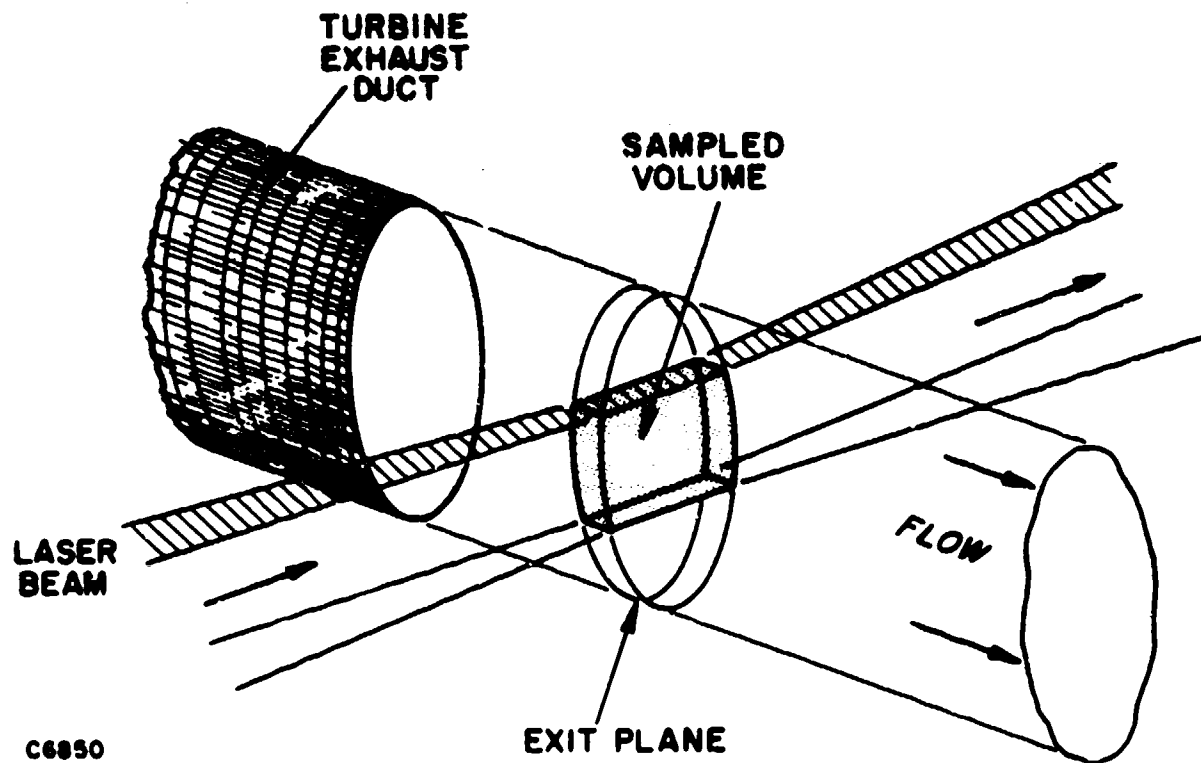


Figure 32 Rectangular Laser Beam Image in Turbine Exhaust is Oriented to Sample the Maximum Number of Stream Lines and is Matched to Monochrometer Entrance Slit

TABLE IV

TRANSMITTER/RECEIVER CHARACTERISTICS
(Conceptual Design)

	<u>Effective f No.</u>	<u>Height</u> (cm)	<u>Height/i</u>	<u>Width</u> (cm)	<u>Width/i</u>
<u>Transmitter</u>					
Laser Output Spatial Filter Slit	6	.490	.0817	.0123	.00205
Laser Beam Image in Exhaust	7	.572	.0817	.0143	.00205
<hr/>					
<u>Receiver</u>					
Laser Beam Image in Exhaust	4	.572	.143	.0143	.00357
Monochrometer Entrance Slit	7	1.00	.143	.0250	.00357

c. Monochrometer

The monochrometer chosen for the conceptual design is the Model 1702 produced by SPEX Industries which has the following specifications.

Focal Length	750 mm
Spectral Range	1750 Å to 1.5 μ
Aperture in UV	f/7
Grating Size	102 mm x 102 mm
Grating Ruling	3000 lines/mm
Dispersion	4 Å/mm
Scattered Light	10 ⁻⁴ to 10 ⁻⁶
Scanning Speed	.4 to 5000 Å/min.

This monochrometer has been used by AERL in many of our Raman applications and is rugged and lightweight and is well suited for field use.

The standard 1702 is equipped with a synchronous motor which drives a scanning mechanism. By means of an external accessory the motor may be operated in a stepping mode for convenient interfacing with the remote automatic system control. The specifications of the scanning mechanism are as follows:

Readout Accuracy	better than \pm Å over 6000 Å
Periodic Error	better than \pm 0.2 Å over 100 Å (i.e., one turn of lead screw)
Readability	better than \pm 0.1 Å
Resettability	better than \pm 0.3 Å

Limit switches mounted at each end of the lead screw protect the entire instrument from damage should it be left on inadvertently.

d. Electronics - Detection and Display

An RCA 8850 photomultiplier will be used in the conceptual design. This tube is a state-of-the-art tube which is well suited for low light level applications such as laser Raman scattering, laser communications, and astronomical photometry. AERL is now using the RCA 8850 tube with satisfactory results in other laser Raman programs.

The gated integrator into which the PM signal is fed will be custom built at AERL, based on the detailed designs of similar gated circuitry built by AERL for previous laser Raman projects. The gate width will be 20 nanoseconds to fully accommodate the 10 ns width at

half maximum pulsed nitrogen laser pulse. The charge accumulated on the integrator will be converted into a pulse train in which the number of pulses is proportional to the charge on the integrator. The total number of pulses thus produced for each Raman species in a sample time is stored in a counter. This again is a standard technique used at AERL in precision low light level photometry.

A logic network processes the information stored in the pulse counter and displays in digital form on a control panel the concentrations by weight of the various species. A conceptual design of the control and display front panel is shown in Figure 33.

An "auto-sync" unit will be incorporated into the electronic detection system as shown in the block diagram of Figure 29. The purpose of the "auto-sync" unit is to ensure that the timing of the gate which controls the gated integrator is maintained in precise synchronism with the timing of the laser optical pulse. The two inputs to the "auto-sync" unit are the gate from the gate generator and an electrical pulse produced from the laser optical pulse. The synchronism between these two pulses is monitored and maintained by appropriate adjustments in the timing of the two outputs from the "auto-sync" unit, i.e., the input to the laser trigger and the input to the gate generator. The "auto-sync" unit maintains synchronism to a fraction of a nanosecond, independent of drift in the triggering of the pulsed nitrogen laser or other critical components.

The functions the operator would perform and the related system response are the following:

<u>Operator Function</u>	<u>System Response</u>
1. Observe status monitor for satisfactory equipment operating characteristics.	None - ready lights indicate satisfactory condition, i.e., power on, laser operating.
2. Set main position switch on "N ₂ CAL."	Monochrometer stepping motor adjusts grating position for molecular nitrogen Raman channel at 2330 cm^{-1} (3658 Å). Gate pulses are injected into the gated integrator continuously.
3. Tune "N ₂ CAL" meter for maximum signal by means of coarse/fine adjustments.	Meter reading proportional to counting rate of N ₂ Raman. Adjustment controls vary the setting of the "auto-sync" unit. Sub-nanosecond stability is required by this circuitry.

Operator Function

System Response

4. Select sample time, for example, 2 seconds.

Determines period of time over which gate pulses are injected into the gated integrator for each species determination.
5. Set main position switch on "MONITOR." Depress reset button. Depress start button.

In continuous repetitive multiplex sequence the following occurs:

 - 5.1 Monochrometer stepping motor adjusts grating position for N₂ Raman, previous N₂ count storage is reset gate pulses injected for 2 seconds, total N₂ count stored in logic network, total N₂ count appears on N₂ CAL meter.
 - 5.2 Monochrometer stepping motor adjusts grating position for CO₂ Raman at 1409 cm⁻¹ (3539 Å), gate pulses injected for 2 seconds, total CO₂/1409 cm⁻¹ count stored in logic network.
 - 5.3 Monochrometer stepping motor adjusts grating position for CO₂ Raman at 1388 cm⁻¹ (3537 Å), gate pulses injected for 2 seconds, total CO₂/1388 cm⁻¹ count compared in logic network with CO₂/1409 cm⁻¹ count to determine temperature, total CO₂/1388 cm⁻¹ count, suitably weighted for temperature dependence is divided in logic network by stored N₂ count, normalized weight % displayed on digital meter.
 - 5.4 Monochrometer stepping motor adjusts grating position for CO Raman at 2143 cm⁻¹ (3634 Å), gate pulses are injected for 2 seconds, total CO count is divided, with appropriate temperature dependence, in logic network by stored N₂ count, normalized PPMW displayed on digital meter.
 - 5.5 Repeats 5.4 for NO at 1876 cm⁻¹ (3599 Å). Display normalized as PPMW on NO_x meter.
 - 5.6 Repeats 5.4 for CH at ~ 2920 cm⁻¹ (~3740 Å). Display normalized as PPMW on C_xH_y meter.
 - 5.7 Repeats 5.4 for "other" at wavelength arbitrarily preset. Could be used to monitor NO₂ for inclusion in NO_x reading or to monitor formaldehyde for example.
 - 5.8 Repeats 5.1 to 5.8.

Operator Function

System Response

- | | |
|---|--|
| 6. Depress Stop Button | Sequencing and detection is inactivated. Display retains data until reset. |
| 7. Set main position switch on "SELECT." Set display switch on desired species.
Depress reset button.
Depress start button. | Wavelength sequencing is inactivated; display of desired species is upgraded every sample time. All other species (except N ₂) not monitored. Normalization and calibration with respect to N ₂ and temperature carried out as in Steps 5.1, 5.2 and 5.3. |

e. Physical Equipment Considerations

As seen in Figure 28, the conceptual design system is built in two transportable shelters, each capable of being transported separately without disassembly. This illustration shows the laser transceiver mounted and operating on the transporting vehicle. The data collection terminal has been removed from the vehicle to where it may be placed during operation. The system will operate with either or both shelters mounted on or off the vehicle. The truck illustrated is a commercially available model, such as an International Harvester Loadstar 1700, with a 234 wheelbase, a low sided steel platform body, and a hydraulically operated tail gate. This vehicle will not be a deliverable end item.

The laser transceiver, consisting of the laser, transmitter, receiver and monochrometer subsystems, closed circulating cooling system, output section of the high voltage power supply, high pressure nitrogen supply, vacuum pump, and air compressor, will be housed in a lightweight, high strength, insulated all-weather, mobile shelter. This commercially available, square corner, military electronic type equipment shelter has roof, floor, walls, and doors constructed of inner and outer aluminum skins with foamed-in-place polyurethane insulation, reinforced with aluminum extrusions for structural strength and a flexible equipment installation scheme. Air exhaust fans and filtered air inlets will ensure a well ventilated enclosure. Heating will be accomplished by thermostatically controlled portable electric heaters. Air conditioning equipment is not contemplated at this time. Lifting and tie-down swivel type rings, combined with a lifting/tie-down sling supplied with the shelter, will assure adequate attachment to the transporting vehicle, and provide a means of installing and removing the shelter from the vehicle. Vibration isolation skids will be mounted on the underside of the shelter. These skids will reduce vibration within the enclosure during transit and while at the test site.

A large door at the end of the shelter toward the rear of the transporting vehicle will allow easy equipment access. Three quartz windows, one for transmitting and two for receiving, will be installed in this door. A smaller side door and rugged portable steel steps will provide convenient personnel access.

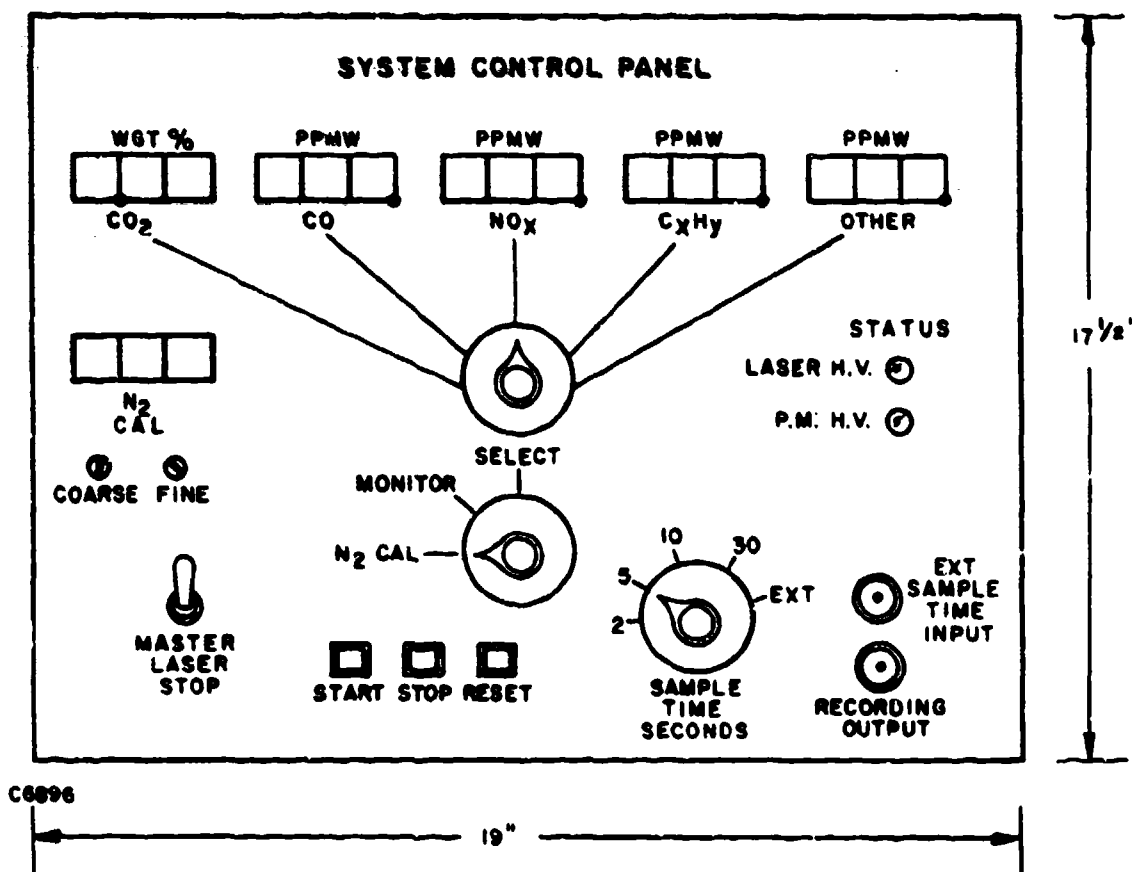


Figure 33 Control and Display Front Panel

The overall size of this shelter is approximately 16' long x 7.5' wide x 7' high, and it will weigh approximately 2500 pounds unloaded, and 8100 pounds full equipped.

The data collection terminal consists of the laser control section, high voltage power supply control section, and data display/control section, and will be housed in a commercially available acoustical enclosure. Interlocking panels of perforated interior and solid exterior skins with sound absorption material between, and rigid channel construction for strength will form the wall and roof panels. Floor panels will be constructed from solid sheet metal inner and outer skins, supported by a rigid filler and reinforcement angles. Vibration isolation skids will be mounted on the underside of the shelter. These skids will reduce vibration within the enclosure during transit and while at the test site. Lifting and tie-down will be accomplished in the same manner as with the laser transceiver shelter. The resulting structure will be suitable for use in the environmental conditions we expect to encounter while performing its primary function; that is, isolation from high sound pressure levels. With the shelter in the "near field" to the engine being operated, personnel will be required to wear ear protection.

This shelter will be equipped with air conditioning and thermostatically controlled electric heat. A door at one end of the shelter will allow easy equipment and personnel access. A window in the opposite end will allow a view of the test area. The overall size of this shelter is approximately 7.5' long x 4' wide x 7' high, and it will weigh approximately 2100 pounds unloaded, and 2900 pounds fully equipped.

The acoustic attenuation properties of both the laser transceiver shelter and the data collection terminal shelter, as obtained from vendors, is shown in Figure 34 as a plot of attenuation in dB as a function of acoustic frequency in cycles per second. Figure 35 shows the sound level expected from a typical engine exhaust, together with curves showing the sound level from the same engine as attenuated by the shelters according to the attenuation data of Figure 34.

A structural dynamic analysis of a typical laser transceiver equipment configuration was carried out, assuming that it was exposed to a full 130 dB overall sound pressure level without attenuation. This analysis showed that with proper design, the sound pressure levels to be expected are a relatively benign environment and should cause no appreciable stress or deflection of the optics. If felt desirable, it should be noted that there exists the possibility of testing the system in the USAF acoustic chamber facility.

f. External Electric Power Requirements

The transceiver shelter will not contain its own source of power; it will depend on an external source. A 120/208 VAC, 60 Hz, 3 phase, 5 wire

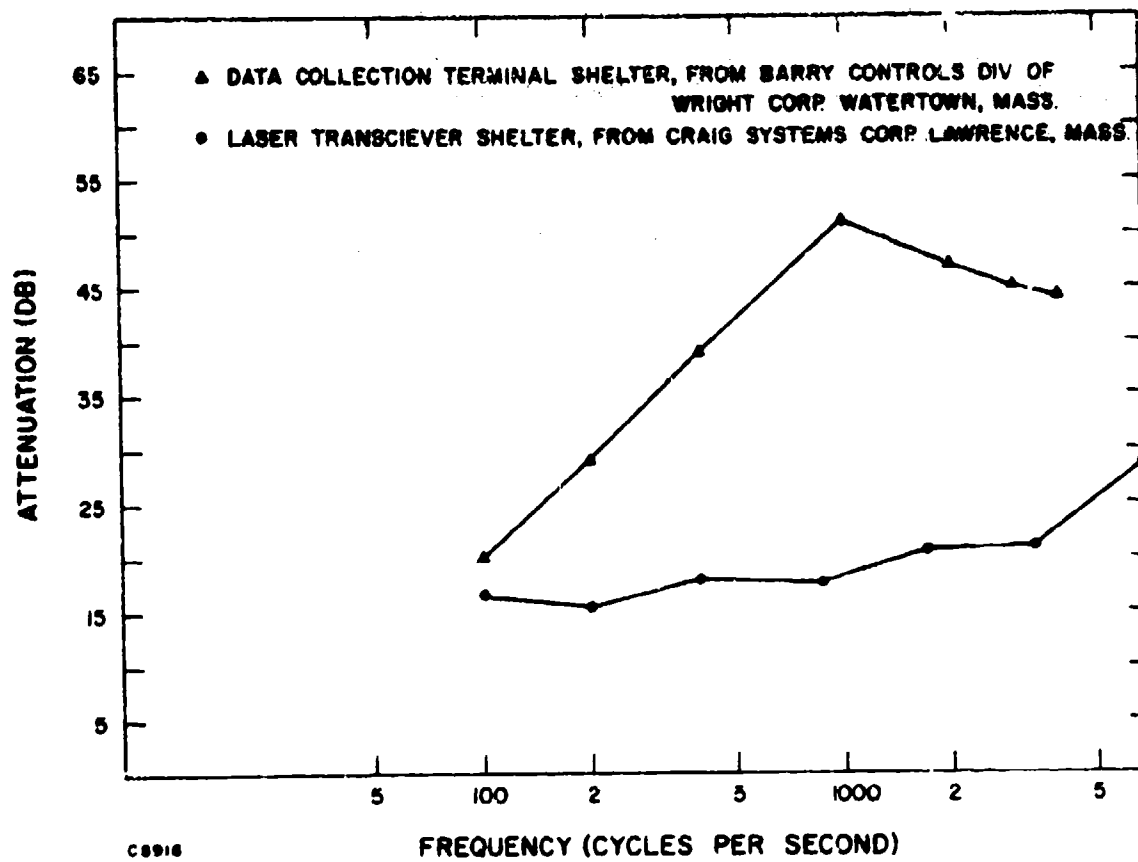


Figure 34 Acoustic Attenuation Characteristics of Equipment Shelters

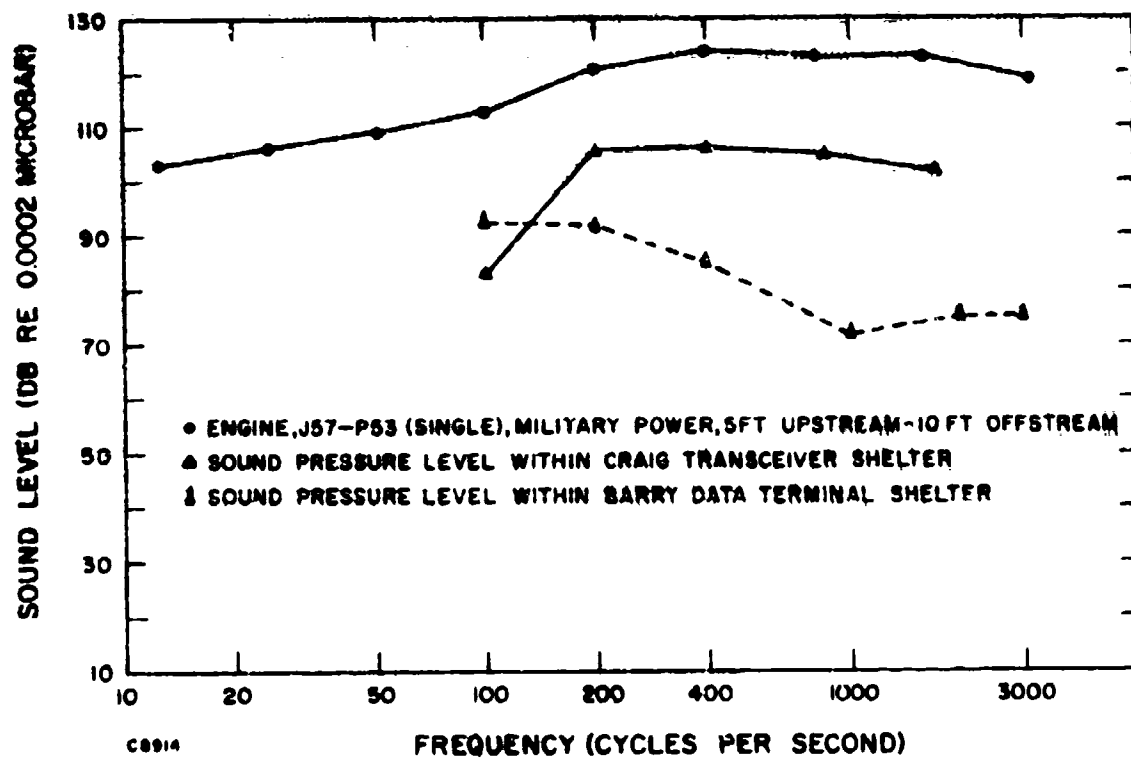


Figure 35 Acoustic Levels Encountered from Typical Engine within and without Shelters

150 ampere electrical service will be required and may originate at a commercial source of power, or at a portable ground power unit with this capability. The input power cable will terminate at the transceiver shelter, where the power distribution equipment will be located.

The 21000 BTU/hour cooling system, the low volume air compressor, the 5 cubic feet/minute vacuum pump, the receiver and monochrometer subsystems, lighting, heating, and ventilating equipment located within this shelter will require approximately 60 amperes.

A branch circuit with a 60 ampere capability will deliver power to the data collection terminal for the 20 kilovolt 800 milliampere power supply control section, the laser control section, the data display/control section, lighting, heating, and air conditioning equipment. The whole system will have a 30 ampere contingency safety factor. Connection between the shelters will be via a 5-wire power cable.

The nature of the equipment contained in each shelter is such that ground rods will be required. These rods will be driven in close proximity to each shelter, and connected to a ground buss within the shelter. All equipment requiring high voltage will be connected to the ground buss, as well as being grounded via the ground carried in all AC power circuits.

REFERENCES

1. Sharma, R., AERL, private communication.
2. Lapp, Goldman and Penny, paper 71-1084, Joint Conference on Sensing of Environmental Pollutants, Palo Alto, November 8-10, 1971.
3. Schwiesow, R.L., paper 71-1086, Joint Conference on Sensing of Environmental Pollutants, Palo Alto, November 8-10, 1971.
4. Leonard, Donald A., Program Summary, Development of a Laser Raman Aircraft Turbine Engine Exhaust Emissions Measurement System, AERL, RN 892, July 1971.
5. Fouche and Chang, Appl. Phys. Letters, 18, 579 (1971).
6. Murphy, Holzer and Bernstein, Appl. Spectroscopy 23, 211 (1969).
7. Herzberg, Gerhard, "Spectra of Diatomic Molecules," Van Nostrand Co., 1950.
8. Johnson, M.C., "Raman Remote Gas Sensor," paper CP-31A, Clean Air Congress, Washington, D.C., December 6-11, 1970.
9. Hall and Blacet, J. Chem. Phys. 20, 1745 (1952).
10. Sakurai and Broida, J. Chem. Phys. 50, 2404 (1969).
11. Moon, P., J. Franklin Institute 230, No. 5 (1940).
12. Sharma, R., "Polarization Characteristics of Raman Scattered Radiation as a Function of Angle Between Incident and Scattered Beams," to be published.

APPENDIX IV
REMOTE PROBING OF A VOLUME
AT FINITE CONJUGATES

by

J. L. Monroe

Reprinted from Optical Engineering 13, 79 (1974).

Remote Probing of a Volume at Finite Conjugates

J. L. MUNROE

Avco Everett Research Laboratory, Inc.

(Received February 5, 1974)

ABSTRACT

When a remote volume is irradiated and the resulting isotropically scattered signal collected by an optical system, the calculation of the resulting signal is not easily performed. However, for rectangular apertures, the expressions are concise and lend themselves to ordinary numerical techniques. These expressions are presented with sample results.

INTRODUCTION

A recurring problem in optics is the remote probing of a volume at finite conjugates by a non-imaging device such as a spectrometer. A typical example of this problem would be Raman scattering measurements of a gaseous exhaust, a problem which has been considered by Nielsen.⁽¹⁾⁽²⁾ The illumination of the probed volume is both a relatively simple part of the problem and strongly dependent on the type of light source used. In this treatment, the illumination is modeled as an expanding rectangle of uniform irradiance, a model which is representative of many illumination geometries and yet allows the properties of the receiving system to be easily observed. The results of this treatment are readily extended to cases involving other illumination geometries.

Similarly, isotropic scattering is assumed within the probed volume to allow the properties of the receiving optics to be easily treated. This treatment can also be extended to cases involving less ideal scattering distributions.

The signal collected from an isotropically scattering point is proportional to the effective solid angle into which it can radiate. As shown in Appendix A, the solid angle subtended by a rectangle at a general point can be expressed in relatively concise closed form. For this reason, all apertures

are assumed to be rectangular, an assumption which results in extensive savings in computational time and applies directly to slits, monochrometers and spectrometers. This treatment can be extended to circular apertures at the expense of an increase in computational complexity.

GEOMETRICAL CONSIDERATIONS

The amount of flux that can be accepted by a spectrometer is limited by the etendue of the spectrometer, the product of the area of the entrance slit and the solid angle subtended by the spectrometer optics at the entrance slit. This is the principle of conservation of radiance. The implication is that the collecting optics can do no more than fill the spectrometer slit and the spectrometer optics. Consequently, in designing the collecting optics (the optics that relays flux from the volume being probed to the spectrometer), the output cone is fixed as being identically the acceptance cone of the spectrometer optics.

The etendue relationship is also maintained between the entrance window (the image of the spectrometer slit formed within the volume being probed) and the solid angle subtended by the entrance pupil at the entrance window. This situation is shown schematically in Figure 1 and Figure 2.

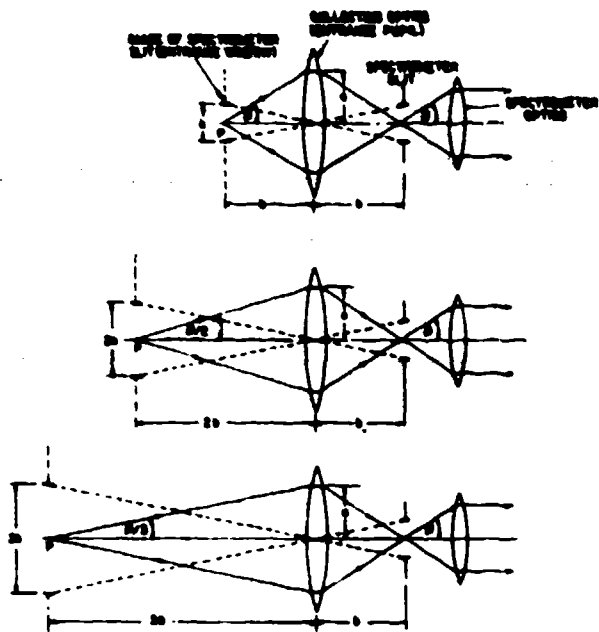


Figure 1. For a fixed pupil, the increase in the size of the entrance window from focusing further into the volume is exactly offset by the decrease in solid angle into which each point "P" effectively radiates.

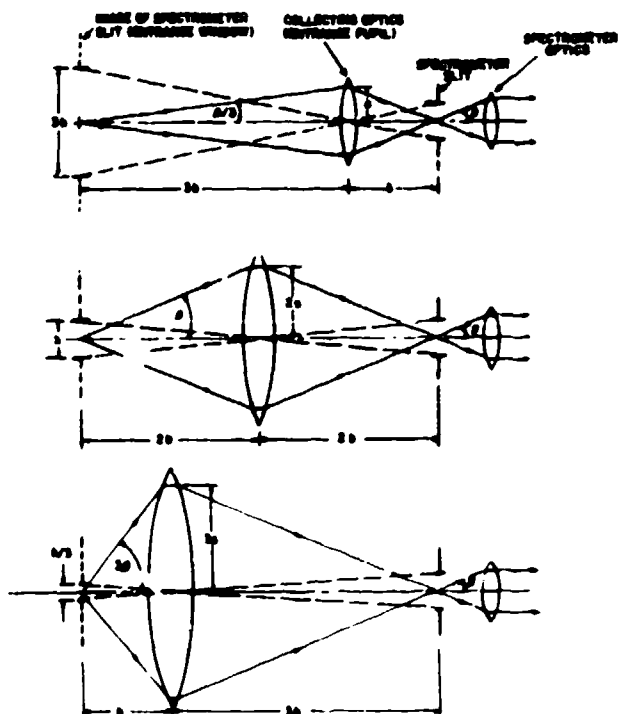


Figure 2. For a fixed separation between the spectrometer and the probed volume, the increase in solid angle collected by moving the collecting optics closer to the volume is exactly offset by the decrease in the size of the entrance window. Compare with Figure 1.

Note from Figure 2 that for a given geometry, there is an upper bound on useful aperture size for the collecting optics; apertures larger than this upper bound result in no additional signal.

SIGNAL COLLECTED

A scattering medium can be treated as a volumetric distribution of point sources or equivalently as volumetrically varying intensity function $J(X, Y, Z)$ where

$$J \text{ (watts/steradian/unit volume)} = HNo$$

and

$$H \text{ (watts/unit area)} = \text{Irradiance of incident flux.}$$

$$N \text{ (volume}^{-1}\text{)} = \text{Number of scattering points per unit volume.}$$

$$\sigma \text{ (area)} = \text{Scattering cross-section}$$

The flux, F , collected from this intensity distribution and presented to the spectrometer is proportional to the solid angle Ω subtended by the effective pupil area (defined below) at the center of a differential radiating volume, dV , in question

$$\frac{dF}{dV} \text{ (watts/unit volume)} = J(X, Y, Z) \Omega(X, Y, Z)$$

Defining Z as the optical axis, it is convenient to rewrite this as a summation for sheets of equal ΔZ

$$\Delta F(Z) = \sum_Y \sum_X J(X, Y, Z) \Omega(X, Y, Z) \Delta X \Delta Y \Delta Z$$

If the number of scattering points per unit volume is a constant, since σ is an experimental constant, the relative strength of the signal arriving from each sheet of width ΔZ can be obtained from

$$\Delta F(Z) \propto \sum_Y \sum_X H(X, Y, Z) \Omega(X, Y, Z) \Delta X \Delta Y \Delta Z \quad (1)$$

Since the irradiance distribution $H(X, Y, Z)$ is usually well known and easily described for a given illumination system, the solution of (1) depends upon a complete description of $\Omega(X, Y, Z)$, the solid angle subtended by the effective pupil area at the point (X, Y, Z) .

THE EFFECTIVE SOLID ANGLE

Consider a point "P" within the scattering volume and, for simplicity of explanation, lying on the axis of symmetry (Figure 3). From Figure 3, it is clear that the rays from point "P" which enter the spectrometer slit must satisfy two conditions:

1. The rays must pass through the entrance window.
2. The rays must enter the pupil of the collecting optics (taking into account any obscurations).

The locus of these rays is the effective solid angle into which the point "P" radiates signal.

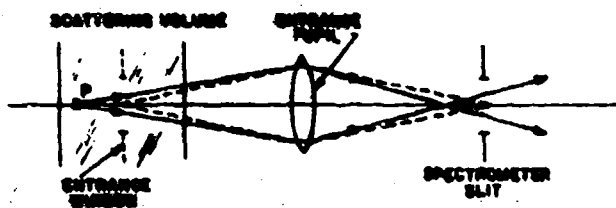


Figure 3. Geometry of Point "P" within Scattering Volume Radiating into Spectrometer Slit.

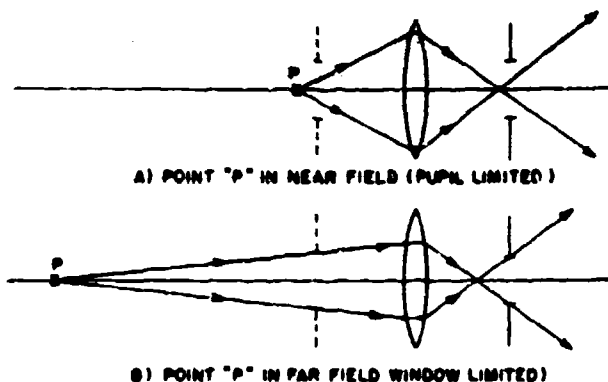


Figure 4. Solid Angle Limitations for Points in Near Field and Far Field.

Figure 4 shows the two extreme regions for a simple aperture; in the immediate region of the window (the region producing most of the signal), the solid angle is limited entirely by the pupil of the optical system (near field) whereas far from the immediate region of the entrance window, the solid angle is limited entirely by the size of the entrance window.

When the window is rectangular, there is a transition region (intermediate field) where the solid angle is also limited by the narrow dimension of the window. This transition is shown schematically in Figure 5 in the form of what available aperture (cross-hatched) the point would "see" as it moves from the near field to the far field.

Figure 5 illustrates why slit width can be so much more sensitive than slit height; for a slit, the solid angle can decrease by several magnitudes before the slit height has any appreciable effect.

When the entrance window is much smaller than the entrance pupil, the evaluation of (1) can be simplified by assuming symmetry for positive and negative displacements from the entrance window. This situation frequently occurs, for example, when a spectrometer entrance slit is imaged within a luminous volume at small magnification.

For calculating the solid angle subtended by the available aperture, all that need be known are the size and location of the entrance window and the entrance pupil. For many geometries, the range of interest along the optical axis is small compared to the distance to the entrance window and thus the angular extent of the external optics as measured from "P" is all that need be known. Since parallax is negligible, the collecting optics can be represented as a pupil subtending the proper angles and located on a plane at some convenient distance which is large compared to the slit dimensions.

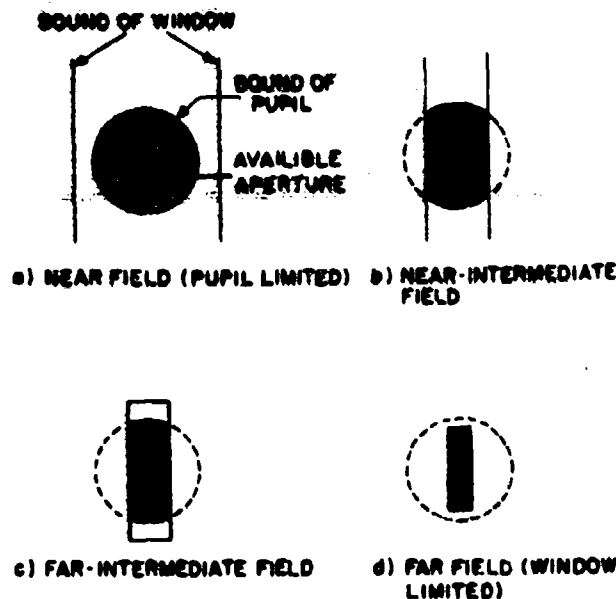


Figure 5. Apparent Aperture Seen by Point "P" as it Shifts from Near Field to Far Field.

CALCULATION OF EFFECTIVE SOLID ANGLE FROM POINT "P"

Calculation of the available solid angle Ω "seen" from a general point "P" is greatly simplified if all apertures and obscurations are assumed to be rectangular since the solid angle subtended by a rectangle at a general point "P" can be solved in relatively concise closed form (see Appendix A). This assumption causes no significant loss of generality.

The solid angle Ω subtended by a rectangle at a point is given by

$$\begin{aligned} \Omega = & \tan^{-1} \left(\frac{A_1 A}{D \sqrt{A_1^2 + A^2 + D^2}} \right) \\ & - \tan^{-1} \left(\frac{B_1 A}{D \sqrt{B_1^2 + A^2 + D^2}} \right) \\ & - \tan^{-1} \left(\frac{A_1 B}{D \sqrt{A_1^2 + B^2 + D^2}} \right) \\ & + \tan^{-1} \left(\frac{B_1 B}{D \sqrt{B_1^2 + B^2 + D^2}} \right), \end{aligned} \quad (2)$$

where:

$$A = Y_c + \frac{H}{2} - Y \quad B = Y_c - \frac{H}{2} - Y$$

$$A_1 = X_c + \frac{W}{2} - X \quad B_1 = X_c - \frac{W}{2} - X$$

$(X_c, Y_c, 0)$ = Geometric Center of Rectangle

H = Height of Rectangle

W = Width of Rectangle

(X, Y, D) = Coordinate of point at which solid angle is being calculated.

By inspection it can be seen that for unrotated rectangles the portion of one rectangle which can be viewed through a second rectangle is itself a rectangle. Consequently, the calculation of the available solid angle for an all rectangular optical system (including rectangular obscurations) reduces itself to the determination of the portion of the rectangle which can be "viewed". Appendix B details a procedure for calculating the "viewed" rectangle and the results of Appendix B are used with the results of Appendix A to calculate the associated solid angle. The net solid angle is thus the solid angle subtended by the entire aperture minus the solid angles associated with the obscurations.

ILLUMINATION CONSIDERATIONS

A scattering volume is not self-luminous; that is, all scattering is of the incident flux and thus the results depend upon the geometry of the illumination system. However, with reasonable care in the system design, the resultant signal will only depend upon the total incident flux.

For a geometry in which the entrance window is much smaller than the entrance pupil, most of the signal received is

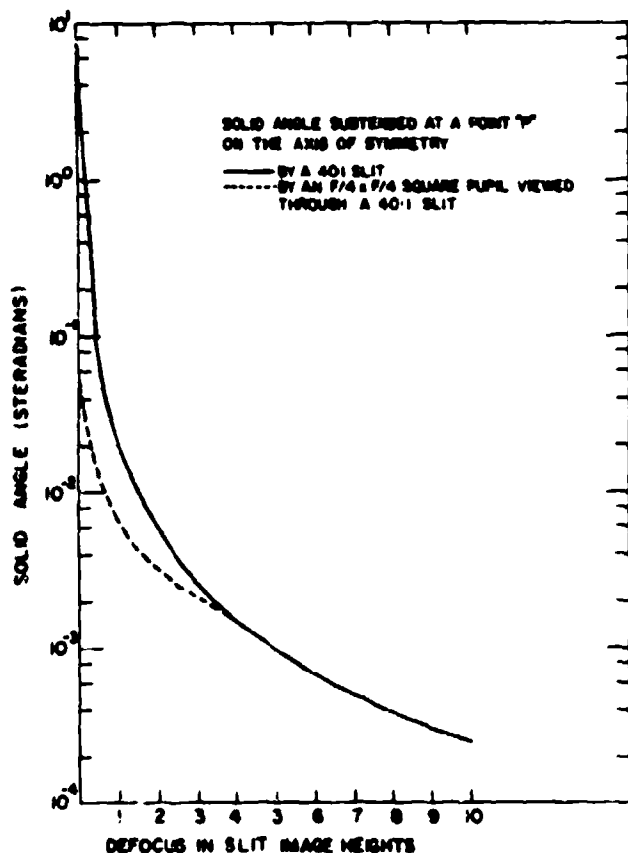


Figure 6. Theoretical Limits of a Typical Geometry.

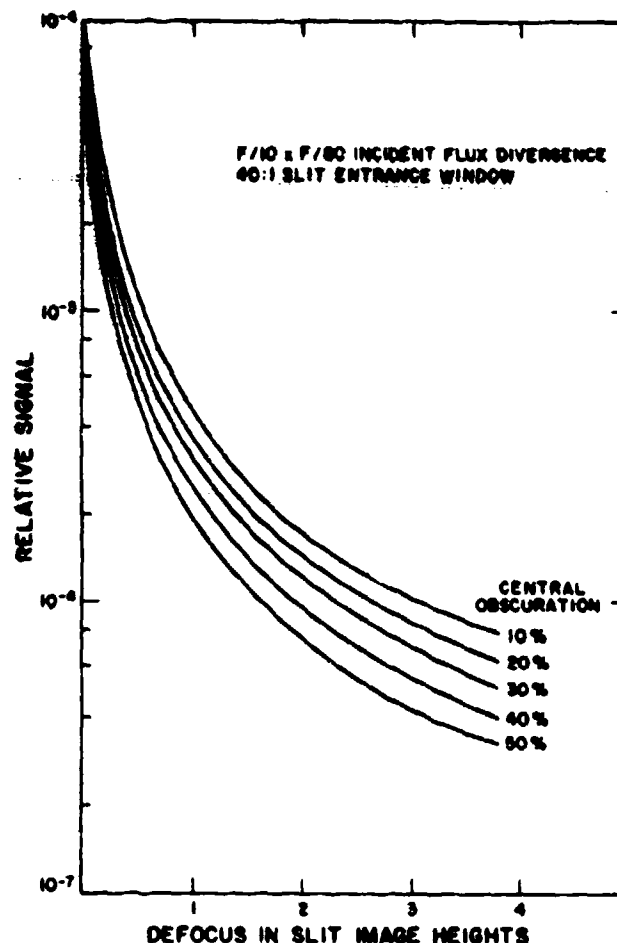


Figure 7. Relative Signal for $F/4 \times F/4$ Square Pupil with Varying Central Obscuration (by Area).

from the immediate region of the entrance window. Thus, to maximize the signal, all of the incident flux should pass through the entrance window. In general, it matters little in terms of total signal received if the window is underfilled, but if the window is overfilled, the signal will drop almost proportionally to the fraction of flux missing the window.

Other parameters such as the choice of coaxial or extra-axial illumination must be considered in terms of the whole experiment. Effects to be considered include resultant blockages of the entrance pupil and strong scattering sources outside the volume of interest.

For the sample calculations included, the illumination was modeled as a uniform rectangle focused coincident with the entrance and expanding as a uniform rectangle of decreasing irradiance on either side of focus. This was consistent with experimental results for the particular system of interest but in no way is this analytical method limited to such a simplified illumination model.

TYPICAL CALCULATIONS

The limitation on the depth of the volume which significantly contributes to the signal is set by the solid angle subtended at each point "P" within the volume by the fraction of the entrance pupil which can be "seen" through the entrance window. This is illustrated in Figure 6 for the ideal cases of infinite collecting optics (solid line) and a square

pupil subtending $F/4 \times F/4$ at the entrance window (dashed line). The choice of (spectrometer) slit image height as a unit of length is convenient because the optical system can be modified without changing the results—only the conversion to "defocus" (axial separation from gaussian image) need be in absolute units.

Figure 6 demonstrates that the fundamental limitation on signal collected away from gaussian focus is the size of the window rather than the size of the pupil of the collecting optics. The solid angle subtended by an infinite pupil viewed through a 40:1 window is only significantly different from the solid angle subtended by an $F/4 \times F/4$ pupil viewed through the same window in the immediate neighborhood of gaussian focus. Note that the infinite aperture case is identical to the solid angle subtended by the window itself.

Calculations (not shown) for the effects of incident flux spreading with defocus showed the effects to be so small as to be imperceptible when combined with the effects of Figure 6. Similarly, as long as the incident flux falls within the entrance window, the return signal is maximized. For these reasons, the following figures which include effects of the incident flux assume the incident flux to be representable by an arbitrary $F/10 \times F/80$ divergence rate and a coincident image at the entrance window.

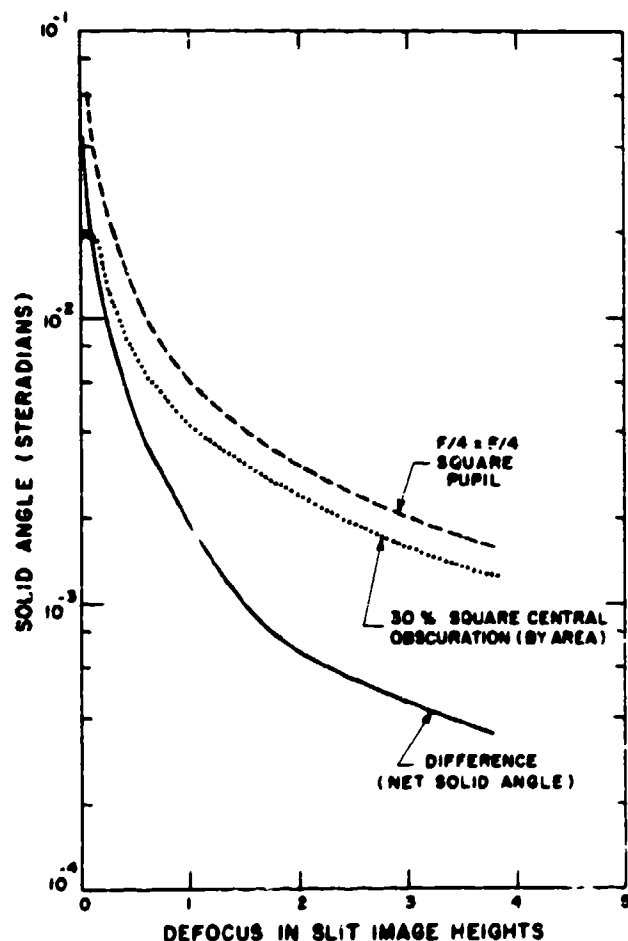


Figure 8. Solid Angles Subtended at a Point on the Axis of Symmetry through a 40:1 Slit Showing Reduction of Net Solid Angle.

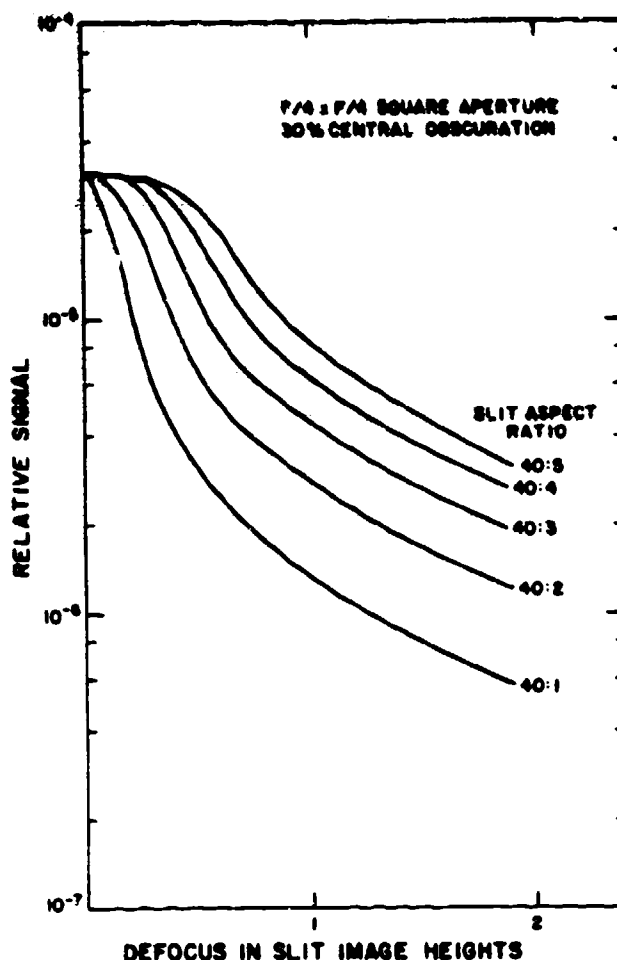


Figure 9. Relative Signal for Varying Slit Width.

Figure 7 demonstrates that even under the most ideal circumstances, most of the signal collected is from a very small region around the entrance window. Figure 5 shows the relative signal arriving from various depths in the volume for the nominal incident flux distribution and a nominal $F/4 \times F/4$ collecting system with varying central obscuration. Note that both the ordinate and abscissa have been expanded from that on Figure 6.

Figure 8 is a detail for a typical case showing how a central obscuration compounds the lack of signal with depth. The net solid angle (solid line) is now the difference of the solid angles subtended by the unobscured pupil (dashed line) and obscuration (dotted line) as "seen" through the entrance window.

Figure 9 shows the effect of widening the spectrometer slit for a typical geometry. Note the change in the ordinate scale. The resultant gain in signal collected is nearly proportional to the increase in slit width, but still the signal is from a small region around the entrance window.

CONCLUSIONS AND SUMMARY

For a remote measurement, the upper bound on signal is set by the etendue of the detector. With properly designed collecting optics, this upper bound can nearly be achieved in practice. For a spectrometer detector, properly designed, col-

lecting optics merely means that the entrance slit and entrance pupil of the spectrometer are filled; when these conditions are satisfied, the return signal is maximum.

Most of the parameters of the collecting optics, including diameter and focal length, serve to control the location and extent of the volume which contributes signal, but have virtually no effect on the total amount of signal collected. Increases in signal can only come from increasing the etendue of the detector or by increasing the amount of flux incident on the scattering medium.

The strength of the return signal is relatively insensitive to the geometry of the flux incident upon the scattering medium provided that the flux passes through the entrance window of the collecting system. Flux that does not pass through the entrance window is effectively lost.

When the entrance window is much smaller than the entrance pupil, the return signal is predominantly from the immediate vicinity of the entrance window. The extent of the volume contributing significant signal is typically of the same magnitude as the long dimension of the entrance window (which is itself an image of the spectrometer entrance slit). The long dimension of the entrance window (or slit image height) thus is a convenient unit of measure for depth probed.

APPENDIX A

CALCULATION OF THE SOLID ANGLE SUBTENDED BY A RECTANGLE AT A POINT

Consider a rectangle of height H and width W centered at a point (X_c, Y_c) (see Figure A-1). A differential area dA within the rectangle subtends a differential solid angle $d\Omega$ at a point $P(U, V, D)$

$$d\Omega = \frac{dA \cos \theta}{R^2}$$

where:

$$R^2 = (U - X)^2 + (V - Y)^2 + D^2$$

$$\cos \theta = \frac{D}{R}$$

Hence the solid angle subtended by the rectangle at the point P is:

$$\Omega = \int_{(X_c - \frac{W}{2})}^{(X_c + \frac{W}{2})} \int_{(Y_c - \frac{H}{2})}^{(Y_c + \frac{H}{2})} \frac{D dY dX}{[(X-U)^2 + (Y-V)^2 + D^2]^{3/2}}$$

The Y integration can be put into the form (see Reference 1)

$$\int \frac{d\phi}{(a + b\phi^2)^{3/2}} = \frac{\phi}{a\sqrt{a + b\phi^2}},$$

By a change of variables

$$\phi = Y - V$$

$$\phi = X - U$$

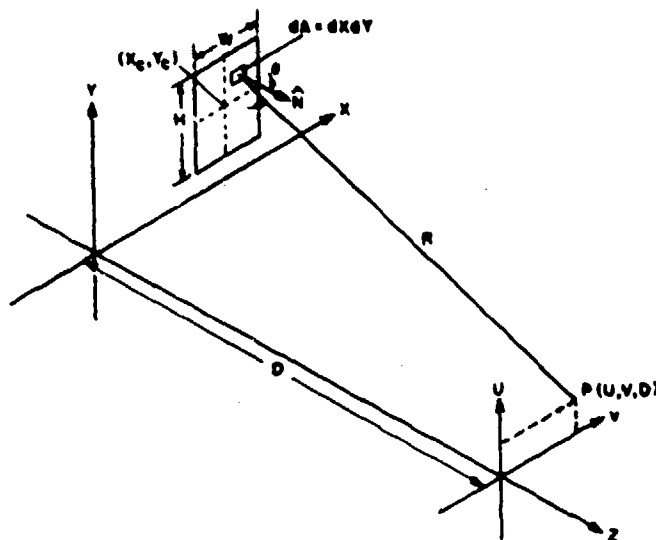


Figure A-1. Geometry for Calculation of Solid Angle Subtended by Rectangle at Point.

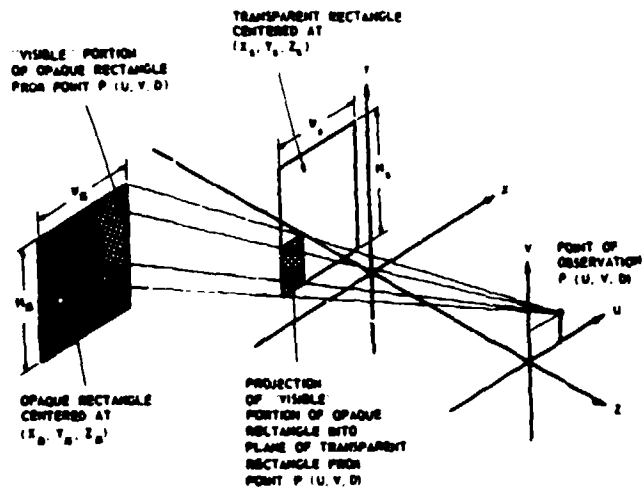


Figure B-1. Geometry for Calculation of "Visible" Portion of Opaque Rectangle Viewed through a Transparent Rectangle from a General Point "P".

Resulting in

$$\Omega = \tan^{-1} \frac{A_1 A}{D\sqrt{A_1^2 + A^2 + D^2}} - \tan^{-1} \frac{B_1 A}{D\sqrt{B_1^2 + A^2 + D^2}} - \tan^{-1} \frac{A_1 B}{D\sqrt{A_1^2 + B^2 + D^2}} + \tan^{-1} \frac{B_1 B}{D\sqrt{B_1^2 + A^2 + D^2}}$$

Where

$$A = Y_c + \frac{H}{2} - V$$

$$B = Y_c - \frac{H}{2} - V$$

$$A_1 = X_c + \frac{W}{2} - U$$

$$B_1 = X_c - \frac{W}{2} - U$$

APPENDIX B

CALCULATION OF "VISIBLE" PORTION OF OPAQUE RECTANGLE VIEWED THROUGH A TRANSPARENT RECTANGLE FROM A GENERAL POINT "P"

Consider a transparent rectangle of height H_s and width W_s centered at (X_s, Y_s, Z_s) and an opaque rectangle of height H_m and width W_m centered at (X_m, Y_m, Z_m) (Figure B-1).

The four corners of the transparent rectangle are:

$$SLU = \left(X_s - \frac{W_s}{2}, Y_s + \frac{H_s}{2} \right) \quad SRU = \left(X_s + \frac{W_s}{2}, Y_s + \frac{H_s}{2} \right)$$

$$SLB = \left(X_s - \frac{W_s}{2}, Y_s - \frac{H_s}{2} \right) \quad SRB = \left(X_s + \frac{W_s}{2}, Y_s - \frac{H_s}{2} \right)$$

Similarly the four corners of the opaque rectangle are:

$$MLU = \left(X_m - \frac{W_m}{2}, Y_m + \frac{H_m}{2} \right) \quad MRU = \left(X_m + \frac{W_m}{2}, Y_m + \frac{H_m}{2} \right)$$

$$MLB = \left(X_m - \frac{W_m}{2}, Y_m - \frac{H_m}{2} \right) \quad MRB = \left(X_m + \frac{W_m}{2}, Y_m - \frac{H_m}{2} \right)$$

When "viewed" from a point $P(U, V, D)$, the portion of the opaque rectangle which is "visible" through the transparent rectangle is that portion of the opaque rectangle which when projected into the plane of the transparent rectangle from the point "P" lies within the transparent rectangle (Figure B-1).

The center of the projected opaque rectangle in the plane of the transparent rectangle is (X_p, Y_p) , where

$$X_p = U + (X_m - U) \frac{Z_s - D}{Z_m - D}$$

$$Y_p = V + (Y_m - V) \frac{Z_s - D}{Z_m - D}$$

The four corners of the projected opaque rectangle are:

$$PLU = \left(X_p - \frac{W_p}{2}, Y_p + \frac{H_p}{2} \right) \quad PRU = \left(X_p + \frac{W_p}{2}, Y_p + \frac{H_p}{2} \right)$$

$$PLB = \left(X_p - \frac{W_p}{2}, Y_p - \frac{H_p}{2} \right) \quad PRB = \left(X_p + \frac{W_p}{2}, Y_p - \frac{H_p}{2} \right)$$

Where:

$$H_p = H_m \left| \frac{Z_s - D}{Z_m - D} \right|$$

$$W_p = W_m \left| \frac{Z_s - D}{Z_m - D} \right|$$

and the absolute value signs serve to keep lengths and widths positive.

Note that the case of $Z_m = D$ (point of observation within plane of opaque rectangle) is indeterminate but is a trivial special case which can be solved by inspection.

To compute the bounds of the "visible" portion of the opaque rectangle, Fortran type Min and Max functions can be resorted to. These functions translate respectively as the minimum argument within the parentheses and the maximum argument within the parentheses.

$$LEXT = \text{MAX} \left(X_s - \frac{W_s}{2}, X_p - \frac{W_p}{2} \right)$$

$$REXT = \left(\text{MIN} X_s + \frac{W_s}{2}, X_p + \frac{W_p}{2} \right)$$

$$UEXT = \left(\text{MIN} Y_s + \frac{H_s}{2}, Y_p + \frac{H_p}{2} \right)$$

$$BEXT = \left(\text{MAX} Y_s - \frac{H_s}{2}, Y_p - \frac{H_p}{2} \right)$$

From examination of Figure B-2, the following logic can be applied:

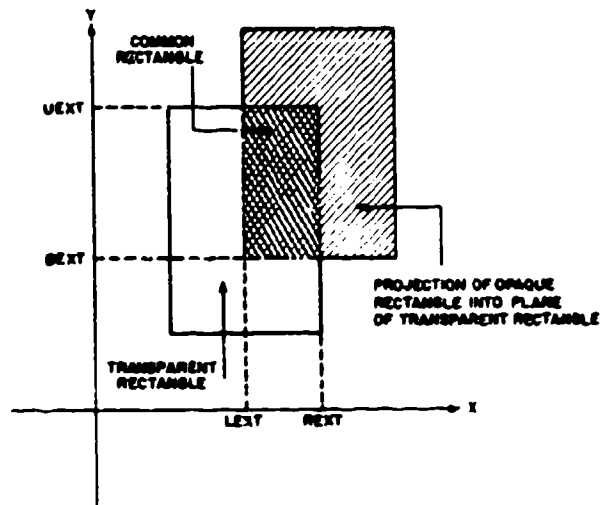


Figure B-2. Determination of Bounds of Rectangle Common to Transparent Rectangle and Projection of Opaque Rectangle into Plane of Transparent Rectangle.

A. If $REXT < LEXT$

or

If $UEXT < BEXT$

no portion of the opaque rectangle is "seen".

B. If $REXT - LEXT = W_s$

and

If $UEXT - BEXT = H_s$

the opaque rectangle fills the transparent rectangle, otherwise the general case:

Center of common rectangle = (X_B, Y_B)

$$X_B = (L_{EXT} + R_{EXT})/2$$

$$Y_B = (U_{EXT} + B_{EXT})/2$$

The height of the common rectangle is H_B , the width W_B

$$H_B = U_{EXT} - B_{EXT}$$

$$W_B = R_{EXT} - L_{EXT}$$

For all cases, the common rectangle is in the plane of the transparent rectangle

$$Z_B = Z_S$$

ACKNOWLEDGEMENTS

I would like to thank Dr. P. G. DeBaryshe for the many invaluable discussions throughout this effort. This effort was supported by the Air Force Aero Propulsion Laboratory, Air Force Systems Command, United States Air Force, Wright-Patterson Air Force Base, Ohio, under contract No. F33615-71-C-1875.

REFERENCES

1. J. Rud Nielsen, J. Opt. Soc. Am. 20, 701 (1930).
2. J. Rud Nielsen, J. Opt. Soc. Am. 37, 499 (1947).
3. G. Pettit Bois, "Tables of Indefinite Integrals," Dover Publications, Inc. New York, 1961.

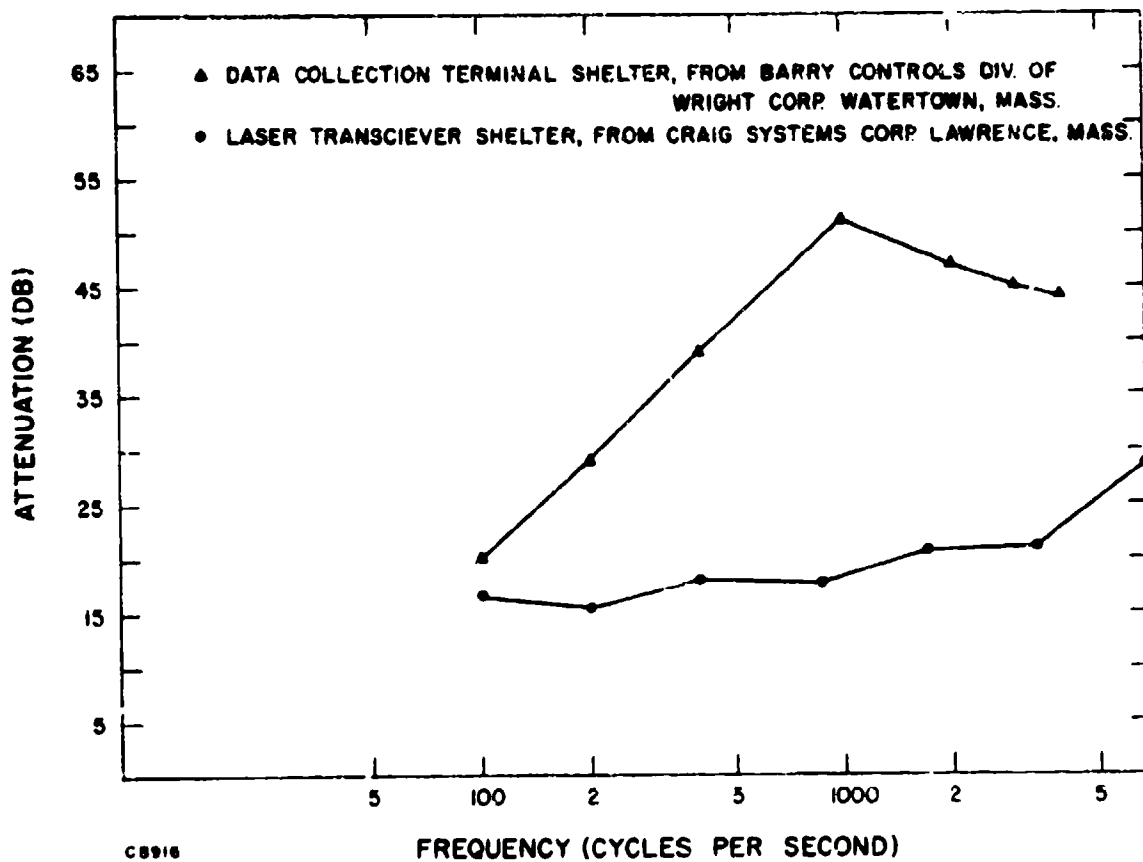


Figure 34 Acoustic Attenuation Characteristics of Equipment Shelters